USING CHEMO-THERMO-MECHANICALLY COUPLED CRYSTAL PLASTICITY SIMULATIONS TO INVESTIGATE THE PROCESS OF WHISKER FORMATION IN β – SN THIN FILMS

By

Aritra Chakraborty

A DISSERTATION

Submitted to
Michigan State University
in partial fulfillment of the requirements
for the degree of

Chemical Engineering – Doctor of Philosophy

2019

ABSTRACT

USING CHEMO-THERMO-MECHANICALLY COUPLED CRYSTAL PLASTICITY SIMULATIONS TO INVESTIGATE THE PROCESS OF WHISKER FORMATION IN β – SN THIN FILMS

By

Aritra Chakraborty

β-Sn (Sn) whiskers growing from tin coatings in electronic devices have been a serious concern to its reliability as they nucleate in unpredictable locations, can grow to a length of several millimeters, and hence, are able to short-circuit different parts of an electronic assembly. It was found that alloying Sn with lead (Pb) mitigated whisker formation. However, with the drive towards lead-free electronics from early 2000, due to the hazardous nature of Pb, reliability problems due to tin whiskers resurfaced, thereby, rekindling an interest to understand their governing mechanisms in order to propose efficient mitigation strategies. With such a drive, significant research has been published highlighting different whisker characteristics (morphology, propensity, and kinetics). However, to date, there is no unified theory that could explain the formation of these filamentous structures, with sometimes even contradicting observations between different research groups. Despite some contradictions, it is widely accepted that tin whiskers are a result of stress-driven diffusion in the film, with diffusion occurring primarily through the grain boundary network. Stresses in these films can originate from various sources, such as, upon deposition, indentation, thermal expansion mismatch, and by formation of voluminous Cu_6Sn_5 intermetallic compounds at the interface between a copper substrate and the film. Among these sources, thermal straining has been used to deliberately control the stresses in films deposited on a Silicon (Si) substrate (having a lower thermal expansion coefficient than β-Sn) to analyze the effect of applied stress on whisker propensity.

In the present work such experimental conditions of thermally straining β-Sn films is mimicked using simulaitons, and the resulting mechanics and kinetics are investigated using fully coupled chemo-thermo-mechanical simulations in a crystal plasticity continuum mechanical framework. The goal of the is to identify crystallographic and geometric factors that modu-

late the stress-driven transport of atoms along the grain boundary network. In that regard, first a thermo-mechanical study is done that highlights the dominating influence of global film-texture compared to grain geometry and grain-size distribution. It is also established that whisker nucleation is indeed a local phenomenon as no long-range stress gradients are found. More involved chemo-thermo-mechanical simulations are performed to understand the kinematics and kinetics of atom redistribution in these thermally strained films for two loading conditions. Based on these simulations it is inferred that plastic relaxation plays a dominant role in stress evolution compared to diffusion kinetics. The dominant role of film-texture on determining whisker nucleation sites (low compressive locations in the biaxially strained film) can be attributed to the high anisotropy of the body-centered tetragonal β-Sn crystal structure that involves an elastic anisotropy, a thermal anisotropy, and a very complex plastic anisotropy. The complex plastic anisotropy arises due to the availability of multiple slip families with a small number of slip systems per family. Plasticity readily happens in Sn even at room temperature, which corresponds to about 0.6 T_{m}, and, therefore, requires the establishment of an accurate constitutive description.

In that regard, the second half of this work focuses on establishing the reliability of Inverse Indentation Analysis (*IIA*) as a means to identify such constitutive plastic parameters for different crystal structures. In this method, the error in experimental and simulated indentation response (both in load–displacement *and* surface topography) is minimized to obtain the constitutive material parameters. The reliability of this *IIA* method is first established for face-centered cubic (fcc) materials, where it is found that any crystal orientation is adequately sensitive for the optimization to identify the parameters. Such is not the case for less symmetric hexagonal materials, where the efficacy of the *IIA* method relies heavily on the selected crystal orientation, and it is proposed to select crystal orientations that are sensitive to all slip families considered in the constitutive description. Further efforts will apply the proposed *IIA* method to β-Sn.

ACKNOWLEDGEMENTS

I express my deepest gratitude to my advisor, Dr. Philip Eisenlohr, for his immense patience, support, and continuous encouragement to strive for excellence during my graduate research. It has been a real pleasure to work and learn from Dr. Eisenlohr. His ability to explain complicated things through simple examples; investigating a scientific problem systematically; and always having an open mind to new ideas, are things I will always look up to for the rest of my life. With his constant guidance and support (both professional and personal), I was able to contribute my part in the field of crystal plasticity multi-physics modeling, after coming from a background in chemical engineering.

I would like to thank Dr. Thomas Bieler, whose willingness to help me and answer my numerous questions with enthusiasm, is something I cherished thoroughly during my graduate study. My approach to research, and the associated technical challenges, have been significantly influenced by the several discussions which I had with Dr. Bieler. I would also like to thank Dr. Kalyanmoy Deb, for his insights regarding fundamentals of optimization algorithms. His course on optimization for engineering applications introduces a vast array of different algorithms as well as their physical and mathematical basis, that helped me formulating my own optimization module. I also want to thank my other committee member, Dr. Donald Morelli, for providing several interesting perspectives regarding my research. I extend my sincere thanks to Dr. Martin Crimp, Dr. Carl Boehlert, and all of their students (the entire metals research group), as well as the members of the Computational Materials Mechanics research group, for the stimulating discussions and the valuable suggestions that helped me shape my graduate research work. I also thank Dr. Greg Swain, in the Department of Chemistry, for allowing me to perform electro-deposition experiments in his lab, and his student Kirti Bhardwaj for her immense help with the experiments.

A massive thanks to Dr. Praveen Kumar from Indian Institute of Science, Bangalore, India, and Dr. Piyush Jagtap, now in Brown University, for introducing me to the world of tin whiskers.

It has been a pleasure to get to know Piyush, who has been a great friend, and also familiarized me with the experimental intricacies related to whiskers. My sincere thanks to Dr. Pratheek Shanthraj and Dr. Martin Diehl in Max-Planck-Institut für Eisenforschung, Düsseldorf, Germany, for their constant help and guidance in developing the multi-physics solver in DAMASK and making it open source. They have been immensely patient and always willing to help me with any queries I had. I also thank Dr. Lik Chuan Lee and Dr. Seungik Baek from the Department of Mechanical Engineering, for always being there for any queries on mechanics and numerical methods. It is great to have interacted and learned from them.

My graduate study would not have been so smooth without the constant support of all of my friends in Michigan State University who have become my family here, especially— Sap Da, Preetam, Sabya, Kanchan, Kirti, Sayli, Tarang, Yashesh, Oishi, Chetan, Indraroop, Chen, Tridip Da, Tias, Atri, Natalia, David, Alex, Eric, Joe, Mariana, Jialin, Hong Kang (and surely many more).

Last but not the least, I am grateful for my parents, friends, and family members in India for always loving and supporting me, and encouraging me to chase my ambition.

Parts of this research work was funded by NSF grant DMR-1411102. For any errors or inadequacies that may remain in this work, of course, the responsibility is entirely my own.

TABLE OF CONTENTS

LIST OF TABLES

LIST OF FIGURES

CHAPTER 1

GENERAL INTRODUCTION

1.1 Motivation

Whiskers are generally referred to as filamentous structures that show a high aspect ratio in their length (height) compared to their cross-section area (width). The growth of these filamentary metal structures on metals was first observed in 1945 from Cd-electroplated condenser that led to the short-circuit failure of the electronic equipment [Cobb, 1946] . Three years later the growth of (tin) Sn filaments from Sn coated connectors was also identified which caused a short-circuit failure of telephone transmission lines of the Bell Telephone Corporation [Compton et al., 1951]. Other metal films with low melting points, such as Zn, Ag, and Cu, were also found to exhibit similar whiskering behaviors [Coleman et al., 1957, Brenner, 1957], however Sn whiskers have been the most extensively researched among them because of their significant use in electronic devices.

Sn coatings are frequently applied on electronic components due to their favorable properties such as excellent solderability, ductility, electrical conductivity, and corrosion resistance [Lee and Lee, 1998]. Thus, the functional degradation of electronic devices, and sometimes their complete failure due to the formation of Sn whiskers is a major reliability concern. It was discovered empirically in 1960s that addition of lead (Pb) to pure Sn prevented whisker formation [Arnold, 1966], which led to the successful employment of whisker-resistant solutions for soldering and coating problems in electronic devices. Since Pb alloying mitigated the long-standing problem of whisker formation in electronic devices, it reduced the attention to understand the mechanisms causing such whiskers and their growth kinetics. However, after the legislative directive to ban Pb from electronic goods due to its hazardous nature [Parliament and of the European Union, 2003] a strong move towards Pb-free electronics resulted, causing a renewed interest in this 70 year old problem of whisker formation that led to a pool of ex-

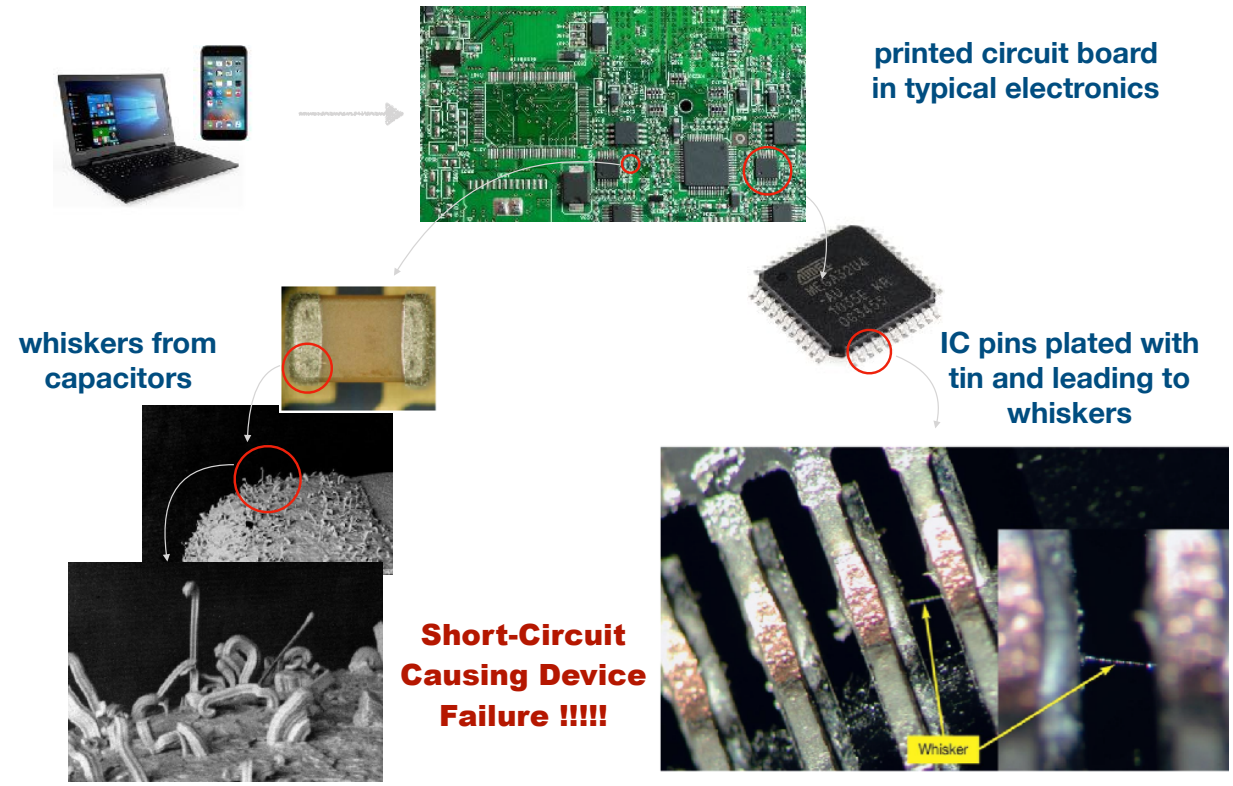

Figure 1.1: Image showing device failure due to short circuit by formation of Sn whiskers joining two pins in an integrated circuit chip in a printed circuit board. NASA whisker web-site

perimental and theoretical investigations over the past couple of decades. Such an exponential drive towards understanding critical factors governing the formation of Sn whiskers from electroplated coatings was further motivated by the fact that pure Sn or Sn-based alloys have been considered as the most suitable candidates to replace effectively and economically PbSn alloys [Chen et al., 2007, Abtew and Selvaduray, 2000].

Even though the electronic industry was one of the most affected due to formation of Sn whiskers causing short-circuit by bridging two components of the electronic assembly, shown schematically in Fig. 1.1, other sectors that have suffered due to whiskers include automobiles, space shuttles, nuclear power plants, and medical devices. Figure 1.2 shows a whisker joining two components of a potentiometer (left) present in the brake peddle in a Toyota Camry, mak-

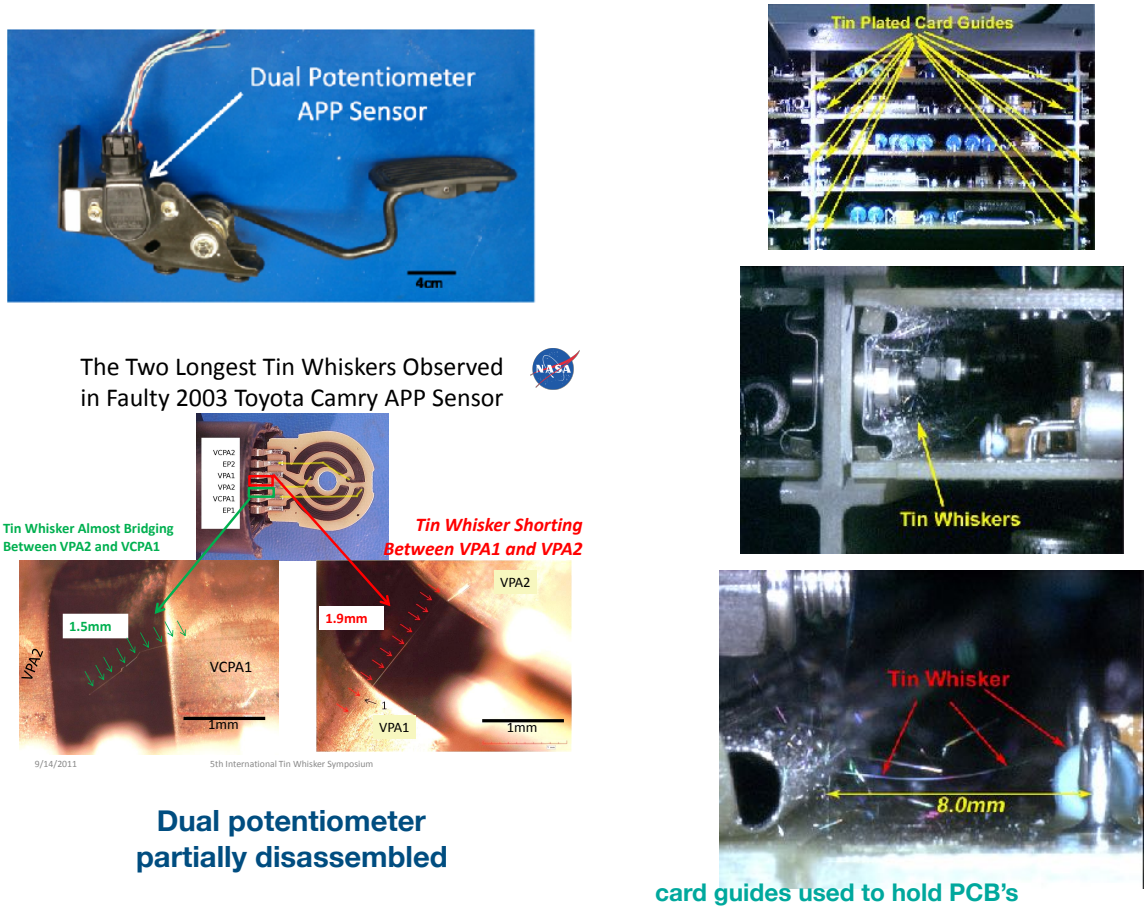

Figure 1.2: Other device failures due to whisker formation- left: potentiometer in brake peddle in Corolla 2003; right: card guides used in space shuttles to hold printed circuit boards (2008). NASA whisker web-site

ing them recall all their 2003 models, and (right) the two components of card guides used to hold printed circuit boards in space shuttles that are connected by whisker. Huang et al. [2018] highlights the risk of Sn whisker growth in nuclear power plants and the need for managements at all levels to come together in taking steps in conducting risk assessment and quality assurance studies.

A more recent article [Alagarsamy et al., 2018] focuses on the importance of whisker mitigation strategies for producing reliable devices and the high stakes associated with failure of such devices. From Fig. 1.3 it appears that even in 2016 there have been considerable amount of device failure cases that are attributed to formation of tin whiskers, thereby further motivating the

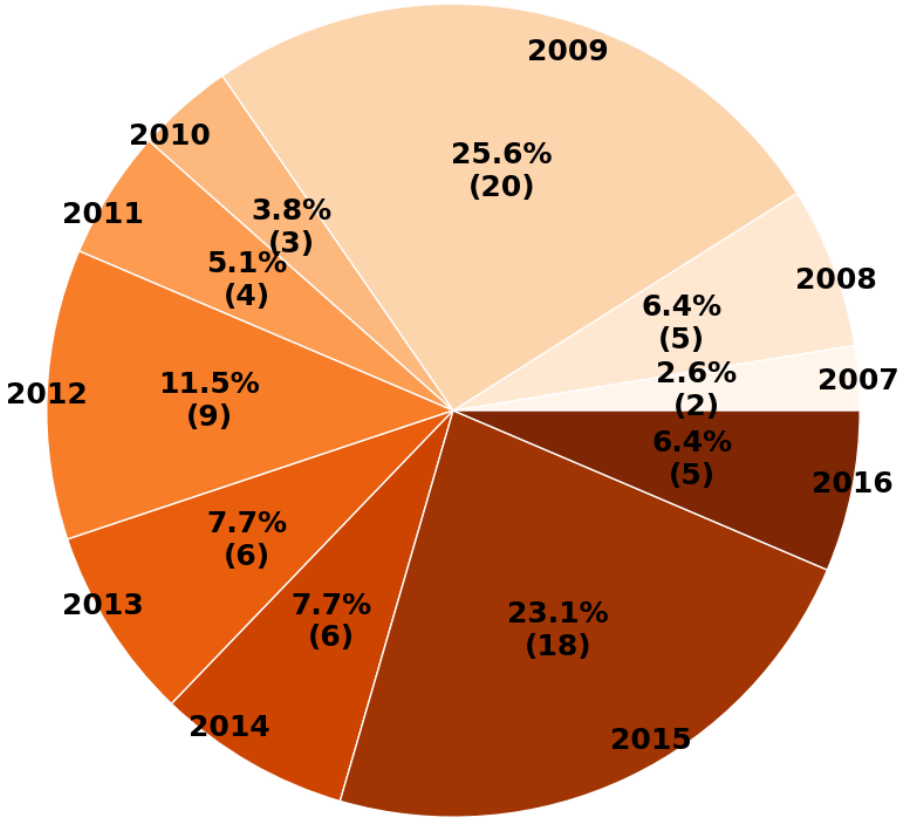

Figure 1.3: Number of reported cases of medical device failure due to Sn whisker formation from 2006-2016. [Alagarsamy et al., 2018]

need to properly understand the factors causing such filamentary protrusions. Further cases of failures due to whisker formation is well documented in NASA whisker web-site.

Therefore, with the rekindled drive to understand mechanisms causing whisker formation, multitude of experimental observations and a few numerical studies over the past couple of decades have been performed in order to identify their root causes and propose efficient and reliable mitigation strategies. However, even today there lacks a comprehensive understanding of this phenomena [Zhang et al., 2015b] that limits the confident prediction of (i) the apparent random whisker locations, (ii) their observed spatial densities, (iii) their wide array of morphologies, and last but not least (iv) their variable incubation periods which prevents formulation of a consistent whisker growth model. In the next section a brief overview of the current

understanding is laid out followed by the objectives of the present work.

1.2 Overview

Tin whiskers are believed to be “perfect" single crystals [Fisher et al., 1954, LeBret and Norton, 2003] emanating from single grains only [Choi et al., 2003, Galyon and Palmer, 2005, Boettinger et al., 2005, Zhao et al., 2006, Tu et al., 2007, Nakadaira et al., 2008, Wang et al., 2014, Stein et al., 2015b], with diameters approximately 1-2 µm (comparable to the grain size) and with atoms being added from the bottom [Koonce and Arnold, 1953]. Their typical growth rates have been reported to be around $1\,\text{Å}\,\text{s}^{-1}$ [Ellis et al., 1958, Glazunova and Kudryavtsev, 1963, Furuta and Hamamura, 1969] which might vary in presence of externally applied stresses [Fisher et al., 1954]. Starting from their initial observation there have been multiple theories that are proposed to describe the process of whisker formation, such as dislocation-based mechanisms [Eshelby, 1953, Frank, 1953, Lindborg, 1976, Lee and Lee, 1998], whisker being a result of dynamic recrystallization and abnormal grain growth [Boguslavsky and Bush, 2003, Vianco and Rejent, 2009, Etienne et al., 2012, Vianco et al., 2015], and whiskers proving to be a stress-relaxation means for the film and growing from grains having inclined grain boundaries [Tu and Li, 2005, Smetana, 2007, Galyon, 2011, Chason et al., 2013, He and Ivey, 2015]. Among the aforementioned theories, the stress relaxation theory is the most discussed and relevant one due to the immense experimental support [Zhang et al., 2015b], and hence would be the focus of this work. Even with this general agreement of stress being the cause of whisker formation, there exists several discrepancies in literature in terms of its nature (compressive, tensile, or both), the extent of the gradient, effect of plastic deformation, role of surface oxide layer, and most importantly the effect of crystal structure and orientation. In this work we try to address some of the open questions and aim to highlight the impact of β-Sn crystal anisotropy in governing the overall process.

Stress in β-Sn films can arise from a number of causes such as indentation [Yang and Li, 2008], bending [Crandall et al., 2011], thermal expansion mismatch between the film and

its substrate [Pei et al., 2017], or, the most commonly observed, by formation of voluminous Cu_6Sn_5 intermetallic compounds at the interface between a Cu substrate and the Sn film [Chason et al., 2013]. Especially for the latter two stress origins, a gradient of decreasing hydrostatic stress forms between the film–substrate interface and the film surface [Hektor et al., 2018]. Measurements of film stress evolution (quantified from film-on-substrate curvature measurements) indicates that plastic relaxation plays an important role and notably modulates the whisker propensity [Chason et al., 2008]. Since among these stress fields in the film, stresses induced by thermal expansion mismatch can be carefully controlled and its effect can be quantified through experiments, so our focus in this work is to analyze the stress fields and the subsequent stress-driven diffusion generated by thermally straining the system. Moreover, it is our hypothesis that in addition to macroscopic gradients induced by the external loading conditions, the polycrystalline nature and the inherent anisotropy of β-Sn can be expected to further modulate the hydrostatic stress (and its gradients) within the film. In consequence, a spatially varying chemical potential of Sn atoms would result, which then acts as the driving force for atomic redistribution.

The mass redistribution is likely to be occurring solely via grain boundaries since at the typical operating temperatures the self-diffusivity of Sn is orders of magnitude slower in the bulk than on a grain boundary (GB) [Jagtap et al., 2017] causing us to focus our attention to stresses generated along the grain boundary network of the film. Based on the overall understanding and current knowledge, the key facts can be summarized as:

- Whisker formation is a stress relief mechanism that occurs in films with predominantly columnar grain structure by atom attachment at subsurface boundaries of oblique surface grains that do not extend through the complete film thickness. Whether such oblique grains occur naturally during the deposition process, or whether they are triggered by stress, in service conditions, is not yet established.

- The associated atom flux is driven by a positive gradient of hydrostatic stress that low-

ers the chemical potential of atoms on the whisker grain boundaries relative to other grain boundaries. Typically, stress gradients develop between the base and surface of a Sn film in response to a number of possible causes, for instance, the growth of intermetallic compounds (typically Cu_6Sn_5 for Cu substrates), thermal expansion mismatch of the substrate, or local indentation. Nevertheless, whisker formation is also triggered by macroscopically homogeneous compression or tension [Crandall et al., 2011].

- Since bulk self-diffusivity of Sn is roughly ten orders of magnitude slower than grain boundary (GB) diffusion at typical operating temperatures, the atom flux is exclusively supported on the GB network and the transport is modulated by the grain boundary hydrostatic stress.

- Incubation periods of largely varying duration are observed, depending on the mechanical load either already present and/or developing within the film. Typically, the whisker nucleation rate, as well as the individual whisker elongation rate, decrease over time, particularly for decreasing film stress.

- The film stress evolution (quantified from film-on-substrate curvature measurements) indicates that plastic relaxation plays an important role and could notably modulate the whisker propensity.

From the incidence of the drive to develop effective whisker mitigation strategies from early 2000, there has been a wide range of experimental observations, however, there has been limited progress in developing accurate and practical models capable of capturing this complex multi-physics system. Some of the modeling efforts are highlighted next, while a more detailed review on relevant literature is presented in Chapter 2.

A major shortcoming of the existing models of whisker growth (transport of atoms towards a particular “whisker grain") is the fact that they generally tend to sidestep the question of the nucleation event and postulate a constant, non-zero level of stress being maintained at the whisker root grain boundaries once the nucleation has happened [Tu and Li, 2005, Sarobol

et al., 2013, Pei et al., 2017]. Around this location of fixed stress, a radially symmetric stress gradient emerges when balancing the underlying source of compressive film stress, plastic relaxation, and diffusive mass redistribution. Subsequent ad hoc fitting of an observed film stress evolution was possible with the stress level at the whisker root being comparable to the flow stress of Sn at ambient temperatures. Such a significant resistance against atom influx at the whisker root was qualitatively rationalized based on a frictional component exerted by the grain boundaries against out-of-plane whisker grain motion [Sarobol et al., 2013], a resistance that increases with decreasing obliqueness (inclination from the surface normal). Nevertheless, it remains elusive why plastic relaxation of the whisker grain would not continuously decrease its compressive stress. Furthermore, all current models [Tu and Li, 2005, Buchovecky et al., 2009a, Sarobol et al., 2013, Pei et al., 2017] effectively simplify the geometry into one dimension, partly consider plastic relaxation mechanisms to various degrees of sophistication, and prescribe a fixed stress condition of *the* whisker grain, which can then be fitted to reproduce observed whisker growth rates. Yet, none of those models can be regarded as truly *predictive*, since many open and critical aspects of whisker formation are not explicitly addressed by them. First and foremost, the specific events triggering particular grains to grow a whisker are ignored and cannot be deduced from the simulation results, posing the question about the rarity of such an event as observed from the whisker density measurements. Secondly, the long-range stress gradient (extending about 50 µm, [Pei et al., 2017]) that is predicted to develop around a whisker grain is difficult to measure and has yet to be confirmed experimentally, while some contrary observations have been reported about the dominant influence of vertical stress gradients [Sobiech et al., 2008]. Moreover, geometrically simplified models disregard the effect of elastic and plastic anisotropy of Sn, and hence, cannot account for the measured influences of the global film texture on whisker propensity. Since whisker nucleation is ultimately a *local phenomenon* [Buchovecky, 2010, Sobiech et al., 2011], specifics of the whisker grain neighborhood in terms of geometry and crystal orientations are very likely strong decisive factors.

Therefore, an important goal of the proposed research is to enhance past modeling and

simulation efforts by employing three-dimensional, full-field, and chemomechanically coupled crystal plasticity simulations of stressed tin films for which actual whisker nucleation sites are known. The major question to be addressed with this simulation framework is whether an oblique (surface) grain is not only a necessary but also a *sufficient* condition to trigger whisker formation, i.e., would *any* oblique grain in an otherwise columnar film experience conditions that lead to perpetual accretion of atoms to this grain? In this study, first a residual stress evolution study is performed for thermally stressed films to analyze the spatial variation of such stress fields. The idea is to see whether sufficient atoms can be transported to whisker grain root producing shear that is high enough to break the native oxide layer and push out the whisker. From the initial thermo-mechanical model, the role of microstructure and material anisotropy is also analyzed to identify the critical factor(s) that significantly influence the atom redistribution. Following, the thermo-mechanical model, a fully coupled chemo-thermo-mechanical model is developed to study the kinematic consequence of such atom redistribution, in terms of the grain boundary (GB) hydrostatic stress, the normal traction, and the shear traction. Moreover, from such spatially resolved full-field simulations of atom redistribution under thermomechanical driving forces, the role of the GB network in modulating the atom flux and its net transport capacity can be related to the apparently shallow stress gradient that is often inferred from experimental observations.

Additionally, the β-Sn plasticity is yet to be fully established in literature due to the complex tetragonal crystal structure. In that regard, an efficient methodology using inverse analysis is developed to identify critical plasticity parameters (such as the initial flowstress, also referred as critical resolved shear stress (CRSS)) for each of the slip families in low-symmetry materials by minimizing the error between the experimental and simulated single crystal nanoindentation data. Development of this inverse analysis framework, along with its performance for different crystal structures will also be highlighted in this work, using virtual experimental data.

Overall the thesis chapters can be summarized as:

- Chapter 2 contains a literature review about the current understanding about the whisker

growth mechanisms, existing models and their drawbacks, effect of process parameters, and existence of contradicting observations, thereby further motivating the need of full-field three dimensional analysis for such problems.

- Chapter 3 provides the background and formulation of full-field thermomechanical simulations in a crystal plasticity framework along with significant results about the effects of global film texture, grain geometry, grain size distribution, and crystal anisotropy on grain boundary hydrostatic stress which modulates the atom transport in the film.

- Chapter 4 provides details about the development of the fully coupled multi-physics chemo-thermo-mechanical model. The preliminary results obtained from the coupled simulations are discussed for two different boundary conditions in terms of their kinetics, average film-stress, and the shear contributions.

- Chapter 5 highlights the Inverse Indentation Analysis (*IIA*) framework that is developed to identify critical plasticity constitutive parameters, along with the means to perform a high sensitive parameter selection, and its performance for high symmetric face-centered cubic materials.

- Chapter 6 discusses the strategy to use the *IIA* framework for low symmetry hexagonal materials, highlights the importance of crystal orientation selection for materials having multiple slip families, and the reliability of the *IIA* method for hexagonal materials.

- Chapter 7 provides an overview about the key understanding gained through this work along with suggestions about the possible path forward in developing efficient crystallography based whisker mitigation strategies.

Apart from the developments in the current field of tin whisker research, with the development of such multi-physics models to study stress-driven diffusion would open many new doors to analyze transport mechanisms of condensed matter in complex (non-hydrostatic) mechanical stress fields, a topic of long-lasting interest [Larché and Cahn, 1973, Ostrovsky and

Bokstein, 2001, Chakraborty et al., 2008, Brenner, 1956]. Moreover, understanding how stresses influence the formation of metallic wire structures would help in efficiently designing functional nanostructures (such as nanowires) and nanocomponent assemblies, especially, as these have unique electrical, mechanical, optical, and magnetic properties. Hence, by understanding mechanisms causing Sn whiskers, such a knowledge could then be efficiently transferred to fabricate other metallic nanowires by suitably controlling the stresses causing them [Cui et al., 2009, Erdem Alaca, 2009, Wang et al., 2008, Karim et al., 2006, Saka et al., 2007, Shim et al., 2009, Lu and Saka, 2009].

CHAPTER 2

LITERATURE REVIEW

2.1 Background

This chapter explores relevant literature used for the current work, and has been divided into three sections. In the first section, the anisotropy of β-Sn crystal structure is discussed along with a comparison between its creep behavior as a bulk material to that of a film using existing data from literature. Subsequently, a detailed review is done on the relevant aspects of tin whisker mechanisms along with different factors modulating the kinetics of the formation of such filamentous structures from films. Finally, a review about the finite strain continuum mechanical framework that is used to perform the crystal plasticity multi-physics simulations is discussed along with some of the critical numerical challenges.

2.2 Material properties and anisotropy of tin

Tin melts at $T_\mathrm{m} = 505\,\mathrm{K}$ (232 °C), thus, ambient temperature corresponds to a homologous temperature $T/T_\mathrm{m} = 0.6$. The low-temperature allotrope α–Sn (gray tin) is non-metallic with a diamond cubic lattice structure, and is thermodynamically stable only below 13 °C. β-Sn (white tin) has a body-centered tetragonal (bct) crystal structure with $c/a = 0.545$, and is generally stable to well below room temperature since the β to α transformation is kinetically hindered. (In this text "β-Sn", "Sn", and "tin" are used synonymously for β-Sn.)

The bct structure of β-Sn causes high anisotropy with regard to the elastic modulus, thermal expansion coefficient, and plastic behavior, thus rendering its behavior highly sensitive to crystal orientation. For example, the Young's modulus and thermal expansion coefficient of β-Sn in $\langle 0\,0\,1\rangle$ is twice as that in $\langle 1\,0\,0\rangle$ direction [Lee et al., 2015]. Plastic deformation of tin under ambient and elevated temperatures is generally comparable to other metallic materials, i.e., follows a typical power-law relation between (stationary) deformation rate and applied (unidirectional)

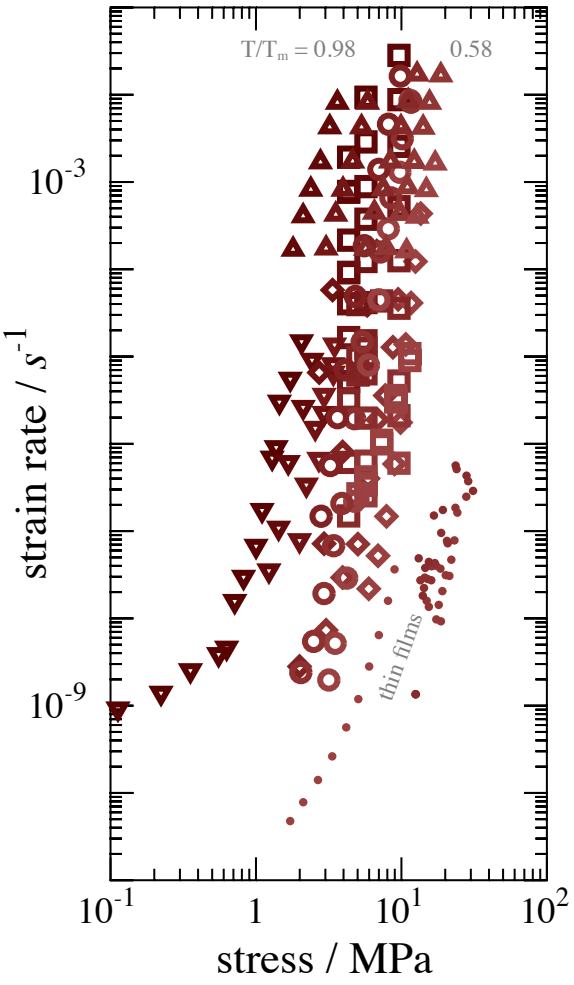

Figure 2.1: Deformation resistance of bulk tin (open symbols, [Mohamed et al., 1973, Mathew et al., 2005, Weertman and Breen, 1956, McCabe and Fine, 2002, Adeva et al., 1995]) and thin films (dots, [Boettinger et al., 2005, Chason et al., 2014]) under various loading conditions and homologous temperatures (shades of red).

stress (Fig. 2.1). However, a review done on plastic deformation of β-Sn by Yang and Li [2007] reveals the incomplete understanding of its slip activity. This is due to the differences in selecting governing factors for plastic deformation, such as resistance to forest dislocation [Fujiwara and Hirokawa, 1987] or 'effective yield strength' [Sidhu and Chawla, 2008]. The orientation dependence of active slip systems was also investigated by analyzing ideal shear deformation of β-Sn single crystal using first-principles density functional theory (DFT) [Kinoshita et al., 2012] for a perfect crystal, which suggested that the most active slip systems are on $\{1\,1\,0\}$ planes. On the other hand, indentation studies by Fujiwara [1997] on β-Sn revealed the slip activity of $\{1\,0\,0\}$ and $\{1\,1\,0\}$ planes to be the most likely. Though there has been some consensus on the available slip systems (see Table 2.1), their relative activity has yet to be quantified by any constitutive model [Bieler et al., 2011].

Table 2.1: Slip families in β-Sncrystal structure [Lee et al., 2015].

Mode	**Slip family**	**Multiplicity**
1	$\{1\,0\,0\}\ \langle 0\,0\,1]$	2
2	$\{1\,1\,0\}\ \langle 0\,0\,1]$	2
3	$\{1\,0\,0\}\ \langle 0\,1\,0]$	2
4	$\{1\,1\,0\}\ \langle 1\,\bar{1}\,1]$	4
5	$\{1\,1\,0\}\ \langle 1\,\bar{1}\,0]$	2
6	$\{1\,0\,0\}\ \langle 0\,1\,1]$	4
7	$\{0\,0\,1\}\ \langle 0\,1\,0]$	2
8	$\{0\,0\,1\}\ \langle 1\,1\,0]$	2
9	$\{0\,1\,1\}\ \langle 0\,\bar{1}\,1]$	4
10	$\{0\,1\,1\}\ \langle 1\,0\,0]$	4
11	$\{0\,1\,1\}\ \langle 1\,\bar{1}\,1]$	8
12	$\{2\,1\,1\}\ \langle 0\,\bar{1}\,1]$	8
13	$\{2\,1\,1\}\ \langle \bar{1}\,1\,1]$	8

The self-diffusivity of tin exhibits a large disparity between bulk and grain boundary, with the latter diffusion coefficient being orders of magnitude higher [Meakin and Klokholm, 1960, Coston and Nachtrieb, 1964, Huang and Huntington, 1974, Lange and Bergner, 1962]. Consequently, mass transport for typical in-service temperatures is exclusively supported by the grain boundary network. Moreover, tin forms a tenacious oxide that effectively suppresses sur-

face diffusion even under relatively small partial pressures of oxygen, and whose presence have been reported to influence whisker growth in terms of maintaining compressive stresses in the film by Tu et al. [2007].

2.3 Current understanding of tin whisker formation

In this section relevant background regarding whisker morphology and proposed growth mechanisms is discussed. Some of the prominent models to describe the process of whisker formation is highlighted along with their underlying limitations, thereby requiring further effort in advanced computational efforts to predict whisker nucleation and motivating the present work. Despite the large body of research been dedicated to determining the mechanisms of whisker formation [Galyon, 2005] for over seven decades, the whole process is still not well understood and an accepted whisker mitigation technique in place of Pb addition is yet to be determined. Although it is by now generally accepted that stress is the driving force for whisker growth [Galyon, 2005, Chason et al., 2008, Jadhav et al., 2010b, Tu et al., 2007, Sobiech et al., 2008, Lee and Lee, 1998, Smetana, 2007, Vianco and Rejent, 2009], this knowledge alone does not explain the subsequent steps leading to their actual formation.

2.3.1 Whisker geometry and crystallography

Figure 2.2 highlights exemplary whisker morphologies out of the vast geometries and microstructures reported in the expansive body of whisker investigations over seven decades (see [Galyon, 2005] for an overview). Whisker diameter is comparable to the grain size of the film from which it grows and remains consistent during growth with some times sharp bends [Buchovecky, 2010]. Time-series evolution of growing whiskers confirmed that the atom attachment happens at the base of the whisker and not at the top or side, along with the fact that they originate from a single grain [Jadhav et al., 2010a, Susan et al., 2013]. Focused ion beam (FIB) sections through the base of whiskers reveal that these whiskers typically originate from a non-columnar sub-surface grain that does not extend through the film thickness [Boettinger

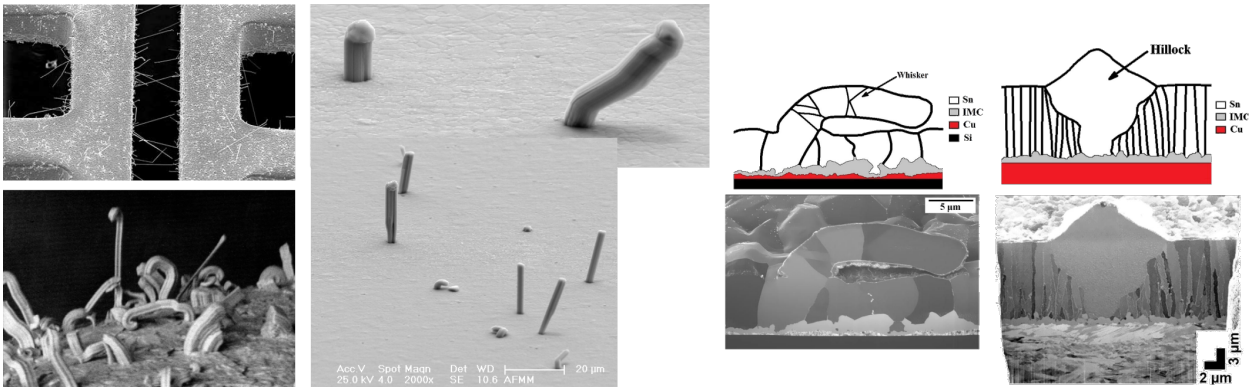

Figure 2.2: Examples of tin whiskers, hillocks, and smaller protrusions. Top left image by Peter Bush (SUNY Buffalo) [Boguslavsky and Bush, 2003], bottom left image from NASA metal whisker photo gallery, center images by Piyush Jagtap and Praveen Kumar (IISc Bangalore, unpublished), cross sections cut by focussed ion beam and corresponding sketches on right by [Chason et al., 2013].

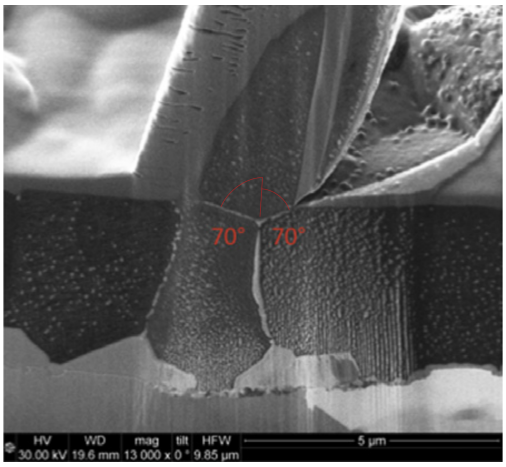

Figure 2.3: "Oblique grain" with shallow grain boundaries at the base of a typical whisker [Sarobol et al., 2013].

et al., 2005, Smetana, 2007, Jagtap et al., 2017], and is frequently termed an "oblique grain" or "chevron grain" (Fig. 2.3) in literature (and henceforth in this text).

Whiskers can contain multiple crystal orientations Fortier and Kovacevic [2012] (as in Fig. 2.2 third column), but whiskers mostly consist of single crystals [Galyon, 2005, Susan et al., 2013, Tu et al., 2007, Osenbach et al., 2005, LeBret and Norton, 2003] that are oftentimes straight with occasional abrupt changes (kinks) or more gradual changes in growth direction (see Fig. 2.2 first and second column). Extensive time lapse observations were made to capture the effect of these kinks on the kinetics of whisker growth by Susan et al. [2013]. In the same

study, two types of kinks were observed during the growth of a whisker. In one case, referred in the text as type A, sharp kinks appeared at the base of the whisker with the morphology and orientation remaining unchanged for the remainder of the growth period; while in case of type B kinks, orientation and morphological changes were observed during the whisker growth process. Moreover, the type A kinks did not influence the growth rate of the whisker, while with type B kinks, a significant decrease or complete stoppage of whisker growth was observed. Such a case of intermittent growth have also been reported in other studies [LeBret and Norton, 2003, Jiang and Xian, 2006]. This observed morphological and kinetics change (increase and decrease in whisker diameter as shown in Fig. 2.2 second column) during the process of whisker growth was attributed to the dynamic and erratic behavior of the grain boundaries of the underlying whisker grain. Apart from these long and mostly straight whiskers, a second protruded morphology is observed that has a much lower aspect ratios (Fig. 2.2 last column) and is termed “hillock". Hillocks are characterized by their much wider base than the typical grain size of the film and involve significant grain boundary migration [Chaudhari, 1974, Boettinger et al., 2005, Osenbach et al., 2007]. Oftentimes a whisker have been observed with such a wider base at the bottom [Lin and Lin, 2008], indicating that the growth mode (whisker or hillock) can vary over time.

With careful electron backscatter diffraction measurements of Type A kinked whiskers it was observed that these whiskers are single crystals, in that the crystal lattice orientation remains unchanged across the kinks with the kink angle representing the angle between the two growth directions [Susan et al., 2013].

It has been observed experimentally by Stein et al. [2015b] that the active growth direction of whiskers corresponds to low index directions, $\langle 0\,0\,1\rangle$, $\langle 1\,0\,1\rangle$, and $\langle 1\,1\,1\rangle$ with occasional presence of low index $\langle 2\,0\,1\rangle$ and $\langle 1\,0\,2\rangle$ directions. Such a favorability of growth directions to be low-index directions were also observed by others [Buchovecky, 2010]. However, whether there exists any correlation between the underlying whisker grain to the growth direction (mechanism) is still under active debate [Susan et al., 2013, Chason et al., 2013]. Such a lack of any apparent unique-

ness for a plausible whisker grain was also observed through recent full-field multiphysics simulations [Chakraborty and Eisenlohr, 2018] as well as diffraction studies [Jagtap et al., 2017, Pei et al., 2016]. Reported whisker densities range from 1000 cm^{-2} to 10000 cm^{-2} after one to two months of aging [Tu, 1973, Lee and Lee, 1998] with a random distribution across the film surface, with two whiskers occasionally erupting much closer than the mean spacing, thus emphasizing the importance of local neighborhood of the whisker. It is also important to notice that whisker density depends on the plating (processing) conditions to deposit these films, however there exists couple of orders of magnitude difference between the number of whisker nucleation spots (where a grain "pops" out but does not grow long) to that of the number of long whiskers [Susan et al., 2013].

2.3.2 Tin film plating and resulting microstructure

The most common route to synthesize films is via electrochemical plating, where the substrate acts as the anode with a Sn based electrolyte, and pure Sn acting as anode. Based on the electrodeposition conditions the resulting film properties vary greatly, which in turn affects the whisker propensity. The deposition conditions generally include deposition time, bath temperature, electrolyte composition, and current density which subsequently then affects film global properties such as thickness, grain structure, and coating composition as well as local properties such as crystalline orientation distribution (film texture). Various studies have been performed to correlate such effects, like for example according to [Jagtap and Kumar, 2015], changing the electrodeposition bath temperature from 30 °C to 60 °C (at fixed current density of 30 $mA\,cm^{-2}$) altered the film grain structure from columnar to mostly equiaxed and thus resulted in a reduction of whisker propensity by 4 orders of magnitude. The effect of electrolyte composition on the resulting film texture (crystallographic direction along the film normal) along with the subsequent whisker propensity have also been studied [Lal and Moyer, 2005, Sarobol et al., 2010, Sobiech et al., 2011]. Sobiech et al. [2011] concluded that columnar Sn deposited on copper (Cu) substrate exhibited {3 2 1} fiber texture, while electrolyte composition

of Sn90Pb10 (wt. %) on Cu exhibited {1 1 0} film texture. Lal and Moyer [2005] confirmed that films with ⟨2 2 0⟩ were less whisker prone compared to ⟨3 2 1⟩ fiber texture, which depended on the amount of organic additives in the electrolyte. Based on the effect of minor alloying of Cu and Pb, Sarobol et al. [2010] generated a defect-phase diagram to identify those combinations of compositions that showed the least whisker propensity. Film texture (crystallographic direction along the film normal) also depended on the substrate composition as studied by [Jagtap et al., 2018] who reported a dominant film texture of {1 0 0} when it was deposited on Cu substrate or brass (Cu-35 wt %), as compared to a {1 1 0} film texture when the substrate had a nickel (Ni) underlayer. A wide array of literature exists that compare different film properties on whisker growth (and propensity) such as film thickness [Pinol et al., 2011, Jadhav et al., 2010b, Chason et al., 2011, Cheng et al., 2011, Jadhav et al., 2012a, Lu and Hsieh, 2007], grain size [Jadhav et al., 2010b, Chason et al., 2011, Jadhav et al., 2011, Pei et al., 2012], plating conditions [Pinol et al., 2011, Yen et al., 2011, Sobiech et al., 2010, Vicenzo et al., 2010], microstructure [Jadhav et al., 2011, Boettinger et al., 2005, Yu et al., 2010, Mathew et al., 2009, Okamoto et al., 2009] and composition [Jadhav et al., 2011, Boettinger et al., 2005, Kao et al., 2006, Moon et al., 2010]. However, a direct comparison to isolate the governing factors is difficult from such studies due to the huge variability in the processing conditions. For example, Jagtap et al. [2018] reported a higher whisker propensity for films deposited on brass (Cu-35 wt %) substrate that had {1 0 0} film texture as compared to those deposited on pure Cu using stannous sulfate as the electrolyte, while films deposited by [Stein et al., 2015b] on a nominally similar substrate and having {0 0 1} film texture showed lesser whisker propensity as compared to those on pure Cu using methane sulfonic acid with organic additives as the electrolyte. This comparison brings forward the existing contradiction in tin whisker literature, along with the significant influence of film texture, as well as the need for a systematic study for accurately identifying the governing mechanisms for whisker growth.

2.3.3 Causes of whiskers

To accurately identify the underlying mechanisms leading to whisker formation is highly complicated as it involves a multitude of concurrent processes, such as interdiffusion, phase transformation, stress generation and relaxation. It is a general consensus in the tin whisker research community that stress is required to generate such protrusions. In most observations whiskers are observed under compressive stresses in the film, however there have been reports of whisker under tensile stresses as well [Crandall et al., 2011] while some observations have emphasized more on the importance of the stress gradient rather than the sign of the stress itself [Sobiech et al., 2008]. Moreover, even though whiskers are a result of stresses in the film, they are not the only stress relaxation mechanism, and other mechanisms such as plasticity (creep) dictate the amount of stress in each layer [Chason and Jadhav, 2016]. This was first demonstrated by [Fisher et al., 1954] in the 1950s, who showed that whisker growth rates scale with externally applied (compressive) stress. Apart from external loading impositions such as indentation or bending [Yang and Li, 2008, Crandall et al., 2011] , compressive stress can also arise from, for instance, residual stress during the deposition process, thermal expansion mismatch of film and substrate, electromigration , or displacive phase transformations such as those resulting from corrosion or the formation of voluminous intermetallics (Cu_6Sn_5) in connection with Cu substrates [Lee and Lee, 1998]. Sn films deposited on silicon (Si) substrates develop compressive biaxial stresses upon heating due to the thermal expansion mismatch between the film and the substrate [Pei et al., 2016]. It was also observed that increased compressive stresses due to electromigration can significantly increase the growth rate of Sn whiskers from films by up to $8\,\text{Å}\,\text{s}^{-1}$ [Liu et al., 2004]. The suggested mechanism is that the direction electron flow induces Sn migration from cathode to the anode side thereby leading to the build-up of compressive stresses and thus formation of Sn whiskers on the anode side. Among the aforementioned causes of stress generation, the most commonly observed is due to the formation of Cu_6Sn_5 resulting from interstitial diffusion of Cu from the substrate into the film and mostly at the Sn grain boundaries. Sobiech et al. [2011] observed a direct correlation between the amount of

Cu_6Sn_5 formation to the whisker nucleation propensity, and proposed that a regular (homogenous) Cu_6Sn_5 morphology reduces whisker nucleation propensity, while Chason et al. [2013] found no such correlation. As mentioned earlier, these stresses primarily relaxed by plasticity and the diffusive transport of Sn atoms from a region of high compression (low tension) to a region low compression (high tension) via the grain boundaries.

The Sn film features that are observed to have a prominent effect on whisker propensity are its thickness and the grain characteristics (size, structure, and orientation) [Walsh and Low, 2016, Ashworth et al., 2015]. Increasing the film thickness increases the whisker incubation period thereby reducing the whisker propensity, since a thicker layer is more effective in relaxing the imposed stresses as compared to a thiner film [Illés and Horváth, 2013]. Chason et al. [2013] established that the maximum compressive stress in the film (caused by continuous precipitation of Cu_6Sn_5 at the substrate interface) decreases with increasing film thickness by etching the same electrodeposited tin film on a Cu substrate, thus indicating that thicker films are plastically softer and can relax more efficiently. With the lower level of net compressive stress in the film, the whisker density and rate of whisker formation also decreased. Other measurements of stress relaxation kinetics on two similar films deposited on Si substrate and having different thickness also confirmed that thicker films relax stresses more easily as compared to thiner films [Shin and Chason, 2009b]. In this study, it was also found that the plastic deformation kinetics of tin films were consistent (in terms of activation energy and stress exponent) with β-Sn bulk behavior and that the presence of native surface oxide layer on top impedes plastic relaxation.

Even though [Lee and Lee, 1998] found no systematic effect of grain structure on whiskering, recent studies have clearly demonstrated that films with equiaxed grain morphology is more efficient in stress relaxation as compared to those with columnar structure which show higher whisker propensity [Sauter et al., 2010, Jadhav et al., 2012b, Sobiech et al., 2011].

The effect of grain orientation (film texture) have also been attributed as one of the decisive factors for whisker or hillock propensity with some textures being more whisker proponent than others [Jagtap et al., 2017, 2018, Sarobol et al., 2010]. However, there is no conclusive study that

clearly demonstrates the effect of film texture.

The role of the native tin oxide layer on whisker propensity is also not fully understood. The presence of native surface Sn-oxide layer is conceived by many authors as an important parameter for whisker formation [Tu et al., 2007, Kumar et al., 2008, Lee and Lee, 1998, Tu and Li, 2005, Chason et al., 2008, Buchovecky et al., 2009a,b, Boettinger et al., 2005]. Experimental [Kumar et al., 2008, Chason et al., 2008] and theoretical [Buchovecky et al., 2009a,b] investigations indicate that without the presence of a (passivating) oxide layer the compressive stress generated by Cu_6Sn_5 formation could relax uniformly via Coble creep [Coble, 1963] along the entire layer surface, i. e. Sn atoms could diffuse from the columnar grain boundaries to the free surface of Sn [Shin and Chason, 2009a]. However, Moon et al. [2005] concluded that the surface oxide can only have a minimal effect on whisker growth by comparing (under ultrahigh vacuum) the Ar^+ sputter-cleaned part of an electrodeposited Sn-1.5 wt % Cu film to the part still containing the native oxide film. This notion was also supported by a recent investigation that observed whisker formation on a compressed Au film, i. e. for a material without any surface oxide [Crandall et al., 2012]. Nevertheless, systematic removal of the surface oxide from a fraction of the film surface in patches comprising many β-Sn grains resulted in whisker formation exclusively from those cleared areas [Su et al., 2011]. However, very local oxide removal on top of only a few grains did not trigger whisker formation from any one of those uncovered grains, while a whisker originated from a close-by grain that was still covered by surface oxide [Jadhav et al., 2010a].

2.3.4 Whisker mitigation strategies

With the move towards Pb free electronics after it was accidentally discovered to inhibit whiskers [Arnold, 1966], there have been some whisker mitigation strategies, but unfortunately none of them are as effective as Pb alloying was known to be. These strategies to minimize, prevent, or inhibit whisker growth include (i) alloying tin with either bismuth (Bi) [Sandnes et al., 2007, Baated et al., 2011a, Jadhav et al., 2012b] or Ag [Baated et al., 2011a] which produces a

more equiaxed film grain structure that is more efficient in plastically relaxing the generated stresses than columnar structures would, and thereby reducing the driving force for whisker formation; (ii) annealing, or “post-bake treatment", to reduce the residual stress [Dittes et al., 2003] and promote forming a more morphologically homogeneous layer of intermetallic compounds [Sobiech et al., 2008] as compared to their generally observed irregularity; and (iii) using of a nickel (Ni) underlayer to prevent the formation of Sn-Cu intermetallic [Dittes et al., 2003, Baated et al., 2011b]. The alloying strategies have some associated challenges, such as reduction of fatigue life upon adding Bi, while an undesired dendritic growth is often associated with Ag addition. The application of conformal (polymeric or metallic) coatings is also effective in reducing the whisker nucleation density and their growth, but not necessarily eliminate device failure due to them, as sometimes whiskers have been reported to pierce through the coatings [Hunt and Wickham, 2010, Mahan et al., 2014, Doudrick et al., 2015]. Thus, these solutions appear to be more temporal and therefore to have a conclusive mitigation strategy, a more comprehensive understanding about whisker nucleation and growth is required. It is our believe that performing full-field high fidelity simulations would help in designing crystallographic based mitigation strategies which would be much more effective than the above mentioned phenomenological solutions.

2.3.5 Growth modes of whiskers

Critically examination of the growth morphologies of whiskers/hillock can provide significant insights into the mechanism controlling their growth, since their shape and orientation is closely related to the way in which atoms are accredited into them. To get a hold of the complete picture, one must consider how the stress in the films get generated, followed by the mechanism by which this stress governs the material redistribution in the film by transporting Sn atoms to the whiskering grain, and finally how this transported material gets incorporated into the whisker. In this section the some of the experimental observations of whiskers from the immense studies performed by Dr. Eric Chason’s research group at Brown University is con-

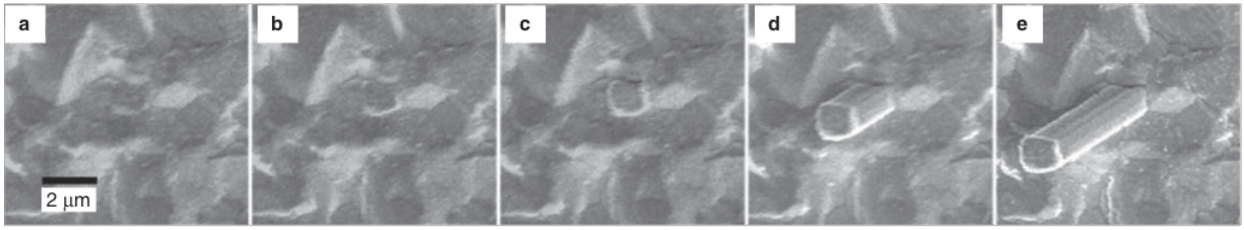

Figure 2.4: Nucleation and growth of a whisker 14 h (a), 14.3 h (b), 14.6 h (c), 17 h (d), 21 h (e) after deposition (onto Cu substrate) [Jadhav et al., 2010a].

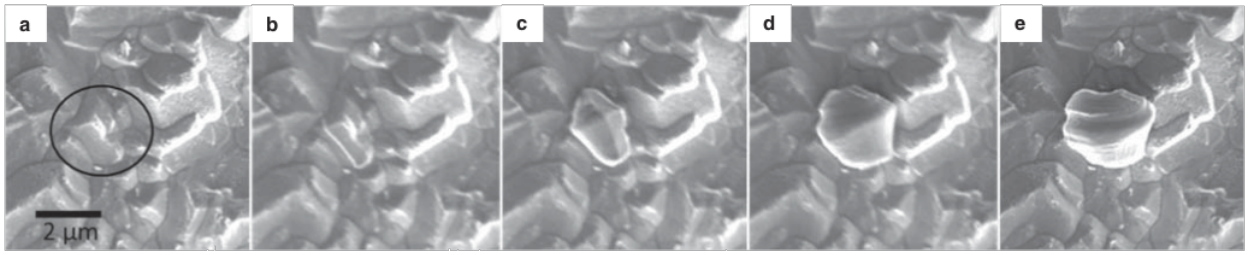

Figure 2.5: Growth of a hillock with extensive rotation imaged 6 h (a), 8 h (b), 12 h (c), 18 h (d), 50 h (e) after deposition [Jadhav et al., 2010a].

sidered in an attempt to highlight the relation between whisker growth mechanism and their subsequent morphology.

The time series evolution of whisker nucleation and growth as observed by Jadhav et al. [2010a] is shown in Fig. 2.4. By examining the sequence from (a) to (c), it is apparent that there exists a rapid change in the surface morphology around the location from where the whisker will grow by lifting (breaking through) the oxide layer on the surface. The details about the breakage of the oxide layer is, however, not clear from the images. With the emerging whiskers there exists no other surface contamination or other defects either on the whisker grain or any other grain surrounding it. Thus the microstructure and grain morphology of the whisker grain and its neighborhood remains pretty much unchanged both during whisker nucleation as well as during its growth. Moreover, once the oxide-layer was cracked (whisker nucleation stage), the whiskers were observed to grow in a nearly constant direction and had a short phase of fast initial growth that quickly decays to a nearly uniform rate. While in other experiments whiskers were observed to grow intermittently with pauses during their growth or had sharp bends or kinks [Galyon, 2005, Ellis et al., 1958, Tu et al., 2007, Sobiech et al., 2008]. Such variability in

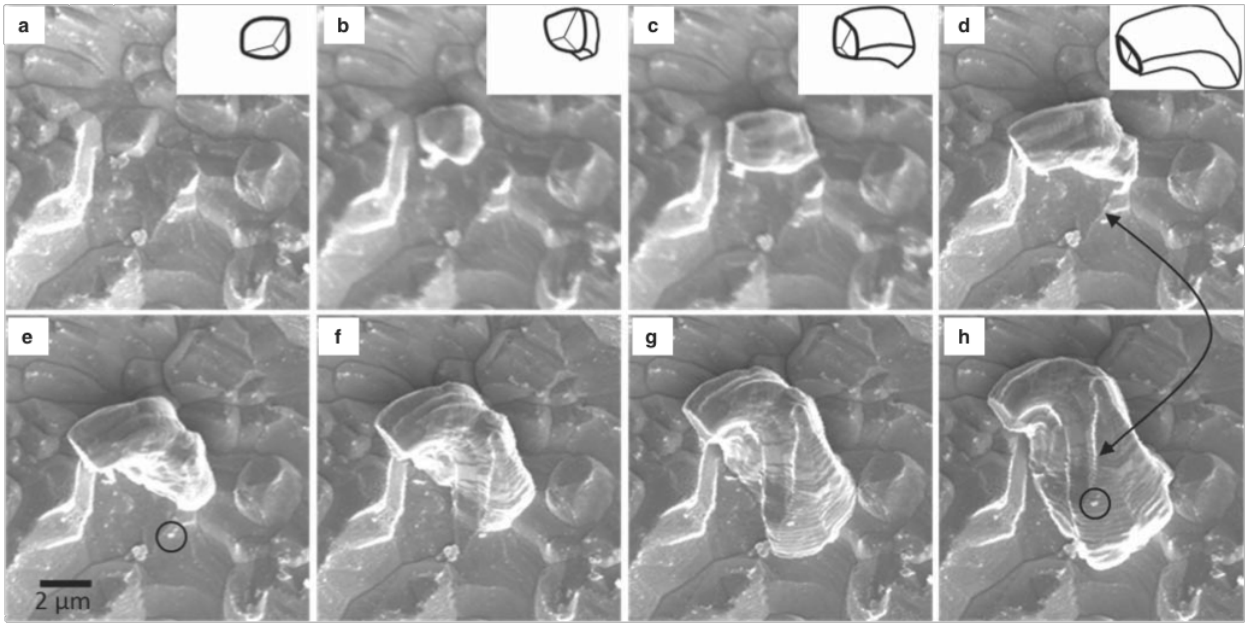

Figure 2.6: Sequence of complex hillock growth with varying cross-section and partial bending 6 h (a), 12 h (b), 18 h (c), 32 h (d), 44 h (e), 56 h (f), 76 h (g), 138 h (h) after deposition. Insets show schematic of shape evolution highlighting rotation of the original surface. Arrows point to grain boundary features in (d) that are visible as ridges on side of the hillock in (h). From [Jadhav et al., 2010a].

whisker growth mechanisms and their subsequent morphologies were attributed to the different environmental conditions by Jadhav et al. [2010a]. For example, the difference due to the samples being kept in air or measured in an scanning electron microscope (SEM) instrument with a poorer ($> 4 \times 10^{-4}$ Pa) quality base vacuum, and thus suggesting that the presence of oxygen, water vapor, or other gases may play a role in the non-uniform growth of whiskers.

Figure 2.5 shows a (short) whisker where one side looks to remain attached to the surface. It appears that the growth of this whisker progresses in a 180° curved fashion until the whisker tip hits the surface of a neighboring grain. The rotation seems to happen due to one side growing outward at a much faster rate compared to the opposite side. Since there appears to be no morphological changes of material above the surface, material extrusion occurs clearly by addition of Sn atoms at the base of the whisker.

The primary difference between the growth mechanisms leading to whisker or hillock formation is the fact that with hillocks there is believed to be lateral grain growth attributed by

the high degree of grain boundary mobility, while in case of whiskers there exists limited lateral grain boundary movement which compels the whisker to simply grow upward. The hillock growth sequence, as depicted in Fig. 2.6, also appears to start at a single grain similar to a whisker initiation. The top surface of this hillock however rotates (similar to Fig. 2.5) as it grows until it is oriented approximately perpendicular to the film surface. During this growth of the hillock where it pushes upward, its base starts to widen simultaneously (Fig. 2.6 d–h), indicative of the extensive lateral grain growth by the hillock grain as suggested earlier. As the hillock consumes adjacent grains, the horizontal grain growth is roughly constrained by the grain boundaries on the surface which reduces the kinetics of the process with further growth of the hillock grain. This interface between the growing hillock grain and the neighboring unchanged (stationary) grains determine the horizontal hillock boundary. The sequence of this growth often proceeds in a step-wise manner, with an increment in horizontal grain-growth followed by an increment in the vertical growth, thereby leading to striation marks (horizontal steps) on the side surfaces of the hillock. These striations can be comprehended to correspond to the size of the base of the hillock when it was pushed out of the surface which can be utilized to recreate the history of the hillock morphology.

2.3.6 Models of whisker formation

Jadhav et al. [2010a] proposed a conceptual long-range transport model for whisker growth, as illustrated in Fig. 2.7, based on the observed growth morphologies and the small changes in grain volumes in the immediate vicinity of the whiskers and hillocks. Such a notion of long-range transport i.e., accretion of atoms to the whisker grain from a large area has also been experimentally observed by Reinbold et al. [2009]. For a film that is under compressive stress, the chemical potential difference between the inclined and the vertical grain boundaries would support the mass transport of atoms towards these oblique (inclined) surface grains. Such an effect of grain geometry in maintaining the chemical potential was also proposed by Smetana [2007] who also suggested a following grain boundary sliding motion to eject the whisker up-

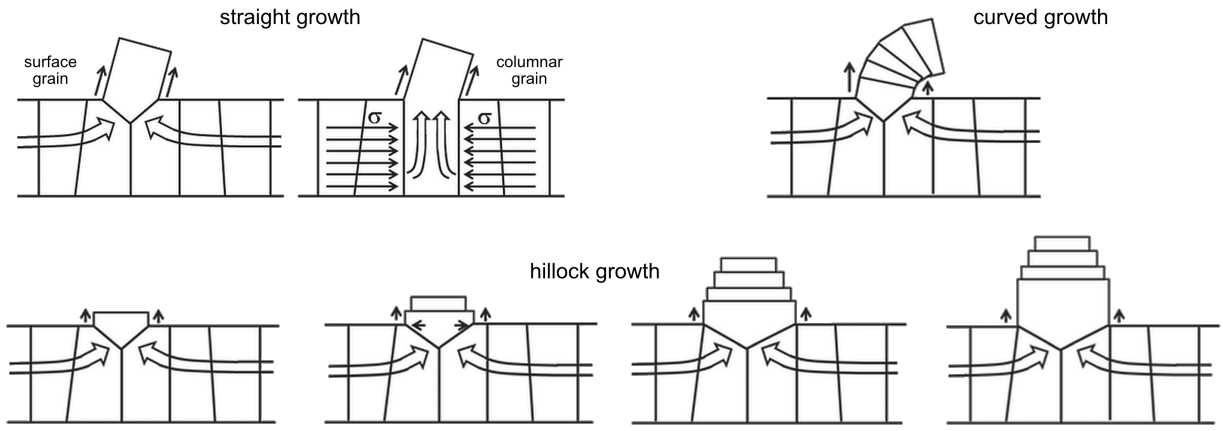

Figure 2.7: Conceptual understanding of whisker and hillock formation mechanisms [Jadhav et al., 2010a].

ward. Subsequently, vertical growth (top left) results when the mass flux (as indicated by thick arrows in Fig. 2.7) into the whisker grain occurs evenly in all the grain boundaries of the whisker grain and in a specific way which results in a consistent and particular crystal direction (as indicated by thin arrows). The reason for such a coordinated accretion of atoms is yet to be uncovered in literature as it appears to encompass a high degree of complexity. Vertical whisker growth from columnar grains would then require a strong mechanical bias to maintain a stress gradient and hence a subsequent chemical flux to the whisker grain boundaries. Such a mechanical bias for the whisker grain is often attributed to plasticity, i.e., the whisker grain undergoes a high degree of plastic deformation which also reduces its strain energy density [Sun et al., 2011]. The dislocation slip causing this plasticity would also help in redistributing volume to above the surface, however, the rationalization of the strict crystallographic growth as a result of conservative dislocation glide is difficult to comprehend. Curved whisker morphologies (top right in Fig. 2.7) has been rationalized by a sizable imbalance of mass influx between some grain boundary faces of the whisker grain as compared to the rest, and the subsequent lack of fast enough redistribution of the accredited mass across all the grain boundary surfaces. Hence, the surface(s) receiving the most flux grows the most, thereby generating the curved morphology. However, such a curved whisker geometry has been rationalized based on a different frictional

resistance argument by Sarobol et al. [2013]. As mentioned earlier and shown again in bottom row in Fig. 2.7, the growth of hillocks is conceptually similar to that of the whisker with the distinctive feature that the grain boundaries (of the hillock grain) are (intermittently) moving concurrently during the vertical growth of the (hillock) grain.

Some researchers have, however, laid more emphasis on the stress gradient and not on the nature of the stress itself– meaning they have proposed whisker growth even in a tensile stress state, but having a suitable stress gradients that allow for coordinated transport of atoms to the "whisker grain" . In this regard, Sobiech et al. [2011] emphasized on the importance of both in-plane and through thickness stress gradient as well. According to him, formation of Cu_6Sn_5 along the Sn grain boundaries at the Cu/Sn interfaces induces in-plane compressive stress in the Sn layer, particularly in the depth range of the Sn coating where Cu_6Sn_5 formation proceeds. Following, close to the surface of the Sn layer results in in-plane tensile stress condition that is most pronounced at those surface locations where formation of Cu_6Sn_5 is most distinctive, as observed underneath the whisker. As a consequence, both negative out-of-plane residual stress-depth gradients, in the direction of increasing depth, and negative in-plane residual stress gradients in the direction of whisker nucleation site towards whisker surroundings occur. This then provides the driving forces for the transport of Sn atoms to the whisker nucleation site.

In the following, some of the prominent theories regarding mechanisms of whisker growth and their shortcomings are briefly highlighted.

The first theories on whisker growth was based on atomic movement through dislocations, wherein Peach [1952] proposed that whiskers grow as a means to reduce the dislocation energy brought about by screw dislocations present in the center of the whisker grain. Eshelby [1953], Frank [1953] also tried to explain the extruded whisker growth by transfer of atoms from the base of the whisker brought about by a dislocation from either a Frank-Read source at the bottom or due to the stress-gradient caused by surface oxidation respectively. Other dislocation based theories of whisker growth such as a two-stage diffusion-dislocation based model pro-

posed by Lindborg [1976], where a dislocation loop expands by climb till the force is balanced following a dislocation glide to protrude as whiskers. Lee and Lee [1998] also proposed growth of whiskers from a prismatic loop under the action of a Peach-Koehler force due to the stress field that is present in the film due to the formation of intermetallic compounds (IMCs) at the substrate-film interface. However, such dislocation based theories have seldom been accepted in the whisker research community based on the facts that whiskers were observed to grow from the base and not from the tip Koonce and Arnold [1953]; the lack of dislocations being observed in the whisker grain; and the fact that for such theories to hold true the whisker growth axis should always be parallel to Burgers vector (slip direction or “close-packed direction") which is not observed in the transmission electron microscopy (TEM) studies LeBret and Norton [2003].

Since tin is at high homologous temperature under ambient conditions, it readily deforms plastically when loaded and recrystallizes around 30 °C. These facts motivated whisker formation theories based on recrystallization. Early proponents of the “recrystallization theory for whisker growth" include [Ellis et al., 1958, Glazunova and Kudryavtsev, 1963, Furuta and Hamamura, 1969] who proposed that whiskers grew as a means to lower the strain energy in the film. Ellis et al. [1958] even famously stated that “whisker growth is but a special case of recrystallization and growth involving mass transport”. Since β-Sn has a low melting point that lets it exhibit high temperature plasticity even at room temperature, the grains undergoing large deformation (and hence with higher strain energy) served to be the nucleation sites which then led to whisker growth by recrystallization. Kakeshita et al. [1982] also supported the notion that recrystallization is a necessary step for whisker formation based on his experimental studies between two types of films: one having large well-polygonized grain morphology while the other having small, non-polygonized grain structure. He attributed the first scenario to be a situation in which recrystallization had already happened thereby requiring no further need to grow whiskers, while the latter being the case which did not undergo recrystallization and hence lowered the energy by whisker growth. Based on this theory small , sub-micron, grains recrystallized to form grains with a size of about 1 µm to 2 µm, which then become probable

whisker grains. Following, Boguslavsky and Bush [2003] proposed the spontaneous whisker formation as an “abnormal grain growth" mechanism where new atoms are added to the lattice of the whisker grain by the process of recrystallization as a means to minimize the strain energy (stored as dislocations) in the whisker grain. Such a notion is also guided by the fact that the recrystallization temperature of tin is around 30 °C and thus enabling room temperature recrystallization. It was also proposed that the whisker nucleation sites were those areas that underwent severe plastic deformation as well as ones that are highly misoriented with respect to its neighbors “which gives the needed growth mobility" for the new grains to grow [Vianco and Rejent, 2009, Vianco et al., 2015]. Even though the above “recrystallization based theories" of whisker growth were quite prevalent, there have been certain direct contradictions such as the fact that the propensity of whisker growth is larger in large crystallized grains as compared to small-grain deposits, [Boguslavsky and Bush, 2003] which is in direct contradiction with the findings of Furuta and Hamamura [1969]. Moreover, based on the experimental observations by Jadhav et al. [2010a], Pei et al. [2012], Jagtap et al. [2017] the whisker grain was found to exist from the beginning and not formed later as a result of recrystallization. Furthermore, throughout the literature it has been vaguely proposed that there exists some long-range diffusion of Sn atoms into the whisker grain and the crystal orientation of the whisker grain and its neighborhood plays a significant role in the growth of the whiskers. However, with the μ-X-Ray diffraction (μ-XRD) studies by Pei et al. [2016] it was observed that there lacks any peculiarity in the stress and strain fields at the vicinity of the whisker grain. Such a lack of uniqueness was also observed in the fraction of high-angle grain boundaries between the whisker grain and its neighbors. Moreover, this underlying assumption that recrystallization by itself is a long-range mass transport mechanism is inherently difficult to comprehend as atoms would only undergo slight displacements (of less than interatomic distances) when swept by the reorientation front that transfers them from their initially occupied crystal lattice to the new one.

The origin and magnitude of mass transfer by long-range diffusion was first formulated by Tu [1994]. In his model, he simplified the growth kinetics as a radially symmetric diffusion

problem where the tin atom flux is collected from the measured average area per whisker. The stress gradient supporting this flux varied from the average (compressive) film stress at a far away point (field of transport) to a zero stress condition at the centrally located whisker grain. The zero-stress boundary condition for the whisker grain was rationalized by the presence of a "weak oxide" layer on top in that, once the surface oxide on top has been fractured by the vertical expansion of the whisker grain it could easily accommodate any new atoms being added into the whisker grain boundary, as opposed to an intact oxide layer that would provide a mechanical constraint. The major shortcoming of this model being, in order to fit the experimentally observed whisker growth rates, the required compressive stresses in the film needs to be much higher compared to those obtained typically in experiments. This model was later improved by Hutchinson et al. [2004], where the collection cross section was increased from a monoatomic layer to the full film height. More recently, [Sarobol et al., 2013] refined the assumption of zero stress boundary condition at the whisker root (proposed by Tu) by considering additional frictional resistance to atom accretion onto the boundaries of an oblique whisker grain. In this modification, accretion of atoms is restricted to happen at the fraction of the whisker grain boundary area that are considered as horizontal facets while a sliding friction stress is postulated to act on the vertical parts of the grain boundary. This frictional force opposes the outward motion of the whisker whose magnitude depends on the inclination of the whisker grain boundaries. This led to the rationalization of the experimentally observed preference for shallow whisker grains. Furthermore, by making the sliding resistance depend on the sliding velocity, their proposed non-steady state growth model could predict similar "stick–slip" growth that is observed experimentally [Eshelby, 1953, Chason et al., 2008]. In this model, the effect of grain geometry and size, film stress, and oxide layer thickness was highlighted, however the origin of a favorable stress gradient was not specified.

The most advanced improvement of the radially symmetric long-range transport diffusion model centered on a predetermined whisker grain has been reported by Pei et al. [2017] building on former works from the same group at Brown University [Buchovecky et al., 2009b, Bu-

chovecky, 2010]. In this nascent formulation, the conditions dictating the stress evolution in the film and the subsequent diffusion to the whisker base emerge as a natural outcome from the balance between the strain generation, through Cu_6Sn_5 formation or via thermal expansion mismatch, and the subsequent stress relaxation, via rate-dependent plasticity and diffusive mass transport leading to whiskers, in the chemomechanically coupled system. Diffusive transport is explicitly triggered by reducing the compressive stress boundary condition at the central whisker grain to a predetermined value with respect to its surroundings. This value is most often attributed to the yield stress of Sn and the underlying reasoning being this whisker grain has undergone more plasticity compared to its neighbors. In these simulations, a stress profile develops around the whisker grain such that the amount of mass diffusing into the whisker grain and the subsequent whisker growth velocity is determined by the applied strain rate rather than the actual whisker spacing. Model validation is done by comparing to the experimentally obtained stress profile and whisker growth rates, thereby leading them to conclude that the local microstructure is of less importance, as the simple isotropic model without any hardening could capture the important physical processes determining the whiskering and the rate-dependent plasticity. However, such an information of the local microstructure might be crucial in isolating grains that are more probable to whisker formation, and hence addressing the critical question of whisker nucleation. The two ideas which exist regarding a grain forming whiskers are either an oblique (inclined) grain boundary which are either preexisting or later formed via lateral grain growth [Chason et al., 2014] or weak grains that undergo significant amount of plastic deformation. None of the two notions is conclusive as contradicting observations have been reported, and it is our believe that these questions could be answered via three-dimensional full-field chemo-thremo-mechanical simulations in a crystal plasticity framework which takes into account the effect of crystal anisotropy.

2.4 Modeling framework

Crystal plasticity (CP) material solvers can accommodate the effect of crystal anisotropy and neighborhood texture in determining the overall response of the system under applied boundary conditions. In the same context, “full–field" simulations correspond to the fact that the simulation geometry incorporates spatial grain information obtained from experiments. In this work the CP simulations are performed using the open source “Düsseldorf Advanced Material Simulation Toolkit” (DAMASK) [Eisenlohr et al., 2014] developed in Max-Planck-Instiut für Eisenforschung GmbH (MPIE)[Roters, 2011, Roters et al., 2012, 2019]. Various constitutive models and homogenization schemes for crystal plasticity simulations at different length scales are available in the DAMASK software, which also provides a flexible interface with commercial finite element (FE) packages such as ABAQUS and MSC.Marc. Apart from it being the material point solver (to solve constitutive field equations), DAMASK also has its own integrated boundary value solver that uses spectral methods that reduces computation time significantly compared to finite-element based solvers [Eisenlohr et al., 2013, Shanthraj et al., 2015, Diehl, 2016]. The crystal plasticity (CP) model is based on a continuum mechanical finite strain framework that describes the mechanical behavior of the body under consideration, and also needs the “microstructure" or grain information. Material response is then obtained by solving for global equilibrium conditions along with inter-grain compatibility (achieved through the prescribed homogenization scheme) that also ensures the fulfillment of the local compatibility and equilibrium condition at each discretization point, an approach much different from the early plasticity models that enforced uniform strain Taylor [1938] or resolved shear stress Sachs [1929] distribution within each grain.

In this section, first a brief background about continuum mechanics is provided to introduce the different continuum mechanical expressions and their relevance. Subsequently, a brief overview is given about the concepts of general crystal plasticity theory as well as the numerical methods used to solve the respective field equations. However, the constitutive models used to run the simulations are not described in this section and will be explained separately in

subsequent chapters where the simulation results are discussed.

2.4.1 Continuum mechanics

In the field of continuum mechanics the mechanical behavior of a body is modeled as a hypothetical continuous mass rather than discrete particles. Based on this assumption, any object would then completely fill the space it occupies. This has the advantage that the deformation behavior of the material could be described using continuous mathematical functions, while the disadvantage being discontinuities in the body, such as cracks, are neglected. To have a consistent solution for a problem in a continuum mechanical framework, the following sets of equations has to be supplied:

- deformation compatibility
- mechanical equilibrium or balance of forces
- constitutive description

In continuum mechanics the kinematics of deformation is described through various stages in the deformation history of the body or configurations. Even though the body occupies different configurations, there still exists continuity during the deformation such as:

- The material points forming a closed curve at any instant will always form a closed curve at any subsequent time.
- The material points forming a closed surface at any instant will always form a closed surface at any subsequent time and the matter within the closed surface will always remain within.

In this sense, the reference (undeformed or time-independent) configuration occupying a region $\mathscr{B}_0$ in space (with infinite number of material points) under certain (time-dependent) loading would attain the current (deformed or time-dependent) configuration occupying a region $\mathscr{B}_t$ in space. The location of the material points filling $\mathscr{B}_0$ is given by $\mathbf{x} \in \mathscr{B}_0$, and that in

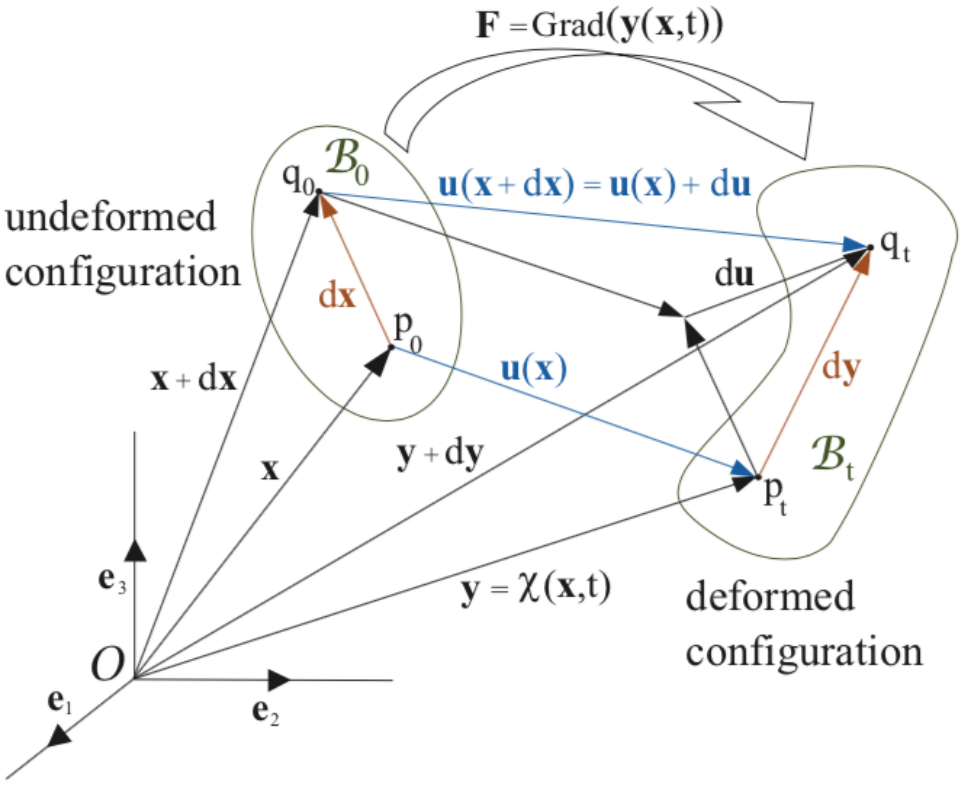

Figure 2.8: Kinematics of a continuum body undergoing deformation [Diehl, 2016].

$\mathscr{B}_t$ is given by $\mathbf{y} \in \mathscr{B}_t$, as illustrated in Fig. 2.8. Each configuration can have its own basis vectors, however using a general orthonormal Cartesian coordinate system for both configurations avoids the complexity of representing vectors with different basis for different configurations. In general there exists two ways to describe the motion of a body, i.e., either as Lagrangian (material) description or Eulerian (spatial) description. In the Lagrangian description the reference configuration is also the undeformed configuration and the position and physical properties of the particles are described in terms of the reference configuration coordinates and time. It can be thought as if an observer standing in the frame of reference of $\mathscr{B}_0$ observed how the body changes over time to reach $\mathscr{B}_t$. Since, the choice of reference configuration is arbitrary in general, the results obtained in Lagrangian description are independent of the choice of initial time and reference configuration. While Eulerian or spatial description focuses on the current configuration and is akin to observing what happens to a fixed point in space. In this work, like

in most cases of solid mechanics, the motion is described using the Lagrangian description, where a deformation map $\chi(\mathbf{x}) : \mathbf{x} \in \mathscr{B}_0 \rightarrow \mathbf{y} \in \mathscr{B}_t$ is used to map points $\mathbf{x}$ in the reference configuration to points $\mathbf{y}$ in the current configuration. The displacement $\mathbf{u}$ of a material point at a fixed deformation state (fixed t) is then given by:

$$\mathbf{u}(\mathbf{x}) = \chi(\mathbf{x}) - \mathbf{x} \tag{2.1}$$

A line segment d$\mathbf{x}$ in an infinitesimal neighborhood of a material point $\mathbf{x}$ in the reference configuration is then pushed forward into the current configuration by:

$$\mathbf{y} + \mathrm{d}\mathbf{y} = \mathbf{y} + \frac{\partial \mathbf{y}}{\partial \mathbf{x}} \cdot \mathrm{d}\mathbf{x} + \mathscr{O}(\mathrm{d}\mathbf{x}^2). \tag{2.2}$$

Neglecting terms of higher order, d$\mathbf{y}$ can be expressed as:

$$\begin{aligned} \mathrm{d}\mathbf{y} &= \frac{\partial \mathbf{y}}{\partial \mathbf{x}} \cdot \mathrm{d}\mathbf{x} \\ &= \underbrace{\mathrm{Grad}\, \chi}_{=:\mathbf{F}(\mathbf{x})} \cdot \mathrm{d}\mathbf{x}, \end{aligned} \tag{2.3}$$

where $\mathbf{F}(\mathbf{x})$ is the second order tensor called the deformation gradient. $\mathbf{F}(\mathbf{x})$ maps the infinitesimal line segment d$\mathbf{x}$ in the reference configuration to d$\mathbf{y}$ in the current configuration Roters et al. [2019]. As illustrated in Fig. 2.8 the deformation gradient tensor $\mathbf{F}$ (the argument $\mathbf{x}$ or the spatial dependence is assumed implicitly) is a 2-point tensor, meaning it has one basis in the reference configuration and the other one in the current configuration. Since $\mathbf{F}$ is a mapping function its inverse, $\mathbf{F}^{-1}$, exists as well which maps elements from current configuration back to the reference configuration. The commonly observed terms “push forward" and “pull back" on a quantity refers to the operation by $\mathbf{F}$ or $\mathbf{F}^{-1}$ on that quantity to either map into current configuration (from reference configuration) or back into reference configuration (from current configuration) respectively.

The material velocity field is defined as:

$$\begin{aligned} \mathrm{d}\mathbf{v} &= \frac{\mathrm{d}\mathbf{u}(\mathbf{x})}{\mathrm{d}t} \\ &= \dot{\mathbf{u}}, \\ &= \dot{\chi}, \end{aligned} \tag{2.4}$$

where $\mathbf{u}$ ($\mathbf{x}$) is the material displacement field which varies with time (deformation). Since the reference configuration is assumed to be time-independent, i.e., $\mathrm{d}\mathbf{x}/\mathrm{d}t = 0$, the relation $\dot{\mathbf{u}} = \dot{\chi}$ holds. The velocity gradient $\mathbf{L}$ is then the spatial gradient of the velocity field, $\partial\mathbf{v}/\partial\mathbf{y}$ and can also be expressed as:

$$\mathbf{L} = \dot{\mathbf{F}}\mathbf{F}^{-1} \tag{2.5}$$

The deformation gradient, in general, is associated with a rotation and a stretch, and since it is invertible it can also be decomposed uniquely by a “polar decomposition":

$$\begin{aligned} \mathbf{F} &= \mathbf{VR} \\ &= \mathbf{RU}, \end{aligned} \tag{2.6}$$

where $\mathbf{R}$ is the rotation tensor and $\mathbf{U}$ and $\mathbf{V}$ represents the right and left stretch tensors respectively. Depending on the configurations various strain and stress measures exist, for example if we want to express the strain completely in reference configuration then it is expressed as GREEN–LAGRANGE strain tensor defined as $(\mathbf{F}^{\mathrm{T}}\,\mathbf{F} - \mathbf{I})/2$; while a strain measure completely in current configuration is the EULER–ALMANSI strain tensor defined as $(\mathbf{I} - \mathbf{F}^{-\mathrm{T}}\mathbf{F}^{-1})/2$. Thus, the push forward for GREEN–LAGRANGE strain tensor is the EULER–ALMANSI strain tensor.

Similar to the above mentioned strain measures, the stress measures of the body undergoing deformation can be expressed in different configurations. The CAUCHY stress tensor σ is expressed completely in the current (or deformed) configuration since it is defined as the force expressed in the current configuration acting on an infinitesimal area also in the current configuration and hence is a symmetric tensor. Similarly, the second PIOLA–KIRCHHOFF stress-tensor is a symmetric tensor represented completely in the reference (stress-free) configuration. In static equilibrium without any body forces the equilibrium condition:

$$\sigma_{ij,j} = 0, \tag{2.7}$$

which is conveniently written in the finite strain theory as,

$$\begin{aligned} 0 &= \mathrm{Div}\,\mathbf{P} \\ &= \nabla \cdot \mathbf{P} \end{aligned} \tag{2.8}$$

where **P** represents the non-symmetric first PIOLA–KIRCHHOFF stress tensor.

With this brief continuum mechanical overview, the crystal plasticity framework where the simulations are performed in this work is explained next.

2.4.2 Crystal Plasticity Multi-physics framework

Crystal plasticity (CP) models are well-established laws that take into account the affect of material anisotropy in response to an external load and hence is a powerful tool in computational materials science to investigate structure–property relationships. The CP modeling technique has been successfully implemented to study a wide range of micromechanical phenomena ranging from evolution of slip resistance and strain hardening in single crystals to mechanical response in a polycrystalline aggregate [Roters et al., 2010b, 2019]. Even though the formulation of this modeling framework originated to investigate the plastic deformation of a material by crystallographic slip on discrete slip systems, with increasing variability in the environmental conditions of applications leading to drastic microstructural changes in the system (such as phase transformation, crack nucleation, high temperature deformation), this CP framework has recently been extended to include the complex coupling of other constitutive field equations (damage, reaction-diffusion, thermal, electromigration) to formulate a more unified and general multi-physics tool in order to have a better representation of the physical system and hence higher accuracy in prediction [Shanthraj et al., 2016, 2019]. In this work, the open source crystal-plasticity multiphysics framework DAMASK was modified to include the stress-driven diffusion kinetics in order to simulate the mass transport in tin films. Integration of the new constitutive law along with the subsequent numerical strategy into the existing modeling framework is relatively straightforward due to the modular structure of DAMASK [Roters et al., 2019], and some of its relevant features will be discussed in the subsequent paragraphs in the context of solving coupled field equations in this framework.

In DAMASK, the constitutive equations are prescribed in the single crystal level which are then homogenized by appropriate homogenization schemes to get the overall system response.

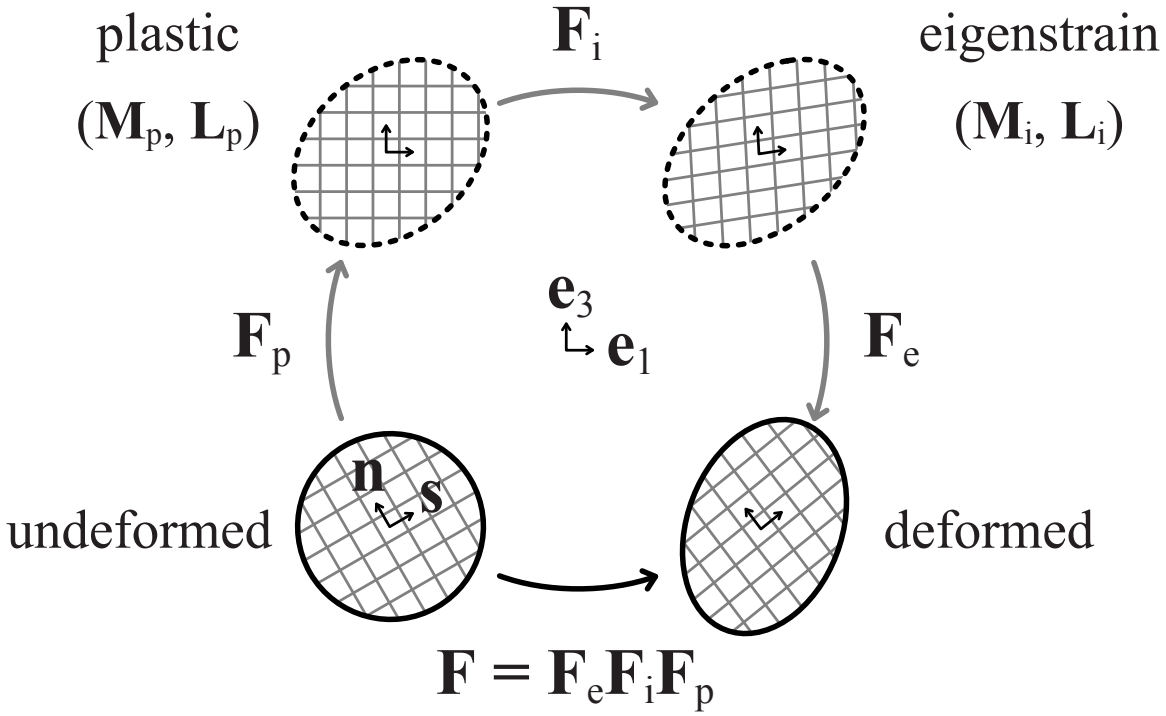

Figure 2.9: Illustration of the intermediate configurations resulting from the multiplicative decomposition of the deformation gradient [Roters et al., 2019]. Selecting the crystal orientation as initial value of $\mathbf{F}_p(t=0) = \mathbf{O}_0$ guarantees that the lattice coordinate system in the plastic configuration always coincides with the lab coordinate system [Ma et al., 2006].

In this work the full-field simulations are performed where each grain in the polycrystalline aggregate is spatially resolved into a large number of material points/voxels and the field equations are solved at each of these material points hence no homogenization scheme is needed. Moreover, as mentioned earlier, the current work includes the effect of stress-driven mass transport hence a strong coupled numerical framework is required to intimately include the kinematic consequences of such transport– both at a constitutive (governing transport equation) and at the continuum (subsequent kinematics due to transport) levels.

In this context, the numerical framework in DAMASK is based on the finite deformation theory where the deformation gradient,$\mathbf{F}$, governing the motion of the body is multiplicatively decomposed into first a lattice preserving plastic deformation gradient, $\mathbf{F}_p$, followed by the intermediate lattice distorting or “eigenstrain" deformation gradient, $\mathbf{F}_i$, and finally the elastic

deformation gradient, $\mathbf{F}_e$ as illustrated in Fig. 2.9.

$$\mathbf{F} = \mathbf{F}_e\mathbf{F}_i\mathbf{F}_p \tag{2.9}$$

The plastic deformation gradient $\mathbf{F}_p$ maps the undeformed (initial) configuration into a volume conserving plastically deformed configuration, while $\mathbf{F}_i$ maps the subsequent volume non-conserving eigenstrain configuration that accommodates stress-free strains (“eigenstrains") such as thermal strains or chemical strains. The final deformed configuration mapping (that involves both rotation and stretch) is obtained by the elastic deformation gradient, $\mathbf{F}_e$. Moreover, to avoid unnecessary rotations of the continuum quantities due to the difference in reference frames of the individual grains and the global (lab) frame, the first deformation map ($\mathbf{F}_p$) is initialized with the orientation matrix corresponding to the initial crystal orientation $\mathbf{O}_0$, i. e. $\mathbf{F}_p(t = 0) = \mathbf{F}_e{}^T(\text{t= 0}) = \mathbf{O}_0$ such that the plastic configuration of each crystal corresponds to a common cube orientation [Ma et al., 2006]. Following this, the current orientation matrix ($\mathbf{O}$) can then be calculated from $\mathbf{F}_e$ through the polar decomposition [Roters et al., 2019].

The second PIOLA–KIRCHHOFF stress tensor $\mathbf{S}$ depends on the GREEN–LAGRANGE strain tensor as:

$$\mathbf{S} = \mathbb{C} \cdot \mathbf{E}_e, \tag{2.10}$$

where $\mathbb{C}$is the stiffness tensor. The stress $\mathbf{S}$, along with the microstructural state (given by the corresponding constitutive equation(s)), drives the plastic velocity gradient $\mathbf{L}_p$ as well as the eigenstrain velocity gradient $\mathbf{L}_i$ (summation of both the thermal and chemical velocity gradients). The velocity gradients are given by:

$$\mathbf{L} = \dot{\mathbf{F}}\mathbf{F}^{-1} \tag{2.11}$$

This interdependency among the various kinematic quantities is illustrated in Fig. 2.10 which also shows the self-consistent numerical strategy. In that, first the plastic velocity gradient ($\mathbf{L}_p$) is solved by a predictor-corrector scheme under an assumed $state$ and the eigenstrain (intermediate) velocity gradient $\mathbf{L}_i$. With a obtained $\mathbf{L}_p$ and the previously fixed $state$, the following eigenstrain velocity gradient(s) are solved sequentially (depending on the problem there

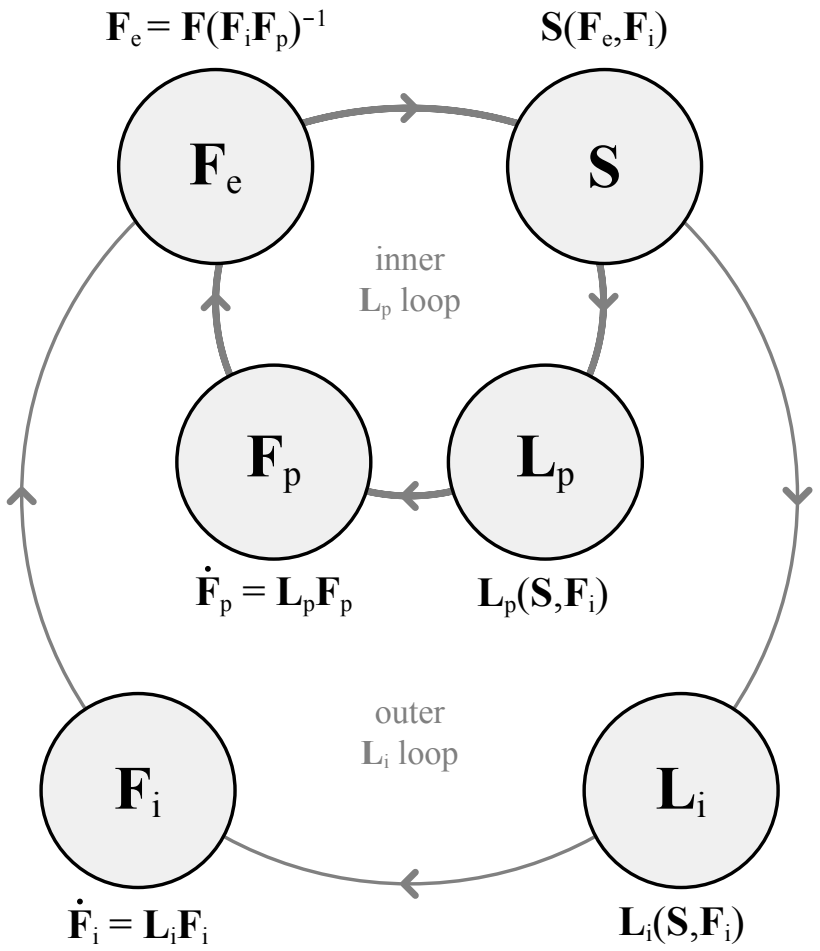

Figure 2.10: Solution strategy for the various kinematic quantities, [Roters et al., 2019].

might be multiple sources of $\mathbf{L}_i$). Finally, a check is performed to see whether the obtained velocity gradients is consistent with the assumed $state$ or not [Shanthraj et al., 2019, Roters et al., 2019]. If the difference between the assumed and the predicted $state$ is below the prescribed tolerance, the solution is considered to be converged otherwise the next iteration starts. The numerical strategies to solve the differential equations as well as the subsequent integration is mentioned briefly in the subsequent section.

2.4.2.1 Numerical schemes

The solution of the boundary value problem, i.e., static equilibrium is obtained numerically using one of the many existing techniques. The most common methods of solving such static

equilibrium problems is either via finite element method (FEM,) [Courant, 1943, Zienkiewicz, 1967, Bathe, 2014, Zienkiewicz et al., 2013] or through spectral methods using fast FOURIER transform (FFT) introduced first by [Moulinec and Suquet, 1994] and later modified by [Lebensohn, 2001, Kaßbohm et al., 2006, Spahn et al., 2014, Eisenlohr et al., 2013, Willot, 2015, De Geus et al., 2017]. The critical difference between FEM and FFT method being, in FEM the solution of the field equation is approximated by local shape functions (lower-order polynomials) that are non-zero in a finite domain ("element") and are then summed over to get the total approximate (weak form) solution. While the spectral FFT methods approximate the whole domain by one large set of basis functions [Shanthraj et al., 2019]. When these globally non-zero ansatz functions (except at their roots) are trigonometric the method uses the fast FOURIER transform to solve for them, and hence referred as FFT. The FEM method has been the most popular in solving micromechanical field equations due to the possibility of investigating systems having complex geometries, while the spectral FFT based methods inherently investigates a periodic system.

As mentioned earlier, the open source multi-field material point solver, DAMASK, used in this study has its inherent spectral FFT boundary value solver but could also be used in conjunction with commercially available FEM solvers as a user material subroutine such as MSC-Marc and ABAQUS. In Chapter 5, the use of the material solver DAMASK along with commercial FEM solver MSC-Marc is discussed with respect to nanoindentation simulations, while the coupled thin film micromechanical simulations in Chapters 3 and 4 are performed using the FFT based spectral solver of DAMASK.

The key thing for any material solver is to provide a measure of stress (**S**, **P**, or σ depending on the solver) for an input measure of deformation gradient, **F**. The following outlines the steps undertaken by the material solver in DAMASK to evaluate a consistent value of stress for a given value of **F** at each material point. As mentioned earlier, the partitioning of the global **F** field received from the boundary value solver into **F** at each material point and the subsequent homogenization of the stress at each material point into a global stress field is handled

by the “partitioning and homogenization" module in DAMASK based on the provided scheme, and is excluded in this section (see [Roters et al., 2019] for further details). Thus, at each time step and with a known $\mathbf{F}$ at each material point the following system of equations is solved in a self-consistent way:

$$\mathbf{F} = \mathbf{F}_\mathrm{e}\mathbf{F}_\mathrm{i}\mathbf{F}_\mathrm{p} \tag{2.12a}$$

$$\dot{\mathbf{F}} = \mathbf{L}\mathbf{F}, \text{ for both the inelastic deformation gradients,} \tag{2.12b}$$

$$\mathbf{L} = \sum_n f_n(\mathbf{S},\ldots), \text{ for both the inelastic velocity gradients,} \tag{2.12c}$$

where the second PIOLA–KIRCHHOFF stress, which is the work conjugate of the GREEN–LAGRANGE strain tensor, is obtained from the elastic constitutive equation, $\mathbf{S} = f\,(\mathbf{E}_\mathrm{e},\ldots)$. These equations are solved in an implicit manner with the velocity gradient integrals being approximated as (with a fixed material state) for a time interval Δt:

$$\frac{\mathbf{F}_\mathrm{p}(t) - \mathbf{F}_\mathrm{p}(t_0)}{\Delta t} = \mathbf{L}_\mathrm{p}(t)\mathbf{F}_\mathrm{p}(t) \text{ and} \tag{2.13a}$$

$$\frac{\mathbf{F}_\mathrm{i}(t) - \mathbf{F}_\mathrm{i}(t_0)}{\Delta t} = \mathbf{L}_\mathrm{i}(t)\mathbf{F}_\mathrm{i}(t), \tag{2.13b}$$

which results in the inelastic deformation gradients at the end of the time increment being

$$\mathbf{F}_\mathrm{p}(t) = \left(\mathbf{I} - \Delta t\mathbf{L}_\mathrm{p}(t)\right)^{-1}\mathbf{F}_\mathrm{p}(t_0) \text{ and} \tag{2.14a}$$

$$\mathbf{F}_\mathrm{i}(t) = \left(\mathbf{I} - \Delta t\mathbf{L}_\mathrm{i}(t)\right)^{-1}\mathbf{F}_\mathrm{i}(t_0), \tag{2.14b}$$

from which $\mathbf{F}_\mathrm{e}$ can be calculated using Eq. (2.12a). The unknowns for the above system of coupled non-linear algebraic equations, $\mathbf{F}_\mathrm{e}$, $\mathbf{F}_\mathrm{i}$, and $\mathbf{F}_\mathrm{p}$, whose solution would then provide a stress state satisfying the multiplicative decomposition as well as fulfilling the constitutive laws for the respective velocity gradients, represented here as generic functions Eq. (2.12c).

Since, the different fields (given by either $\mathbf{L}_\mathrm{i}$ for thermal and chemical stresses or $\mathbf{L}_\mathrm{p}$ for mechanical stresses) are completely coupled, their solution is obtained using a two-level

predictor–corrector scheme (as shown in Fig. 2.10) by my minimizing the following residuals:

$$\mathbf{R}_\mathrm{p}\left(\widetilde{\mathbf{L}_\mathrm{p}},\widetilde{\mathbf{L}_\mathrm{i}}\right) = \widetilde{\mathbf{L}_\mathrm{p}} - \mathbf{L}_\mathrm{p}\left(\mathbf{M}_\mathrm{p}\left(\widetilde{\mathbf{L}_\mathrm{p}},\widetilde{\mathbf{L}_\mathrm{i}}\right)\right) \text{ and} \tag{2.15a}$$

$$\mathbf{R}_\mathrm{i}\left(\widetilde{\mathbf{L}_\mathrm{p}},\widetilde{\mathbf{L}_\mathrm{i}}\right) = \widetilde{\mathbf{L}_\mathrm{i}} - \mathbf{L}_\mathrm{i}\left(\mathbf{M}_\mathrm{i}\left(\widetilde{\mathbf{L}_\mathrm{p}},\widetilde{\mathbf{L}_\mathrm{i}}\right)\right), \tag{2.15b}$$

with $\widetilde{\mathbf{L}_\mathrm{p}}$ and $\widetilde{\mathbf{L}_\mathrm{i}}$ denoting the predicted values of $\mathbf{L}_\mathrm{p}$ and $\mathbf{L}_\mathrm{i}$. These residuals Eqs. (2.15a) and (2.15b) are then minimized using a modified NEWTON–RAPHSON scheme with a variable step length until a consistent solution is obtained, within a staggered iterative loop [Shanthraj et al., 2019, Roters et al., 2019]. The solution algorithm is outlined in Algorithm 1. Convergence of the NEWTON–RAPHSON scheme is achieved when the residual drops below a given tolerance

$$\epsilon_\mathrm{p} = \max\left(\epsilon_\mathrm{a}, \epsilon_\mathrm{r}\left|\left|\mathbf{L}_\mathrm{p}\right|\right|_2, \epsilon_\mathrm{r}\left|\left|\widetilde{\mathbf{L}_\mathrm{p}}\right|\right|_2\right) \tag{2.16a}$$

$$\epsilon_\mathrm{i} = \max\left(\epsilon_\mathrm{a}, \epsilon_\mathrm{r}\left|\left|\mathbf{L}_\mathrm{i}\right|\right|_2, \epsilon_\mathrm{r}\left|\left|\widetilde{\mathbf{L}_\mathrm{i}}\right|\right|_2\right) \tag{2.16b}$$

where the values of absolute and relative errors (ϵ_a and ϵ_r) are prescribed.

The advantage of formulating the problem as a residual minimization is the use of open source solvers such as PETSc (Portable Extensible Toolkit for Scientific Computation), developed by [Balay et al., 2013] and PETSc team in Argonne National Lab, to find the solution. PETSc has various numerical algorithms to solve a system of linear or non-linear equations in the most efficient way and is a fundamental package for the usage of DAMASK. The spatial gradients of the mechanical field quantities are calculated using the forward-backward finite difference variant introduced by Willot [2015], Schneider et al. [2015] that reduces the frequently observed fluctuations in the results (also known as the "Gibbs phenomenon"). The gradient and divergence calculations for the chemical field quantities are performed in real space. The microstructural state integration is done using an implicit fixed point iterative scheme [Kalidindi et al., 1992]. For the spectral solver used in this work, the static equilibrium (i.e. the boundary value problem) equation is solved using the direct variational formulation originally introduced by Eisenlohr et al. [2013] and later modified by Shanthraj et al. [2015] using the "basic" scheme which is a collocation based approach at the grid points [Eisenlohr et al., 2013].

Algorithm 1: Self-consistent integration of kinematic quantities at a fixed internal material state [Roters et al., 2019].

Data: $[\mathbf{F}]_{t_n}$, $[\mathbf{F}_\mathrm{p}]_{t_{n-1}}$, $[\mathbf{F}_\mathrm{i}]_{t_{n-1}}$
Result: $[\mathbf{F}_\mathrm{p}]_{t_n}$, $[\mathbf{F}_\mathrm{i}]_{t_n}$, $[\mathbf{F}_\mathrm{e}]_{t_n}$, $[\mathbf{S}]_{t_n}$

Initialisation:

$$[\widetilde{\mathbf{L}_\mathrm{p}}]^0_{t_n} = [\mathbf{L}_\mathrm{p}]_{t_{n-1}},$$
$$[\widetilde{\mathbf{L}_\mathrm{i}}]^0_{t_n} = [\mathbf{L}_\mathrm{i}]_{t_{n-1}},$$

$j = 1$

$\mathbf{L}_\mathrm{i}$ loop:

while $\|\mathbf{R}_\mathrm{i}\|_2 \geq \epsilon_i$ **do**

$$[\mathbf{F}_\mathrm{i}]_{t_n} = \left(\mathbf{I} - \triangle t [\widetilde{\mathbf{L}_\mathrm{i}}]^{j-1}_{t_n}\right)^{-1} [\mathbf{F}_\mathrm{i}]_{t_{n-1}}$$

$k = 1$

$\mathbf{L}_\mathrm{p}$ loop:

while $\|\mathbf{R}_\mathrm{p}\|_2 \geq \epsilon_p$ **do**

$$[\mathbf{F}_\mathrm{p}]_{t_n} = \left(\mathbf{I} - \triangle t [\widetilde{\mathbf{L}_\mathrm{p}}]^{k-1}_{t_n}\right)^{-1} [\mathbf{F}_\mathrm{p}]_{t_{n-1}}$$
$$[\mathbf{F}_\mathrm{e}]_{t_n} = [\mathbf{F}]_{t_n} [{\mathbf{F}_\mathrm{p}}^{-1}]_{t_n} [{\mathbf{F}_\mathrm{i}}^{-1}]_{t_n}$$
$$[\mathbf{S}]_{t_n} = f\left([\mathbf{F}_\mathrm{e}]_{t_n}, [\mathbf{F}_\mathrm{i}]_{t_n}\right)$$
$$\mathbf{R}_\mathrm{p} = [\widetilde{\mathbf{L}_\mathrm{p}}]^{k-1}_{t_n} - \mathbf{L}_\mathrm{p}\left([\mathbf{S}]_{t_n}, [\mathbf{F}_\mathrm{i}]_{t_n}\right)$$
$$[\widetilde{\mathbf{L}_\mathrm{p}}]^{k}_{t_n} = [\widetilde{\mathbf{L}_\mathrm{p}}]^{k-1}_{t_n} - \alpha_\mathrm{p}\left(\partial_{\widetilde{\mathbf{L}_\mathrm{p}}} \mathbf{R}_\mathrm{p}\right)^{-1} \mathbf{R}_\mathrm{p}$$
$k = k+1$

end

$$\mathbf{R}_\mathrm{i} = [\widetilde{\mathbf{L}_\mathrm{i}}]^{j-1}_{t_n} - \mathbf{L}_\mathrm{i}\left([\mathbf{S}]_{t_n}, [\mathbf{F}_\mathrm{i}]_{t_n}\right)$$
$$[\widetilde{\mathbf{L}_\mathrm{i}}]^{j}_{t_n} = [\widetilde{\mathbf{L}_\mathrm{i}}]^{j-1}_{t_n} - \alpha_\mathrm{i}\left(\partial_{\widetilde{\mathbf{L}_\mathrm{i}}} \mathbf{R}_\mathrm{i}\right)^{-1} \mathbf{R}_\mathrm{i}$$
$j = j+1$

end

Apart from the above (relatively detailed) overview of the computational framework, the individual constitutive laws will be discussed as a part of simulation details in each chapter, along with a few lines about the continuum mechanical finite strain framework to allow for a coherent reading.

2.5 Summary

The coupled numerical framework described in this chapter provides a convenient tool to investigate the kinematics associated with the stress assisted transport of Sn atoms along the grain boundary network in tin films along with the associated effect of the stress on their kinetics. Moreover, since β-Sn has a very high homologous temperature even at room temperature, the added coupling of the mechanical (plastic and elastic) effects on the overall kinematics of the system cannot be neglected. The full-field calculations performed in this work take into account both the long-range and the short-range grain interactions thereby including the effects of grain neighborhoods in determining the overall stress-fields that in turn dictate the transport, [Liu et al., 2010]. The high material anisotropy of β-Sn that can significantly affect the overall system response of the film under load was incorporated easily in this crystal plasticity framework. The most critical advantage of the current framework is the ability to directly incorporate experimentally observed data (grain size distribution, and crystal orientation) into the simulations so as to have a direct comparison between the experimental and simulated results, thereby ensuring the fidelity of the simulated results.

In Chapter 3, full-field thermo-mechanical simulations of tin films are performed by mimicking the experiments of Pei et al. [2016]. The constitutive equations used for the different fields along with the simulated geometry are described. Critical outcomes from such simulations helped in proposing a hypothesis for the whisker nucleation process (and its subsequent growth) that is not in contradiction with the existing stress-controlled whisker formation theories in literature, along with highlighting the effects of film global texture, local grain geometry, and grain size distribution.

Following, the thermo-mechanical model was improved to add the stress-driven transport field equation along with its kinematic consequence in Chapter 4. The details of the constitutive field equations along with the numerical solution strategy that was developed to solve the flux equations with components having high property contrast is also explained. The goal of the simulations discussed in this chapter is to highlight the contribution of whisker formation on the overall stress-relaxation of the system. Moreover, the kinematic consequence of such mass redistribution is also addressed.

As mentioned previously, β-Sn has a very high plastic anisotropy with 13 slip families that are available to accommodate the plastic shape change. Moreover, since it shows high temperature plasticity even at room temperature ($300\,\mathrm{K} \approx 0.6 T_\mathrm{m}$) the plastic contribution to overall deformation becomes crucial thus requiring an accurate description of its plasticity. Even though the coupled chemo-thermo-mechanical simulations are performed using available data for β-Sn plasticity [Lee et al., 2015], which are the initial flowstress values (also referred to as critical resolved shear stresses (CRSS) of the different slip families), these values are yet to be established definitively. Thus, in order to estimate reliable values of these initial flow stresses, a modified Inverse Indentation Analysis (*IIA*) methodology is proposed, originally developed by Zambaldi et al. [2012], where the plasticity parameters are identified by comparing experimental and simulated single crystal nanoindentations. In Chapter 5, the details of the modified methodology are provided along with its reproducibility and robustness for symmetric face-centered cubic materials (with single slip family) using virtual experimental references. Following, the reliability of this methodology is studied for lower symmetric hexagonal commercially pure titanium (assuming three slip families), also using virtual experimental references, in Chapter 6. Having established the reliability, the next step would be to implement such a methodology for even more anisotropic β-Sn (having 13 slip families) and to compare the identified parameters with those existing in literature. This would facilitate in performing high-fidelity coupled multi-field material simulations with an accurate material description.

Apart from the general progress towards developing this robust multi-field material simula-

tion system with high phase contrast between components (such as the difference in diffusivity of Sn atoms in the bulk and the grain boundaries), the goal of this work is to analyze the critical process of whisker nucleation and its governing factors. Once we are able to determine which grains (or what are the dictating conditions) could lead to whiskers, better crystallographic mitigation strategies could be proposed (such as global or local film texture control) and the reliability issues due to whiskers could be avoided.

CHAPTER 3

THERMOMECHANICAL CRYSTAL PLASTICITY MODELING OF THERMALLY STRAINED β – Sn FILMS

3.1 Background

In this chapter, three-dimensional full-field thermo-mechanically coupled crystal plasticity simulations of thermally strained β-Sn thin films are shown using the numerical framework discussed in the previous chapter in Section 2.4. The objective of this work is to better understand the conditions governing the generally rare nucleation of whiskers from these films through the simulated results after validating them with experimental results. Critical aspects of this study include determination of crystallographic and geometric factors that significantly affect the hydrostatic stress along the grain boundary network of the film, and hence would influence the subsequent stress-driven mass transport along these boundaries prior to the onset of any whisker formation. In this work, the film is approximated as a periodic structure with approximately hundred columnar grains on an rigid isotropic substrate mimicking the experimental conditions of [Pei et al., 2017], where a compressive biaxial stress is imposed in the film upon heating the film-substrate system, due to differences in their coefficient of thermal expansion. A dilatational layer akin to air with negligible stiffness and strength compared to the film is also added on the top of the film. This dilatational layer avoids the need of having periodic boundaries, Maiti and Eisenlohr [2018], as well as, could later be adjusted to mimic the mechanical effect of any surface oxide layer. Critical observations from these simulations include the spatial variability of the hydrostatic stresses along the grain boundary network which also varies based on the global film texture; stress-gradients not exceeding one or two grain sizes; and negligible effect of grain geometry or grain size distribution as compared to film texture (local crystallographic neighborhood), affirming the notion that whisker formation is indeed a local phenomena as reported in literature Buchovecky [2010], Sobiech et al. [2011]. From these sim-

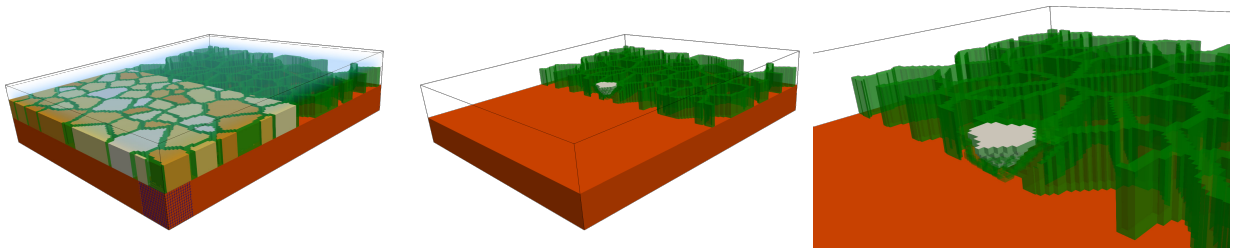

Figure 3.1: Discretized geometry of a tin film between a rigid isotropic substrate (orange, partly showing voxel size in the corner of left image) and soft dilatational "air" (faint blue). Boundary region between columnar tin grains (shades of yellow) is highlighted (green) and constitutes the (sub)volume of the film for which hydrostatic stress gradients are assumed to drive atom diffusion. Selected grains of the columnar film shown at left are transformed into an oblique surface grain (gray volume in the middle and right views). Chakraborty and Eisenlohr [2018]

ulations it is also inferred that β-Sn films having a fiber texture and with their fiber axis parallel to $\langle 0\,0\,1]$ is less whisker prone compared to the films having their fiber axis parallel to $\langle 1\,0\,0]$. In the following, Section 3.2, the details about the simulation geometry, boundary conditions, and input texture information is discussed followed by a brief account of the continuum mechanical framework and constitutive field equations. After highlighting the results in Section 3.3 a hypothesis about a plausible whisker formation mechanism is laid in Section 3.4 along with a summary of the results from the study. Parts of the work in this chapter is already published in Chakraborty and Eisenlohr [2018].

3.2 Simulation details

In this section the details about the coupled thermo-mechanical simulations mimicking one of the experimental conditions in Pei et al. [2017] is outlined.

3.2.1 Geometry discretization, film texture, and boundary conditions

The simulated geometry consists of a 1 µm thin film of body-centered tetragonal (bct) β-Sn with 103 columnar grains above a 1.4 µm rigid isotropic substrate, which has a smaller coefficient of thermal expansion, and a 0.8 µm layer of dilatational material mimicking free surface condition. The entire geometry is discretized by a regular grid of $128 \times 148 \times 32 = 606\,208$ voxels, each of

volume $0.1 \times 0.1 \times 0.1\,\mu m^3$ as illustrated in Fig. 4.2 (left). To analyze the effect of oblique shaped surface grains, in some simulations one (or few) columnar grain(s) are made oblique (inclined grain boundaries) as exemplified in Fig. 4.2 (right).

Poisson–Voronoi tessellation of the tin film volume (using 103 seed points) results in a relatively narrow grain size distribution. To arrive at wider distributions, grain growth is simulated through curvature-driven (and in-plane only) motion of the grain boundaries Eisenlohr et al. [2017].

Crystallographic orientations of each grain are selected such that a particular crystallographic direction is predominantly aligned with the film normal direction, resulting in a fiber texture for the film. The three fiber textures considered in this work are ⟨1 0 0], ⟨1 1 0], and ⟨0 0 1] (crystallographic notations adopted from Lee et al. [2015]), which are referred to as "green", "blue", and "red" in accordance with the standard inverse pole figure color mapping.

All three layers (substrate, film, and air) are initially stress-free, heated by 40 K in 20 min, and then kept at constant temperature to observe stress relaxation for another 160 min (black curve in Fig. 3.2), which is similar to the experimental conditions of Pei et al. [2017]

The resulting thermo-mechanically coupled system was solved under periodic displacement boundary conditions using the "basic" scheme of the spectral solver Shanthraj et al. [2015], Eisenlohr et al. [2013] that is part of the open-source Düsseldorf Advanced Material Simulation Kit (DAMASK).

3.2.2 Continuum mechanical framework

The continuum mechanical framework on which the thermo-mechanical simulations are performed is based on the finite strain deformation theory as described in detail in the previous chapter Section 2.4.1. A very brief highlight is also mentioned in here for the sake of ease in reading through the subsequent sections describing the constitutive field equations.

The deformation gradient field describes the translation of material points originally located at $\mathbf{x}$ in the undeformed configuration to a new location $\mathbf{y}$ in the current (or deformed) configu-

ration by the deformation gradient tensor given as:

$$\mathbf{F} = \frac{\partial \mathbf{x}}{\partial \mathbf{y}}. \tag{3.1}$$

In the present context, such a deformation is brought about by contribution of different processes such that the total deformation gradient can be decomposed Meggyes [2001] as

$$\mathbf{F} = \mathbf{F}_\mathrm{e}\,\mathbf{F}_\mathrm{th}\,\mathbf{F}_\mathrm{p} \tag{3.2}$$

into a lattice-preserving inelastic deformation gradient $\mathbf{F}_\mathrm{p}$, a lattice-distorting inelastic deformation gradient $\mathbf{F}_\mathrm{th}$, and an elastic deformation gradient $\mathbf{F}_\mathrm{e}$. $\mathbf{F}_\mathrm{p}$ maps the undeformed configuration to the "plastic" configuration. $\mathbf{F}_\mathrm{th}$ accounts for the thermal expansion and maps the plastic to the "intermediate eigenstrain" configuration. Lastly, this intermediate eigenstrain configuration is mapped to the final "deformed" configuration by $\mathbf{F}_\mathrm{e}$.

It is important to note that for the simulations shown in this chapter the intermediate eigenstrain configuration is accounted for solely by the thermal strain, while in the next chapter, Chapter 4, this eigenstrain will also account for the kinematics due to atom transport via an additive decomposition .

The time evolution of both inelastic deformation gradients $\mathbf{F}_\mathrm{p}$ and $\mathbf{F}_\mathrm{th}$ is given in terms of their respective velocity gradients $\mathbf{L}_\mathrm{p}$ and $\mathbf{L}_\mathrm{th}$ following the flow rules

$$\dot{\mathbf{F}}_\mathrm{p} = \mathbf{L}_\mathrm{p}(\mathbf{M}_\mathrm{p}, \ldots)\,\mathbf{F}_\mathrm{p} \tag{3.3}$$

$$\dot{\mathbf{F}}_\mathrm{th} = \mathbf{L}_\mathrm{th}(\mathbf{M}_\mathrm{th}, \ldots)\,\mathbf{F}_\mathrm{th}. \tag{3.4}$$

Both velocity gradients are driven by their respective work-conjugate Mandel stresses

$$\mathbf{M}_\mathrm{p} = (\mathbf{F}_\mathrm{e}\,\mathbf{F}_\mathrm{th})^\mathrm{T}\mathbf{F}_\mathrm{e}\,\mathbf{F}_\mathrm{th}\,\mathbf{S} \approx \mathbf{S} \tag{3.5}$$

$$\mathbf{M}_\mathrm{th} = (\det \mathbf{F}_\mathrm{th}{}^{-1})\mathbf{F}_\mathrm{th}\,\mathbf{S}\,\mathbf{F}_\mathrm{th}{}^\mathrm{T}, \tag{3.6}$$

where $\mathbf{S} = \mathbb{C} : (\mathbf{F}_\mathrm{e}{}^\mathrm{T}\mathbf{F}_\mathrm{e} - \mathbf{I})/2$ (using Hooke's law) is the second Piola–Kirchhoff stress, $\mathbb{C}$ the fourth-order stiffness tensor, and $\mathbf{I}$ the second-order identity tensor. In addition, the velocity gradients also depend on the material state and associated constitutive parameters.

Static equilibrium for this coupled system of equations is found by a staggered iteration scheme that solves $\mathbf{F}_\mathrm{p}$ under fixed $\mathbf{F}_\mathrm{th}$ and material state, then for $\mathbf{F}_\mathrm{th}$ at still fixed material state, and eventually for consistent material state within each time increment as described previously in Section 2.4.2.1 and can also be found in Shanthraj et al. [2019].

3.2.3 Constitutive description

The employed crystal plasticity framework naturally allows to incorporate the anisotropy in elasticity, plasticity, and thermal expansion. Thermal expansion due to a change in temperature T gives rise to the eigenstrain velocity gradient

$$\mathbf{L}_\mathrm{th} = \frac{\dot{T}\alpha_{ii}}{1+\alpha_{ii}(T-T_0)} \qquad i = 1,2,3, \tag{3.7}$$

which is used in the description of body-centered tetragonal (bct) β-Sn and the isotropic substrate. The matrix of (anisotropic) thermal expansion coefficients is denoted by α and the initial temperature by T_0.

The plastic velocity gradient is additively composed from slip rates

$$\mathbf{L}_\mathrm{p} = \sum_\alpha \dot{\gamma}^\alpha \mathbf{s}^\alpha \otimes \mathbf{n}^\alpha, \tag{3.8}$$

where the unit vectors $\mathbf{s}^\alpha$ and $\mathbf{n}^\alpha$ indicate the slip direction and slip plane normal for each slip system (indexed by α) of the different slip families in β-Sn. The resolved shear stress

$$\tau^\alpha = \mathbf{M}_\mathrm{p} \cdot \left(\mathbf{s}^\alpha \otimes \mathbf{n}^\alpha\right) \tag{3.9}$$

is the driving force for slip at rates

$$\dot{\gamma}^\alpha = \dot{\gamma}_0 \left|\frac{\tau^\alpha}{g^\alpha}\right|^n \mathrm{sgn}\left(\tau^\alpha\right), \tag{3.10}$$

with material parameters $\dot{\gamma}_0$ and n. The dislocation defect structure is parameterized phenomenologically Peirce et al. [1982], i.e., slip on each system α faces a resistance g^α that evolves due to slip on all systems (indexed by β) as

$$\dot{g}^\alpha = \sum_\beta h_0 \left|1-\frac{g^\beta}{g_\infty}\right|^a \mathrm{sgn}\left(1-\frac{g^\beta}{g_\infty}\right)\left|\dot{\gamma}^\beta\right|, \tag{3.11}$$

with initial hardening slope h_0, hardening exponent a, and saturation slip resistance g_∞ Hutchinson [1976]. This phenomenological crystal plasticity model is used to describe the mechanical behavior of the tin film. The substrate, in experiment, is typically an order of magnitude thicker than the film and is therefore assumed isotropically elastic with stiffness selected large enough so that on its further increase the system response did not change. The layer of soft dilatational material on top of the film ensures a free surface condition and uses the constitutive description proposed by Maiti and Eisenlohr [2018]. The components of the anisotropic thermal expansion, elastic stiffness tensor, and constitutive parameters for β-Sn crystal plasticity are adopted from Lee et al. [2015] and are listed in Table 3.1 along with corresponding values for the substrate and dilatational "air".

3.3 Simulation results

The selected constitutive parameters result in the stress relaxation behavior shown in Fig. 3.2 when thermally straining the film-on-substrate assembly (illustrated in Fig. 4.2). The solid colored lines reflect three different crystallographic textures, characterized by the crystallographic direction (either ⟨1 0 0], ⟨1 1 0], or ⟨0 0 1]) that has the highest probability of being normal to the film surface. The simulated stress responses of a tin film for all the three textures and with a fixed grain structure seem to generally agree closely with the experimentally measured relaxation behavior Pei et al. [2017] for which the actual film texture was not reported. The dashed vertical line at 20 min in Fig. 3.2 indicates the time of maximum film stress and is selected as the instance for data analysis. Since the diffusion of Sn atoms is localized on the grain boundary network and driven by a gradient in hydrostatic stress, the quantity of interest is the grain boundary hydrostatic stress of magnitude p, locally obtained by averaging pairs of voxels separated by a grain boundary.

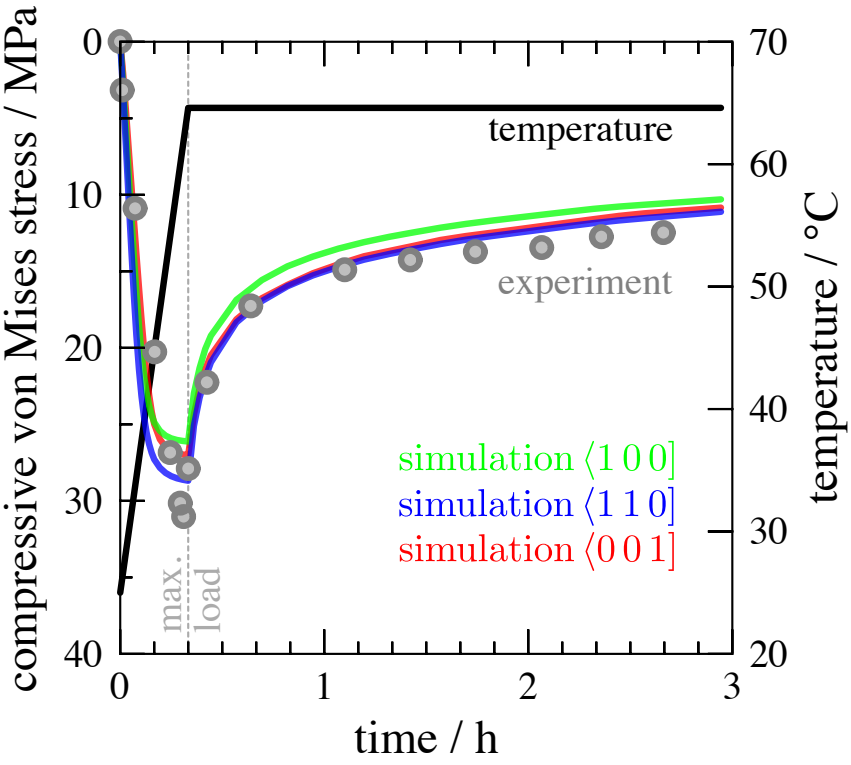

Figure 3.2: Forced temperature change of tin films on rigid substrate (black) and resulting compressive von Mises stress in the film simulated for different film fiber textures (colored lines) compared to measured stress evolution on a Si substrate (circles from Pei et al., 2017). Point of maximum load is reached after 20 min (at end of heating) and serves as reference for all subsequently reported stress values. Chakraborty and Eisenlohr [2018]

3.3.1 Spatial variability of grain boundary hydrostatic stress

The spatial variability of the grain boundary hydrostatic stress developing in the tin film in response to the thermomechanical loading is shown in Fig. 3.3. The magnitude of compressive stress ranges from about 0 MPa to 40 MPa (close to the substrate and at maximum load, see Fig. 3.2) and exhibits substantial heterogeneity that reflects the heterogeneity of grain morphology and lattice orientation in this grain patch. In the case of ⟨1 0 0] as dominant crystallographic direction aligned with the film normal, i. e. the "green" texture in Fig. 3.3, the variability of compressive hydrostatic grain boundary stress markedly decreases from the film–substrate interface to a more homogenous range of 20 MPa to 30 MPa at the film surface (right to left in Fig. 3.3), due to the reduced mechanical constraint towards the film surface. Additionally,

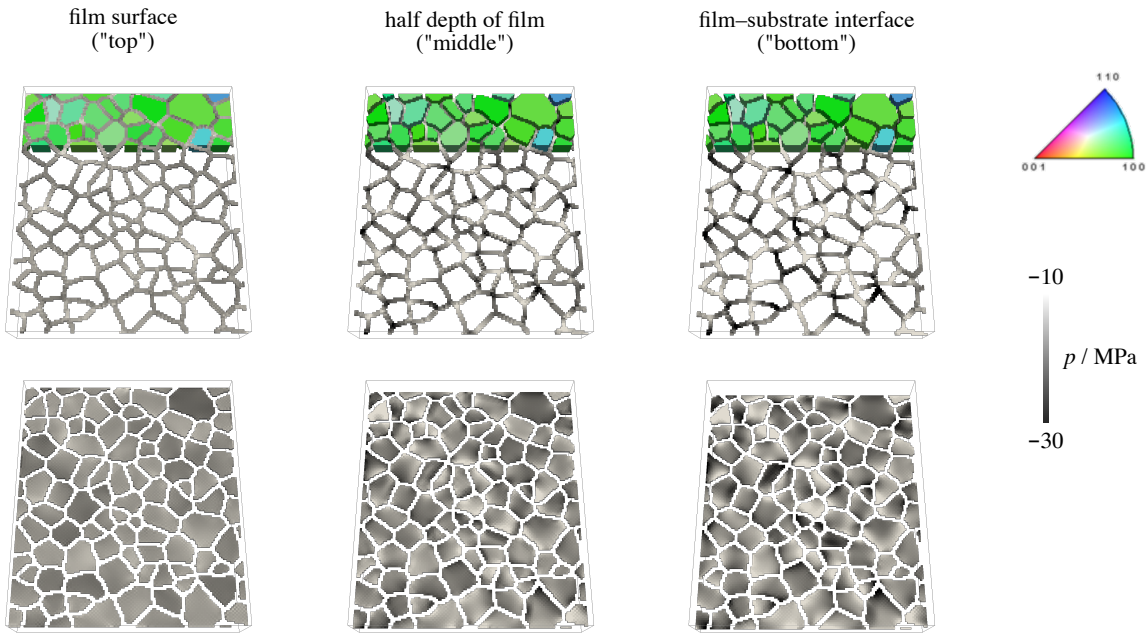

Figure 3.3: Spatial variability of grain boundary (top) and bulk grain (bottom) hydrostatic stress p for maximum load (reached after 20 min, see Fig. 3.2) illustrated at three different depths through the film (surface to substrate from left to right). Substrate is not shown while part of the columnar grain structure of the tin film is illustrated and colored according to the crystallographic direction that is parallel to the surface normal (close to ⟨1 0 0] in this example, see color code in standard stereographic triangle). Chakraborty and Eisenlohr [2018]

within the limited spatial extent of the polycrystalline structure discretized in this investigation, there is no indication of correlated long-range stress gradients (spanning multiple grains), which is consistent with reported experimental observations Pei et al. [2016].

3.3.2 Effect of film texture

β-Sn exhibits strong anisotropy, therefore, crystallographic texture is likely a significant influence in the development of film stress magnitude and its heterogeneity. The distributions of hydrostatic pressure p as function of film texture (green, blue, and red) and depth within the film are plotted in Fig. 3.4 at the same three film depths as shown in Fig. 3.3. Similar to the case of a green fiber texture that is spatially mapped in Fig. 3.3, both other fiber textures (blue and red) show a decrease in the range of p from the film–substrate interface to the film surface (dark to light color shades in Fig. 3.4). The overall width of the hydrostatic stress distributions is no-

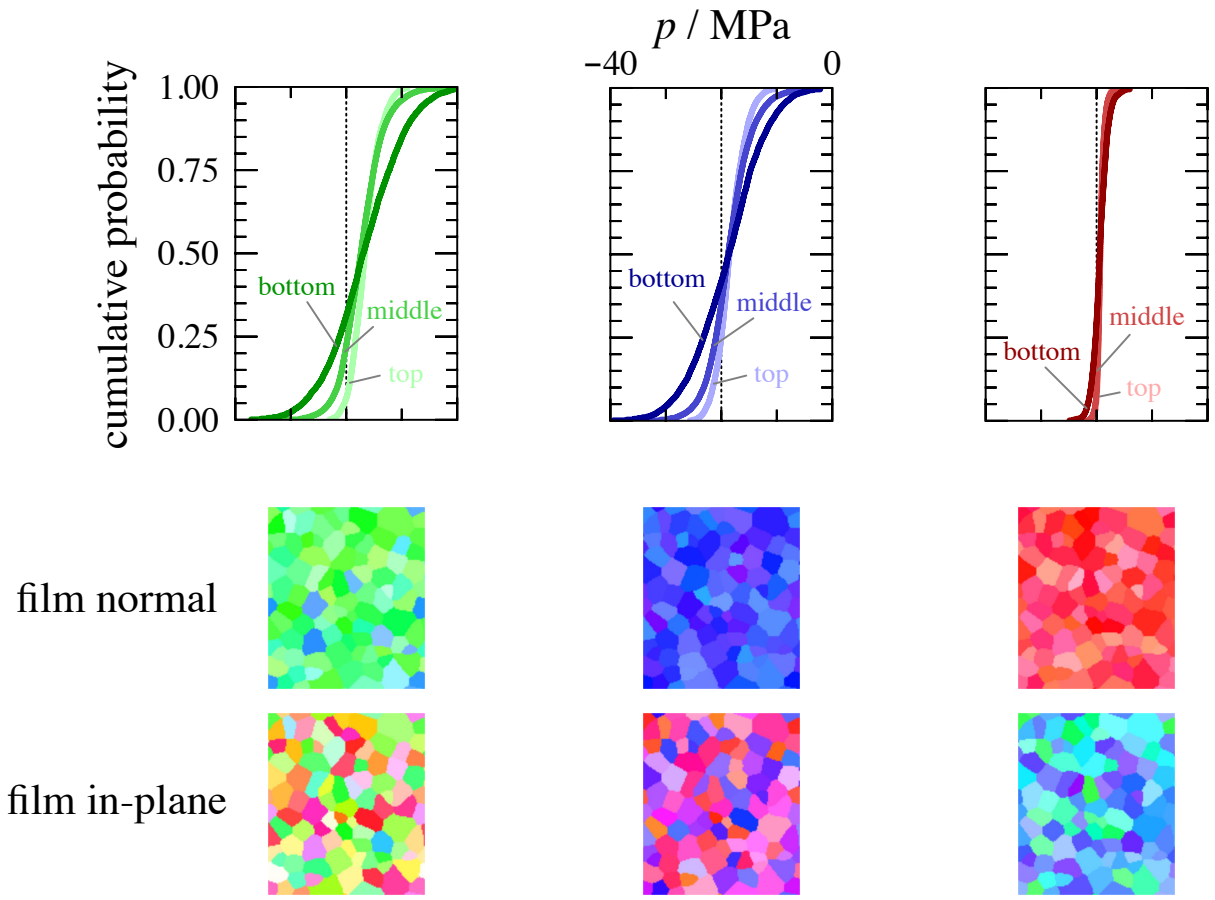

Figure 3.4: Distributions of grain boundary hydrostatic stress at three different depths within tin films of either green, blue, or red fiber texture (⟨1 0 0⟩, ⟨1 1 0⟩, and ⟨0 0 1⟩, from left to right). Light, medium, and dark line shades correspond to the layer depths shown in Fig. 3.3 left, center, and right, i.e., at the film surface, middle, and substrate interface. Inverse pole figure maps of film normal and one in-plane direction illustrate the three different textures assigned to otherwise identical grain structure. Chakraborty and Eisenlohr [2018]

tably wider at all depths in the films that have either green or blue fiber texture in comparison to the film with a red fiber texture. This stark contrast between green/blue compared to the red texture may be connected to the fact that only the red fiber texture has a transversely isotropic thermal expansion.

To analyze the relative influences of thermal and mechanical anisotropy, the actual thermal expansion anisotropy of β-Sn is changed from $40 \times 10^{-6}\,\mathrm{K}^{-1} = \alpha_{[0\,0\,1]} \neq \alpha_{[0\,1\,0]} = \alpha_{[1\,0\,0]} = 20 \times 10^{-6}\,\mathrm{K}^{-1}$ to an isotropic case with $\alpha_{[0\,0\,1]} = \alpha_{[0\,1\,0]} = \alpha_{[1\,0\,0]} = 20 \times 10^{-6}\,\mathrm{K}^{-1}$. The p distributions resulting for these two cases in films of fixed grain structure and with the three different

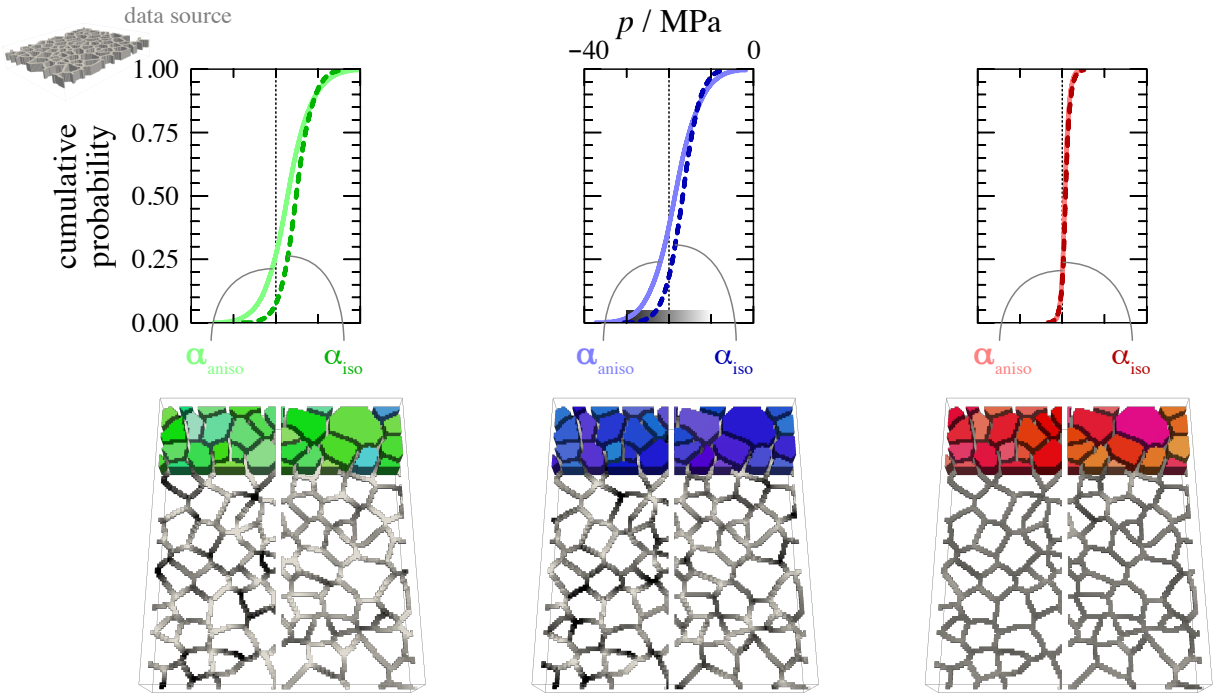

Figure 3.5: Comparison of grain boundary hydrostatic stress distributions between films with anisotropic and isotropic thermal expansion (solid and dashed) having either ⟨1 0 0], ⟨1 1 0], or ⟨0 0 1] fiber texture (green, blue, and red from left to right). Hydrostatic stress maps at the substrate interface reveal no qualitative change in the high degree of spatial variability (left and right halves, bottom row). Chakraborty and Eisenlohr [2018]

fiber textures ⟨1 0 0], ⟨1 1 0], and ⟨0 0 1] are shown in Fig. 3.5. There is almost no change in the stress distribution for the red fiber texture (Fig. 3.5 right), which remains very narrow. In contrast, the stress distributions for both the green and blue textures reduce appreciably in width and slightly shift to lower compressive stress values. The latter effect being caused by the reduced effective magnitude of thermal expansion when lowering $\alpha_{[0\,0\,1]}$ from 40 to $20 \times 10^{-6}\,\mathrm{K}^{-1}$. The observed high degree of spatial variability in p does not qualitatively change for any of the three textures even after changing to isotropic thermal expansion (Fig. 3.5 bottom). Consequently, the still appreciable difference in the spread of hydrostatic stress on the grain boundary network for the green/blue fiber texture compared to the red one has to be attributed to the mechanical (elastic and plastic) anisotropy of β-Sn.

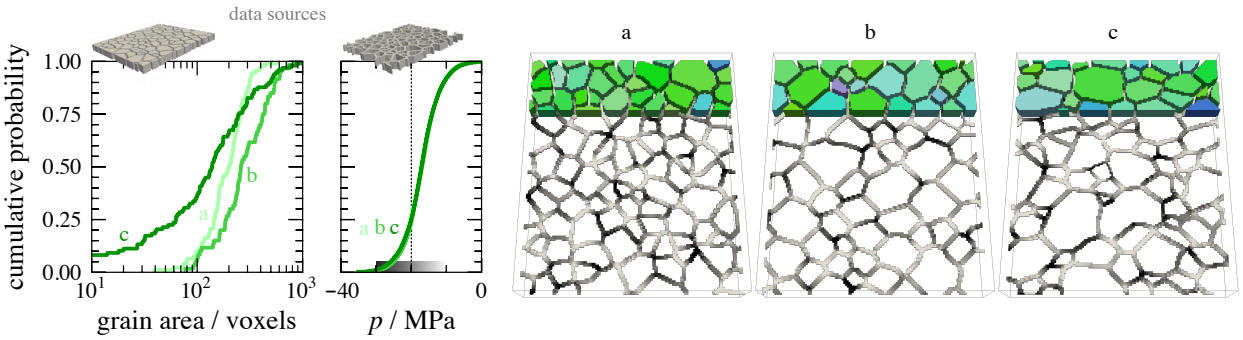

Figure 3.6: Variation of grain area distribution (left) for three different film structures (labelled “a”, “b”, and “c”) and their associated distributions of hydrostatic stress on the grain boundary network (middle) for films having ⟨1 0 0] fiber texture (see inverse pole figure coloring of partly shown grain structure). Spatial maps (right “a" to “c") show the film layer directly atop the (invisible) substrate and illustrate the rapid oscillation of p consistently observed for each of the three structures. Chakraborty and Eisenlohr [2018]

3.3.3 Effect of grain size distribution

A further potential influence on the p distribution is the film grain size distribution. To analyze its role, three different film grain structures are compared: the film grain structure mentioned before (here labelled “a”), a version of it after being subjected to artificial grain growth and resulting in a wider distribution (labelled “b”), and an experimentally measured film patch (labelled “c”) Jagtap et al. [2017], all having about a hundred grains. All three grain structures are again subjected to the thermal boundary conditions shown in Fig. 3.2 (black curve). Despite the significant variation in their grain size distribution (Fig. 3.6 left), the p distribution resulting for each film structure remains essentially identical (Fig. 3.6 right). While not shown in Fig. 3.6, the observed invariance in p despite significant changes in grain size distribution is similarly obtained for films with ⟨1 1 0] and ⟨0 0 1] (blue and red) fiber textures. Apparently, the influence of grain morphology on the grain boundary hydrostatic stress distribution is minute compared to that of the texture.

3.3.4 Effect of oblique surface grains

Focused ion beam prepared cross-sectional views of tin whiskers reveal that they grow from oblique grains, i. e., grains that feature inclined grain boundaries. Such a shape is geometrically necessary when whisker growths is being facilitated by accretion of atoms at these boundaries. However, it is not clear whether the presence of such a grain geometry in itself entails a locally relatively low compressive stress state favorable for initial atom addition to the root of a *potential* whisker grain. To gauge how strongly the sheer presence of oblique grains alters the p distribution in the film and, in particular, along the grain boundary network, one (or several) randomly selected grain(s) in the columnar film (subscript "col") are changed to an oblique geometry. The resulting change $p - p_{\mathrm{col}}$ in the overall as well as the spatial distribution of grain boundary hydrostatic stress is analyzed for the exemplary case of ⟨1 0 0] (green) film fiber texture.

Figure 3.7 (left) presents the distribution of changes in hydrostatic stress on the entire grain boundary network for three cases with an isolated transformation of one grain ("a" to "c") and one additional case with multiple oblique grains ("d"). The observed change for the majority of affected locations is limited to about 5 MPa (corresponding to a relative change of about 10 %). This change is strongly localized to the immediate vicinity of the affected grain(s), as exemplified by the spatial maps of the change in p_{col} in the film layer closest to the substrate (Fig. 3.7 bottom). The limited range of influence, which extends only to the boundaries of the directly neighboring grains, is even more apparent in the maps of relative stress changes (Fig. 3.7 top).

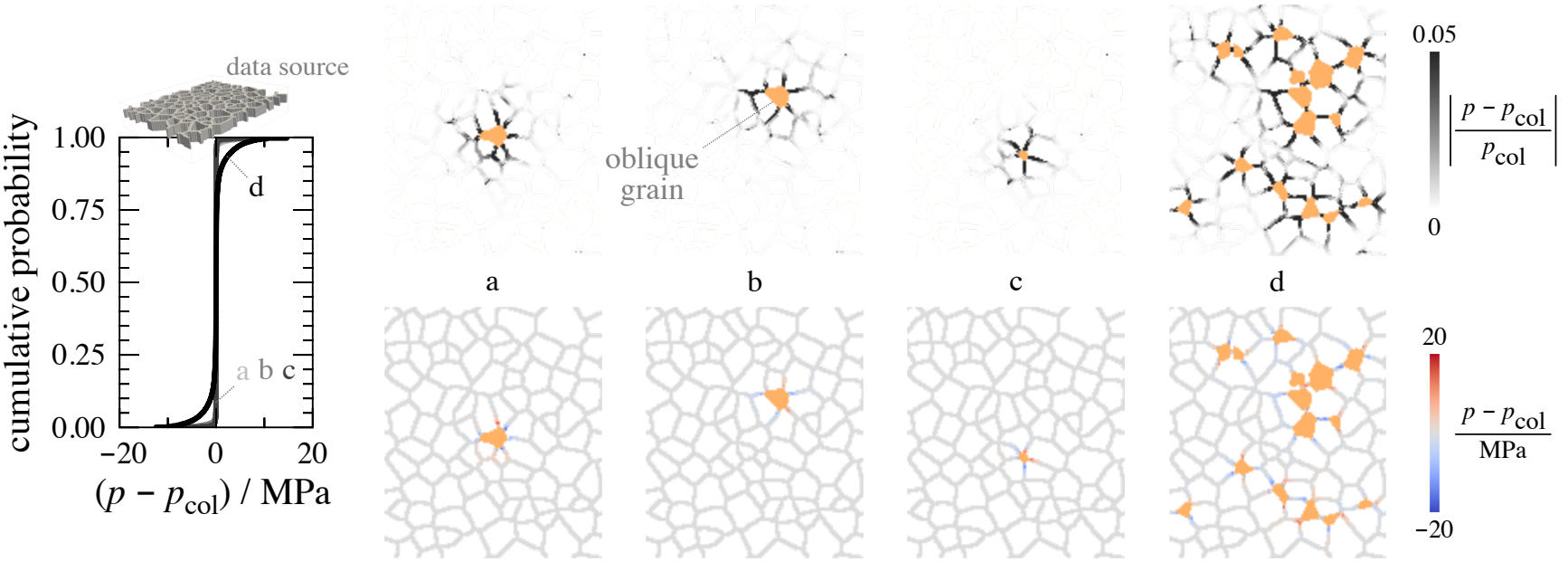

Figure 3.7: Distribution of change in hydrostatic stress p across the grain boundary network due to transformation of one ("a" to "c") or multiple ("d") columnar grains into oblique ones. These geometrical alterations affect only a small fraction of the grain boundary network, as demonstrated by the narrow overall distributions (left). Spatial maps confirm the localized influence of oblique grains on the relative (top) and absolute (bottom) change in p for the film layer closest to the substrate (termed "bottom" in Fig. 3.3) with the transformed (formerly columnar) grain shown in orange. Chakraborty and Eisenlohr [2018]

3.3.5 Effect of β-Sn crystal anisotropy

β-Sn crystal is highly anisotropic due to its body-centered tetragonal crystal structure. The anisotropy is exhibited both in mechanical (elastic and plastic) as well as thermal anisotropy, and hence would have a significant impact on the stress evolution in the film. The effect of crystal anisotropy is investigated by comparing simulated grain boundary p distributions obtained upon making the β-Sn crystal isotropic in its thermal behavior only (left column in Fig. 3.8), elastic behavior only (middle column in Fig. 3.8), and both elastic and thermal behavior (right column in Fig. 3.8), and comparing each of them with the reference case where the crystal is having both mechanical and thermal anisotropies (see Fig. 3.8). It appears from Fig. 3.8 (comparing left and middle columns) that both the thermal and elastic anisotropy of β-Sn is having equally strong influence on the p distribution along the grain boundary network. Moreover, by comparing the darker curves (labelled 'IV') in the right column in Fig. 3.8, where only the plastic anisotropy of β-Sn is influencing the p distribution, the dominant role of β-Sn plasticity can be inferred, and this effect appears to be different for different film textures.

This study highlights the inadequacies of simplistic isotropic models being previously used to describe the material behavior of β-Sn, as well as motivates us to identify strategies to establish accurate plastic parameters of β-Sn.

3.3.6 Establishment of local crystallographic effect

In this section the "localized effect" of texture in governing hydrostatic stress along the grain boundary network is studied by considering an exemplary textured film, $\langle 1\,0\,0]$, as shown in top row in Fig. 3.9. The aim of this investigation is to verify whether a subpart of entire geometry could be studied to get an idea about the different stresses (shear and normal) generated along the grain boundary statistically by changing grain morphology and orientation neighborhood but keeping the global texture same. Hence, it is more logical to perform such analysis for a reference grain in the film and then varying it's neighborhood after a certain grain sizes each time and analyze the changes in the resulting hydrostatic stress distribution along the grain

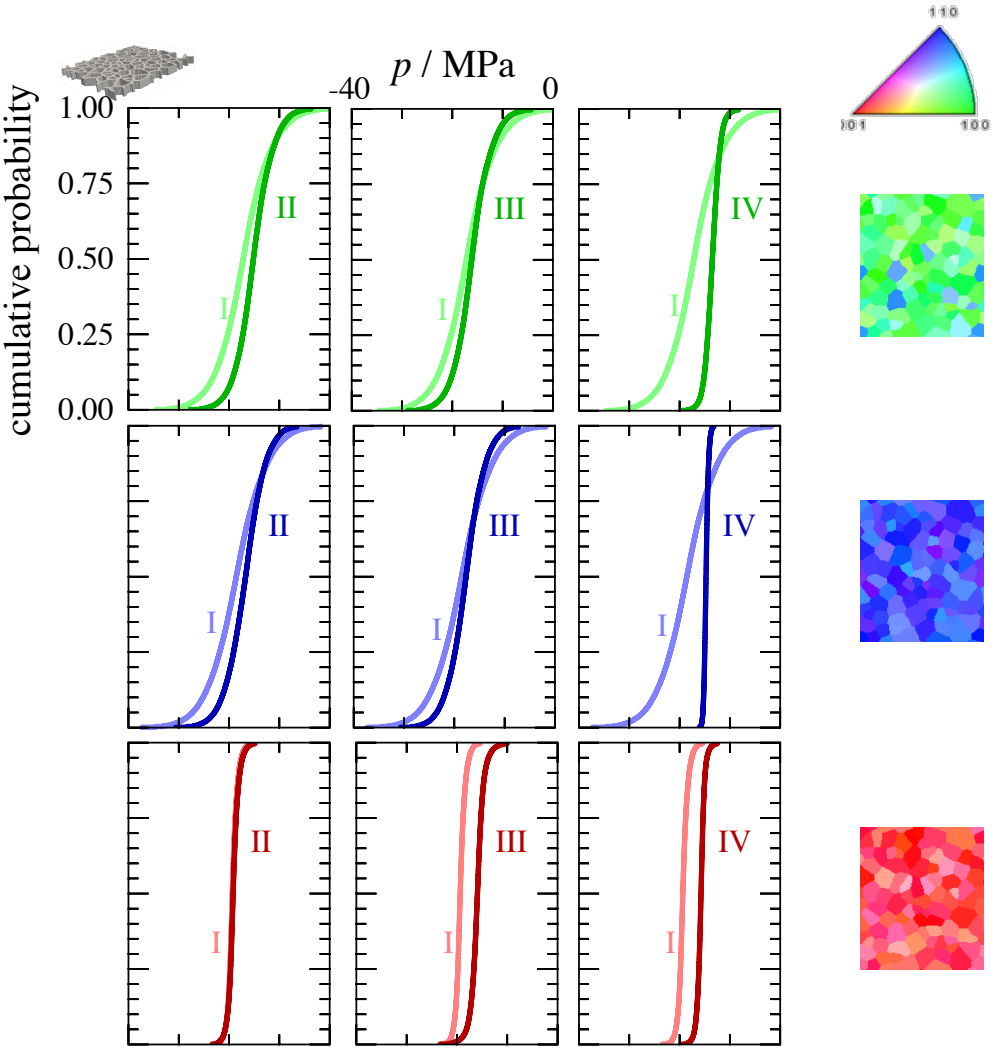

Figure 3.8: Distribution of hydrostatic stress p across the grain boundary network (and at maximum load) for three different global film textures, top row: $\langle 100 \rangle$; middle row: $\langle 110 \rangle$; and bottom row: $\langle 001 \rangle$. In each of the plots, lighter curves labelled 'I' corresponds to the p distribution for a simulation having both mechanical and thermal anisotropy which act as a reference distribution. This reference distribution is compared to the p distributions obtained upon making β-Sn thermally isotropic but mechanically anisotropic (darker curves, labelled 'II', in left column); thermally anisotropic but elastically isotropic (darker curves, labelled 'III', in middle column); and both thermally and elastically isotropic (darker curves, labelled 'IV', in right column), i.e., keeping only plastic anisotropy.

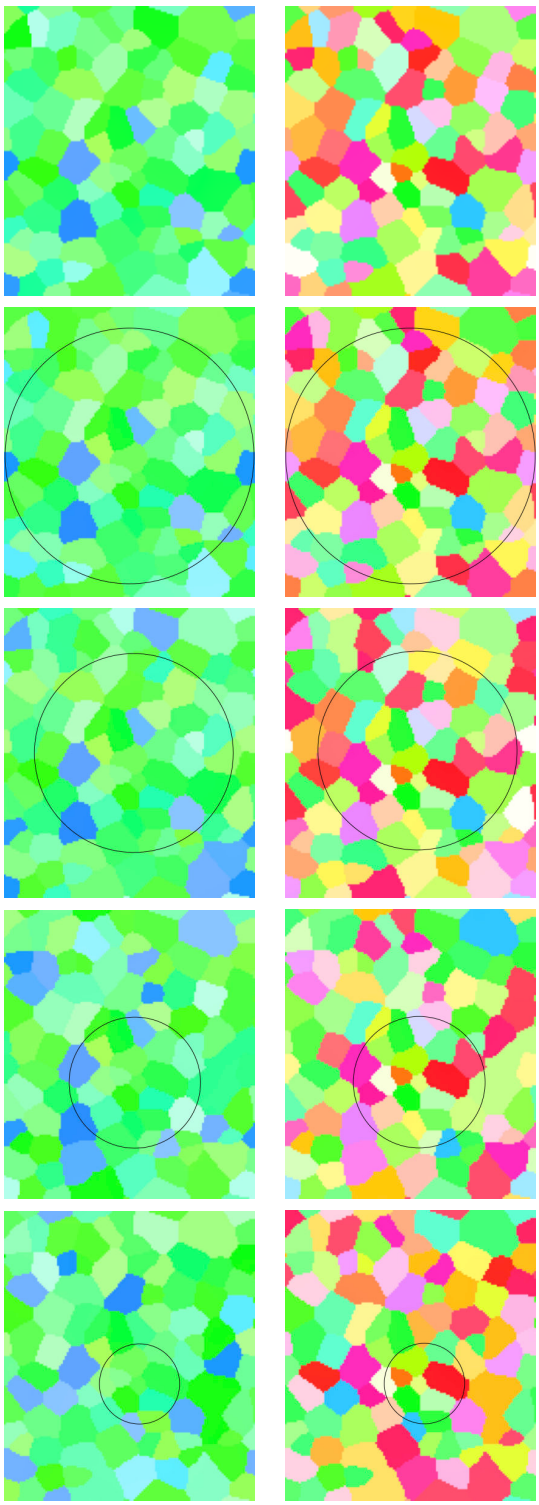

Figure 3.9: Top row shows the reference texture (right: out of plane ; left: in-plane) and grain morphology for the ⟨100⟩ film used earlier. In the subsequent images the texture and grain morphology of the part inside the black circle remains unchanged while outside the grains are shuffled along with a shuffling of the texture. Top to bottom shows a gradual decrease in the area of unchanged part (radius of the black circle) from about 5 grain sizes (second row) to ≈ one adjacent grain from the reference (central) grain.

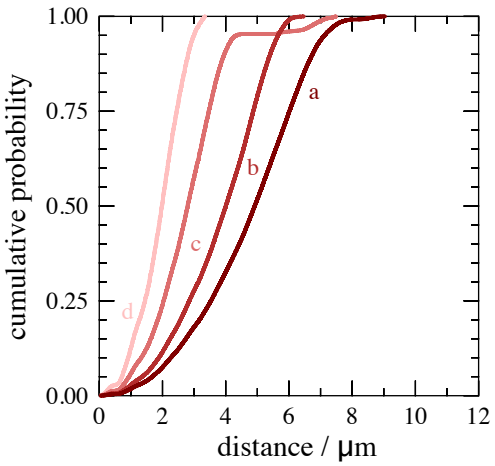

Figure 3.10: Distance distribution of the unchanged part, approximate distances between unchanged voxels and the central voxel of the black circles in Fig. 3.9 with “a", “b", “c", and “d" representing rows 2 to 5.

boundary network for such a change. Rows 2-5 in Fig. 3.9 illustrates this example, where the unchanged area with respect the central reference grain (central grain in the black circle) is gradually decreased, see Fig. 3.9 for the distance distribution of the unchanged part.

Subsequently, the difference between the hydrostatic stresses along the grain boundary network as compared at maximum load for the different cases (rows 2 to 5 in Fig. 3.9) to that of the reference (row 1 in Fig. 3.9) is shown in Fig. 3.11 for the film-substrate interface (left) and at the film surface (right).

As evident from Fig. 3.11 presence of difference in stresses from the reference case correlates well with the demarcation between the changed and the unchanged part (black vertical line in Fig. 3.11). Thus, if the grain of interest is the central grain in the black circles in Fig. 3.9 then its stress along the grain boundary network leading to it depends on the extremely local crystallographic neighborhood, and hence a subpart of the entire geometry (leading to one or two grain diameters) could be used to study the influence of crystallographic neighborhood on the stresses.

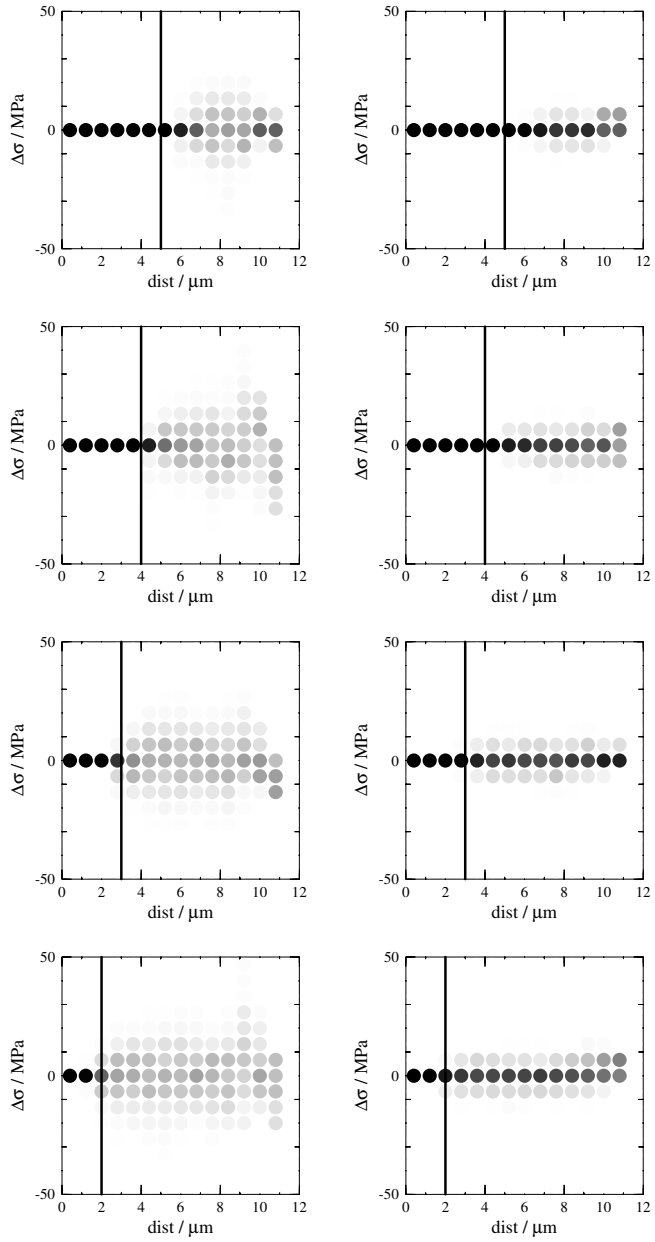

Figure 3.11: Differences in hydrostatic stresses along the grain boundary network for the different radii of unchanged texture and grain morphology (rows 2 to 5 in Fig. 3.9) with that of the reference case (row 1 in Fig. 3.9) at the film-substrate interface (left) and film surface (right). This is a 2-D histogram plot where the shade of gray represents the value meaning darker black circles correspond to zero change in the stress values (y-axis), and the location of the circles indicate the distance from the central grain's voxel. The black line, in each case, indicates the approximate distance between the changed and unchanged part in the film from the central grain (radius of the black circle in Fig. 3.9)

3.4 Discussion

Hydrostatic stress alters the chemical potential of atoms and, thus, a spatial variation in p will cause a driving force for atom migration from areas of high pressure to those of low pressure, resulting in an opposite flux of vacancies. Potential locations for whisker formation are then associated with areas of low hydrostatic stress and would attract atoms from areas experiencing more compressive stress. An overall wider range of p is intensifying this imbalance of chemical potential, which might be attributed to a higher propensity for whisker formation (everything else remaining unchanged). Under this premise, a tin film with ⟨001] (red) fiber texture should exhibit a lesser degree of whisker formation than films having either ⟨110] or ⟨100] (blue or green) texture, since the simulation results in this study reveal the former film texture to result in a much narrower p distribution compared to the latter two. Influence of film texture could then be one possible explanation for the contradicting observations reported in literature about the propensity of whisker formation for tin films on brass substrates. For instance, with nominally similar brass substrate compositions, Stein et al. [2015a] reported lower whisker propensity for a ⟨001] film, while Jagtap et al. [2018] found higher propensity but on a ⟨100] film. Hence, a more direct experimental verification of the hypothesis that the width of the hydrostatic stress distribution in tin films is of prime importance to understanding whisker formation would require thermally-strained tin films varying only in their texture.

The changes in the distribution of p resulting from the artificial case of isotropic thermal expansion shown in Fig. 3.5 indicate that the (unaltered) mechanical anisotropy plays at least as important a role as the thermal anisotropy in causing hydrostatic stress that develops in thermally stressed β-Sn films. Hence, for accurate predictions of β-Sn film behavior it is quintessential to include the β-Sn crystal anisotropy in the modeling framework.

According to the findings reported in Fig. 3.6 and Fig. 3.7, neither the grain size distribution nor the replacement of columnar by oblique grain geometry drastically alters the local and global p distribution. Thus, the oblique shape in itself can only be a *necessary* condition for a grain to grow a whisker He and Ivey [2015], Galyon [2011], Smetana [2007] but *cannot be a*

sufficient condition since this shape does not intrinsically generate favorable hydrostatic stress gradients for influx of Sn atoms that would be required for whisker growth.

Based on the study investigating the role of crystal anisotropy, Fig. 3.8, it appears that both mechanical and thermal anisotropies are equally influencing the p distribution along the grain boundary network, and hence needs to be accounted for to have accurate predictions.

The present work investigated the influence of crystallographic texture, grain size distribution, and presence of oblique grains on the development of hydrostatic stress p in thermally strained columnar tin films on a rigid substrate while excluding any vacancy diffusion. The main findings can be summarized as follows.

- Tin films with $\langle 0\,0\,1]$ texture show a comparably small spread in overall hydrostatic stress. In contrast, for the other two investigated textures ($\langle 1\,0\,0]$ and $\langle 1\,1\,0]$) large overall stress variability is observed. Hence, $\langle 1\,0\,0]$ films are expected to be more prone to whisker growth compared to $\langle 0\,0\,1]$ films.

- For all three fiber textures, no smooth long-range stress gradients are observed, as p spatially oscillates over distances comparable to the grain size, i.e., p is essentially uncorrelated after a distance of one to two grains.

- Neither grain size distribution nor the presence of oblique surface grains notably alters the p distribution.

- β-Sn crystal anisotropy has a significant role in the stress evolution in the film, and hence simplistic isotropic models would be inadequate in providing high fidelity solutions.

- A local substructure could be used to study the influence of crystallographic neighborhood on the resulting grain boundary stresses, and hence the subsequent atom redistribution.

The results are consistent with the following hypothesized chain of events leading to whisker formation: The whisker nucleation site will be a location that exhibits low compressive stress

relative to its immediate grain neighborhood. The occurrence of such neighborhoods is expected to be predominantly determined by the crystallographic orientation distribution of the film. Due to the locally high chemical potential of vacancies, atoms will migrate to this location along the grain boundary network. Provided that the grain in question is an oblique surface grain, the influx of atoms (i) increases the shear forces along its surface grain boundary traces and (ii) decreases the imbalance of chemical potential, which reduces further influx. If the pressure that builds up due to the inflowing atoms exceeds the resisting force of an oxide layer or other surface coating *before* the equilibration of chemical potential shuts down further atom flux, a circumferential crack in the surface cover develops. Surface cracking removes the former kinematic constraint on the inclined grain boundaries such that the chemical potential of vacancies at the boundaries of this grain becomes higher than any of the remaining grains in the film, excluding other "whiskering" grains in similarly relaxed conditions. The whisker can then grow from this grain by draining atoms from a now progressively enlarging area of influence. Such growth can continue as long as the hydrostatic stress in the collection volume exceeds the energy required to create fresh whisker surface (based on a balance of surface and lattice strain energy [Choi et al., 2003], a hydrostatic stress of about 1 MPa is sufficient to support a whisker of 2 μm diameter).

Table 3.1: Material properties for dilatational air, body-centered tetragonal β-Sn, and isotropic substrate.

	Value	**Unit**
Air		
C_{11}	10.0	GPa
C_{12}	0.0	GPa
$g_0 : g_\infty$	0.333 : 0.667	MPa
h_0	1.0	MPa
a	2	
M	3	
n	20	
$\dot{\gamma}_0$	10^{-3}	s^{-1}
β-Sn		
C_{11}	72.3	GPa
C_{12}	59.4	GPa
C_{13}	35.8	GPa
C_{33}	88.4	GPa
C_{44}	22.0	GPa
C_{66}	24.0	GPa
$g_0 : g_\infty \{1\,0\,0\}\langle 0\,0\,1]$	8.5 : 11.0	MPa
$g_0 : g_\infty \{1\,1\,0\}\langle 0\,0\,1]$	4.3 : 9.0	MPa
$g_0 : g_\infty \{1\,0\,0\}\langle 0\,1\,0]$	10.4 : 11.0	MPa
$g_0 : g_\infty \{1\,1\,0\}\langle 1\,\bar{1}\,1]$	4.5 : 9.0	MPa
$g_0 : g_\infty \{1\,1\,0\}\langle 1\,\bar{1}\,0]$	5.6 : 10.0	MPa
$g_0 : g_\infty \{1\,0\,0\}\langle 0\,1\,1]$	5.1 : 10.0	MPa
$g_0 : g_\infty \{0\,0\,1\}\langle 0\,1\,0]$	7.4 : 10.0	MPa
$g_0 : g_\infty \{0\,0\,1\}\langle 1\,1\,0]$	15.0 : 10.0	MPa
$g_0 : g_\infty \{0\,1\,1\}\langle 0\,\bar{1}\,1]$	6.6 : 9.0	MPa
$g_0 : g_\infty \{2\,1\,1\}\langle 0\,\bar{1}\,1]$	12.0 : 13.0	MPa
h_0	20	MPa
a	2.0	
n	6	
$\dot{\gamma}_0$	2.6×10^{-8}	s^{-1}
$\alpha_{\langle 1\,0\,0]}$	20×10^{-6}	K^{-1}
$\alpha_{\langle 0\,0\,1]}$	40×10^{-6}	K^{-1}
Substrate		
C_{11}	270.0	GPa
C_{12}	90.0	GPa
$\alpha_{\langle 100\rangle}$	1×10^{-6}	K^{-1}

CHAPTER 4

FULLY COUPLED CHEMO-THERMO-MECHANICAL MODELING OF THERMALLY STRAINED β – Sn FILMS

4.1 Introduction

In this chapter, fully coupled chemo-thermo-mechanical simulations of tin films are performed to analyze the stress-driven diffusion kinetics in these films preceding whisker nucleation and growth, as well as to understand the extent of their kinematic consequence. In this regard, the transport is most likely to occur solely along the grain boundary network since the grain boundary diffusivity of Sn is orders of magnitude higher than the Sn bulk diffusivity [Jagtap et al., 2017]. Like in the previous chapter showing thermo-mechanical simulations, Chapter 3, in this chapter as well, the coupled simulations mimic the experimental conditions of Pei et al. [2017] where a tin film deposited on a rigid silicon substrate is under biaxial compressive stress when the system is heated (with a specific heat rate), due to the differences in the thermal expansion coefficient of the film and the substrate. The choice of mimicking such a simulation is because of the large degree of control on the applied stress on the system, as compared to other sources of stress such as formation of Cu_6Sn_5 intermetallic compounds, indentation [Yang and Li, 2008], or bending [Crandall et al., 2011].

The simulations are performed using the open source simulation software DAMASK wherein the effect of crystal anisotropy (elastic, plastic, and thermal) could easily be incorporated to account for the film texture effects. With successful full-field three-dimensional fully coupled simulations, performed herein, several complex processes causing a particular grain to nucleate a whisker (and subsequently grow) can be de-convoluted and investigated sequentially to determine the most critical factors and hence allow us to propose reliable mitigation strategies to avoid whiskers. The numerical framework and the various aspects of DAMASK, such as formulation of residuals for field equations, calculation of spatial gradients using a

forward-backward scheme, and solution of the boundary value problem using the inherent spectral based FFT solver, have already been outlined in relative detail in Section 2.4 and can be obtained in further detail in [Roters et al., 2019, Eisenlohr et al., 2014]. However, for the current fully coupled simulations the residual formulation for the thermal and stress-driven transport field equations have been revisited from their original formulation [Shanthraj et al., 2019, Svendsen et al., 2017] to better account for the stark phase contrast in the diffusivity of the transported species between the grain boundaries and the grain bulk.

The chapter is structured as follows: in Section 4.2, first the constitutive equations for the coupled chemo-thermo-mechanical model is outlined in Section 4.2.1, followed by the numerical method to formulate the residual for the thermal and chemical field equations Section 4.2.2. Subsequently in Section 4.3 the details of simulation geometry and means to extract relevant information is provided which is followed by the results and discussion Section 4.4.

4.2 Model development

The continuum mechanical solution framework of DAMASK is formulated based on the finite-strain framework involving a multiplicative decomposition of the total deformation gradient

$$\mathbf{F} = \mathbf{F}_\mathrm{e}\,\mathbf{F}_\mathrm{in}\,\mathbf{F}_\mathrm{p} \tag{4.1}$$

into a lattice-preserving plastic deformation gradient $\mathbf{F}_\mathrm{p}$ that maps to the plastic configuration, a lattice-distorting inelastic deformation gradient $\mathbf{F}_\mathrm{in}$ mapping further to the eigenstrain configuration, and an elastic deformation gradient $\mathbf{F}_\mathrm{e}$ that maps the eigenstrain configuration to the final deformed configuration. As explained in Chapter 2, the intermediate eigenstrain (or stress-free strain) configurations account for both the thermal strain due to difference in the thermal expansion coefficients as well as the kinematics modulated by the transport of atoms. The time evolution of the plastic and intermediate deformation gradients $\mathbf{F}_\mathrm{p}$ and $\mathbf{F}_\mathrm{in}$ is given in

terms of their respective velocity gradients $\mathbf{L}_\mathrm{p}$ and $\mathbf{L}_\mathrm{in}$ following the flow rules

$$\dot{\mathbf{F}}_\mathrm{p} = \mathbf{L}_\mathrm{p}(\mathbf{M}_\mathrm{p}, \ldots)\,\mathbf{F}_\mathrm{p} \tag{4.2}$$

$$\dot{\mathbf{F}}_\mathrm{in} = \mathbf{L}_\mathrm{in}(\mathbf{M}_\mathrm{in}, \ldots)\,\mathbf{F}_\mathrm{in}. \tag{4.3}$$

Both velocity gradients are driven by the respective work-conjugate Mandel stresses

$$\mathbf{M}_\mathrm{p} = (\mathbf{F}_\mathrm{e}\,\mathbf{F}_\mathrm{in})^\mathrm{T}\mathbf{F}_\mathrm{e}\,\mathbf{F}_\mathrm{in}\,\mathbf{S} \approx \mathbf{F}_\mathrm{in}{}^\mathrm{T}\mathbf{F}_\mathrm{in}\,\mathbf{S} \tag{4.4}$$

$$\mathbf{M}_\mathrm{in} = (\det\mathbf{F}_\mathrm{in}{}^{-1})\mathbf{F}_\mathrm{in}\,\mathbf{S}\,\mathbf{F}_\mathrm{in}{}^\mathrm{T}, \tag{4.5}$$

where $\mathbf{S} = \mathbb{C} : (\mathbf{F}_\mathrm{e}{}^\mathrm{T}\mathbf{F}_\mathrm{e} - \mathbf{I})/2$ is the second Piola–Kirchhoff stress with fourth-order stiffness tensor $\mathbb{C}$ and second-order identity tensor $\mathbf{I}$, and further depend on the material state and associated constitutive parameters. The intermediate plastic velocity gradient $\mathbf{L}_\mathrm{in}$ is additively decomposed into its constituents, which in this study are the thermal velocity gradient $\mathbf{L}_\mathrm{th}$ and chemical velocity gradient $\mathbf{L}_\mathrm{ch}$

$$\mathbf{L}_\mathrm{in} = \mathbf{L}_\mathrm{th} + \mathbf{L}_\mathrm{ch} \tag{4.6}$$

and have their individual constitutive equations mentioned in the next section.

The interdependency of the velocity gradients makes the system fully coupled and is solved based on the staggered solution strategy outlined in Section 2.4 and explained in detail in [Shanthraj et al., 2019]. The boundary value problem is solved using the “basic" scheme of the spectral based FFT formulation also outlined in Section 2.4.

4.2.1 Constitutive equations

Similar to the previous Chapter 3, the employed crystal plasticity framework incorporates the anisotropy in elasticity, plasticity, and thermal expansion as well as different bulk and grain boundary diffusivity. The governing equations dictating the kinematics are given by their corresponding velocity gradients. The plastic velocity gradient is additively composed from slip rates

$$\mathbf{L}_\mathrm{p} = \sum_\alpha \dot{\gamma}^\alpha\,\mathbf{s}^\alpha \otimes \mathbf{n}^\alpha, \tag{4.7}$$

with the unit vectors $\mathbf{s}^\alpha$ and $\mathbf{n}^\alpha$ indicating the slip direction and slip plane normal for each slip system (indexed by α) of the different slip families in β-Sn. The resolved shear stress

$$\tau^\alpha = \mathbf{M}_\mathrm{p} \cdot \left(\mathbf{s}^\alpha \otimes \mathbf{n}^\alpha\right) \tag{4.8}$$

drives the slip at rates

$$\dot{\gamma}^\alpha = \dot{\gamma}_0 \left|\frac{\tau^\alpha}{g^\alpha}\right|^n \mathrm{sgn}\left(\tau^\alpha\right), \tag{4.9}$$

with material parameters $\dot{\gamma}_0$ and n. The phenomenological plasticity law of [Peirce et al., 1982] is used in this study to describe the mechanical behavior of the film, where dislocation slip on each slip system is a function of a critical resistance g^α, which evolves during slip as

$$\dot{g}^\alpha = \sum_\beta h_0 \left|1 - \frac{g^\beta}{g_\infty}\right|^a \mathrm{sgn}\left(1 - \frac{g^\beta}{g_\infty}\right) \left|\dot{\gamma}^\beta\right|, \tag{4.10}$$

with initial hardening slope h_0, hardening exponent a, and saturation slip resistance g_∞ [Hutchinson, 1976].

The thermal velocity gradient (accounting for the thermal strain in the system)

$$\mathbf{L}_\mathrm{th} = \frac{\dot{T}\alpha_{ii}}{1 + \alpha_{ii}(T - T_0)} \qquad i = 1,2,3, \tag{4.11}$$

is constitutively related to the thermal expansion and the change in temperature T for both the body-centered tetragonal (bct) β-Sn and the rigid isotropic substrate, α being the coefficient matrix of thermal expansion, and T_0 indicates the initial temperature. The constitutive equation responsible for the temperature change is given by:

$$\rho Cp \frac{\partial T}{\partial t} = -\nabla \cdot \mathbf{f_T} + \dot{q}, \tag{4.12}$$

where $\dot{q}$ represents the rate at which the film–substrate system is heated. $\mathbf{f_T}$ is the heat flux and ρ and Cp representing the density and specific heat of the system.

Transport of any species is determined by the differences in their fluxes, which depends on their chemical potential. In general, the chemical potential has a concentration term and an energy term, chapter 2 in Porter and Easterling [1992]. However, in the current formulation

where the diffusive flow is considered only along the grain boundaries, the concentration term in the flux equation is neglected making the the chemical potential a sole function of the grain boundary normal stress.

Thus the flux equation for such a system that is relatively dilute (such that the thermodynamic factor relating the diffusivity and the mobility can be neglected) is then given as:

$$J = -\frac{DC}{kT}\nabla\mu \tag{4.13}$$

with D being the diffusivity of the species (in current study its value corresponds to tin grain boundary diffusivity), C represents the concentration of the diffusing species, ∇ is the spatial gradient operator, and k and T represents the Boltzmann constant and temperature. The chemical potential μ is a function of atomic volume Ω and grain boundary normal stress [Buchovecky et al., 2009b], and is given as

$$\mu = -\Omega\sigma_{\mathrm{n}}, \tag{4.14}$$

$$\sigma_{\mathrm{n}} = \sigma \cdot (\mathbf{n}\otimes\mathbf{n}) \tag{4.15}$$

where n represents the grain boundary normal. With single diffusing species the right hand side C in Eq. (4.13) is inverse of the atomic volume, $C = 1/\Omega$ [Tu et al., 2007]. The atom flux due to the in-plane gradient in chemical potential, relevant for the present study concerning grain-boundary diffusion, is then given by

$$J = -\frac{DC}{kT}(\mathbf{I}-\mathbf{n}\otimes\mathbf{n})\nabla\mu \tag{4.16}$$

$$= -\frac{D}{kT}(\mathbf{I}-\mathbf{n}\otimes\mathbf{n})\nabla\sigma : (\mathbf{n}\otimes\mathbf{n}) \tag{4.17}$$

where the diffusion along the grain boundary normal direction is eliminated by the modified diffusivity expression, $D(\mathbf{I}-\mathbf{n}\otimes\mathbf{n})$. However, in the present study the grain boundary, normal is not yet incorporated in the model leading to the approximation of the above flux Eq. (4.17) by

$$J = -\frac{D}{kT}(\mathbf{I}-\mathbf{n}\otimes\mathbf{n})\nabla\sigma : (\mathbf{n}\otimes\mathbf{n}) \tag{4.18}$$

$$\approx -\frac{D}{kT}\nabla\sigma_{\mathrm{h}} \tag{4.19}$$

with

$$\sigma_{\mathrm{h}} = \frac{1}{3}\,\mathrm{Tr}\,\mathbf{M}_{\mathrm{in}} \tag{4.20}$$

Since the flux is limited to the thickness δ_{GB} of the grain boundary, the flux per linear cross-section grain boundary (i.e., for a width of δ_{GB} and per length along the other area direction) follows as

$$J_{\mathrm{GB}} = -\frac{D_{\mathrm{GB}}\delta_{\mathrm{GB}}}{kT}\nabla\sigma_{\mathrm{h}} \tag{4.21}$$

The spatial gradient in the grain boundary flux J_{GB} entails a rate of change

$$\dot{N} = \nabla \cdot J_{\mathrm{GB}} \tag{4.22}$$

of atoms on the grain boundary area, which translates into a rate of monolayer accumulation (or loss) given by:

$$\dot{m} = \Omega^{1/3}\nabla \cdot \left(\Omega^{1/3}\, J_{\mathrm{GB}}\right), \tag{4.23}$$

where $\left(\Omega^{1/3} J_{\mathrm{GB}}\right)$ corresponds to the flux for an atomic length, and its divergence for an atomic distance $\Omega^{1/3}$ gives the monolayer atom addition. The above transport of atoms due to the accumulation Eq. (4.23) is schematically shown for a grain boundary voxel in the simulation geometry in Fig. 4.1, where the flux vector J_{GB} represents the grain boundary flux for a grain boundary of width δ_{GB}per unit length along the other area direction (corresponding to z-direction in Fig. 4.1).

Finally, the kinematic consequence (chemical strain) per monolayer is expressed as

$$\mathbf{L}_{\mathrm{ch}} = \epsilon\,\dot{m}\,\frac{\Omega^{1/3}}{d}\,\underbrace{(\mathbf{n}\otimes\mathbf{n})}_{\approx\mathbf{I}} \tag{4.24}$$

where ϵ is the strain coefficient which is negative (reducing strain upon addition) for vacancy transport and positive (increasing strain upon addition) for atom transport.

This fully coupled system of partial differential equations is solved numerically using a staggered solution scheme, while the individual constitutive equations are solved by formulating a residual, and minimizing it using the open source library PETSc to get the requisite solution.

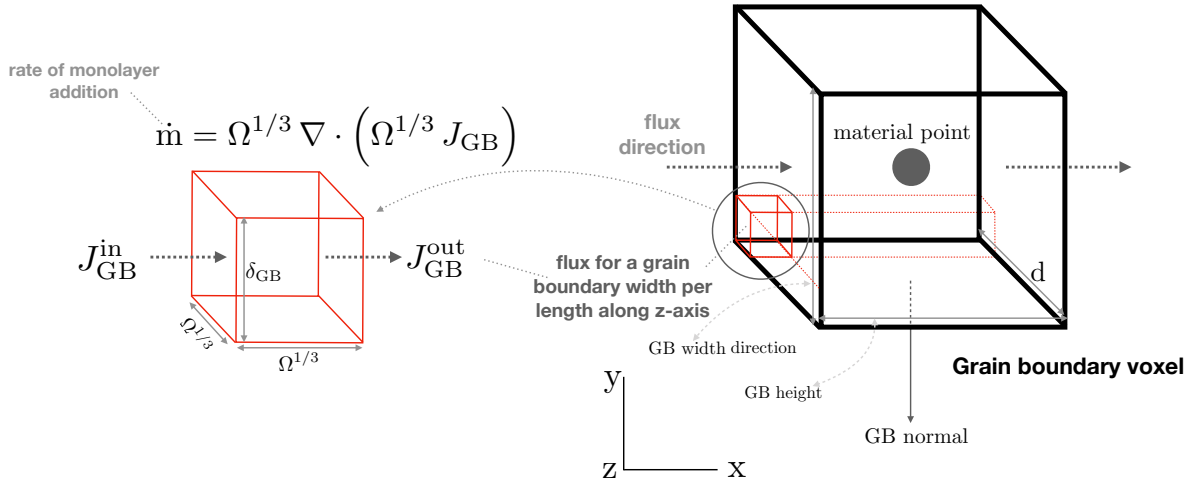

Figure 4.1: A representative voxel with a material point showing the flux direction (along x-axis) and grain boundary normal direction, n, along y-axis. The grain boundary flux per unit line cross section along z-direction, for an atomic distance is given by ($\Omega^{1/3}$ J_{GB}). Subsequently, the rate of monolayer addition is represented by $\dot{m}$ which corresponds to the divergence of this flux through another atomic distance of $\Omega^{1/3}$.

4.2.2 Residual formulation

The solution of the transport equation for stress-driven mass transfer as shown by equations Eqs. (4.21) and (4.22) that gives the number of atoms accumulated per unit height of the film per unit time is solved by formulating as a residual minimization problem. The advantage of formulating such a residual is the ability to use one of the several in-built numerical methods in the open source package PETSc to solve this residual in the most efficient way. The critical aspect of solving the flux equation as a field (and not a constant out of the divergence term in Eq. (4.23)) is due to the presence of the strong contrast in the diffusivity of the Sn atoms in the bulk compared to the grain boundaries. It is noted that the grain boundaries in the current simulation are represented by ≈ 2 voxels from each of the grains next to the boundary (similar

to the geometry used in Chapter 3). Thus, for the interface between two grains, the boundary comprises of a total of ≈ 4 voxels, 2 from each grain with the orientation of their parent grain.

To properly account for this contrast in bulk and grain boundary diffusivities for each material point the flux is calculated using the minimum diffusivity between itself and its neighbor. This is justified in the sense that if an atom is trying to diffuse from the bulk to the boundary it would not be able to diffuse due to the very low bulk diffusivity, while if an atom is trying to diffuse from the boundary to the bulk it will also be restricted since it cannot displace an atom in the bulk (again due to low bulk diffusivity). The situation is similar to a series of chemical reactions where the rate controlling step is the slowest reaction.

4.3 Simulation details

4.3.1 Simulation geometry and boundary conditions

A reduced microstructure with ≈ 30 grains from the original microstructure consisting of ≈ 100 grains (which was used for the thermo-mechanical analysis in Chapter 3) is used as a test case to analyze the kinematic consequence of the fully coupled chemo-thermo-mechanical processes. Moreover, one of the 30 grains in the microstructure is made “oblique" (inclined grain boundaries) and is considered as the reference grain for performing any grain comparison study. The reduced geometry is representative of the crystallographic effects for this reference grain, since the neighborhood effects are highly localized (as established in Section 3.3.6).

The reduced layered geometry consists of a 3.0 µm thin film with 30 grains of body-centered tetragonal (bct) β-Sn (generated using Poisson-Voronoi tessellation with 30 seed points) between a 1.2 µm thick elastic rigid isotropic substrate at the bottom and a 0.6 µm soft dilatational material on top as shown in Fig. 4.2. This layer of soft dilatational material on top of the film ensures a free surface condition, thus mimicking “air", and uses the constitutive description proposed by Maiti and Eisenlohr [2018]. The substrate thickness is much lower than that observed in reality to reduce the computation cost, however, its stiffness is significantly increased (around 32 times higher Young’s modulus compared to real β-Sn) to make it rigid. This value for

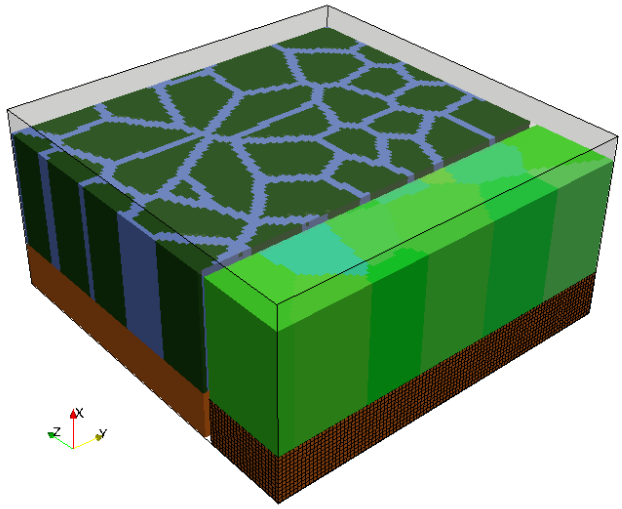

Figure 4.2: Discretized geometry of a tin film between a rigid isotropic substrate (orange, showing voxel size) and soft dilatational "air" (faint gray). Boundaries (light blue) between the columnar grains (green) have different chemical (diffusion) properties but share thermal and mechanical properties with the bulk. Part of the geometry also reveals the global ⟨1 0 0] film texture.

the substrate stiffness is high enough to ensure its rigidity in that further increasing the value did not affect the simulation results. The entire geometry is discretized by a regular grid of $48 \times 96 \times 96 = 442\,368$ voxels, each of volume $0.1 \times 0.1 \times 0.1\,\mu m^3$, also shown in Fig. 4.2. The grain orientations are selected to represent a fiber texture with the fiber axis (the film normal direction) being aligned with a particular crystal direction, which in this case is chosen as ⟨1 0 0], as shown partly in Fig. 4.2. Biaxial compressive stresses generated in the film upon heating due to the different thermal expansion of β-Sn and the substrate (the film having an order of magnitude higher expansion coefficient than the substrate). The resulting stresses relax by plasticity and chemical transport (stress-driven diffusion). Diffusional flow occurs only through the grain boundaries (highlighted in shade of blue in Fig. 4.2) due to much higher (ten orders of magnitude) grain boundary diffusivity compared to grain bulk diffusivity [Jagtap et al., 2017]. The present study solves this coupled chemical-thermo-mechanical problem in a crystal plasticity framework, thereby incorporating the effect of crystal orientation on the micro-mechanical response.

In this work, the initially stress-free layered geometry (substrate, film, and air) is heated to two different conditions– i) 20 K; and ii) 40 K in 10 and 20 min respectively, with a subsequent relaxation of about 60 min. Since diffusion of tin atoms is considered in this study, the flow is allowed only in the tin film (specifically along the grain boundaries). The chemical flux at the film surface is restricted by specifying a zero diffusivity value for the dilatational air layer, thus mimicking the presence of a passivating oxide layer that prevents vacancies to diffuse into the film from the surface. These boundary conditions give rise to a coupled chemical-thermo-mechanical system of partial differential equations, described in Section 4.2.1 which are then solved using the "basic" scheme of the spectral solver [Shanthraj et al., 2015, Eisenlohr et al., 2013] that is part of the open-source Düsseldorf Advanced Material Simulation Kit (DAMASK) [Roters et al., 2019].

The β-Sn constitutive parameters are obtained from [Lee et al., 2015] listed in Table 4.1 along with the constitutive parameters used for the substrate and air. The thermo-mechanical model using these constitutive parameters have already been validated using experimental data in the previous chapter Section 3.3.

4.4 Results and Discussion

To determine the macroscopic consequence of the stress-driven diffusion kinematics, Fig. 4.3 compares the average von Mises stress evolution of the film for a fully coupled simulation (blue curves) to that of a solely thermo-mechanical simulation (red curves) for the two loading conditions of a 20 K change of temperature in 10 min (black curve in left figure) and that of a 40 K change of temperature in 20 min (black curve in right figure) followed by a relaxation of about 60 min for both. Based on the results, there appears to be negligible influence of the diffusional kinematics on the average stress evolution of the film. However, it is critical to point out that considering such a kinematic consequence lowers (by a small amount) the average stress in the film as the blue curves are closer to zero stress compared to the red curves in Fig. 4.3, which is expected from such a process. Also, the above observation is more prominent

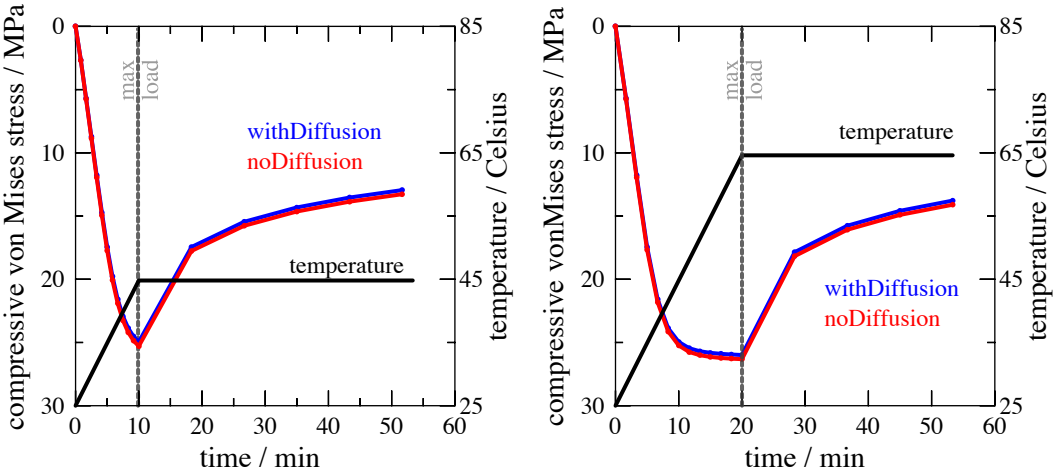

Figure 4.3: Average von Mises stress evolution in the film for the coupled chemo-thermo-mechanical model (blue) to that of the case of without any diffusional flow (red), for a temperature change of 20 K (left) and 40 K (right) in 10 and 20 min respectively (shown by the black curve), followed by a relaxation of about 60 min. The dashed dark gray line represents the point of maximum load/strain in the system, which is used as a reference location for further comparison in the study.

in the later stages of loading and the succeeding relaxation stages.

In the next section, the kinematic effect of the stress-driven diffusion is analyzed for the grain boundary network that serves as the sole conduit for the transport of Sn atoms.

4.4.1 Kinematic consequence

In this section, the aim is to analyze the effect of the kinematic consequence of the atom redistribution in the film (along the grain boundary network) by comparing the results obtained “with diffusional" flow to that of the case where the “no diffusional" flow is considered (purely thermo-mechanical simulations).

The kinematic effect of the diffusional flow is integrated in the model through the eigenstrain velocity gradient $\mathbf{L}_i$, as mentioned in Section 4.2.1, along with the thermal strain (refer to Section 2.4 for further details). Figure 4.4 shows this effect by comparing the determinant of the eigenstrain deformation gradients (representing the relative volumetric change) along the grain boundary network for the two temperature boundary conditions (left: 20 K, and right:

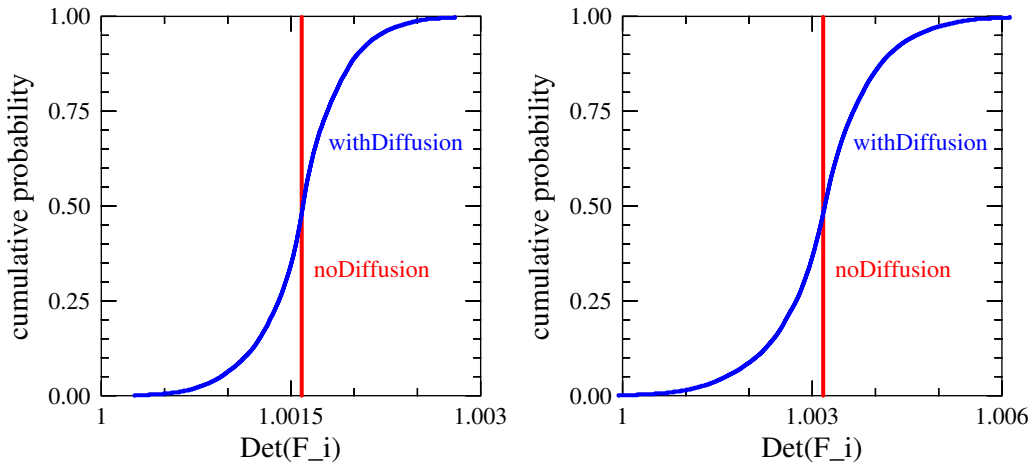

Figure 4.4: Kinematic consequence of atom redistribution is shown by comparing distribution of determinant of the eigenstrain deformation gradients $\mathbf{F}_i$ along the grain boundary network, at maximum load for the coupled chemo-thermo-mechanical model (blue) to the case of without any diffusional flow (red), for a temperature change of 20 K (left) and 40 K (right).

40 K). The redistribution of mass increases the volume at locations where atoms get added and decreases in areas of atom depletion, as can be seen by the solid blue curve. The red curve corresponds to the applied thermal strain which is uniform across the film.

The pressure along the grain boundary network modulates the atom redistribution and is shown at the maximum strain condition for the film–substrate interface (where the stresses are maximum) under the two loading conditions in the left and right columns in Fig. 4.5 respectively. The veracity of the flux equations and the overall model is confirmed by the fact that the transport of atoms occurs from regions of high compression ("blue") to regions of lower compression ("red") as seen by comparing pressure and concentration plots in Fig. 4.5. Moreover, the high degree of spatial variation in pressure distribution along the grain boundary network is reflective of the global film texture of ⟨1 0 0], similar to the pressure variations shown in Section 3.3, which also supports the fact that the reduced geometry (with 30 grains) is representative of the overall geometry (with 100 grains) when the texture is the same.

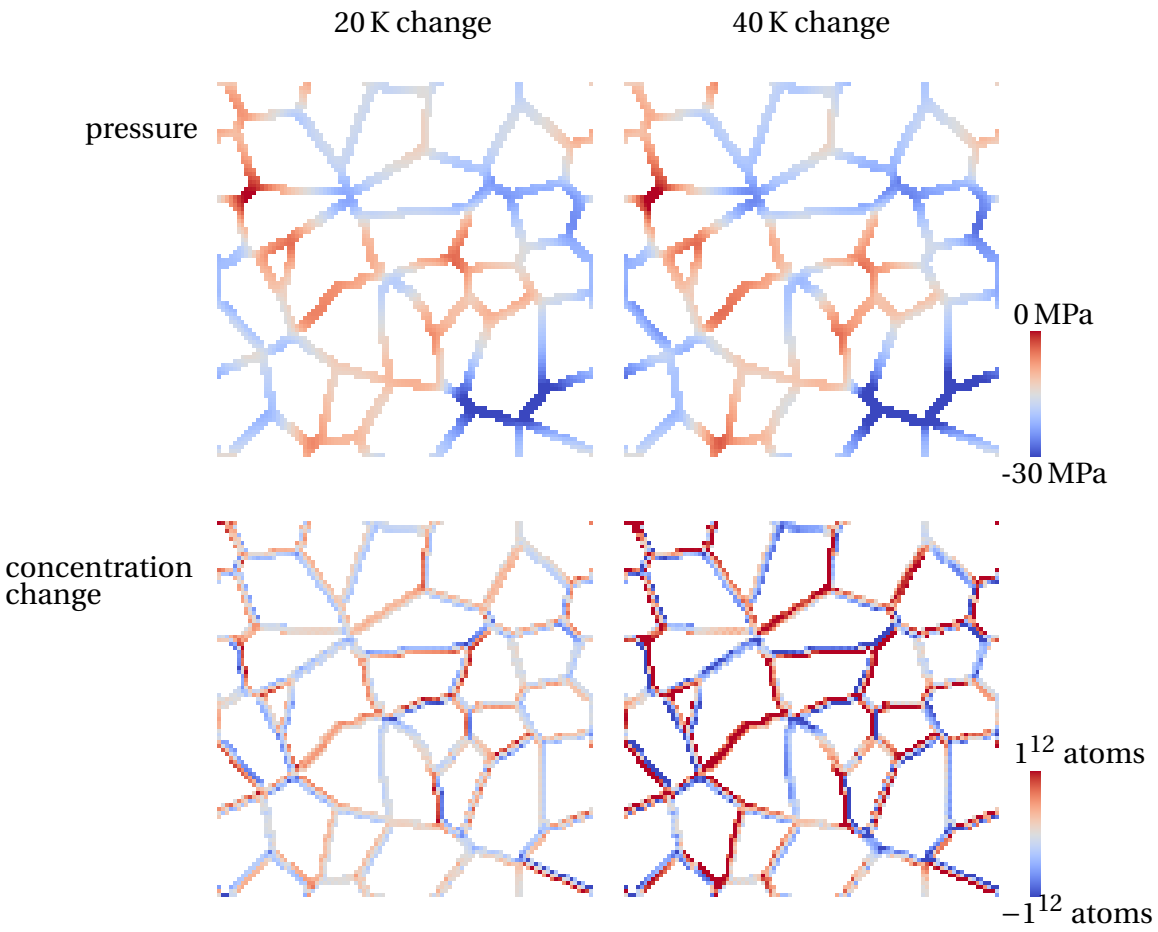

Figure 4.5: Spatial variation of the pressure (top row) and the concentration change in number of atoms (bottom row), per grain boundary area, for the two loading conditions of 20 K (left column) and 40 K (right column) at the maximum load and at the film–substrate interface. As expected, locations of low compression (“red" regions) in the pressure plots (top row) correspond to locations of atom gains (“red" regions) in the concentration plots (bottom row).

4.4.2 Comparison of different stresses

Whiskers are very likely to grow by addition of atoms at the base of the whisker grain (oblique surface grains) and then by breaking the tin oxide layer on top (that forms instantaneously). Similar to the work of Chakraborty and Eisenlohr [2019], the different tractions (shear and normal) acting along the grain boundaries are analyzed to get an idea about the approximate ranges, with a notion that they might have a mechanistic affect. An exemplary visualization with an oblique grain boundary is shown in Fig. 4.6, where most of the normals are identified properly with the exception of a few scattered normals. This small scatter is unlikely to affect

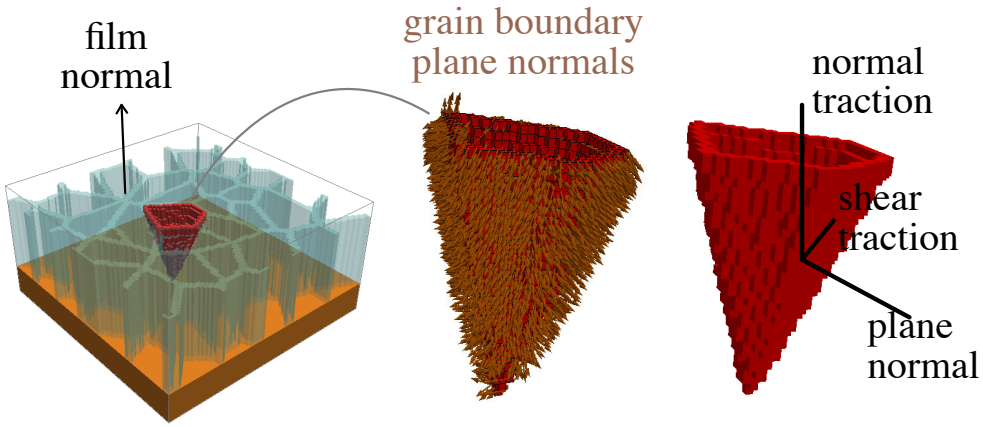

Figure 4.6: Normal (along film normal direction) and shear (in the boundary plane) traction components (right) derived at each point of the grain boundary based on the local boundary plane normal (middle) of an exemplary (oblique) grain isolated from the entire film (left, only grain boundary network shown).

the overall distribution of the values.

To gauge the effect of the kinematics of atom redistribution on these traction values, distribution plots of the pressure variation, normal tractions (i.e., traction on the grain boundary plane acting along film normal direction) and a shear traction (i.e., traction acting in the plane of the boundary) are shown for the two loading conditions (of 20 K, top row, and 40 K, bottom row) at the film–substrate interface (solid line) and at the film–surface (dashed line) in Fig. 4.7. For all the conditions, the magnitude of the value at the film–surface is much smaller than that at the film–substrate interface due to the free surface condition. Also, for both loading conditions investigated here, the kinematic consequence of the diffusional flow reduced the pressure distribution (blue curves being narrower than red curves in left column in Fig. 4.7), while negligible effect of such kinematics could be seen for the traction values. This might indicate that just by addition of atoms along the grain boundary network does not kinematically alter the stresses sufficiently to break the oxide layer on top. However, such a case might also be specific to the presently considered microstructure, a more reliable estimation can be made by performing a statistical estimation of the variation of these stresses under different initial microstructures.

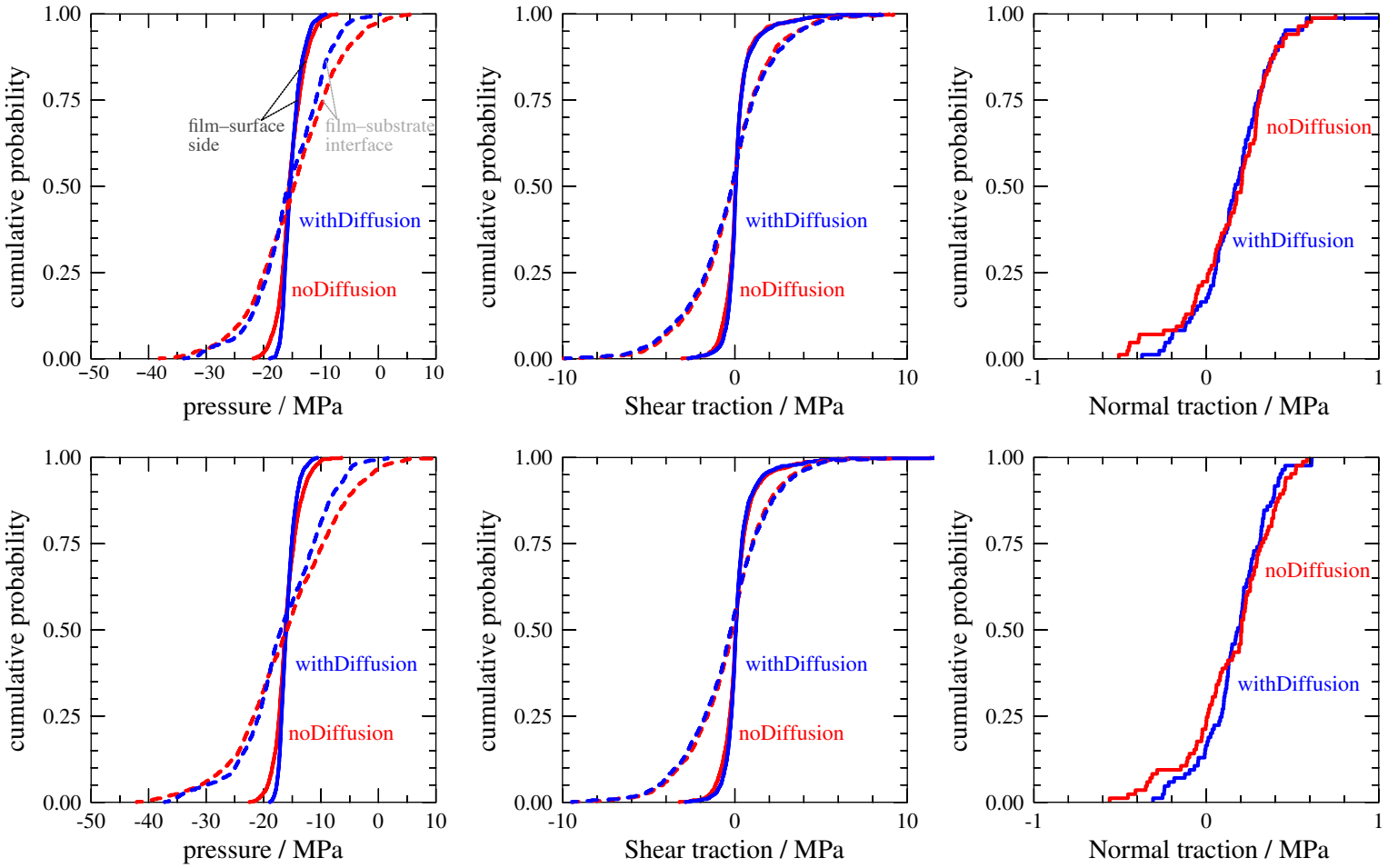

Figure 4.7: Probability distribution plots for pressure (left), a shear component of the traction (middle), and the traction component acting along the film normal direction (right, for only the oblique grain boundary) along the grain boundary network, all computed at maximum strain condition. The solid and dashed lines correspond to the distribution of these values at the film–surface and film–substrate interface respectively.

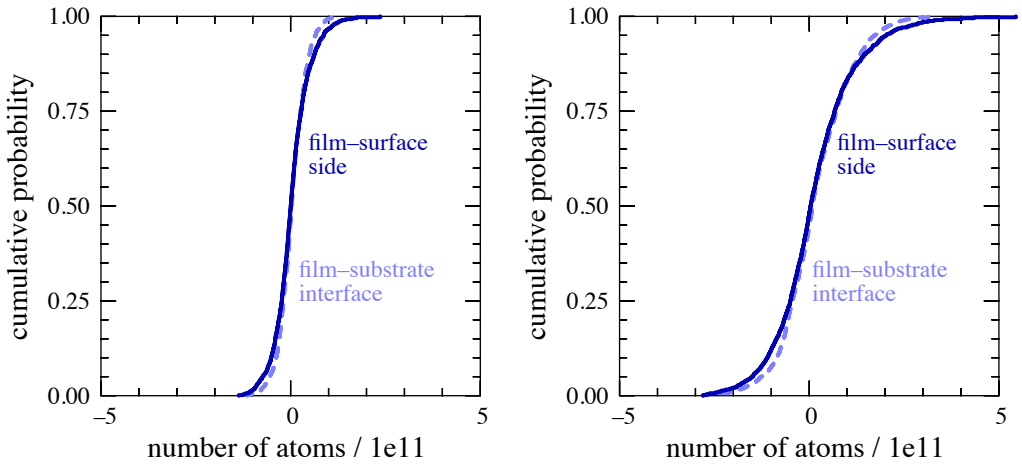

Figure 4.8: Areal concentration (per grain boundary surface in m^2) distribution within the grain boundary network at the film–substrate interface (dashed curves) and at the film surface (solid curves) for a load of 20 K (left) and 40 K (right) at the maximum strain condition.

It would also be interesting to see from a mechanistic point of view, how the tractions acting along the grain boundary normal affect the extrusion of material out from the film facilitated by the oblique geometry of the grain. Another critical drawback of the currently considered transport model is the possibility of flux along the grain boundary normal direction which is unlikely to happen in the case of the grain boundary diffusion.

The areal concentration (per grain boundary surface in m^2) variation at the film–substrate interface (dashed lines) and at the film surface (solid lines) for the two loading conditions (left: 20 K and right: 40 K) is shown in Fig. 4.9. Qualitatively, the concentration variation looks similar between the film–substrate interface and the film–surface, which is reflective of the stronger dominance of the in-plane gradient as compared to the vertical potential gradient.

4.4.3 Kinetics of the transport

To analyze the kinetics of the diffusion process, the evolution of concentration of an exemplary oblique grain boundary over time is shown in Fig. 4.9 for the two loading conditions considered in this study, with each monolayer corresponding to a thickness change of 0.3 nm. For the microstructure (grain morphology and texture) considered in the current study, there is a

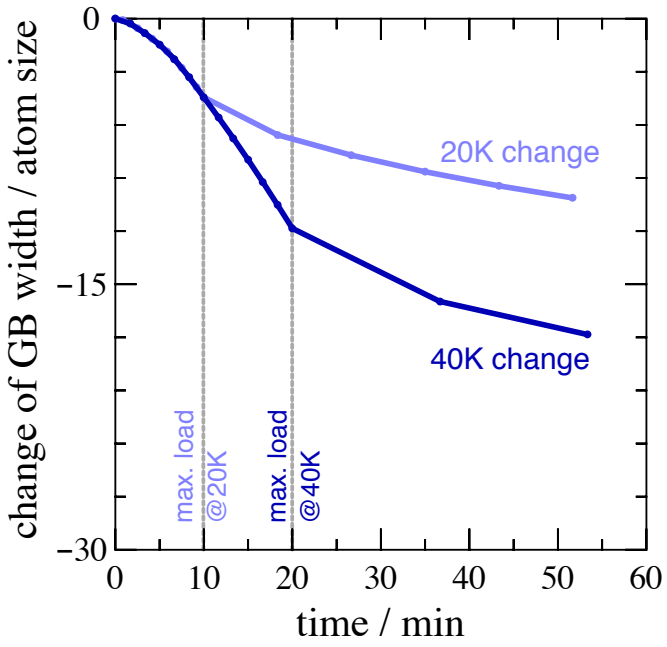

Figure 4.9: Average concentration evolution of the exemplary oblique grain boundary (highlighted in Fig. 4.6) for the two different thermal loading conditions of 20 K and 40 K.

net loss of atoms from the oblique grain indicating that it acts as a source of atoms due to the stress profile developing in the film for the (randomly) chosen grain arrangement. This would also indicate that the considered oblique grain would most likely not be a whisker nucleation site. The rate of loss of atoms (slope of the curves in Fig. 4.9) is more pronounced during loading and reduces markedly during the relaxation stages. Such a result can be attributed to the dominant effect of plastic relaxation as compared to stress relaxation by atom redistribution, since the kinematic consequences due to atom redistribution appeared to be insignificant for the present case. It is also critical to note that the grain boundary diffusivity considered in the current simulations is three orders of magnitude slower than those used in [Buchovecky et al., 2009b], that uses actually measured values of diffusivity, due to numerical convergence. Hence, the kinetics results shown in this study is an underestimation of the actual phenomenon. However, the conclusions drawn (insignificant influence of the diffusional flow on the shear forces and the film average stress evolution as compared to plasticity) would remain unchanged since the kinematic consequence of atom redistribution is very small, as also reported by Buchovecky

[2010] where a change in couple of orders of magnitude in diffusivity did not change the stress results.

4.5 Summary

A generalized fully coupled chemo-thermo-mechanical model in the crystal plasticity framework is outlined in this chapter to study the stress-driven diffusion in tin thin films. By comparing the average film stress evolution with and without the diffusional kinematics, it is concluded that the atom redistribution had limited influence over the film stress which corresponds to the bulk stresses measured experimentally via curvature measurements. Such an observation is contradictory to the reported result of Buchovecky et al. [2009a], where the relaxed stress is 10 MPa higher in the film for the elasto-plastic simulation as compared to that of including grain boundary diffusion in the simulation. Similar results were also reported in Pei et al. [2017] where the strain due to whisker relaxation was about 30 % of the total strain. In our case the kinematic consequence appears to be much lower than that. A plausible reason for such an outcome might be the lower value of diffusivity used in this study compared to those used in the model of Buchovecky et al. [2009a], Pei et al. [2017] where they have used experimentally measured diffusivity values. Another reason for the difference might be the differences in the description of β-Sn plasticity between the present study using a phenomenological power law model, versus that of an isotropic von Mises description used in Buchovecky et al. [2009a], Pei et al. [2017]. This further motivates the need for the accurate description of β-Sn plasticity, which is yet to be established in literature, and a methodology to accurately predict such plasticity parameters would be taken up in the following couple of chapters (Chapters 5 and 6).

The kinematic effect of atom redistribution on the hydrostatic stress and the different traction components (shear and normal) in the grain boundary network are also studied, and it is concluded that the kinematics due atom redistribution considerably affected the grain boundary hydrostatic stress as compared to the different traction components, Fig. 4.7. This might be a standalone result for the studied microstructure. Further insight can be gained via a statistical

analysis of these traction values for various microstructures (i.e., crystal neighborhood and/or texture). Also, for the currently simulation, the oblique grain boundary appears to continuously lose atoms which would make it an atom source and prevent it to nucleate a whisker. This suggests that, contrary to the observation of the oblique grain seen here, there could be a situation where the oblique grain boundary would gain atoms and nucleate a whisker. However, the location of such grains would still be governed by the local crystallographic neighborhood.

The preliminary conclusions made from the present study need to be further established by more detailed analysis. As mentioned, the model proposed herein does not eliminate flux along the grain boundary normal direction, and hence a suitable modification to the current formulation would be to incorporate grain boundary normal to calculate the stress acting along the grain boundary normal direction and use only that quantity as a measure of chemical potential instead of the hydrostatic stress considered presently. Also, the kinetics reported in this work is an underestimation, as the grain boundary diffusivity value used in here is around three orders of magnitude slower than reality. Having the capability of parallel computation would enable to use realistic diffusivity values, as they require a smaller time step than that used for the present simulations. Performing a rigorous statistical study using accurate model description and with different grain microstructures and texture distributions (i.e., initial conditions) would provide a measure of the range of the various stress quantities (shear and normal tractions) and hence increase our insight on whether they are sufficient in breaking the tin oxide layer on top. Moreover, such a statistical study would also provide a distribution of cases where the oblique grain acts as an atom sink (thereby being a potential whisker nucleus), compared to it being an atom source. Such a distribution of grains acting atom sinks, can then be compared to experimentally observed whisker density values.

Table 4.1: Material properties for dilatational air, body-centered tetragonal β-Sn, and isotropic substrate.

	Value	**Unit**
Air		
C_{11}	10.0	GPa
C_{12}	0.0	GPa
$g_0 : g_\infty$	0.333 : 0.667	MPa
h_0	1.0	MPa
a	2	
M	3	
n	20	
$\dot{\gamma}_0$	10^{-3}	s^{-1}
β-Sn		
C_{11}	72.3	GPa
C_{12}	59.4	GPa
C_{13}	35.8	GPa
C_{33}	88.4	GPa
C_{44}	22.0	GPa
C_{66}	24.0	GPa
$g_0 : g_\infty \{1\,0\,0\}\langle 0\,0\,1]$	8.5 : 11.0	MPa
$g_0 : g_\infty \{1\,1\,0\}\langle 0\,0\,1]$	4.3 : 9.0	MPa
$g_0 : g_\infty \{1\,0\,0\}\langle 0\,1\,0]$	10.4 : 11.0	MPa
$g_0 : g_\infty \{1\,1\,0\}\langle 1\,\bar{1}\,1]$	4.5 : 9.0	MPa
$g_0 : g_\infty \{1\,1\,0\}\langle 1\,\bar{1}\,0]$	5.6 : 10.0	MPa
$g_0 : g_\infty \{1\,0\,0\}\langle 0\,1\,1]$	5.1 : 10.0	MPa
$g_0 : g_\infty \{0\,0\,1\}\langle 0\,1\,0]$	7.4 : 10.0	MPa
$g_0 : g_\infty \{0\,0\,1\}\langle 1\,1\,0]$	15.0 : 10.0	MPa
$g_0 : g_\infty \{0\,1\,1\}\langle 0\,\bar{1}\,1]$	6.6 : 9.0	MPa
$g_0 : g_\infty \{2\,1\,1\}\langle 0\,\bar{1}\,1]$	12.0 : 13.0	MPa
h_0	20	MPa
a	2.0	
n	6	
$\dot{\gamma}_0$	2.6×10^{-8}	s^{-1}
$\alpha_{\langle 1\,0\,0]}$	20×10^{-6}	K^{-1}
$\alpha_{\langle 0\,0\,1]}$	40×10^{-6}	K^{-1}
D_{GB}	1×10^{-16}	$\mathrm{m}^2\,\mathrm{s}^{-1}$
D_{bulk}	2×10^{-28}	$\mathrm{m}^2\,\mathrm{s}^{-1}$
δ_{GB}	0.5	nm
Ω	2.7×10^{-29}	m^3
ϵ	1.0	
c_0	0	number of atoms
Substrate		
C_{11}	1500.0	GPa
C_{12}	500.0	GPa
α	1×10^{-6}	K^{-1}

CHAPTER 5

INVERSE INDENTATION ANALYSIS AND ITS APPLICATION IN FACE-CENTERED CUBIC MATERIALS

5.1 Motivation

The incomplete material description of β-Sn arises due to the lack of established plasticity parameters, the initial value of g (sometimes also referred to as critical resolved shear stress, CRSS), in the literature, especially when using the phenomenological material model. This is important since plasticity of β-Sn is known to affect the whisker formation [Chason et al., 2008]. Plastic deformation in the highly anisotropic β-Sn, because of the body-centered tetragonal crystal structure, can be accommodated by the thirteen slip families that are available. Even though the present simulations use reported values for these parameters, a reliable parameter estimation strategy for crystal plasticity constitutive models is lacking. An inverse approach is proposed in this work to identify constitutive parameters that relies on minimizing the error between the simulated and experimental single crystal nanoindentation responses. The method was originally proposed by Zambaldi et al. [2012], however, a study regarding its efficacy has been lacking. In this chapter, the methodology using Inverse Indentation Analysis (*IIA*) is implemented for face-centered cubic (fcc) materials to determine its effectiveness in such a highly symmetric system with only a single slip family and using virtual experimental reference data with a priori known parameter values. Some modifications to the original method are also proposed that resulted in increased effectiveness of the methodology. Critical aspects for an effective optimization, such as sensitivity analysis of each parameters, dimensional reduction, and effect of initial guess, is also discussed. Finally, after establishing the fidelity of the modified *IIA* for fcc materials, its reliability is tested for more asymmetric hexagonal materials (again with virtual experiments) having multiple slip families in Chapter 6. Having established the reliability of the proposed methodology for cubic and hexagonal materials, the next step would be to

implement it for even lower symmetric tetragonal β-Sn, and establish its plastic behavior.

The contents of this chapter is adapted from the already published work in Chakraborty and Eisenlohr [2017].

5.2 Background

The feasibility to determine the adjustable parameters of single crystal plasticity constitutive laws by an inverse approach that minimizes the deviation between the measured and simulated indentation response of individual grains (of a polycrystalline sample) is analyzed in this chapter for the case of face-centered cubic (fcc) crystal structure. Optimization uses the Nelder–Mead (NM) simplex algorithm, that was modified to circumvent regions in parameter space where the evaluation of the objective function fails. A phenomenological power-law is used as the constitutive description for crystal plasticity. Simulated cases of indentation with prescribed constitutive parameter values serve as the virtual reference, often referred to in the chapter as virtual experiments. A sensitivity analysis study is also discussed in order to gauge the relative influence of different adjustable parameters on the overall material response under indentation. Following the sensitivity analysis, the reliability of the methodology is assessed based on it's reproducibility and robustness with different objective functions involving the load–displacement response and residual surface topography for different indentation crystal orientations. It appears that using both information from load–displacement and residual surface topography provides a more convex objective function surface for the optimizer to identify the target values (global minimum) without being significantly influenced by the selected crystal orientation.

The chapter is structured as follows: after a literature review about the development of indentation as a technique to identify material parameters in Section 5.3, the simulation details along with the constitutive material model description are presented in Section 5.4 followed by an explanation about the structure of the inverse optimization strategy in Section 5.6. Critical results obtained from the comprehensive investigation are highlighted in Section 5.7 followed

by a discussion in Section 5.8 and the conclusive remarks in Section 5.9.

5.3 Introduction

The prediction of the mechanical response and internal structural evolution of crystalline solid is challenging due to the inherent anisotropy of the elastic and plastic properties of single crystals. Integration of anisotropy into crystal plasticity (CP) models of deformation has been quite successful (see [Roters et al., 2010b] for a recent review) and is most relevant for metals that exhibit strong crystallographic texture resulting from processing or when one or more dimensions of an engineering component approach the internal grain size of the material. While the sophistication of the underlying constitutive description of deformation and structure kinetics varies among different CP approaches, for all of them the accuracy of prediction largely depends on the values selected for the adjustable constitutive parameters.

Correct identification of constitutive parameter values is an ongoing area of significant research interest as it involves the inverse problem of matching simulation outcomes to experimental reference. One way would be to use experimental reference from polycrystalline (macroscopic) deformation under unidirectional tension or compression in connection with either an isotropic plastic description [Mahnken and Stein, 1996, Kajberg and Lindkvist, 2004] or a phenomenological crystal plasticity material model [Herrera-Solaz et al., 2014]. In [Herrera-Solaz et al., 2014], single crystal material parameters were extracted using a gradient-based Levenberg–Marquardt optimization algorithm that matched stress–strain responses of finite element simulations of representative volume elements to corresponding experiments. A reproducibility study for this approach revealed high reproducibility for some parameters as compared to others [Herrera-Solaz et al., 2015], indicating either the presence of multiple local minima in the objective function surface or lack of sensitivity for certain parameters over others, and thus, calling for further investigation. An alternative and more direct way is to use single crystal (microscopic) deformation since it excludes the problematic convolution caused by multiple grains deforming and interacting in parallel and appears, hence, to be a more

promising venue. Instrumented nano-indentation experiments have been an efficient way to generate microscopic deformation response from multiple orientations in the form of load–displacement curves and surface topography after indentation.

Indentation experiments as a tool to identify material parameters, was first proposed by Huber and Tsakmakis [1999] and Huber et al. [2001] by using an artificial neural network (ANN) and only indentation load–displacement response. Finite element (FE) simulations were performed based on an isotropic plasticity constitutive model including isotropic and kinematic hardening to generate simulated load–displacement curves. Input to the network included the simulated (reference) load–displacement curves while the output corresponded to the parameter values. Multiple FE simulations were performed to train the network. The effectiveness of this FE-ANN methodology was tested by implementing it to identify the material parameters for different materials using experimental load–displacement curves by Klötzer et al. [2006]. It was observed that the methodology could only capture the elastic response with certainty, while there existed a high scatter among the identified plastic parameters. A modification to the FE-ANN methodology was proposed by Hajali et al. [2008] by considering only the loading part of the load–displacement response and using dimensionless material parameters for their identification. However, significant deviation from experimental response to that obtained from FE-ANN parameters were obtained especially in the plastic regime. A different approach, but still using only the indentation load–displacement response, was adopted by Nakamura et al. [2000] wherein he incorporated the sequential stochastic Kalman filter algorithm, used mostly in signal processing, to estimate Young's modulus and Poisson's ratio for functionally graded materials. The strategy was also extended to identify plastic parameters for transversely isotropic materials [Nakamura and Gu, 2007, Yonezu et al., 2009]. Subsequently, with the advent and ease of access in measuring surface topographies, such as by atomic force microscopy or white light interferometry, Bolzon et al. [2004] proposed to include the residual imprint after indentation for estimating the constitutive parameters. They assumed an isotropic elasto-plastic material model and observed that inclusion of topography deviation in the objective function generally

improved the accuracy of parameter estimation in the gradient-based deterministic optimization algorithm that was used. Bocciarelli et al. [2005], Bocciarelli and Maier [2007] extended the scope to elastic-perfectly plastic material models with orthotropic symmetry (using a yield surface approach [Hill, 1948]) for orthotropic materials against both artificial reference data and real experimental data. The general shortcomings associated with gradient-based optimization and strong simplifications in the constitutive description in terms of the final optimization solution depending on the initial parameters was confirmed. Nevertheless, with a priori knowledge of viable plastic parameter ranges such an approach gave satisfactory results for multi-layered systems [Moy et al., 2011a] and aluminum alloys [Moy et al., 2011b]. To reduce the computation cost of evaluating the gradient numerically, several studies focussed on estimating high-quality approximations of the solution field from a limited number of numerical results using proper orthogonal decomposition (POD) with radial basis functions [Buljak and Maier, 2011, Bolzon and Talassi, 2013, Bocciarelli et al., 2014, Hamim and Singh, 2017, Arizzi and Rizzi, 2014]. Other simplifications to reduce computation time of calculating the gradient for gradient-based optimization algorithms have also been investigated using approaches such as parameter coupling [Rauchs and Bardon, 2011], solving the adjoint problem [Constantinescu and Tardieu, 2001] and making dimensionless equations based on a priori FEM simulations [Yonezu et al., 2010, Wang et al., 2010].

In all above studies, deformation behavior has been approximated by simplified material models that hardly consider plastic anisotropy of the material. Sánchez-Martín et al. [2014] postulated values for crystal plasticity constitutive parameters (of a particular Mg alloy, MN11) by comparing hardness values from grain indentation simulations using sets of parameters reported for similar materials in the literature, and choosing that one giving the closest fit to the indentation experiments. Comparing responses between experiment and simulation of axisymmetric instrumented nano-indentation into individual grains by incorporation of a crystal plasticity model was first performed by Zambaldi and Raabe [2010] on face-centered tetragonal γ-TiAl. Their study led to the inverse methodology of identifying crystal plasticity parameters

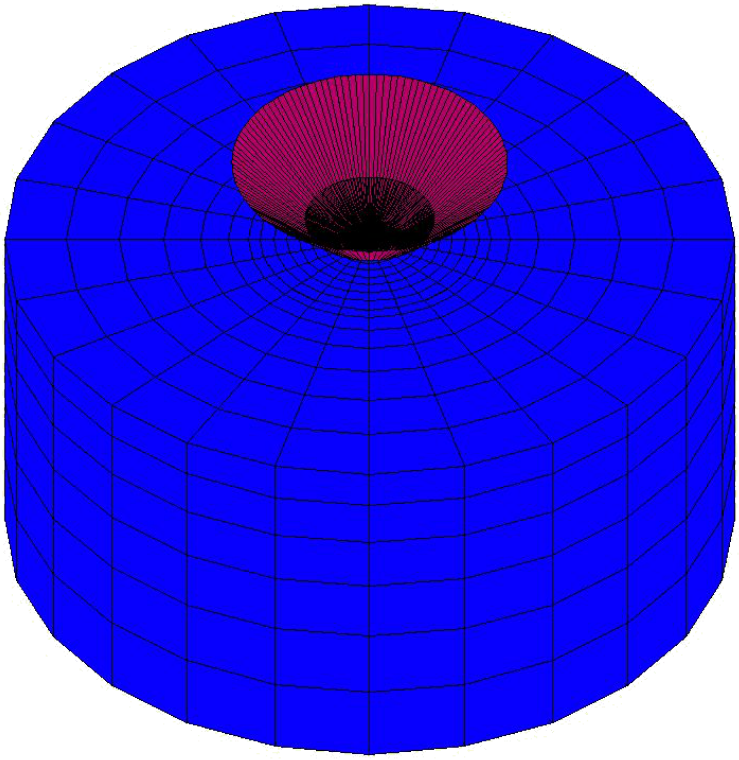

Figure 5.1: Finite element model including indenter and single crystalline substrate. Indentation is simulated by prescribing downward followed by upward motion of the rigid indenter surface at constant velocity. Nodal displacements of substrate are fully restricted on the bottom and side faces.

using gradient-free Nelder–Mead (NM) simplex optimization based on matching the simulated load–displacement and surface topography [Zambaldi et al., 2012] to measured data for hexagonal commercially pure titanium (cp-Ti). However, the constitutive parameters obtained for cp-Ti differed significantly from other reports (see [Li et al., 2013] for summary).

In this chapter the efficacy of the inverse methodology suggested by Zambaldi et al. [2012] is analyzed on face-centered cubic (fcc) crystal systems using “pseudo-experimental" reference data to determine the robustness of such an approach with material orientation.

5.4 Simulation set-up

5.4.1 Finite element discretization

Similar to the previous work, [Zambaldi et al., 2012], a three-dimensional finite element (FE) model of conospherical indentation (see Fig. 5.1) is generated using the open source toolkit "STABiX" [Mercier and Zambaldi, 2014]. The single crystalline cylindrical substrate of height 4 µm and diameter 8 µm is discretized by 4596 linear hexahedral elements based on a mesh sensitivity study (Section 5.7.1). Nodal displacements are fixed on the bottom and outer surfaces. The indenter of radius 1 µm and cone angle of 90° is assumed rigid with a Coulomb friction coefficient of 0.3. Its vertical displacement is linearly varied from zero to 0.5 µm and back in 10 s, which are discretized into 1334 equal increments. All the simulations are performed using the commercial finite element software Marc 2013.1 (MSC Software Corporation, Newport Beach, CA) on compute servers maintained by the Division of Engineering Computing Services at Michigan State University. To reduce the computation time, the geometry is also decomposed into four equal domains (i.e., sectors of 90° each) using the in-built functionality in Marc 2013.1.

5.4.2 Phenomenological material point model

To solve the mechanical boundary value problem posed by conospherical indentation, a phenomenological constitutive model [Peirce et al., 1982] widely used in crystal plasticity and implemented as part of the open source simulation toolkit "Düsseldorf Advanced Material Simulation Toolkit" (DAMASK) [Roters et al., 2012] is interfaced to Marc 2013.1 through the material subroutine "hypela2". A brief overview of the constitutive description is mentioned below, further details can be found in Roters et al. [2010a]. The current model is based on the multiplicative decomposition of the total deformation gradient $\mathbf{F}$ into plastic and elastic components for

describing the kinematics under a large strain framework [Lee, 1969]

$$\mathbf{F} = \mathbf{F}_\mathrm{e}\,\mathbf{F}_\mathrm{p} \tag{5.1}$$

with $\mathbf{F}_\mathrm{p}$ being the plastic deformation gradient and $\mathbf{F}_\mathrm{e}$ relating to the elastic stretch and rotation.

The relation between plastic deformation gradient $\mathbf{F}_\mathrm{p}$ and the plastic velocity gradient $\mathbf{L}_\mathrm{p}$ is given by the flow rule:

$$\dot{\mathbf{F}}_\mathrm{p} = \mathbf{L}_\mathrm{p}\ \mathbf{F}_\mathrm{p} \tag{5.2}$$

The dislocation defect structure is parameterized phenomenologically in terms of slip resistance on each of the twelve $\{1\,1\,1\}\ \langle 1\,1\,0\rangle$ slip systems. The plastic velocity gradient is additively composed from slip rates

$$\mathbf{L}_\mathrm{p} := \sum_\alpha \dot{\gamma}^\alpha\, \mathbf{s}^\alpha \otimes \mathbf{n}^\alpha \tag{5.3}$$

where the unit vectors $\mathbf{s}\alpha$ and $\mathbf{n}\alpha$ indicate the slip direction and slip plane normal for slip system $\alpha = 1,\ldots,12$. The resolved shear stress

$$\tau^\alpha = \mathbb{C}\left(\mathbf{F}_\mathrm{e}{}^\mathrm{T}\mathbf{F}_\mathrm{e} - \mathbf{I}\right)/2 : \mathbf{s}^\alpha \otimes \mathbf{n}^\alpha \tag{5.4}$$

is the driving force for slip at rates

$$\dot{\gamma}^\alpha = \dot{\gamma}_0 \left|\frac{\tau^\alpha}{\tau^\alpha_\mathrm{crss}}\right|^n \mathrm{sgn}\left(\tau^\alpha\right), \tag{5.5}$$

with material parameters $\dot{\gamma}_0$ (reference shear rate) and n (stress exponent). Components of the anisotropic elastic stiffness tensor $\mathbb{C}$ were selected as $C_{11} = 107\,\mathrm{GPa}$, $C_{12} = 61\,\mathrm{GPa}$, and $C_{44} = 29\,\mathrm{GPa}$. The critical resolved shear stress $\tau^\alpha_\mathrm{crss}$ evolves in the course of slip as [Hutchinson, 1976]

$$\dot{\tau}^\alpha_\mathrm{crss} = \sum_\beta q^{\alpha\beta}\, h_0 \left|1 - \frac{\tau^\beta_\mathrm{crss}}{\tau_\mathrm{sat}}\right|^a \mathrm{sgn}\left(1 - \frac{\tau^\beta_\mathrm{crss}}{\tau_\mathrm{sat}}\right)\left|\dot{\gamma}^\beta\right|, \tag{5.6}$$

with adjustable parameters h_0, a, τ_{sat}, and $q^{\alpha\beta}$ reflecting the six types of dislocation interactions observed in fcc systems. In addition to the saturation value τ_{sat}, the initial value of τ_{crss}, denoted as τ_0, is also free to adjust.

In total, the above phenomenological description comprises 12 adjustable parameters in the case of fcc lattice structure, those being $\dot{\gamma}_0$, n, τ_0, τ_{sat}, a, h_0, and six coefficients for dislocation interactions, i.e., self, coplanar, collinear, Hirth lock, Lomer–Cottrell lock, and glissile junction. Since the values of the material parameters $\dot{\gamma}_0$ and n mostly influence numerical stability and only marginally the material micromechanics, they are not considered as adjustable parameters in the optimization [Zambaldi et al., 2012]. Moreover, the six interaction parameters are generally obtained from a lower scale dislocation dynamics simulation and hence are also considered to be constant.

5.5 Global sensitivity analysis

The global sensitivity analysis is performed based on the “elementary effects method" proposed by Morris [1991] to economically collect partial derivatives in a high-dimensional unit domain. Partial derivatives $\partial f/\partial x_i$ are calculated based on pairs of points that only differ by $\Delta = 0.5p/(p-1)$ along the coordinate axis i. Those pairs are selected from a grid that has two points per parameter space dimension and which is populated by r times starting a path at the origin and taking one Δ step along each dimension in random order. The absolute values of the multiple partial derivatives resulting along each dimension are averaged following the suggestion of Campolongo et al. [2007].

$$\mu_i^* := \langle \left| \partial f/\partial x_i \right| \rangle, \tag{5.7}$$

where larger values of μ_i^* indicate a larger influence of parameter i on f. For the current study, $p = r = 4$ were chosen.

5.6 Optimization Methodology

5.6.1 Universal optimization module

Figure 5.2 illustrates the optimization strategy that iteratively adjusts the constitutive parameters, performs crystal plasticity finite element simulation(s) of single crystal indentation, and compares the resulting load–displacement data and/or surface topography to their reference until the deviation meets a given tolerance. The optimizer used in this study is implemented as a general Python class that can be equipped with different stochastic and deterministic optimization algorithms such as Particle Swarm Optimization [Kennedy and Eberhart, 1995] or Nelder–Mead simplex [Nelder and Mead, 1965]. Its universality results from the possibility to be subclassed with an arbitrary evaluation of fitness, which in the present case triggers the CPFE simulation(s), the post-processing of its results to extract load–displacement data and surface topography, and the calculation of the corresponding deviations from a known reference (objective function value).

Since the system of constitutive equations selected in Section 5.4.2 has four adjustable parameters τ_0, τ_{sat}, h_0, and a, the associated optimization problem is four-dimensional. Hence, for such relatively low-dimensional problem, the deterministic Nelder–Mead strategy is chosen as a suitable option for its solution.

5.6.2 Nelder–Mead simplex optimization algorithm

The Nelder–Mead (NM) simplex algorithm, originally proposed in 1965 [Nelder and Mead, 1965], has been one of the best known algorithms to solve a wide class of unconstrained optimization problems due to its simplicity and ease of implementation. The standard NM simplex algorithm constructs a simplex having $N+1$ vertices and iteratively relocates the worst vertex until the simplex has moved and shrunk to an optimum location in the N-dimensional parameter space. Since the NM algorithm does not depend on gradient information, it is very suitable for the present class of inverse problems [Hamim and Singh, 2017]. A simple, yet highly effec-

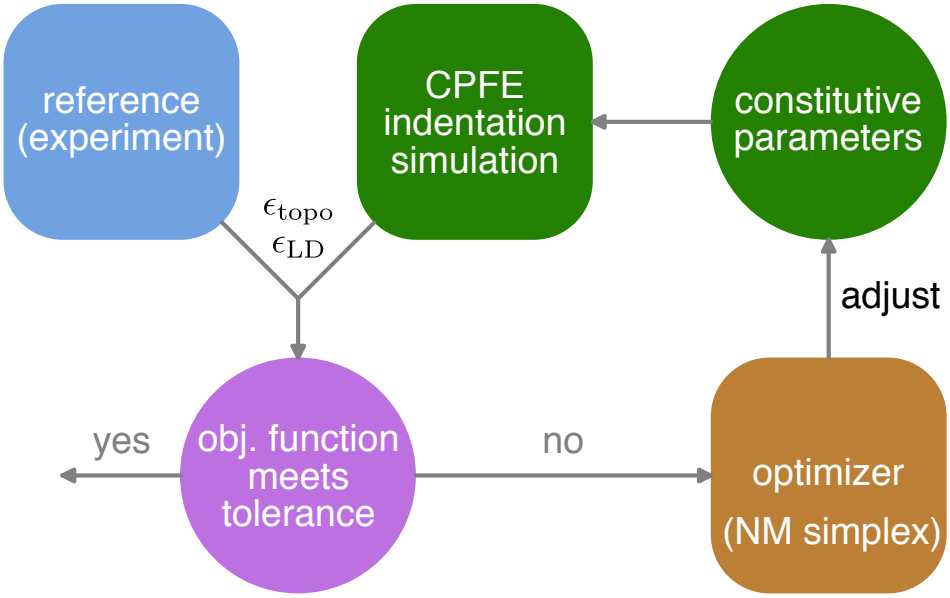

Figure 5.2: Iterative optimization setup to identify adjustable parameters of a crystal plasticity constitutive law. Based on a selected strategy, the optimizer adjusts the parameters, which are then fed as input into the CPFE simulation using the material point model DAMASK. Objective function value is obtained as the load–displacement (ϵ_{LD}) and/or surface topography (ϵ_{topo}) deviation from a given reference.

tive, modification is proposed to the algorithm to move it away from regions where no viable solution to the fitness function can be found (when the FE simulation does not converge). A second modification is to map the domain of parameter space that is assumed to contain the optimum solution onto a unit domain such that distances are independent of the particular direction in parameter space.

The modified algorithm to find the minimum of an objective function f reads:

- Generate $N+1$ random points $\mathbf{p}$ in the remapped parameter space as vertices of the initial simplex, N being the number of constitutive parameters, i. e., the dimension of parameter space.

- Evaluate the objective function f for each vertex to determine the best (subscript “b”), second-worst (subscript “s”), and worst (subscript “w”) one.

- Exclude the worst vertex $\mathbf{p}_\mathrm{w}$ and determine the centroid (subscript “g") of the remaining simplex

$$\mathbf{p}_\mathrm{g} = \langle \mathbf{p} \rangle - \mathbf{p}_\mathrm{w}/N. \tag{5.8}$$

- “Reflection" of $\mathbf{p}_\mathrm{w}$ about the centroid $\mathbf{p}_\mathrm{g}$ to yield

$$\mathbf{p}_\mathrm{r} = \mathbf{p}_\mathrm{g} + \alpha \left(\mathbf{p}_\mathrm{g} - \mathbf{p}_\mathrm{w} \right). \tag{5.9}$$

- Propagate the simplex depending on the following conditions:

  1. If f_r is globally best, check a further “expanded” point

  $$\mathbf{p}_\mathrm{e} = \mathbf{p}_\mathrm{g} + \gamma \left(\mathbf{p}_\mathrm{r} - \mathbf{p}_\mathrm{g} \right) \tag{5.10}$$

  and replace $\mathbf{p}_\mathrm{w}$ with the better of $\mathbf{p}_\mathrm{r}$ and $\mathbf{p}_\mathrm{e}$.

  2. If f_r is better than the current second worst, replace $\mathbf{p}_\mathrm{w}$ by $\mathbf{p}_\mathrm{r}$.

  3. Otherwise contract the better of $\mathbf{p}_\mathrm{w}$ or $\mathbf{p}_\mathrm{r}$ towards

  $$\mathbf{p}_\mathrm{c} = \mathbf{p}_\mathrm{g} + \beta \left(\mathbf{p}_{\mathrm{w}\,|\,\mathrm{r}} - \mathbf{p}_\mathrm{g} \right). \tag{5.11}$$

  Replace $\mathbf{p}_\mathrm{w}$ by $\mathbf{p}_\mathrm{c}$ if f_c improves over f_w, otherwise shrink all vertices according to

  $$\mathbf{p}_j = \mathbf{p}_\mathrm{b} + \delta \left(\mathbf{p}_j - \mathbf{p}_\mathrm{b} \right) \tag{5.12}$$

- Any point for which the objective function cannot be evaluated is relocated to fall somewhere between the centroid of the overall simplex and the reflection of the infeasible point with respect to that centroid

$$\mathbf{p} = \langle \mathbf{p} \rangle + \xi \left(\langle \mathbf{p} \rangle - \mathbf{p} \right), \tag{5.13}$$

with ξ a uniform random number between 0 and 1. The randomness avoids situations when the generated point turns out to be infeasible as well. Previous works on viscoplastic parameter identification using NM simplex algorithm [Kajberg and Wikman, 2007, Kajberg and Lindkvist, 2004, Zambaldi et al., 2012] did not include a strategy to avert infeasible points in parameter space.

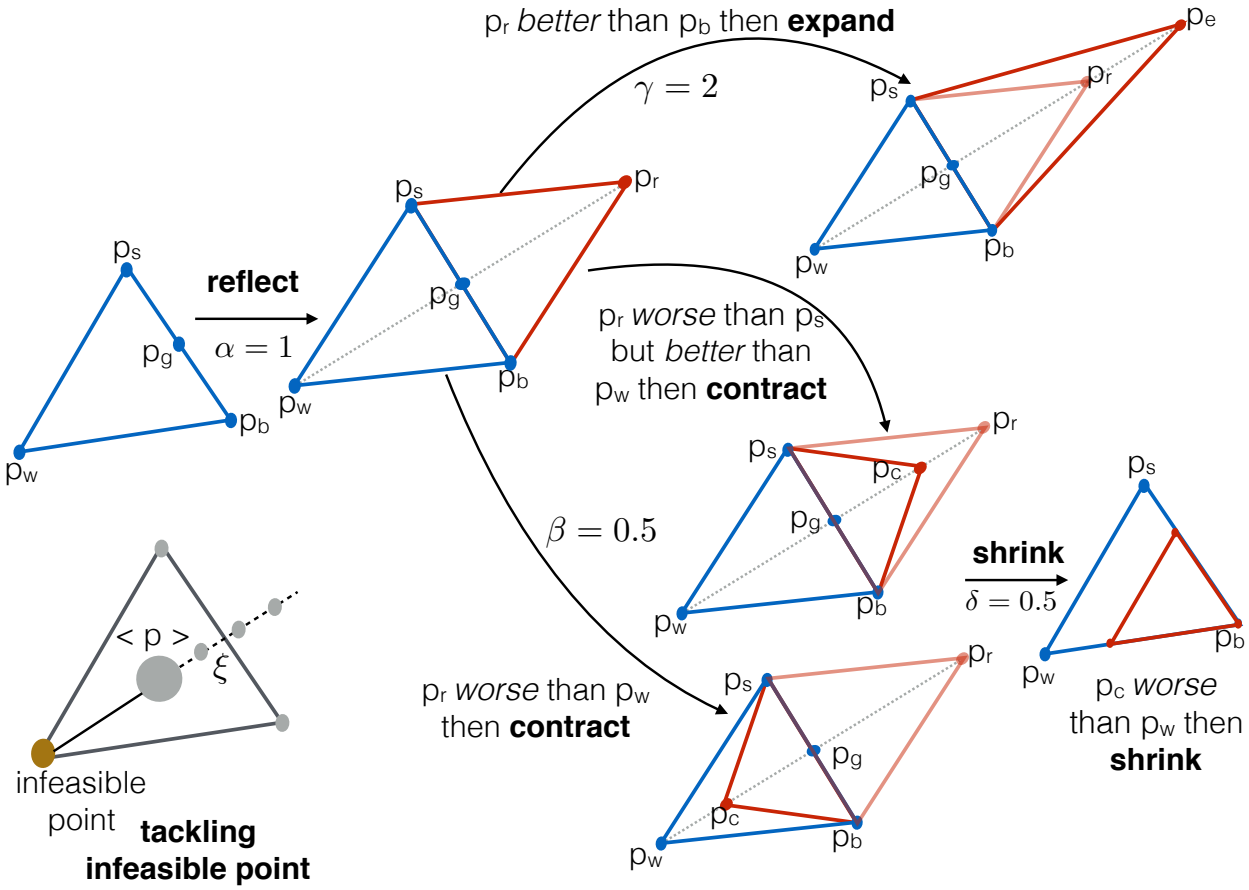

Figure 5.3: Two-dimensional illustration of the sequence of operations performed by the NM simplex algorithm as implemented here. Blue triangle marks the initial simplex, red triangle the one that results from the specific operation mentioned on the connecting arrow. Vertices are labelled by notations as described in the text. The strategy to navigate away from an infeasible vertex is displayed by the gray simplex in the bottom left.

- Moreover, each point is forced to remain within the unit domain.

Since the objective function evaluation requires a finite element simulation and is computationally very expensive, the coefficients of “reflection", “expansion", “contraction", and “shrink", which are the adjustable parameters for the NM simplex algorithm [Singer and Nelder, 2009], are chosen to be $\alpha = 1$, $\gamma = 0.5$, $\beta = 2$, and $\delta = 0.5$, respectively, as assigned in most implementations of NM simplex algorithm. Figure 5.3 illustrates the different operations of the NM simplex algorithm implemented in this study along with the strategy to generate a new point of evaluation when an infeasible point is encountered during the optimization.

5.6.3 Objective function for optimization

Possible input for the objective function are ϵ_{LD} and ϵ_{topo}, i.e. the differences between measured and simulated indentations in terms of load–displacement response $F(h)$ and surface topography $z(x,y)$, respectively. There is clear agreement that the former is essential for a quantitatively correct fit, but the benefit of including the surface topography deviation is not yet ultimately settled [Bolzon et al., 2004, Rauchs and Bardon, 2011, Meng et al., 2016]. To clarify the benefit of ϵ_{topo}, three different alternatives for the objective function (being ϵ_{LD}, ϵ_{topo}, and their average) are tested with regard to reproducibility and robustness. Reproducibility corresponds to the consistency of the identified constitutive parameters as a function of the initial simplex choice, while robustness means the consistency of optimized parameter values between different indented crystal orientations.

The error ϵ_{LD} is obtained by integrating the absolute difference of the loading part of the load–displacement curve between the reference (ref) and optimized simulation (sim) over each time step, i, and normalized by the integral of the reference load–displacement response.

$$\Delta F_i := \left| F_{\mathrm{sim},i} - F_{\mathrm{ref},i} \right| \tag{5.14}$$

$$\epsilon_{\mathrm{LD}} := \frac{\sum_i (\Delta F_{i+1} + \Delta F_i)(h_{i+1} - h_i)}{\sum_i (F_{\mathrm{ref},i+1} + F_{\mathrm{ref},i})(h_{i+1} - h_i)} \tag{5.15}$$

A similar strategy is also used to calculate the error in surface topography ϵ_{topo}: After both topographies are adjusted such that the elevation far from the indent is at zero and interpolated onto a regular grid (256×256), the absolute difference in elevation was integrated over all grid points j and normalized by the integral of the reference topography height. When comparing with real experiments where accurate information of tip geometry is difficult to acquire and may not match the simulated tip, a systematic error arises between experimental and CPFE topography of the tip impression. Hence, only positive heights, corresponding to “pileup" around the indent, were considered for calculating ϵ_{topo}.

$$\epsilon_{\mathrm{topo}} := \frac{\sum_j \left| z_{j,\mathrm{sim}} - z_{j,\mathrm{ref}} \right|}{\sum_j z_{j,\mathrm{ref}}} \tag{5.16}$$

The combined (average) function value of both approaches is termed $\epsilon_{\mathrm{combo}} = (\epsilon_{\mathrm{LD}} + \epsilon_{\mathrm{topo}})/2$.

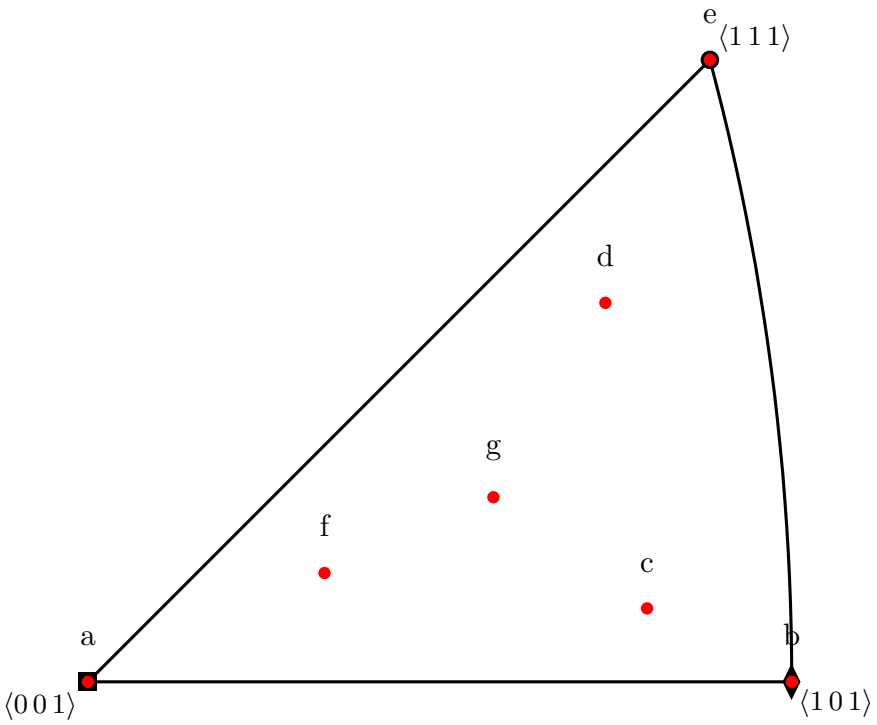

Figure 5.4: Crystallographic orientations of the indentation axis considered in the present study.

5.6.4 Determination of most sensitive constitutive parameters

The global sensitivity analysis, following the "elementary effects method" introduced by Morris [1991] and discussed in Section 5.5, is used to determine the relative influence of the four adjustable parameters, τ_0, τ_{sat}, h_0 and a, on the load–displacement and surface topography response for different crystal orientations. The influence of each of the four parameters are qualitatively ranked based on μ^*, which is the mean of their absolute partial derivatives $\partial f/\partial x$ where x represents a point in the four dimensional parameter space (see 5.6.4 for explanation). Three different cases of determining μ^* were considered wherein ∂f between two points was calculated based on either the deviation in load–displacement response (similar to ϵ_{LD}) or deviation in the surface topography response (similar to ϵ_{topo}) or as the average deviation of both load–displacement and surface topography response (similar to ϵ_{combo}).

For the present analysis the bounds of the four parameters are selected to be $\tau_0 \in [1,100]$ MPa, $\tau_{\text{sat}} \in [1,100]$ MPa, $a \in [2,5]$ and $h_0 \in [5,550]$ MPa, based on the already established crystal plasticity constitutive parameters for fcc aluminum [Kalidindi and Schoenfeld, 2000]. As

mentioned earlier, the value of reference shear rate $\dot{\gamma}_0$ and strain-rate sensitivity parameter n are fixed to $10^{-3}\,\mathrm{s}^{-1}$ and 25, respectively. Table 5.1 summarizes the μ^* values of the four parameters investigated for the three different cases and for seven different crystal orientations labelled in Fig. 5.4. It is to be noted that for the current study there were a few sample points where the CPFE simulations failed to converge and a valid μ^* for that parameter could not be obtained (indicated by "–" in Table 5.1).

From Table 5.1 it is clear that τ_0 and τ_{sat} are the most influential parameters for all three objective functions, followed by the hardening slope h_0 while the hardening exponent a turns out to be the least sensitive for all the five crystal orientations. The sensitivity analysis is repeated with a different value of the stress exponent ($n = 5$) for two different crystal orientations ("a" and "b" in Fig. 5.4) and similar results of τ_0 and τ_{sat} being the most influential parameters followed by h_0 and a are obtained, as shown in the bottom part of Table 5.1. This underpins why some studies (e.g. [Herrera-Solaz et al., 2014, Zambaldi et al., 2012]) did only choose τ_0 and τ_{sat} as design variables in the optimization. Lower sensitivity of hardening parameters akin to the present study are also observed by Alcala et al. [2008].

Thus, the global sensitivity analysis helps to qualitatively rank the most influential parameters in a constitutive law and is very beneficial for the current computationally expensive study of crystal plasticity parameter estimation.

Table 5.1: Results of global sensitivity analysis for the four adjustable parameters using each of the three objective functions ϵ_{LD}, ϵ_{topo}, and ϵ_{combo} and two values (n = 25 and n = 5) for the stress exponent in the kinetics equation described in Section 5.4.2. Tabulated values represent μ^* as described, with larger numbers indicating a higher relative influence of the respective parameter. Crystal orientations are labeled in accordance with Fig. 5.4.

Orientation	ϵ_{LD}				ϵ_{topo}				ϵ_{combo}			
	τ_0	τ_{sat}	h_0	a	τ_0	τ_{sat}	h_0	a	τ_0	τ_{sat}	h_0	a
$n = 25$												
a	1.48	0.50	0.118	0.054	0.66	0.589	0.091	0.062	1.07	0.54	0.104	0.058
b	1.34	0.49	0.345	0.097	0.77	0.670	0.285	0.130	1.06	0.58	0.315	0.113
c	1.47	0.50	0.141	0.093	0.66	0.645	0.117	0.091	1.07	0.57	0.130	0.092
d	1.50	0.52	0.151	0.103	0.63	0.673	0.105	0.091	1.07	0.60	0.128	0.097
e	1.12	0.51	0.150	0.036	0.85	0.750	0.120	0.015	1.00	0.63	0.134	0.025
f	1.42	–	0.122	0.070	0.55	–	0.030	0.050	1.00	–	0.070	0.060
g	1.42	–	0.120	0.070	0.56	–	0.080	0.070	1.00	–	0.100	0.070
$n = 5$												
a	1.44	0.42	0.111	0.05	0.74	0.577	0.119	0.070	1.09	0.50	0.115	0.06
b	1.38	0.42	0.110	0.05	0.75	0.610	0.125	0.075	1.07	0.51	0.117	0.06

5.7 Results

The pseudo-experimental reference indentations are obtained with a parameter set chosen as $\tau_0 = 31\,\text{MPa}$, $\tau_{\text{sat}} = 63\,\text{MPa}$, $h_0 = 400\,\text{MPa}$, $\dot{\gamma}_0 = 10^{-3}\,\text{s}^{-1}$, $n = 25$, and $a = 2.25$, based on those of aluminum [Kalidindi and Schoenfeld, 2000]. The six dislocation interaction parameters are based on [Kubin et al., 2008] with values of self = 1.4, coplanar = 1.4, collinear = 3.0, Hirth lock = 1.0, glissile junction = 1.4, Lomer lock = 1.4. In response to the performed sensitivity analysis, the three most influential parameters are selected as design variables for the optimization with associated search domains of $[20, 40]\,\text{MPa}$ for τ_0, $[40, 70]\,\text{MPa}$ for τ_{sat}, and $[300, 450]\,\text{MPa}$ for h_0.

5.7.1 Influence of finite element mesh size

To determine whether the mesh size influences the parameter value identification, the same optimization is performed with three different discretizations (2532, 4596, and 6696 hexahedral elements with linear shape functions). The influence of the mesh resolution is studied for an exemplary crystal orientation ("a" in Fig. 5.4) using ϵ_{combo} as the objective function. Each NM optimization was started with identical initial simplex, and an error tolerance $\epsilon_{\text{tol}} = 0.005$ was set as the termination criterion.

Figure 5.5 demonstrates the negligible influence of mesh size on the identifiability of the optimized parameters. The fitness evolution (Fig. 5.5a) is similar for all three discretizations and leads to stable final parameters (Fig. 5.5b). Based on these findings, a mesh with 4596 finite elements is selected for the subsequent studies.

5.7.2 Influence of objective function

Figure 5.6 compares for an exemplary indentation direction ("f" in Fig. 5.4) and for all three selected objective functions (ϵ_{LD}, ϵ_{topo}, and ϵ_{combo} from left to right) the load–displacement and surface topography deviations after parameter optimization to within $\epsilon_{\text{tol}} = 0.005$. It is observed that when using either ϵ_{LD} or ϵ_{topo} as the objective function for parameter estima-

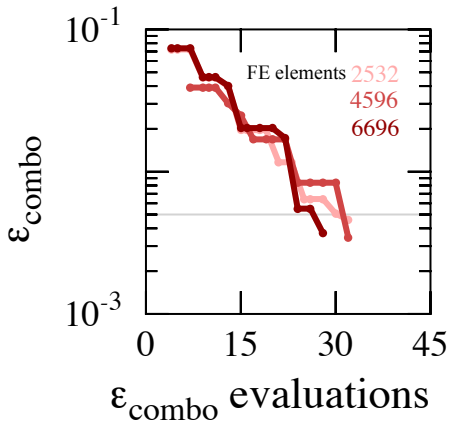

(a) fitness evolution

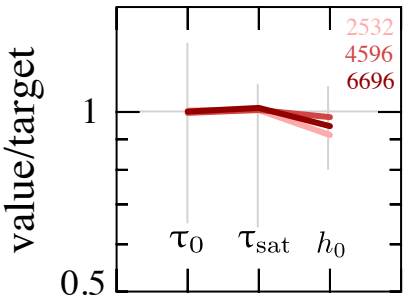

(b) optimized parameters

Figure 5.5: Influence of mesh size on the stability of the implemented inverse analysis. The horizontal line in (a) denotes the tolerance criterion; vertical lines in (b) show the parameter bounds for the optimization.

tion, the respective error in the non-included response (surface topography for ϵ_{LD} and load–displacement in case of ϵ_{topo}) remains relatively large (gray numbers in Fig. 5.6). In contrast, the use of $\epsilon_{\mathrm{combo}}$ minimizes the error in both load–displacement and surface topography responses simultaneously.

5.7.3 Reproducibility of parameter identification for different objective functions

To establish the reproducibility, parameter optimization with the NM algorithm is started from five different (random) initial simplices for each objective function while keeping the indented crystal orientation (“f" in Fig. 5.4) constant. Figure 5.7 shows the relative deviations of the optimized parameters collected from the five runs and compares them among the three objective functions (ϵ_{LD}, ϵ_{topo}, and $\epsilon_{\mathrm{combo}}$) with error tolerances of ϵ_{tol} = 0.2, 0.01, and 0.005. The average standard deviations from the target solution for each of the nine cases shown in Fig. 5.7 is represented by a vertical bar adjacent to the figure. Clearly, with stricter tolerance the standard deviation among multiple optimization runs is reduced, as the length of the vertical bar decreases from top to bottom in each column of Fig. 5.7. It is to be noted that even though the average standard deviations are comparable for ϵ_{LD} and $\epsilon_{\mathrm{combo}}$, the relative scatter in the

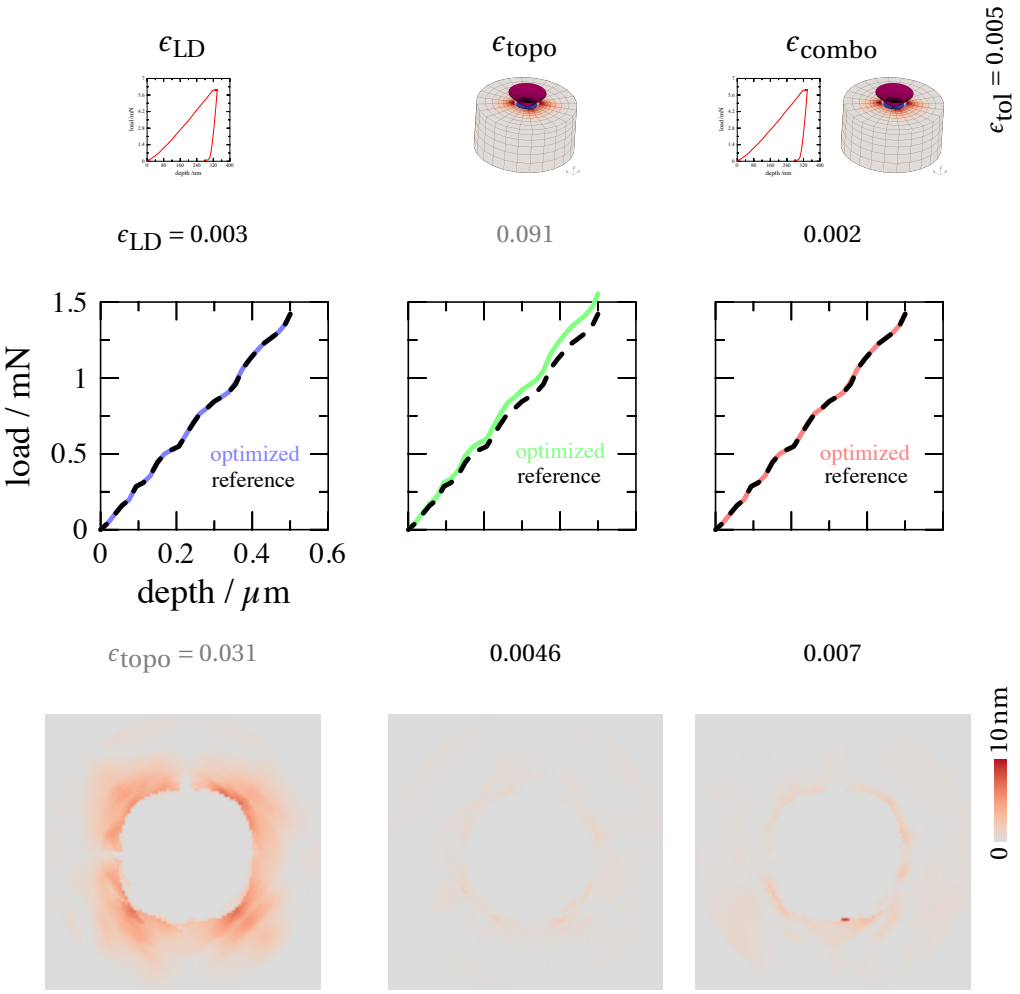

Figure 5.6: Comparison of load–displacement and surface topography deviations (absolute values between 0 to +10 nm) from reference response with parameters optimized to within $\epsilon_{tol} = 0.005$ of the respective objective function (from left to right, ϵ_{LD}, ϵ_{topo}, and $\epsilon_{combo} = (\epsilon_{LD} + \epsilon_{topo})/2$) for an exemplary indentation along direction “f" in Fig. 5.4. The reference load–displacement curve is shown by black.

optimized values for τ_0 and τ_{sat} is negligible when ϵ_{combo} was used as the objective function as compared to ϵ_{LD}. The objective function ϵ_{topo} (based only on surface topography) exhibited the poorest reproducibility, whereas comparable reproducibilities were obtained with ϵ_{LD} and ϵ_{combo}. The large scatter in h_0 is expected since it has the least influence on the fitness among the three design variables (as observed in Table 5.1), rendering h_0 relatively difficult to identify accurately. It is interesting to note (and presently unclear) that h_0 exhibits a comparably high degree of reproducibility for the two other objective functions, ϵ_{LD} and ϵ_{topo}.

It is noted that with the most strict tolerance of 0.005 only three out of five runs generated

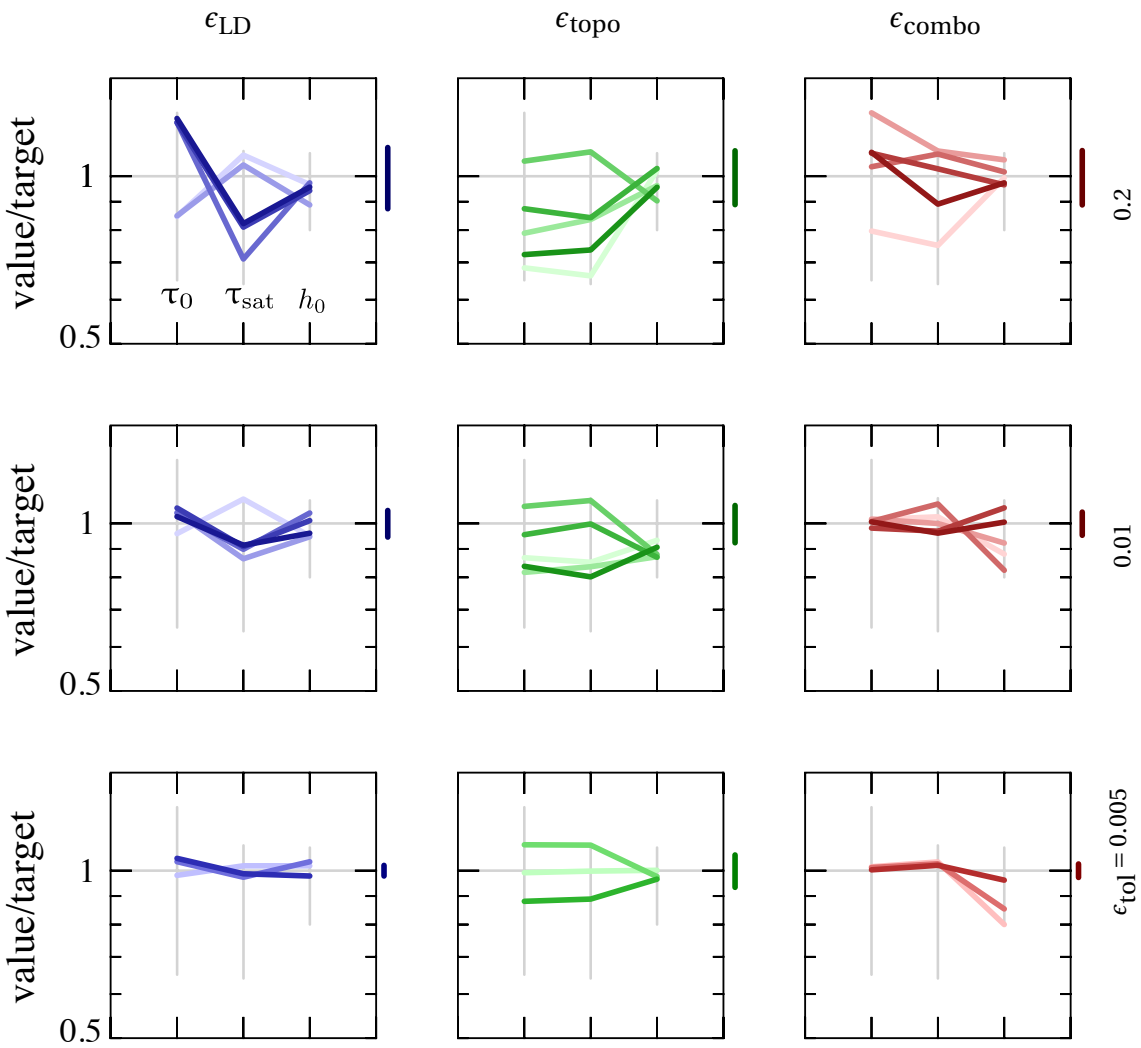

Figure 5.7: Optimized parameter set (τ_0, τ_{sat}, and h_0) using different objective functions (ϵ_{LD}, ϵ_{topo}, and ϵ_{combo}, left to right) and tolerance values ϵ_{tol} (top to bottom) resulting from five random initial simplices for one fixed crystallographic indentation direction. The horizontal gray line marks the target value (= 1), vertical lines span the bounds of each parameter. The vertical bar to the right of each figure represents the standard deviation of the overall parameter set.

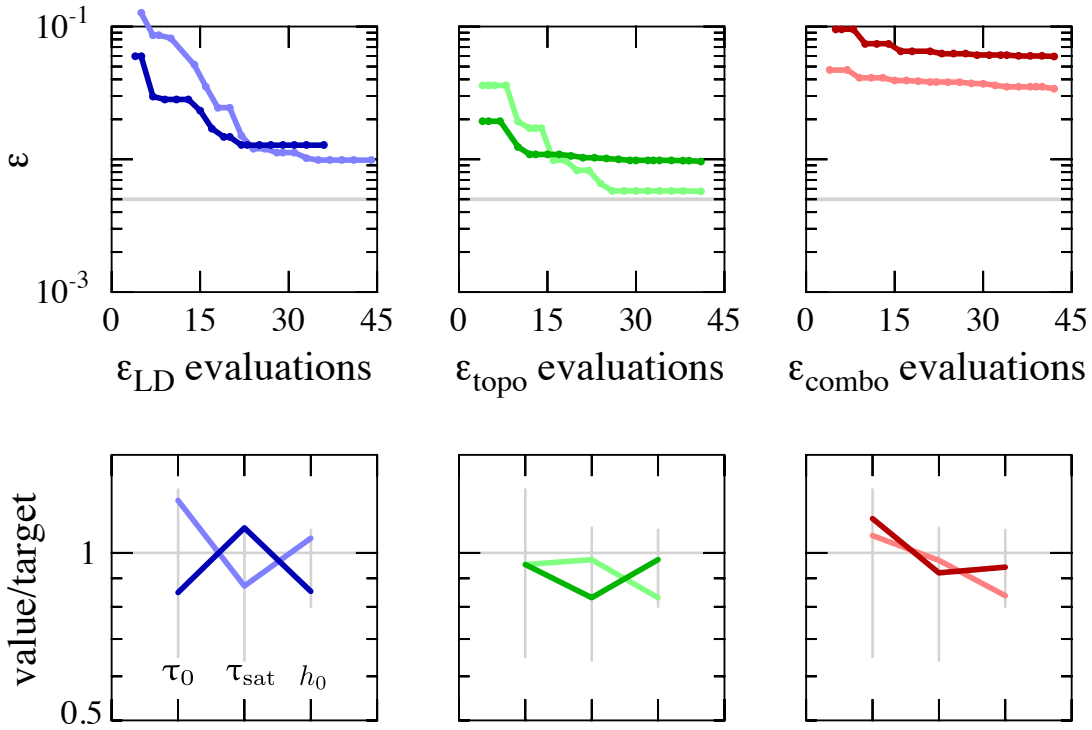

Figure 5.8: Top row corresponds to the evolution of objective function value (for the best point in the simplex) with number of function evaluations (cost) for different objective functions (left to right: ϵ_{LD}, ϵ_{topo}, ϵ_{combo}) that did not reach $\epsilon_{\text{tol}} = 0.005$ (horizontal gray line). The relative deviation between resulting parameter sets and target values is shown in the bottom row. Termination before the maximum allowable number of function evaluations (45) resulted due to the degeneracy of the simplex at a local minimum.

parameters that met this tolerance. The optimized parameter set for these non-converged runs along with the evolution of their fitness (i.e. the objective function value for the best point in the simplex) with number of function evaluations is shown in Fig. 5.8. From the fitness plots in Fig. 5.8 it is evident that in each of the six cases the simplex got stuck in a local minimum with negligible improvement over subsequent generations. Despite all six identified parameter sets being comparably far off the target, it is interesting to note that the objective function values for ϵ_{combo} remain notably larger than those for ϵ_{LD} and ϵ_{topo}.

5.7.4 Robustness of parameter identification for different indentation orientations

To establish robustness, parameter optimization using each of the three objective functions is repeated for seven different crystal orientations (see Fig. 5.4) starting from random initial simplices. The tolerance for minimizing each objective function (ϵ_{LD}, ϵ_{topo}, and $\epsilon_{\mathrm{combo}}$) is set to $\epsilon_{\mathrm{tol}} = 0.005$, consistent with the bottom row in Fig. 5.7, and the number of objective function evaluations is capped at 45 to avoid overly high computational cost incurred by the CPFE simulations.

Figure 5.9 shows the trajectory of the objective function (top row) and the final deviations (bottom row) between target and optimized parameter sets upon either reaching the specified tolerance (gray line at 0.005) or exceeding the allowed number of function evaluations. For ϵ_{LD} as objective function (blue curves, Fig. 5.9e), all three optimized parameters exhibit some scatter of about 10 % around their target values. When ϵ_{topo} is used as objective function (green curves, Fig. 5.9f), the scatter in τ_0 and τ_{sat} is much larger than observed for ϵ_{LD} but h_0 is identified relatively accurately. Despite this apparently large scatter, the ratio $\tau_{\mathrm{sat}}/\tau_0$ after optimization is found to be fairly stable and very close to the correct one, i. e. the relative deviation from their target is virtually the same for τ_0 and τ_{sat}. Finally, with $\epsilon_{\mathrm{combo}}$ as objective function (red curves, Fig. 5.9g), the scatter of τ_0 and τ_{sat} around the target is the smallest among all three objective functions. However, a comparably large scatter of h_0 is observed.

As evident in Fig. 5.9b, the tolerance $\epsilon_{\mathrm{topo}} \leq 0.005$ was not met within the limited number of objective function evaluations for two out of the four selected crystal orientations, which indicates a weak overall gradient in ϵ_{topo} towards the global minimum. In contrast, all seven (four) tested crystal orientations met this tolerance within 45 iterations when using $\epsilon_{\mathrm{combo}}$ (ϵ_{LD}).

Figure 5.9c illustrates for one exemplary case (black line) out of the seven tested indentation orientations (red lines) the typically observed trend of an opposing evolution in the components ϵ_{LD} (blue line) and ϵ_{topo} (green line) that average to $\epsilon_{\mathrm{combo}}$ (black line).

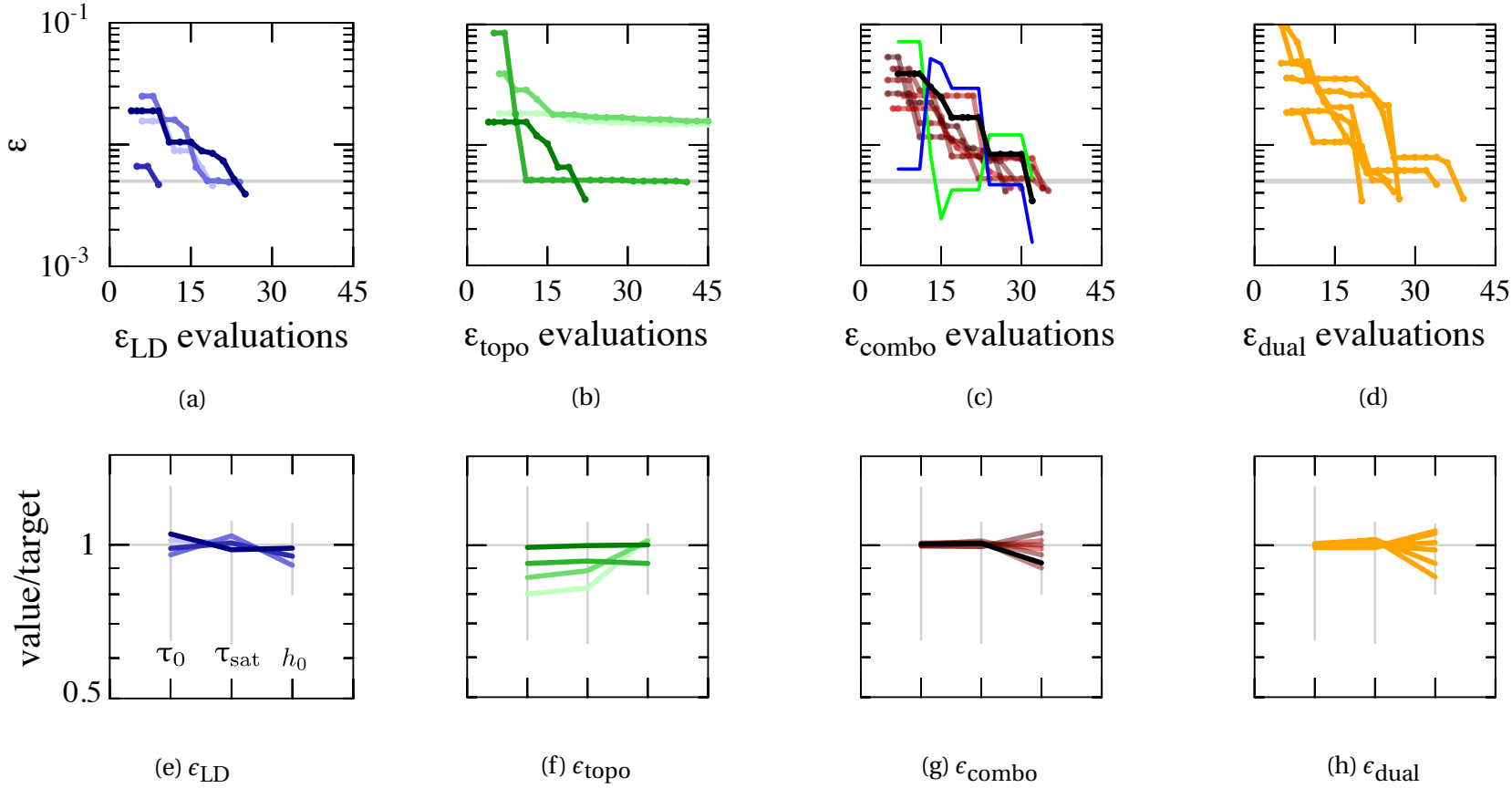

Figure 5.9: Bottom row represents parameter estimation stability for different indentation orientations and different fitness functions (left to right: ϵ_{LD},ϵ_{topo},ϵ_{combo} and ϵ_{dual}). Top row gives corresponding objective function value vs. cost, with tolerance $\epsilon_{\text{tol}} = 0.005$ indicated by the gray horizontal line. The analysis was performed for 4 different crystal orientations for ϵ_{LD} and ϵ_{topo}, 7 different crystal orientations for ϵ_{combo}, and 6 different orientation pairs for ϵ_{dual}. Green and blue curves in c indicate ϵ_{LD} and ϵ_{topo} comprising the black (exemplary) ϵ_{combo} evolution.

5.7.5 Dual-orientation objective function

The concurrent use of multiple orientations in the objective function might improve the parameter estimation quality, as reported, for instance, by Herrera-Solaz et al. [2014]. In order to test for this possibility, an objective function $\epsilon_{\text{dual}} = (\epsilon_{\text{combo}}(a) + \epsilon_{\text{combo}}(b))/2$ that averages the individual fitnesses obtained from two orientations a and b is evaluated for six different orientation pairs chosen from the seven individual orientations of Fig. 5.4. Random initial simplex vertices and the tight tolerance value of $\epsilon_{\text{tol}} = 0.005$ are selected as before and a maximum of 45 objective function evaluations were allowed. The simultaneous use of two orientations in the objective function ϵ_{dual} did not noticeably improve the quality of the optimized constitutive parameters over the single orientation case ϵ_{combo} (compare Fig. 5.9h to Fig. 5.9g). The two most sensitive parameters, τ_0 and τ_{sat}, could again be identified to within a few percent of their respective target values, with h_0 again exhibiting notably larger deviations. However, due to the doubled effort per objective function evaluation, the overall computational cost to reach a specified tolerance (0.005 in the present case) was, on average, about twice as large as in the single orientation case (compare Fig. 5.9d to Fig. 5.9c).

5.7.6 Influence of the reference point

The stability of the NM simplex optimization algorithm is investigated by selecting three different target points (optima) in three different parameter bounds, as listed in Table 5.2. The optimization is performed for an exemplary orientation (“a" in Fig. 5.4) using ϵ_{combo} as the objective function with $\epsilon_{\text{tol}} = 0.005$ and starting with a random simplex.

The different test cases shown in Table 5.2 not only highlights the indifference of the simplex algorithm to reference parameter values but also indicates that even if the reference parameters are close to the boundary of the domain chosen for the optimization, the used NM simplex algorithm with ϵ_{combo} as the objective function is able to successfully identify them.

Table 5.2: Influence of target point in parameter space on the optimized parameter values using ϵ_{combo} as the objective function and $\epsilon_{\text{tol}} = 0.005$. The reference values for each of the parameters are shown in parentheses and the respective bounds chosen for the optimization are shown in brackets.

τ_0 / MPa	τ_{sat} / MPa	h_0 / MPa	ϵ_{combo}
optimized (reference) ; [bounds]	optimized (reference) ; [bounds]	optimized (reference) ; [bounds]	
19.98 (20) ; [10, 40]	63.40 (63) ; [40, 70]	382.0 (400) ; [300, 450]	0.0038
49.60 (50) ; [20, 60]	62.30 (63) ; [40, 70]	416.8 (400) ; [300, 450]	0.0045
30.76 (31) ; [20, 40]	62.50 (63) ; [40, 70]	151.5 (150) ; [60, 300]	0.0040

5.7.7 Prediction of slip system activity

To determine how accurately the slip activity could be captured, the deviation of accumulated shear between the reference parameter simulation (γ_{ref}) and the simulation with optimized parameters (γ_{opt}) is collected from all FE integration points where both accumulated shear values exceeded 1×10^{-4}. This analysis is performed per each of the twelve fcc slip systems for seven different optimized parameter sets as shown in Fig. 5.10. The left column presents these seven constitutive parameter sets, while the right column compares the distribution of the (absolute) point-wise deviation of accumulated shear to the accumulated shear values observed in the reference parameter simulation (excluding points where $\gamma_{\mathrm{ref}} < 10^{-4}$). Gray curves correspond to data on individual slip systems, while the black and red curves represent the overall population across all slip systems.

From Fig. 5.10 it can be inferred that the closer the optimized values are to the target for all three adjustable parameters the better is the slip activity captured. The chosen objective function based on load–displacement and surface topography is rather insensitive to the hardening slope h_0, i.e. the tolerance is met for all seven parameter sets, but h_0 notably influences the slip activities. Thus, including slip mechanics information in the objective function may improve the identification of h_0, however, quantifying individual slip system activity is extremely difficult from real experiments.

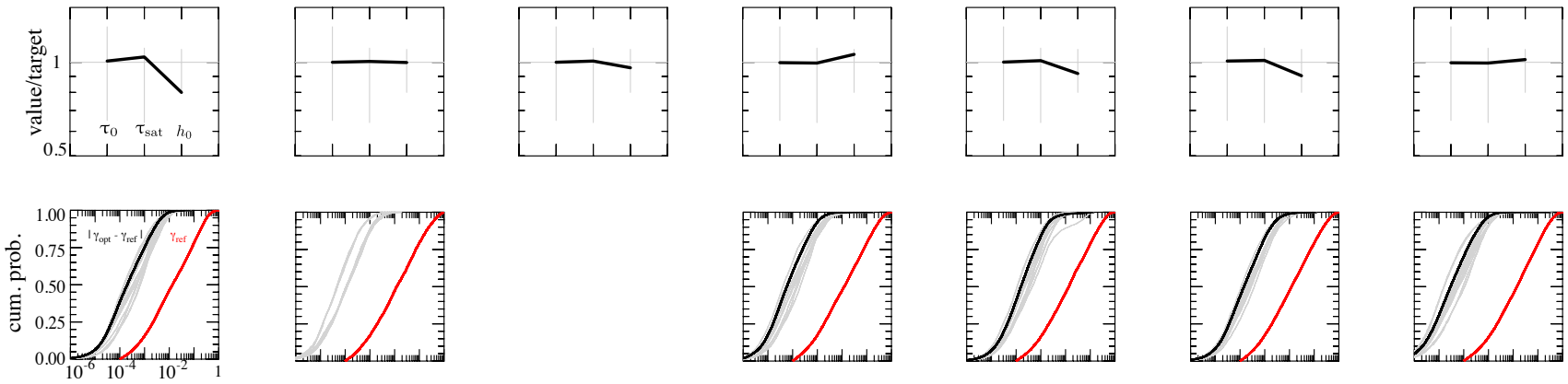

Figure 5.10: Relation between accuracy of slip system response and quality of constitutive parameter identification. Seven sets of optimized parameters (top), each fulfilling $\epsilon_{\text{combo}} \leq 0.005$, sorted by decreasing accuracy, and resulting for the seven crystal orientations shown in Fig. 5.4. Deviation in accumulated shear between simulations using the target (γ_{ref}) and the identified parameters (γ_{opt}) contrasted to the accumulated shear values observed in the reference value simulation (bottom, excluding any $\gamma_{\text{ref}} < 10^{-4}$).

5.8 Discussion

The analysis of reproducibility and robustness for different objective functions reveals a few noteworthy points that are addressed in the following.

The combination of both original objective functions, i.e. $\epsilon_{\mathrm{LD}} + \epsilon_{\mathrm{topo}} = 2\epsilon_{\mathrm{combo}}$, appears to increase the overall steepness of the resulting fitness hypersurface, particularly in the vicinity of the correct parameter set (target). In other words, $\epsilon_{\mathrm{combo}}$ increases faster with "distance" from the target compared to either ϵ_{LD} or ϵ_{topo}. This can be inferred from (i) the generally closer match between the optimized and target values of τ_0 and τ_{sat} observed for $\epsilon_{\mathrm{combo}}$ (Fig. 5.7 right) compared to either ϵ_{LD} or ϵ_{topo} (Fig. 5.7 left and center), in particular at the tightest tolerance (bottom row), and (ii) the consistently larger values of $\epsilon_{\mathrm{combo}}$ compared to either ϵ_{LD} or ϵ_{topo} for (non-converged) solutions that are all comparably far from the target (Fig. 5.8). The latter entails that objective function values of ϵ_{LD} and ϵ_{topo} in local minima are comparable to those found close to the target. Hence, they would fulfill lax tolerances despite being substantially different than the target solution. Correspondingly, $\epsilon_{\mathrm{combo}}$ appears to exhibit a more consistent gradient close to the target point. Moreover, the overall smoothness of the objective function is also likely higher for $\epsilon_{\mathrm{combo}}$ as it balances the oftentimes complementary response of the individual objective functions ϵ_{LD} and ϵ_{topo}.

Another way to interpret the superior performance of $\epsilon_{\mathrm{combo}}$ can be based on the observations made in Figs. 5.9e and 5.9f where, on the one hand, ϵ_{topo} lead to proper identification of the ratio $\tau_{\mathrm{sat}}/\tau_0$, and ϵ_{LD} resulted in a more consistent identification of τ_0. Hence, merging ϵ_{LD} and ϵ_{topo} can be expected to combine both these beneficial attributes, as seems to be indeed the case.

In the course of exploring the parameter space, infeasible points (where the objective function could not be evaluated, i.e., the indentation simulation did not converge) are oftentimes encountered. Nevertheless, the search never terminated due to these obstacles, since the proposed strategy for adjusting the simplex turned out to be successful to continue the search.

The proposed inverse methodology with the modified NM simplex optimization algorithm

appeared to be insensitive to the relative position of the target in the parameter space. This was demonstrated by selecting different values for τ_0, τ_{sat}, and h_0 and performing multiple optimization runs that all resulted in very accurate identification of τ_0 and τ_{sat}, while h_0 exhibited relatively larger scatter.

The choice of using a simulated indentation based on the same constitutive law as used later on for the parameter identification means that, in principle, even an infinitesimal tolerance ($\epsilon_{\text{tol}} \to 0$) can be reached. Figure 5.9c shows examples of stable rates of convergence. However, due to the particular topography of the objective function ϵ_{combo}, i. e. a much higher curvature with respect to τ_0 and τ_{sat} compared to h_0 (a feature comparable to the "Rosenbrock" function), it was not uncommon for the simplex to shrink in size much quicker than approaching the optimum location. Such a relatively small simplex then took many steps to move towards that optimum, hence, the rate of further convergence was notably reduced (not shown in Fig. 5.9c).

In this study, a reasonable tolerance value and number of objective function evaluations are selected owing to the very high computation cost. When comparing the current "computational experiment" with real experimental results, the tightest tolerance achieved in this study ($\epsilon_{\text{tol}} = 5 \times 10^{-3}$) could be extremely challenging since the chosen constitutive description might not be able to capture all aspects that influence the measured load–displacement or surface topography characteristics. On the other hand, a more realistic physics-based constitutive description might enable a closer match between simulation and experimental reference, and, thus, small attainable tolerances.

Concurrently evaluating the responses of two crystallographic indentation directions did not notably reduce the scatter observed in the resulting optimized parameters, in particular with regard to h_0. This is understandable, since virtually any set of τ_0, τ_{sat}, and h_0 identified with one given indentation direction will also fulfill the same objective function tolerance for another indentation direction (see Fig. 5.9g). Hence, the inclusion of this second evaluation does not add sufficiently independent information, but plainly increases the evaluation cost. In case of materials with crystal structures having multiple slip families, such as hexagonal or

tetragonal systems, multiple indentation directions are more likely to yield independent deformation responses since the relative activity among the different slip families typically varies with indentation direction, and hence for those systems choice of crystal orientation(s) would play a more significant role than the present case of fcc materials.

5.9 Summary

Based on the comprehensive analysis performed in this study, it can be concluded that inverse indentation analysis using single crystal nanoindentation is a reliable avenue towards successful identification of material parameters in fcc materials. The sensitivities of the four adjustable parameters of the phenomenological crystal plasticity constitutive law used, τ_0, τ_{sat}, h_0, and a, were indifferent to both crystal orientation and the stress exponent n that characterizes the material flow behavior. A global sensitivity analysis qualitatively revealed the influence of the different constitutive parameters, which then allows to select the most influential adjustable parameters and thus helps to reduce the dimensionality of the optimization problem. Incorporating both load–displacement and surface topography information into an objective function increased the effectiveness of the Nelder–Mead (NM) simplex algorithm to accurately adjust the constitutive parameters. The modification to the NM simplex algorithm proposed in this study appears to be quite effective as it allowed the simplex to overcome infeasible regions in the parameter space. Finally, the indentation response from one crystal orientation turned out to be sufficient in predicting the constitutive parameters τ_0 and τ_{sat} with high confidence, while h_0 had slightly lower confidence. Using these conclusions for more anisotropic crystal structures that have multiple slip families, such as hexagonal commercially available titanium, the reliability of the *IIA* methodology will be taken up in the next chapter Chapter 6.

CHAPTER 6

RELIABILITY OF INVERSE INDENTATION ANALYSES IN HEXAGONAL MATERIALS

6.1 Background

After establishing the reliability of the Inverse Indentation Analysis (*IIA*) for face-centered cubic (fcc) materials with single slip family in Chapter 5, in this chapter this methodology is extended to less symmetric hexagonal materials where multiple slip families can co-activate and in turn can affect the efficacy of this parameter estimation method. For single slip fcc materials the selection of orientation did not have much influence on the output parameters, while for hexagonal materials with different slip family is could dominate (or not) for a particular texture. Hence, it is not unusual to presume that the choice of the crystal orientation to perform this single crystal inverse identification plays an important role. Moreover, for fcc materials, since the objective function for optimization was relatively smooth (convex) the modified deterministic Nelder–Mead simplex optimization algorithm turned out to be efficient, while due to the complexity in the parameter space for hexagonal materials (because of existence of multiple slip families with stark contrast in the slip activities) a hybrid stochastic-followed-by-deterministic optimization algorithm might be better suitable to eliminate infeasible locations in the parameter space.

In this chapter this Inverse Indentation Analysis is tested for exemplary hexagonal material of commercially available titanium (cp-Ti) by considering virtual experimental results as reference. Like for cubic fcc materials in Chapter 5, such virtual experiments provide efficient means to exclusively investigate the reliability of the methodology (since the results are known a priori) while with real experiments there exists additional effects (related to experimental error or shortcoming of the used model) that might affect the result and decrease the efficiency of the methodology. Throughout literature there have been multiple CRSS values of cp-Ti which have been sometimes contradictory Li et al. [2013], thus making it an interesting material to study.

The chapter starts with a brief background about identification of slip parameters in hexagonal materials, Section 6.2, followed by a description of the material model being used to perform the single crystal indentation simulations. Finally, the results of the reliability study is discussed in Section 6.6. It is critical to note that the efficiency of the reliability of the *IIA* methodology is crucial in implementing in even lower symmetric body-centered tetragonal β-Sn that has even higher number of slip families accommodating a deformation (13 available slip families).

6.2 Introduction

Crystallographic slip in hexagonal metals involves a number of geometrically distinct slip families characterized by their slip direction and slip plane, such as basal, prismatic, or pyramidal among which the basal and the prism slip families require much lower shear stresses to slip compared to pyramidal slip systems [Hutchinson, 1977]. Due to the particular hexagonal lattice symmetry, many of those families have only few symmetrically equivalent slip systems (family members). Furthermore, different slip families generally become active at different resolved shear stresses. These intrinsic characteristics render the mechanical processing (rolling, stamping, extrusion) of hexagonal metals technologically much more challenging than for cubic metals such as aluminum or steels. Consequently, substantial effort has and is been devoted to simulate the crystal plasticity of hexagonal metals (and their alloys) with the goal to understand and predict the bulk mechanical response as well as its grain-scale micromechanics [Mayeur and McDowell, 2007, Bieler et al., 2009, Zhang et al., 2010, Yang et al., 2011, Wang et al., 2011, Cheng and Ghosh, 2015, Choi et al., 2012, Hémery et al., 2017, Zhang et al., 2015a, Baudoin et al., 2018]. Thus, the ability to quantify the intrinsic slip resistances becomes crucial in not only the accurate prediction of these single phase materials but also to determine the effect of alloy addition on their plasticity.

A number of methods have been suggested, both experimentally and via simulation, to quantify the so-called critical resolved shear stress (CRSS) at which the different hexagonal slip families become active. A detailed list of such methods can be found in Li et al. [2013] that also

introduced a new methodology to identify the CRSS values of hexagonal systems experimentally by relating the frequency of surface slip trace observations to their theoretical propensity. Zambaldi and coworkers pioneered the idea of iteratively adjusting the CRSS values in a crystal plasticity simulation of single crystal indentation with a conospherical tip until the simulated load–displacement response and remnant surface topography match the corresponding experiment [Zambaldi and Raabe, 2010, Zambaldi et al., 2012]. Herrera-Solaz et al. [2014] obtained single crystal material parameters using a gradient-based Levenberg–Marquardt optimization algorithm that matched stress–strain responses of finite element simulations of a representative volume elements to corresponding experiments with multiple loading conditions. The above two methodologies fall under the class of inverse problems where the proper identification of the CRSS values minimizes the error between the simulated and experimental response. In a more recent study, the plasticity yield parameters (CRSS), in hexagonal Ti-7Al, along with the corresponding evolution of their plastic behavior was investigated both at room temperature and high temperature using far-field high energy X-ray diffraction methods (ff–HEDM) Pagan et al. [2017, 2018]. With such diverse techniques of parameter identification there exists a wide discrepancy in the subsequent reported values of CRSS for the same material, [Li et al., 2013, Wang et al., 2017, Dastidar et al., 2015], thereby decreasing the reliability of such published values. In this chapter the *IIA* methodology, that uses *single crystal* response to identify the CRSS values thereby eliminating the auxiliary effects associated with grain boundaries, precipitates, and crystallographic neighborhood, is used to study it's efficacy for hexagonal materials. The original methodology proposed by Zambaldi et al. [2012] and later modified and studied in detail in [Chakraborty and Eisenlohr, 2017] where its reliability was also established for face–centered cubic materials Chapter 5. As a model hexagonal material, commercially pure titanium (cp-Ti) is analyzed and the possibility of its twinning is neglected to focus exclusively on its slip behavior. Moreover, since comparing actual experimental indentation response with simulation includes the limitations of the underlying crystal plasticity model– the reliability of this methodology is tested against virtual experiments where the expected CRSS values for the

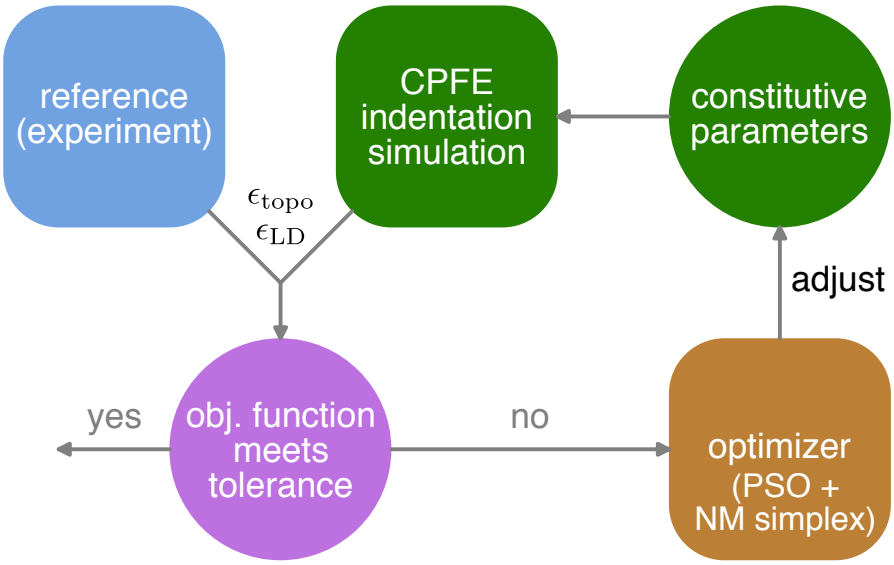

Figure 6.1: Schematic representation of the inverse indentation analysis.

slip families are known a priori.

This chapter starts with a detailed description of the methods, Section 6.3 followed by introducing the concept of virtual experiments in Section 6.4 with the description of the constitutive crystal plasticity model in Section 6.4.1. The reliability study of this method in cp-Ti is detailed in Section 6.6 followed by discussion about some of the concerns regarding the methodology.

6.3 CRSS values from surface topography and instrumented indentation

The CRSS values for different slip families are inversely predicted by comparing the experimental and crystal plasticity finite element (CPFE) simulated single crystal nanoindentation(s) responses with a spheroconical indenter. This Inverse Indentation Analysis (*IIA*) methodology (shown schematically in Fig. 6.1) is associated with an objective function, where the CRSS values are the adjustable parameters for optimization, and an optimization algorithm that minimizes the objective function with the optimum point being the predicted solution for the CRSS values with this methodology. Generally, from indentation tests two major outputs are obtained– the load–displacement response and the subsequent surface topography. It has been estab-

lished in Chapter 5 and in Chakraborty and Eisenlohr [2017], that combining both the load–displacement results with the surface topography provided a better chance of accurately identifying the parameters for the optimizer. Hence, in this study as well, a weighted summation of the error in the load–displacement ϵ_{LD} and surface topography ϵ_{topo} between the simulated and the reference data is used to define the objective function. The chosen weights being 0.3 for ϵ_{LD} and 0.7 for ϵ_{topo}. The choice of giving more weightage to the error in surface topography is based on the assumption that the slip behavior is reflected more significantly (and non-uniquely) in the surface pile–up topography as compared to the load–displacement. Moreover, in this work a hybrid optimization algorithm is used to minimize the objective function constituting at first a stochastic particle swarm optimization(pso) followed by the deterministic Nelder–Mead simplex (NM) to minimize the objective function. The idea behind such a selection is to ensure proper exploration and exploitation of the parameter space, in that, the stochastic algorithm ensures a higher exploration while the deterministic algorithm is a better exploiter.

6.4 Virtual experiments

In the context of this paper, virtual experiments relate to the procedure of generating experimental data with simulations with a priori known parameters. Herein we employ crystal plasticity simulations, that take into account the texture influence of the material, to simulate the material response after single crystal nanoindentation(s). Performing such a virtual experimental analysis is beneficial in determining the reliability of a methodology since the solution is known a priori which leads to proper quantification of the error between the actual solution and the prediction by exclusive consideration of methodology without the influence of other factors (such as precipitates, grain boundaries, inclusions, etc.). The crystal plasticity simulations are performed using the material solver in DAMASK and using the commercially available finite element boundary value problem solver MSC Marc–Mentat. The numerics of the crystal plasticity finite element simulation is the same as that discussed in the previous chapter Chap-

ter 5. The constitutive material description and the geometry used in this study is discussed next.

6.4.1 Constitutive material model

The model framework is based on the finite strain deformation theory where total deformation gradient,$\mathbf{F}$,

$$\mathbf{F} = \mathbf{F}_\mathrm{e}\mathbf{F}_\mathrm{p} \tag{6.1}$$

is multiplicatively decomposed into plastic and elastic components ($\mathbf{F}_\mathrm{e}$ and $\mathbf{F}_\mathrm{p}$, [Lee, 1969]). The relation between plastic deformation gradient $\mathbf{F}_\mathrm{p}$ and the plastic velocity gradient $\mathbf{L}_\mathrm{p}$ is given by the flow rule:

$$\dot{\mathbf{F}}_\mathrm{p} = \mathbf{L}_\mathrm{p}\mathbf{F}_\mathrm{p} \tag{6.2}$$

The plastic velocity gradient

$$\mathbf{L}_\mathrm{p} = \sum_\alpha \dot{\gamma}^\alpha \, \mathbf{s}^\alpha \otimes \mathbf{n}^\alpha \tag{6.3}$$

is additively composed from crystallographic slip at rates $\dot{\gamma}^\alpha$. The unit vectors $\mathbf{s}^\alpha$ and $\mathbf{n}^\alpha$ align with the slip direction and slip plane normal of each slip system $\alpha = 1,\ldots,N$, with N indicating the number of total slip systems across all considered slip families. The resolved shear stress

$$\tau^\alpha = \mathbb{C}\left(\mathbf{F}_\mathrm{e}{}^\mathrm{T}\mathbf{F}_\mathrm{e} - \mathbf{I}\right)/2 : \mathbf{s}^\alpha \otimes \mathbf{n}^\alpha \tag{6.4}$$

is the driving force for slip, where $\mathbb{C}$ denotes the (fourth-order) tensor of elasticity.

Crystallographic slip is commonly modeled based on the phenomenological constitutive description pioneered by Peirce et al. [1982]. In that model, which is also used for this study, the dislocation defect structure is parameterized in terms of a stress g^α that resists slip on system α. This critical resolved shear stress evolves in the course of slip as [Hutchinson, 1976]

$$\dot{g}^\alpha = \sum_\beta q^{\alpha\beta}\, h_0 \left|1 - \frac{g^\beta}{g_\infty}\right|^a \mathrm{sgn}\left(1 - \frac{g^\beta}{g_\infty}\right)\left|\dot{\gamma}^\beta\right|, \tag{6.5}$$

with initial hardening slope $h_0 = 200\,\text{MPa}$, hardening exponent $a = 2.0$, and saturation slip resistance $g_\infty = 300, 200$, and $300\,\text{MPa}$ for basal, prism, and pyramidal $\langle c+a \rangle$ slip families respectively, neglecting the slip on the pyramidal $\langle a \rangle$ planes (as was also done in Zambaldi et al. [2012]). For the current virtual runs $q^{\alpha\beta}$ is selected as 1 for both self hardening($\alpha = \beta$) and latent hardening ($\alpha \neq \beta$). Crystallographic slip occurs at rates

$$\dot{\gamma}^\alpha = \dot{\gamma}_0 \left| \frac{\tau^\alpha}{g^\alpha} \right|^n \operatorname{sgn}\left(\tau^\alpha\right), \tag{6.6}$$

with reference shear rate $\dot{\gamma}_0 = 0.001\,\text{s}^{-1}$ and stress exponent $n = 20$. The kinematics of the material solver outlined above are implemented as part of the open source simulation toolkit "Düsseldorf Advanced Material Simulation Toolkit" (DAMASK) [Roters et al., 2012] which is coupled with the commercial finite element solver MSC Marc to solve the single crystal indentation boundary value problem.

For this inverse analysis the initial value of the g for the three slip families, basal, prism, and pyramidal $\langle c+a \rangle$ (which are the most observed slip families in cp-Ti), are considered as adjustable parameters for optimization with a three-dimensional parameter space. Pyramidal $\langle a \rangle$ slip and twin is neglected to reduce the dimensionality of the problem, while other adjustable parameters of the model such as g_∞ of each family, initial hardening slope h_0, exponents n, and a are all fixed due to their lower sensitivity to the objective function as demonstrated in the previous chapter in Section 5.6.4.

6.4.2 Virtual indentation

The crystal plasticity finite element (CPFE) indentation simulations are performed using commercial software Marc 2013.1(MSC Software Corporation, Newport Beach, CA) and using the material model in DAMASK that is interfaced through the material subroutine "hypela2" on compute servers maintained by the Division of Engineering Computing Services at Michigan State University. The model geometry, shown in Fig. 6.2, consists of 19980 hexahedral elements and 22693 nodes with dimensions of 8 µm x 8 µm x 4 µm. Furthermore, the region close to the in-

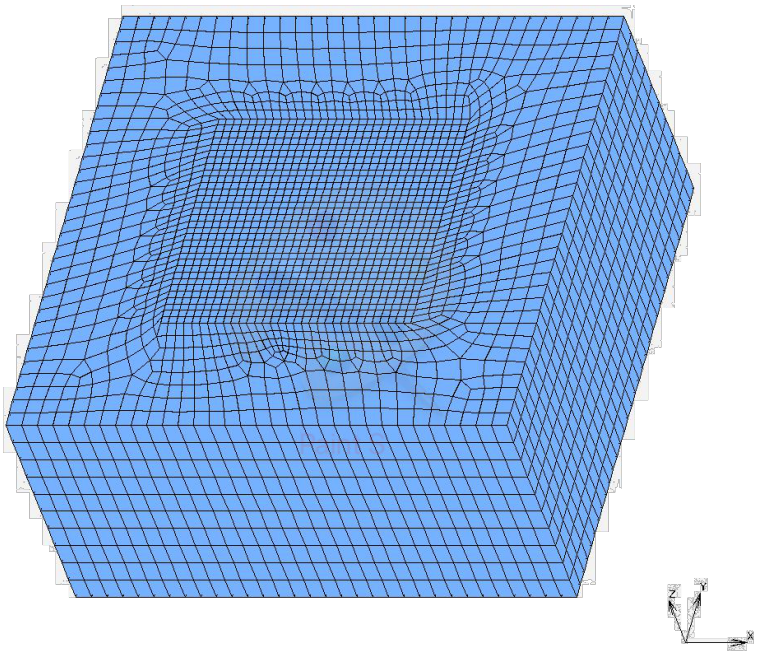

Figure 6.2: Geometry generated in Marc-Mentat to perform the indentation simulations.

denter is finely discretized since it experiences the most deformation. The nodal displacements are fixed on the bottom and outer surfaces. Indentation is performed to a depth of 0.3 µm with a rigid spheroconical indenter of tip radius 1 µm with a cone angle of 90° and no contact friction is considered between the indenter and the substrate. The vertical displacement of the rigid indenter to 0.3 µm is done in 10 seconds discretized into 800 equal increments. Additionally, to reduce the computation time, the geometry is decomposed into four equal domains (i.e., sectors of 90° each) within Marc and then simulated.

6.5 Hybrid optimization algorithm

As mentioned previously the inverse analysis uses a hybrid optimization algorithm that is written in Python. The two algorithms being used are the initial stochastic particle swarm optimization (pso) algorithm described in [Eberhart and Shi] and a modified version of the deterministic Nelder–Mead (NM) simplex algorithm as used in Chakraborty and Eisenlohr [2017]

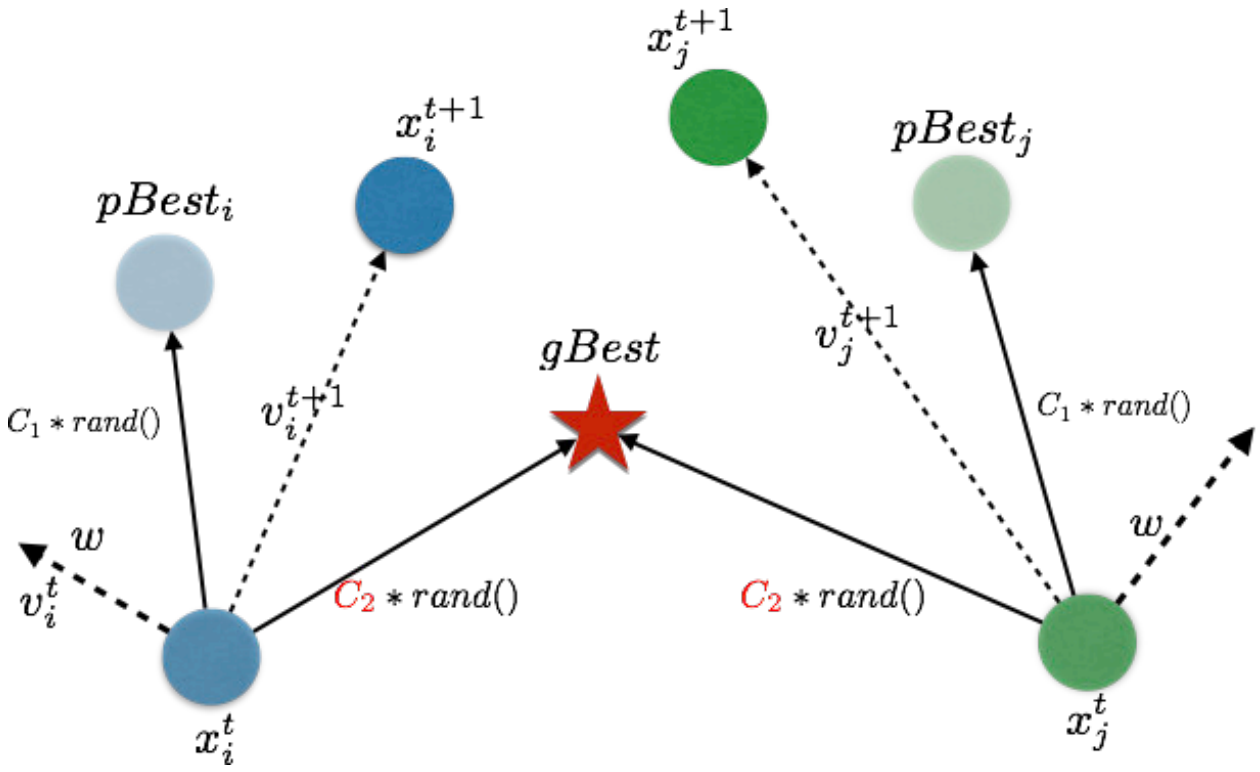

Figure 6.3: Illustration of the stochastic particle swarm optimization algorithm being used in this study for *IIA*.

and initially introduced by Nelder and Mead [1965].

The NM simplex method have also been introduced in detail in previous chapter Chapter 5, and the same is used in this study as well (same value of the algorithm parameters). The reason for choosing this deterministic NM simplex method is two fold– first it is easy to implement, and secondly it is a gradient free method which is highly beneficial since calculation of gradients for such a non-linear FE problem is computationally extremely expensive. The stochastic pso algorithm used in this study uses set of algorithm parameters as suggested by Eberhart and Shi. In this algorithm the trajectory of a particle in the population is governed by two attractors – i) global best position of the particle in the population; and ii) particle's own best position as illustrated in Fig. 6.3. This allows efficient exploration of the parameter space before closing towards the (global) optimum solution. For the i^{th} particle in a D-dimensional space represented as $X_i = (x_{i1}, x_{i2}, \ldots, x_{iD})$ and with the best previous position (position with it's best fitness) given by $P_i = (p_{i1}, p_{i2}, \ldots, p_{iD})$, and with the global best position (position of the global

best fitness) being P_g, the velocity of the particle i, V_i, and their subsequent position $X_{i,new}$ are then given as:

$$V_i = w * V_i + c1 * \text{rand}() * (P_i - X_i) + c2 * \text{rand}() * (P_g - X_i) \tag{6.7}$$

$$X_{i,\text{new}} = X_i + V_i \tag{6.8}$$

$$\tag{6.9}$$

$c1$ and $c2$ are acceleration and are set to 1.2 in this study with w being the inertia weight that was set to 0.3. the rand() are functions generating random numbers between (0,1). The maximum velocity in each direction was also restricted to 75 % in that dimension. It is important to note that the choice of these parameter values are based on a general thumb rule, since due to the high computation cost of each CPFE calculation a parameter sensitivity study is impractical, and hence avoided. Moreover, due to this high computation cost the total number of particles in the population is restricted to 10 (for the current three dimensional problem), which is low and hence an exhaustive exploration is not possible, however, having the subsequent deterministic run did achieve results close to the global minimum as will be shown later.

Another critical aspect of this inverse problem is the present of infeasible regions in parameter space, or combinations of parameter values for which the CPFE simulation fails to converge. For the pso algorithm, whenever such an infeasible point is obtained a very high penalty of 1×10^{10} is returned thereby causing a large penalty in that location. This is possible since the stochastic pso does not rely on the exact value of the fitness to proceed. While for the deterministic NM simplex algorithm where the exact value of fitness is needed to proceed, the algorithm averts any infeasible point by reflecting it about the center of gravity of the current simplex as explained in Section 5.6.2 and also published in Chakraborty and Eisenlohr [2017].

The tolerance for deciding the optimum is set to 2×10^{-2} along with an additional termination criterial of a maximum of 100 FE evaluations for each of the optimization algorithm. The tolerance of 2×10^{-2} is decided such that it is strict enough to capture the relative activity of the different slip families to give a unique solution of the optimization (with respect to the

reference), while lax enough to not require very high FE runs (more than 100). The initial population of 10 particles for the pso algorithm is selected randomly from a domain of 10 MPa to 400 MPa for all the three slip families, while the initial simplex for the deterministic NM simplex algorithm with four points (corresponding to the vertices of the four dimensional simplex in the current problem) is constructed by a random selection from the optimized (final) pso population. Random selection for generating the NM simplex is suitable since the optimized pso population is less scattered and more concentrated in the feasible region in the parameter space. Furthermore, similar to Chakraborty and Eisenlohr [2017], the parameter domain is converted to a unit domain to exclude influence of individual values of the parameters.

6.6 Reliability of inverse indentation analysis

The advantage of using virtual experiments to predict the reliabilities of the different methodologies of prediction of CRSS values is the a priori knowledge of the expectation—hence a fair comparison can be done between the predicted CRSS and the target/expected/input CRSS. The reliability of the *IIA* methodology is assessed based on six different single crystal orientations and for two different CRSS input values.

6.6.1 Selecting orientations for performing the Inverse Indentation Analysis

A key aspect for hexagonal (or other low symmetry materials) is the presence of multiple slip families to accommodate a deformation, hence, any (randomly) selected orientation may not be sufficient in capturing the activity from all the slip families, thereby making some of the slip families less sensitive to deformation. Thus, an effective selection of crystal orientation to perform the *IIA* in hexgonal cp-Ti is crucial to enable the optimizer to accurately identify the slip parameters for all the slip families. Previously, such a consequence was averted by considering all orientations together in [Zambaldi et al., 2012], however, this dependence was not explicitly addressed.

In this study, the relative sensitivities of different slip families(i.e. basal, prism, and pyrami-

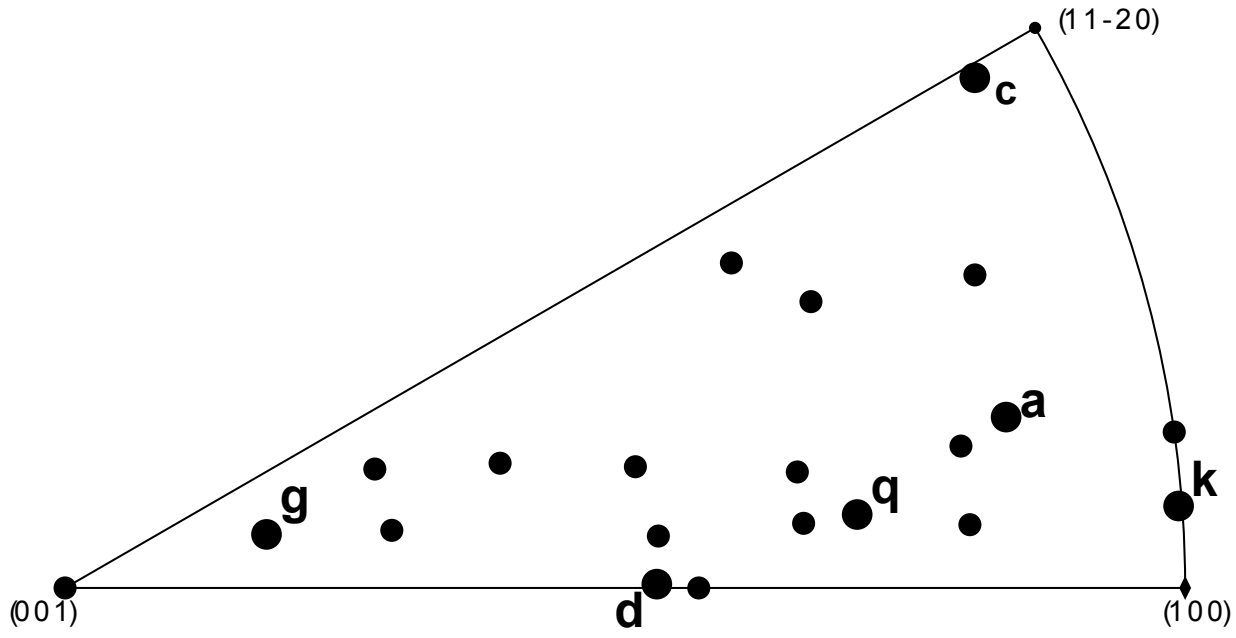

Figure 6.4: Different crystal orientations used to perform the sensitivity analysis in hexagonal cp-Ti.

dal $\langle c+a \rangle$) for different crystal orientations selected from the standard stereographic triangle of hexagonal cp-Ti, shown in Fig. 6.4, is qualitatively analyzed by calculating the change in the combined load–displacement and surface topography responses for a change in the CRSS values for the different slip families for the different crystal orientations.

This sensitivity analysis is performed using a modified method of elementary effects originally proposed by Morris [1991] and modified by [Chakraborty and Eisenlohr, 2017]. The method is also outlined in the previous chapter in Section 5.6.4, where it was used to identify the most sensitive adjustable parameters of the phenomenological power law being used to describe the material behavior. This method essentially provides a efficient way of calculating the derivative of the output function (load–displacement and topography response) with respect to a change in input parameter (CRSS) in a high dimensional space. The efficiency is in selecting relevant points in the parameter space. The sensitivity of a crystal orientation to different slip families' CRSS (parameters) is then calculated by taking the mean of absolute sensitivities for the different parameters for the crystal orientation. It is important to note that such a method is a qualitative estimation of the relative sensitivities and provides a guidance in making an ef-

fective choice of crystal orientations to perform the *IIA*. In this study the sensitivity analysis is performed for all the orientations shown in Fig. 6.4 for the basal, prism, and pyramidal $\langle c+a \rangle$ slip families within the bounds of [50 – 500 MPa] for all the three families. The resulting sensitivities is shown qualitatively in Fig. 6.5 for the three different families (blue – basal; red – prism; and orange pyramidal $\langle c+a \rangle$). The location of the circles correspond to the crystal orientation for which the analysis is done, while the diameter of the circle represents the sensitivity of the particular slip family. Thus, for a crystal orientation having a higher sensitivity for the basal slip family (meaning basal slip systems are dominant in determining the deformation response for that crystal orientation) it would be having a larger circle compared to those of the other slip families at the same location. The importance of performing such an analysis is the underlying assumption that orientation for which a particular slip family is highly sensitive (dominant slip mode; larger circle), the optimization algorithm will have a better chance of accurately predicting the CRSS value of that family when the particular orientation is selected for optimization. Based on the above assumption, a hypothesis can be proposed that states that the crystal orientations where all the slip families are highly sensitive to all the three slip families should be selected to perform the *IIA* for accurate predictions of the adjustable parameters (CRSS) with the least computation time.

6.6.2 Results

To test this hypothesis, six (arbitrary) different crystal orientations are selected, and the reliability of the *IIA* for predicting CRSS values for the three different slip families considered (i.e. basal $\langle a \rangle$, prism $\langle a \rangle$, and pyramidal $\langle c+a \rangle$) is evaluated for two different sets of input CRSS values. The results thus obtained are listed in Table 6.1. As mentioned earlier, the Inverse Indentation Analysis in this study uses a hybrid optimization algorithm with first a stochastic particle swarm optimization (pso) followed by the deterministic NM simplex method. In Table 6.1 the best parameters (global best) obtained after the initial pso run is shown in columns 6, 7, 8, while the final predicted parameters, CRSS, of the optimizer after

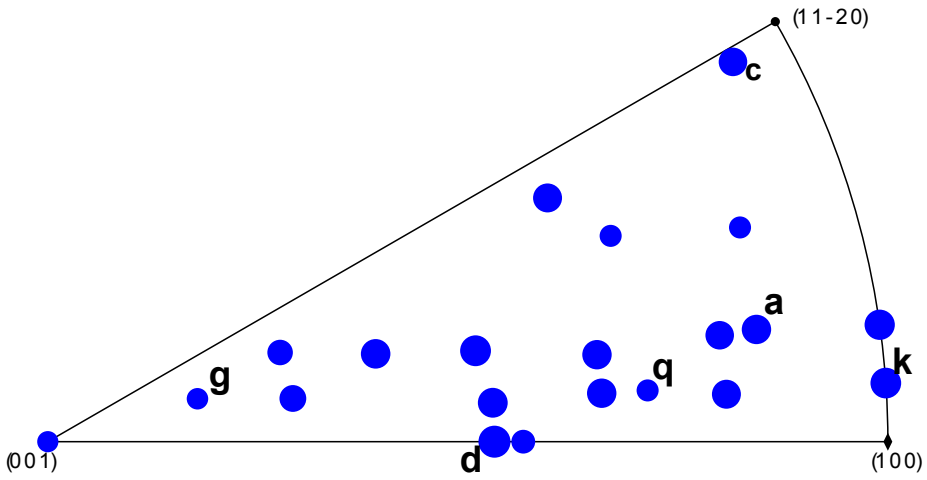

(a) basal $\langle a \rangle$

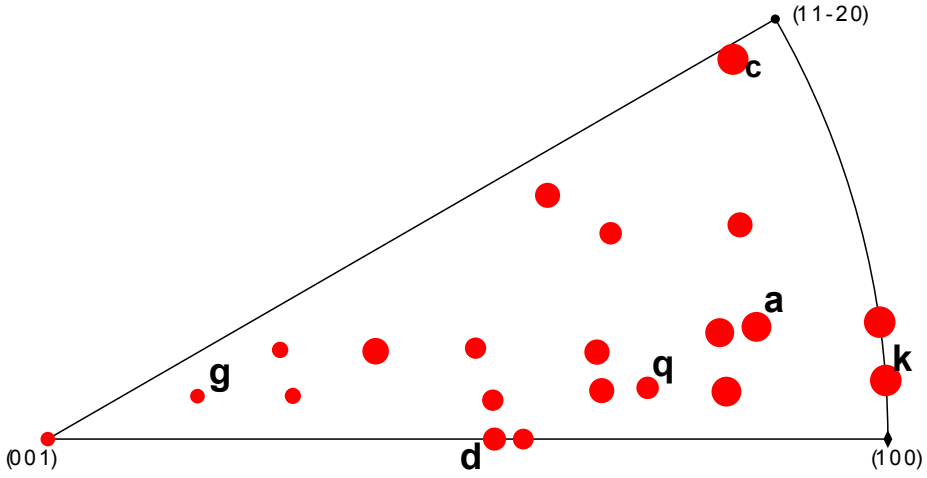

(b) prism $\langle a \rangle$

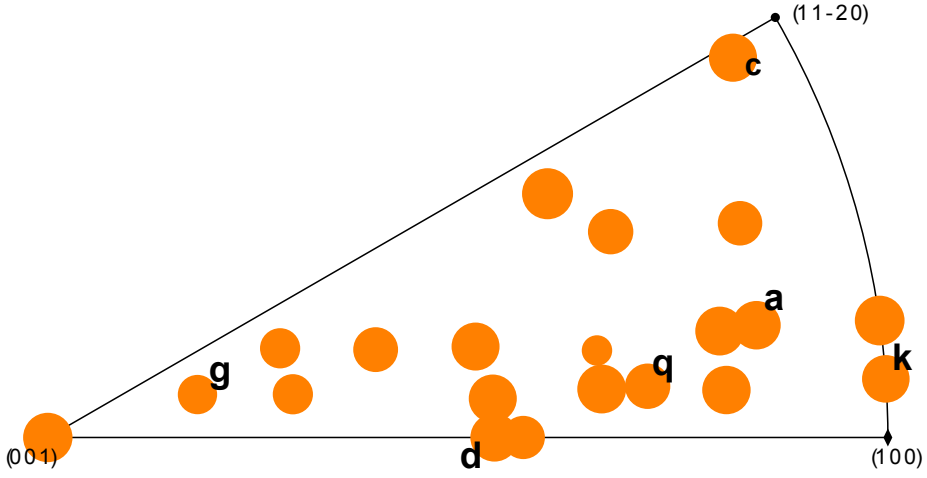

(c) pyramidal $\langle c+a \rangle$

Figure 6.5: Sensitivity of different crystal orientations to deformation on different slip families as represented by the radius of the circles.

the subsequent NM simplex algorithm is shown in columns 10, 11, and 12, for each of the three slip families of basal, prism, and pyramidal $\langle c+a \rangle$ respectively labelled as “basal", “prism" and “pyrCA" in Table 6.1. Rows 2, 3, and 4 shows the sensitivity values for the basal, prism, and pyramidal $\langle c+a \rangle$ slip families respectively based on the sensitivity analysis discussed in the previous section and illustrated in Fig. 6.5. In Fig. 3.11, the first column shows the six single crystal orientations for which the reliability study was done, moreover, the table is divided into two sections – the top six rows shows the *IIA* results with a reference parameter of [80, 110, 180] MPa corresponding to basal, prism, and pyramidal $\langle c+a \rangle$ slip families respectively; while for the bottom six rows the optimization results with a reference parameter of [120, 60, 180] MPa for the three slip families. The reason for choosing such references is based on the fact that in the former case the two most active slip families in cp-Ti, basal and prism, have their CRSS values very close to each other (i.e., 80 and 110 MPa) while for the latter case these values are far apart (i.e., 120 and 60 MPa). Hence, it can be presumed that for the former reference CRSS case where the basal and prism slip families have comparable values, the task of accurately identifying the basal and prism CRSS values is more difficult since both basal and prism systems can lead to the final deformation response at similar global stress state (due to their close activation values) as compared to the latter reference CRSS case. Moreover, the two reference CRSS conditions also represents two classes of hexagonal materials – one (like cp-Ti, c/a ratio less than 1.6333) where the prism is more active than basal; and others (like Ti525, c/a ration greater than 1.6333) where basal is more active than prism slip, thereby further highlighting the efficacy of the *IIA* methodology.

It can also be noticed from Table 6.1 that for both CRSS reference, the final optimized parameters are close to the expected reference for most of the six orientations except orientation “g". Also, in almost all runs (for both reference CRSS references) the optimization proceeded to the subsequent NM simplex run after the initial pso, except for crystal orientation “d" for CRSS reference [120, 60, 180] MPa, where the tolerance of 2×10^{-2} is achieved in the pso step. As can bee seen from the results, such a relatively lax tolerance selected for the current hexagonal

material study, as compared to that set in fcc materials, is strict enough for the predicted parameters to be unique and close to the global minimum (reference CRSS values highlighted in bold in Table 6.1). For the reference input CRSS of [80, 110, 180] MPa corresponding to basal, prism, and pyramidal slip families, the tolerance of 2×10^{-2} is not satisfied for orientations “a", “c", and “q" (apart from “g"). Among the three, for orientations “a" and “c" the NM simplex optimization reached the maximum allowable FE calculations of 100 thereby leading to the termination of the optimization, while for orientation “q" the simplex converged prematurely to a local minimum. For the reference input CRSS values of [120, 60, 180] MPa corresponding to basal, prism, and pyramidal slip families, the tolerance is not achieved for orientation “c" (apart from “g") because the simplex converged prematurely to a local minimum.

Table 6.1: Results of the *IIA* analysis performed for six different crystal orientations labelled in Fig. 6.4 for two different reference **input** CRSS.

Orientation	sensitivity			PSO results				NM results			
	basal	prism	pyrCA	fitness	basal	prism	pyrCA	fitness	basal	prism	pyrCA
80,**110**, **180**											
a	0.43	0.44	0.872	0.1909	165.97	68.47	260.56	0.047	83.06	104.55	179.22
c	0.41	0.47	0.864	0.1736	168.04	66.7	238.7	0.034	81.14	118.1	196.1
d	0.49	0.284	0.865	0.2555	42.7	172.7	330.8	0.007	81.9	110.3	179.3
g	0.247	0.089	0.66	0.1533	400.0	132.6	110.56	0.1533	400.0	132.6	110.56
k	0.46	0.48	0.85	0.153	113.67	93.15	282.4	0.0164	80.0	114.17	187.63
q	0.45	0.48	0.90	0.1161	100.3	100.4	219.4	0.0233	81.31	116.7	192.1
120,**60**, **180**											
a	0.43	0.44	0.872	0.09	168.31	32.91	300.67	0.019	129.7	57.1	185.0
c	0.41	0.47	0.864	0.106	144.5	44.8	394.5	0.098	154.7	38.6	399.0
d	0.49	0.284	0.865	0.004	120.3	60.6	181.1	x	x	x	x
g	0.247	0.089	0.66	0.1441	370.0	68.2	117.1	0.1441	370.0	68.2	117.1
k	0.46	0.48	0.85	0.0325	127.8	53.7	200.2	0.019	129.4	56.0	187.0
q	0.45	0.48	0.90	0.1932	236.7	29.8	269.1	0.012	113.8	61.1	173.6

6.7 Discussion

The intermediate optimum obtained after the stochastic pso algorithm (shown in columns 6, 7, 8 in Table 6.1) shows the limitation of the pso algorithm in achieving the fitness tolerance (of 2×10^{-2}) for most orientations. However, for both reference CRSS runs, the inverse analysis is able to approach the target after the deterministic optimization algorithm for most of the crystal orientations studied (shown in columns 10, 11, 12 in Table 6.1). This is not unexpected, since, the pso algorithm is used to efficiently explore the parameter space in order to identify a feasible region. Moreover, the population size is also quite small (i.e., 10 particles) which also reduces the efficacy of the pso algorithm.

In both cases, the optimization solution is significantly different from the target for the crystal orientation labelled “g" that also has the least sensitivity for all three slip families as compared to the sensitivities of the slip families for all the other five orientations, illustrated and labelled in Fig. 6.6.

As mentioned in the previous section, for some of the orientations in both reference CRSS runs, the tolerance was not met (apart from orientation “g") in the specified number of FE runs. However, the relative influence of each of the slip families is qualitatively captured for all of these orientations that had high sensitivities for all the slip families compared to orientation “g" (where the optimization failed). It is also interesting to note that for the orientations where the objective function tolerance of 2×10^{-2} is met, the optimized values are within 7 % error of the target values, indicating the effectiveness of the chosen tolerance. Thus, the initial hypothesis about selecting crystal orientations where *all* the three slip families are highly sensitive for performing this inverse analysis with the proposed hybrid optimization algorithm appears to be a good one in accurate and reliable estimation of those CRSS values. Therefore, such a methodology can now be used in even lower symmetric body-centered tetragonal Sn to identify its plasticity parameters.

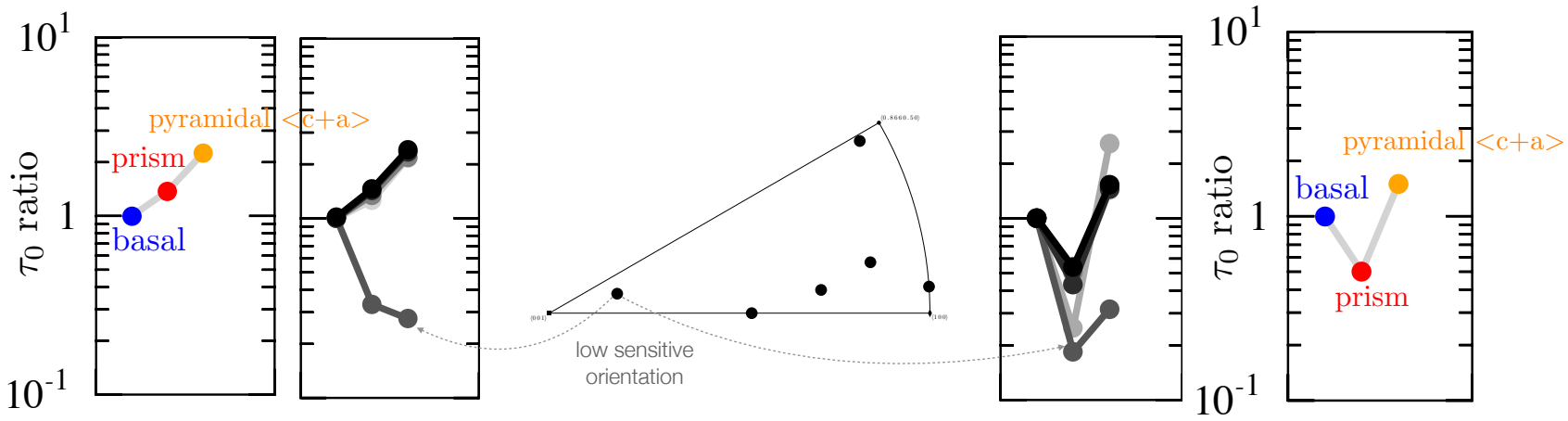

Figure 6.6: Resulting CRSS values for all the six single crystal indentations for the two different reference CRSS.

6.8 Summary

An important challenge for identification of CRSS values for the different slip families using single crystal orientations is the selection of the crystal orientation(s). Most often, a bunch of orientations are selected and used to minimize the error between the simulated and reference responses (load–displacement and/or topography), however, for them the initial guess for the optimizer and/or the parameter bounds are selected based on some a priori knowledge, [Zambaldi et al., 2012]. In this study an attempt was made to design a methodology that would not require any a priori information about the CRSS values and could reach the target solution with a significantly large parameter bounds, close to a black box optimization. To establish the reliability of such an approach, virtual simulations were used as experimental reference (with known CRSS values) and the inverse analysis was employed to see whether the input CRSS can be obtained after final minimization.

The challenge of selecting proper orientation is tackled by selecting an orientation whose indentation response is highly sensitive for all the slip families. From the results of the inverse indentation analysis performed in this study for six different crystal orientations, Table 6.1, it is observed that for the orientation that is least sensitive (“g") for all the three slip families, the optimization algorithm failed to converge to a feasible region (region close to the target) in the parameter space. This is expected since lesser sensitivity implies lesser influence of the parameters on the selected objective function value. For the other five orientations with relatively higher sensitivities, the optimized solution is very close to the target. However, it is important to note that with the selected parameter values for the *IIA* framework (specified tolerance, optimization parameters, and maximum allowable function evaluations) the simplex sometimes converges to a local minima even for high sensitive orientations and the tolerance is not met (“a", “c", “q"). However, even for such cases the relative influence of each of the slip families (CRSS values) is qualitatively captured and it can be predicted that these local minima are in a feasible region in the parameter space and is close to the global minimum (the target solution). Also, it appears that instead of considering multiple crystal orientations in parallel for mini-

mization, using a few high sensitive single orientations separately, is sufficient to conclusively predict the relative slip system resistance of the different slip families for hexagonal materials.

Thus, having established the reliability of the proposed Inverse Indentation Analysis for fcc and hexagonal materials based on orientation selection after performing a sensitivity analysis, this proposed methodology can now be used to identify plasticity parameters for β-Sn and provide even higher fidelity simulation results.

CHAPTER 7

CONCLUSIONS AND FUTURE WORK

7.1 Conclusions

In this thesis a multi-physics fully coupled chemo-thermo-mechanical model in a crystal plasticity continuum mechanical framework is established to investigate the stress-driven diffusion of Sn atoms in tin films undergoing thermal straining, in order to understand the governing factors for the process of whisker nucleation and their subsequent kinetics. Through the initial thermo-mechanical model outlined in Chapter 3, the dominant role of film texture on the grain boundary hydrostatic stress distribution (that solely modulates the atom transport in the film) is established as compared to grain geometry and grain size distribution. It is also predicted from the thermo-mechanical simulations that there lacks any long range spatial gradients in stresses that would promote long-range diffusion thereby re-enforcing the notion that the whisker nucleation process is indeed a local phenomenon. Due to the localized nature of the current problem, it is possible to investigate a reduced geometry for the more involved chemo-thermo-mechanical model discussed in Chapter 4. With the preliminary results from the fully coupled simulations, it can be inferred that the kinematic consequence of atom redistribution has a negligible effect on the film stress relaxation as compared to the plasticity. Moreover, such a kinematic consequence of atoms diffusing from a region of high compression to a region of low compression along the grain boundary network is most pronounced in the hydrostatic stress values and has minimal effect on the shear and normal traction components for the studied microstructure. However, adding the kinematics due to transport indeed reduces the stresses, as compared to the case where no diffusional kinematics is considered. Finally, it is also established that the plastic anisotropy of β-Sn plays an important role in the mechanics, thereby making the use of simple isotropic models insufficient and requiring the establishment of accurate description of the complex plastic behavior observed in β-Sn.

In that regard, an Inverse Indentation Analysis based methodology is investigated in Chapter 5 to identify such constitutive parameters for crystal plasticity material models by minimizing the error between experimental and simulated single crystal nanoindentation response. For such an inverse methodology it is established that using combined load–displacement and surface topography error proved to be a reliable objective function for minimization with a modified Nelder–Mead simplex optimization algorithm. The reliability of this methodology is first established for face-centered cubic materials where it is concluded that the initial flow stress could be accurately identified with negligible error, followed by the saturation stress, and the hardening slope, which is also reflective of their sensitivities to the objective function. Moreover, for fcc materials selecting any random crystal orientation for the inverse analysis proved to be effective in the parameter estimation. Such a flexibility of selecting any random orientations is not possible for low symmetry crystals structures such as hexagonal or body-centered tetragonal. Hence a more intelligent choice of orientation selection for low symmetry materials is proposed in Chapter 6, where first a sensitivity analysis is performed for different regions in the orientation space for the different slip families, and then those orientations are selected where all the considered slip families are sensitive to the indentation loading condition. The reliability of this proposed sensitivity based Inverse Indentation Analysis is established for exemplary hexagonal commercially pure titanium with a hybrid optimization algorithm. Using the hybrid algorithm allowed first an exploration of the parameter space, by using stochastic particle swarm optimization, as well as a final exploitation of a feasible region by deterministic Nelder–Mead simplex algorithm. Having established the reliability of this sensitivity based *IIA* for hexagonal materials with two different reference parameters, this method can then be employed to estimate the plastic parameters (initial flowstress values) of β-Sn.

Additionally, from a technical standpoint, the multi-physics model developed in this work could be easily translated to study other processes involving stress-driven diffusion with additional terms in the field equation– such as stress-corrosion cracking. Moreover, the inverse optimization code developed in this work could be used as a general toolkit for any optimiza-

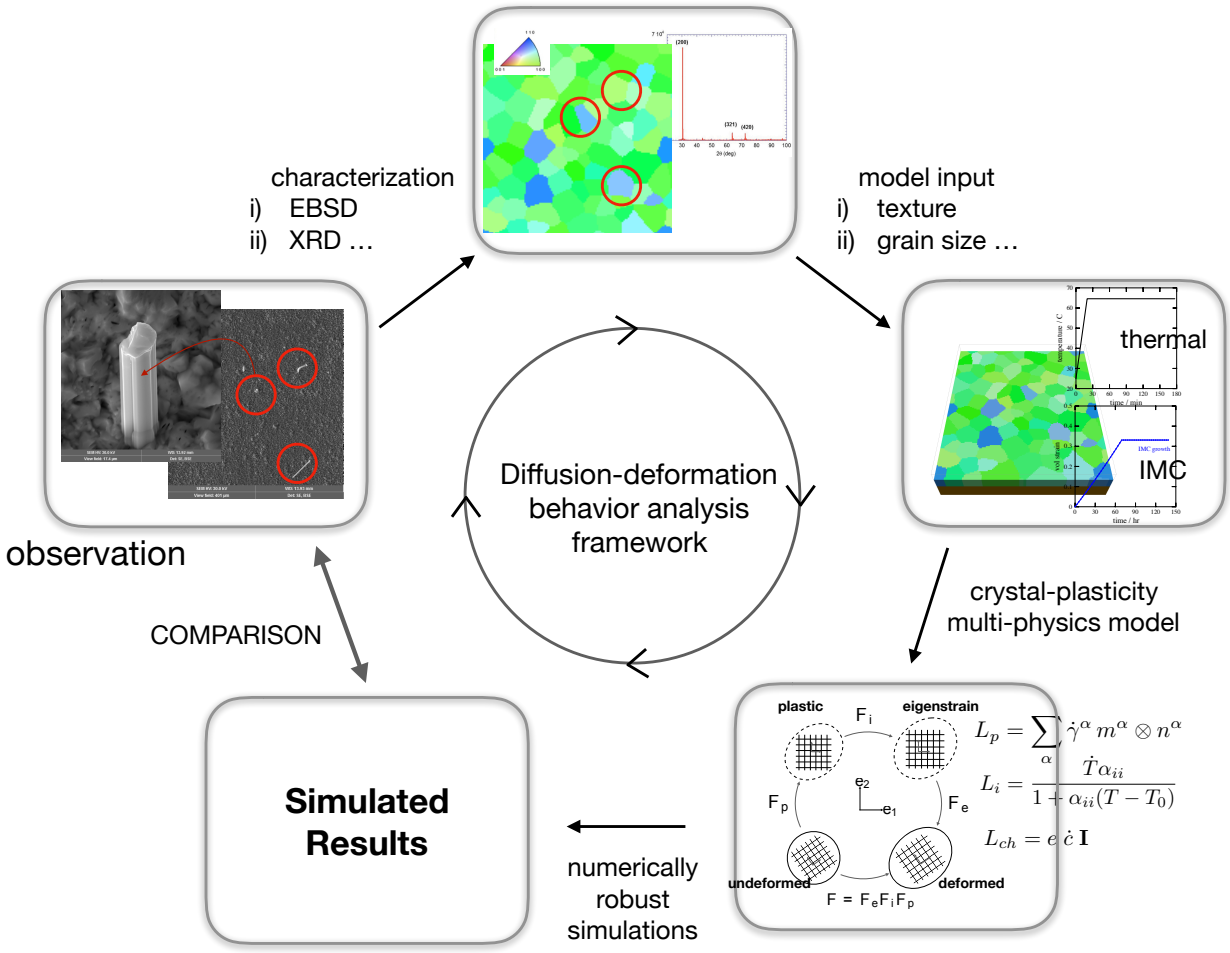

Figure 7.1: Proposed structure for identifying what conditions in the tin film microstructure cause a grain to form a whisker.

tion problem due to its modular structure [Maiti et al., 2018].

7.2 Future work

The ultimate goal of this work is to answer the question of which grains in the tin film microstructure would nucleate whiskers so that we can propose an effective way of whisker mitigation and prevent device failure due to their formation. Figure 7.1 outlines the overall workflow for identification of such grains, where input of the microstructure information for the films using experiments, either electron back scatter diffraction (EBSD) data for grain structure or X-ray diffraction data for overall texture, and feed into the continuum mechanical cou-

pled chemo-thermo-mechanical model in the crystal plasticity framework to simulate the kinetics and stress variation. Subsequently, a one-to-one comparison between the grains where whiskers are observed to grow experimentally with their corresponding stress-state and plastic accommodation from the full-field simulations will help in narrowing the crystallographic governing factors modulating the whisker nucleation process. In an ideal scenario the comparison should be done against the cases where whiskers grow due to Cu_6Sn_5 formation (Sn films deposited on copper or brass substrate) since they are the most common. However, due to the complex state of stresses (and loading condition) it becomes very tricky to draw confident conclusions by comparing experimental observations to simulated results from Cu_6Sn_5 growth boundary conditions. In contrast thermal straining provides a direct comparison between the experiment and simulation, and more practical conclusions can be drawn.

A critical step for having simulation data consistent with the reality is to have an accurate material description of the system. A significant foundation to achieve this has already been laid in this thesis, along with some immediate future work. First and foremost, an important and necessary advancement in the chemo-thermo-mechanical model is the inclusion of grain boundary normal stress as the chemical potential for stress-driven diffusion instead of grain boundary hydrostatic stress (pressure). Secondly, the flux across the grain boundary width (along the grain boundary normal) is not zero leading to atom transport in the normal direction, which is not the case in reality. To avoid this, one way would be to subtract the diffusivity component along the grain boundary normal direction. Therefore, to achieve both the above conditions in simulation, the grain boundary normal at each voxel should be incorporated into the model. Also, in this work the grain boundary shear forces and kinetics are investigated for a single film microstructure. Hence, to get a better quantitative understanding of these shear forces, a statistical analysis needs to be done for different film microstructures (having the same global texture but different local neighborhood for the oblique grain and/or with different global texture, as well) to determine whether these average shear forces are capable of breaking the tin oxide layer (of a given thickness) on top. This analysis is important since whiskers are often

observed to grow after breaking the oxide layer on top. Additionally, the material description would be incomplete without an accurate material model for Sn plasticity. In this thesis, the proposed Inverse Indentation Analysis framework of plasticity parameter estimation is already established for face-centered cubic and hexagonal materials. Hence, the immediate next step would be to identify such parameters (i.e. the initial flowstress or the critical resolved shear stress for the different slip families) for β-Sn. As mentioned earlier, the identification of β-Sn plasticity parameters is important due to its high homologous temperature at operating conditions thereby showing significant plasticity or high temperature creep behavior.

Apart from the simulation works, some experimental studies can also be done to verify some of the conclusions made in this work based on simulated data– such as the role of the global film texture. To achieve this, thin films differing only in texture should be synthesized and then subjected to thermal strain conditions, without the influence of Cu_6Sn_5 to have a fair comparison. Subsequently, it can also be studied whether the film texture can be modulated by controlling the processing conditions in order to obtain a texture that is more resistant to whisker formation (e.g. $\langle 001]$, as observed in this study). Another open question which can be answered through careful experimentation is the relationship between the oblique surface grains to overall whisker density. For achieving such, multiple focus-ion beam sectioning could be done on randomly selected areas in the film and then counting the number of grains having inclined boundaries and compare them to the experimentally observed whisker density values.

Thus, with successful completion of the above proposed work we would be able to understand the century old problem of whisker nucleation from thin films and subsequently prevent them by modifying process variables that lead to microstructures that are less prone forming whiskers.

BIBLIOGRAPHY

BIBLIOGRAPHY

M. Abtew and G. Selvaduray. Lead-free Solders in Microelectronics. *Materials Science and Engineering: R: Reports*, 27(5-6):95–141, 2000. ISSN 0927796X. doi:10.1016/S0927-796X(00)00010-3.

P. Adeva, G. Caruana, O. A. Ruano, and M. Torralba. Microstructure and high temperature mechanical properties of tin. *Materials Science and Engineering A*, 194(1):17–23, 1995. doi:10.1016/0921-5093(94)09654-6.

K. Alagarsamy, K. Mehdi, F. Aleksandra, and Michael G. P. Raising Awareness for Risk of Tin Whiskers in the Medical Industry. *Journal of Biomedical Engineering and Research*, 2(101):1–10, 2018. URL `http://www.jscholaronline.org/articles/JBER/Risk-of-Tin-Whiskers.pdf`.

J. Alcala, O. Casals, and J. Ocenasek. Micromechanics of pyramidal indentation in fcc metals: Single crystal plasticity finite element analysis. *Journal of the Mechanics and Physics of Solids*, 56(11):3277–3303, 2008. ISSN 0022-5096. doi:10.1016/j.jmps.2008.07.004.

F. Arizzi and E. Rizzi. Elastoplastic parameter identification by simulation of static and dynamic indentation tests. *Modelling and Simulation in Materials Science and Engineering*, 22(3):035017–, 2014. ISSN 0965-0393. doi:10.1088/0965-0393/22/3/035017.

S. M. Arnold. Repressing the growth of tin whiskers. *Plating*, 53:96, 1966.

M.A. Ashworth, G.D. Wilcox, R.L. Higginson, R.J. Heath, C. Liu, and R.J. Mortimer. The effect of electroplating parameters and substrate material on tin whisker formation. *Microelectronics Reliability*, 55(1):180–191, jan 2015. doi:10.1016/j.microrel.2014.10.005. URL `https://doi.org/10.1016%2Fj.microrel.2014.10.005`.

Alongheng Baated, Kyoko Hamasaki, Sun Sik Kim, Keun-Soo Kim, and Katsuaki Suganuma. Whisker Growth Behavior of Sn and Sn Alloy Lead-Free Finishes. *Journal of Electronic Materials*, 40(11):2278–2289, aug 2011a. doi:10.1007/s11664-011-1712-z. URL `https://doi.org/10.1007%2Fs11664-011-1712-z`.

Alongheng Baated, Keun-Soo Kim, and Katsuaki Suganuma. Effect of intermetallic growth rate on spontaneous whisker growth from a tin coating on copper. *Journal of Materials Science: Materials in Electronics*, 22(11):1685–1693, mar 2011b. doi:10.1007/s10854-011-0346-5. URL `https://doi.org/10.1007%2Fs10854-011-0346-5`.

S. Balay, J. Brown, K. Buschelman, V. Eijkhout, W. D. Gropp, D. Kaushik, M. G. Knepley, L. C. McInnes, B. F. Smith, and H. Zhang. *PETSc users manual*. Argonne National Laboratory, 2013.

K-J Bathe. *Finite Element Procedures*. K.J. Bathe, 2014. ISBN 978-0-9790049-5-7. URL `http://web.mit.edu/kjb/www/Books/FEP_2nd_Edition_4th_Printing.pdf`.

P. Baudoin, T. Hama, S. Uchida, and H. Takuda. Crystal plasticity analysis of the deformation of a grade 2 CP-Ti oligocrystal. *Journal of Physics: Conference Series*, 1063:012048–, 2018. ISSN 1742-6588. doi:10.1088/1742-6596/1063/1/012048.

T. R. Bieler, P. Eisenlohr, F. Roters, D. Kumar, D. E. Mason, M. A. Crimp, and D. Raabe. The role of heterogeneous deformation on damage nucleation at grain boundaries in single phase metals. *International Journal of Plasticity*, 25(9):1655–1683, 2009. doi:10.1016/j.ijplas.2008.09.002.

T. R. Bieler, B. Zhou, L. Blair, A. Zamiri, P. Darbandi, F. Pourboghrat, T-K Lee, and K-C Liu. The role of elastic and plastic anisotropy of Sn on microstructure and damage evolution in lead-free solder joints. In *Reliability Physics Symposium (IRPS), 2011 IEEE International*, pages 5F.1.1–5F.1.9, 2011. doi:10.1109/IRPS.2011.5784538.

M. Bocciarelli and G. Maier. Indentation and imprint mapping method for identification of residual stresses. *Computational Materials Science*, 39(2):381–392, 2007. ISSN 0927-0256. doi:10.1016/j.commatsci.2006.07.001.

M. Bocciarelli, G. Bolzon, and G. Maier. Parameter identification in anisotropic elastoplasticity by indentation and imprint mapping. *Mechanics of Materials*, 37(8):855–868, 2005. ISSN 0167-6636. doi:10.1016/j.mechmat.2004.09.001.

M. Bocciarelli, V. Buljak, C. K. S. Moy, S. P. Ringer, and G. Ranzi. An inverse analysis approach based on a POD direct model for the mechanical characterization of metallic materials. *Computational Materials Science*, 95:302–308, 2014. ISSN 0927-0256. doi:10.1016/j.commatsci.2014.07.025.

W. J. Boettinger, C. E. Johnson, L. A. Bendersky, K-W Moon, M. E. Williams, and G. R. Stafford. Whisker and Hillock formation on Sn, Sn–Cu and Sn–Pb electrodeposits. *Acta Materialia*, 53 (19):5033–5050, 2005. doi:10.1016/j.actamat.2005.07.016.

I. Boguslavsky and P. Bush. Recrystallization principles applied to whisker growth in tin. In *Proceedings of APEX Conference, Anaheim, USA*, pages S12–4–1 – S12–4–10, 2003.

G. Bolzon and M. Talassi. An effective inverse analysis tool for parameter identification of anisotropic material models. *International Journal of Mechanical Sciences*, 77:130–144, 2013. ISSN 0020-7403. doi:10.1016/j.ijmecsci.2013.09.009.

G. Bolzon, G. Maier, and M. Panico. Material model calibration by indentation, imprint mapping and inverse analysis. *International Journal of Solids and Structures*, 41(11-12):2957–2975, 2004. ISSN 0020-7683. doi:10.1016/j.ijsolstr.2004.01.025.

S. S. Brenner. Tensile Strength of Whiskers. *Journal of Applied Physics*, 27(12):1484–1491, 1956. ISSN 0021-8979. doi:10.1063/1.1722294.

S. S. Brenner. Plastic Deformation of Copper and Silver Whiskers. *Journal of Applied Physics*, 28 (9):1023–1026, 1957. ISSN 0021-8979. doi:10.1063/1.1722900.

E. Buchovecky, N. Jadhav, A. F. Bower, and E. Chason. Finite Element Modeling of Stress Evolution in Sn Films due to Growth of the Cu6Sn5 Intermetallic Compound. *Journal of Electronic Materials*, 38(12):2676–2684, 2009a. doi:10.1007/s11664-009-0911-3.

E. J. Buchovecky. *Numerical Simulation of Stress Generation and Whisker Growth in Sn Films*. PhD thesis, Brown University, School of Engineering, 2010.

E. J. Buchovecky, N. Du, and A. F. Bower. A model of Sn whisker growth by coupled plastic flow and grain boundary diffusion. *Applied Physics Letters*, 94(19):191904–, 2009b. ISSN 0003-6951. doi:10.1063/1.3136865.

V. Buljak and G. Maier. Proper Orthogonal Decomposition and Radial Basis Functions in material characterization based on instrumented indentation. *Engineering Structures*, 33(2):492–501, 2011. ISSN 0141-0296. doi:10.1016/j.engstruct.2010.11.006.

F. Campolongo, J. Cariboni, and A. Saltelli. An effective screening design for sensitivity analysis of large models. *Environmental Modelling & Software*, 22(10):1509–1518, 2007. ISSN 1364-8152. doi:10.1016/j.envsoft.2006.10.004.

A. Chakraborty and P. Eisenlohr. Evaluation of an inverse methodology for estimating constitutive parameters in face-centered cubic materials from single crystal indentations. *European Journal of Mechanics / A Solids*, 66C:114–124, 2017. doi:10.1016/j.euromechsol.2017.06.012.

A. Chakraborty and P. Eisenlohr. A full-field crystal plasticity study on how texture and grain structure influences the evolution of hydrostatic stress in thermally strained β-Sn films. *Journal of Applied Physics*, 124:025302, 2018. doi:10.1063/1.5029933.

A. Chakraborty and P. Eisenlohr. Chemo-thermo-mechanically coupled crystal plasticity simulation of stress evolution in thermally strained β-Sn films. *Journal of Electronic Materials*, 48 (1):85–91, 2019. doi:10.1007/s11664-018-6733-4.

J. Chakraborty, U. Welzel, and E. J. Mittemeijer. Interdiffusion, phase formation, and stress development in Cu–Pd thin-film diffusion couples: Interface thermodynamics and mechanisms. *Journal of Applied Physics*, 103(11):113512–, 2008. ISSN 0021-8979. doi:10.1063/1.2938079.

E. Chason and N. Jadhav. *Mitigating Tin Whisker Risks: Theory and Practice*, chapter Major driving forces and growth mechanisms for tin whiskers, pages 21–42. John Wiley & Sons, Inc., 2016.

E. Chason, N. Jadhav, W. L. Chan, L. Reinbold, and K. S. Kumar. Whisker formation in Sn and Pb–Sn coatings: Role of intermetallic growth, stress evolution, and plastic deformation processes. *Applied Physics Letters*, 92(17):171901–, 2008. ISSN 0003-6951. doi:10.1063/1.2912528.

E. Chason, N. Jadhav, and F. Pei. Effect of layer properties on stress evolution, intermetallic volume, and density during tin whisker formation. *Jom*, 63(10):62–68, 2011. ISSN 1047-4838. doi:10.1007/s11837-011-0178-z.

E. Chason, N. Jadhav, F. Pei, E. Buchovecky, and A. Bower. Growth of whiskers from Sn surfaces: Driving forces and growth mechanisms. *Progress in Surface Science*, 88(2):103–131, 2013. doi:10.1016/j.progsurf.2013.02.002.

E. Chason, F. Pei, C. L. Briant, H. Kesari, and A. F. Bower. Significance of Nucleation Kinetics in Sn Whisker Formation. *Journal of Electronic Materials*, 43(12):4435–4441, 2014. doi:10.1007/s11664-014-3379-8.

P. Chaudhari. Hillock growth in thin films. *Journal of Applied Physics*, 45(10):4339–4346, 1974. ISSN 0021-8979. doi:10.1063/1.1663054.

S-W Chen, C-H Wang, S-K Lin, and C-N Chiu. chapter Phase diagrams of Pb-free solders and their related materials systems, pages 19–37. Springer US, Boston, MA, 2007. ISBN 978-0-387-48431-0. doi:10.1007/978-0-387-48433-4_2.

J. Cheng and S. Ghosh. A crystal plasticity FE model for deformation with twin nucleation in magnesium alloys. *International Journal of Plasticity*, 67:148–170, 2015. doi:10.1016/j.ijplas.2014.10.005.

J. Cheng, F. Yang, P. T. Vianco, B. Zhang, and J. C. M. Li. Optimum Thickness of Sn Film for Whisker Growth. *Journal of Electronic Materials*, 40(10):2069–2075, 2011. ISSN 0361-5235. doi:10.1007/s11664-011-1708-8.

W. J. Choi, T. Y. Lee, K. N. Tu, N. Tamura, R. S. Celestre, A. A. MacDowell, Y. Y. Bong, and L. Nguyen. Tin whiskers studied by synchrotron radiation scanning X-ray micro-diffraction. *Acta Materialia*, 51(20):6253–6261, 2003. ISSN 1359-6454. doi:10.1016/S1359-6454(03)00448-8.

Y. S. Choi, M. A. Groeber, T. J. Turner, D. M. Dimiduk, C. Woodward, M. D. Uchic, and T. A. Parthasarathy. A crystal-plasticity FEM study on effects of simplified grain representation and mesh types on mesoscopic plasticity heterogeneities. *Materials Science and Engineering A*, 553:37–44, 2012. ISSN 0921-5093. doi:10.1016/j.msea.2012.05.089.

H. L. Cobb. Cadmium whiskers. 33(28):28–30, 1946.

R. L. Coble. *J. Appl. Phys.*, 34:1679, 1963.

R. V. Coleman, B. Price, and N. Cabrera. Slip of Zinc and Cadmium Whiskers. *Journal of Applied Physics*, 28(11):1360–1361, 1957. ISSN 0021-8979. doi:10.1063/1.1722654.

K. G. Compton, A. Mendizza, and S. M. Arnold. Filamentary Growths On Metal Surfaces – ''Whiskers''. *Corrosion*, 7(10):327–334, 1951. ISSN 0010-9312. doi:10.5006/0010-9312-7.10.327.

A. Constantinescu and N. Tardieu. On the identification of elastoviscoplastic constitutive laws from indentation tests. *Inverse Problems in Engineering*, 9(1):19–44, 2001. ISSN 1068-2767. doi:10.1080/174159701088027751.

C. Coston and N. H. Nachtrieb. Self-Diffusion in Tin at High Pressure. *The Journal of Physical Chemistry*, 68(8):2219–2229, 1964. ISSN 0022-3654. doi:10.1021/j100790a032.

R. Courant. Variational methods for the solution of problems of equilibrium and vibrations. *Bulletin of the American Mathematical Society*, 49(1):1–23, 1943. doi:10.1090/S0002-9904-1943-07818-4.

E. R. Crandall, G. T. Flowers, R. Jackson, P. Lall, and M. J. Bozack. Growth of Sn Whiskers under Net Compressive and Tensile Stress States. pages 1–5, 2011. doi:10.1109/HOLM.2011.6034820.

E. R. Crandall, G. T. Flowers, P. Lall, E. K. Snipes, and M. J. Bozack. The Influence of Surface Oxides on Whiskering. In *2012 IEEE 58th Holm Conference on Electrical Contacts (Holm)*. IEEE, sep 2012. doi:10.1109/holm.2012.6336581. URL `https://doi.org/10.1109%2Fholm.2012.6336581`.

Q. Cui, F. Gao, S. Mukherjee, and Z. Gu. Joining and Interconnect Formation of Nanowires and Carbon Nanotubes for Nanoelectronics and Nanosystems. *Small*, 5(11):1246–1257, 2009. ISSN 1613-6810. doi:10.1002/smll.200801551.

I. Dastidar, A. L. Pilchak, T. R. Bieler, V. Khademi, M. A. Crimp, and C. J. Boehlert. The Tensile and Tensile-Creep Deformation Behavior of Ti-8Al-1Mo-1V(wt.%). *Materials Science and Engineering A*, 636:289–300, 2015. doi:10.1016/j.msea.2015.03.059.

T. W. J. De Geus, J. Vondřejc, J. Zeman, R. H. J. Peerlings, and M. G. D. Geers. Finite strain FFT-based non-linear solvers made simple. *Computer Methods in Applied Mechanics and Engineering*, 2017. ISSN 0045-7825. doi:10.1016/j.cma.2016.12.032.

M. Diehl. *High-resolution crystal plasticity simulations*. PhD thesis, RWTH Aachen, Aachen, 2016.

M. Dittes, P. Oberndorff, and L. Petit. Tin Whisker Formation – Results, Test Methods and Countermeasures. In *Proc. 53rd Electronic Components & Technology Conf.*, pages 822–826. IEEE, 2003.

K. Doudrick, J. Chinn, J. Williams, N. Chawla, and K. Rykaczewski. Rapid method for testing efficacy of nano-engineered coatings for mitigating tin whisker growth. *Microelectronics Reliability*, 55(5):832–837, 2015. ISSN 0026-2714. doi:10.1016/j.microrel.2015.02.014.

Russel Eberhart and Yuhui Shi. Particle swarm optimization: developments, applications and resources. pages 81–86. doi:10.1109/CEC.2001.934374.

P. Eisenlohr, M. Diehl, R. A. Lebensohn, and F. Roters. A spectral method solution to crystal elasto-viscoplasticity at finite strains. *International Journal of Plasticity*, 46:37–53, 2013. doi:10.1016/j.ijplas.2012.09.012.

P. Eisenlohr, F. Roters, M. Diehl, C. Kords, and P. Shanthraj. DAMASK Web page. 2014. URL `http://damask.mpie.de`.

P. Eisenlohr, P. Shanthraj, B. R. Vande Kieft, T. R. Bieler, W. Liu, and R. Xu. Subsurface Grain Morphology Reconstruction by Differential Aperture X-ray Microscopy. *JOM*, 69(6):1100–1105, 2017. doi:10.1007/s11837-017-2357-z.

W. C. Ellis, D. Gibbons, and R. Treuting. Growth of metal whiskers from the solid. *Growth and perfection of crystals*, 1958.

B. Erdem Alaca. Integration of one-dimensional nanostructures with microsystems: an overview. *International Materials Reviews*, 54(5):245–282, 2009. ISSN 0950-6608. doi:10.1179/174328009X411190.

J. D. Eshelby. A Tentative Theory of Metallic Whisker Growth. *Physical Review*, 91(3):755–756, 1953. doi:10.1103/PhysRev.91.755.2.

A. Etienne, E. Cadel, A. Lina, L. Cretinon, and P. Pareige. Crystallographic Characterization of an Electroplated Zinc Coating Prone to Whiskers. *IEEE Transactions on Components, Packaging and Manufacturing Technology*, 2(11):1928–1932, 2012. ISSN 2156-3950. doi:10.1109/TCPMT.2012.2203134.

R. M. Fisher, L. S. Darken, and K. G. Carroll. Accelerated growth of tin whiskers. *Acta Metallurgica*, 2(3):368–369, 371, 1954. doi:10.1016/0001-6160(54)90053-X.

A. Fortier and R. Kovacevic. Internal Microstructure Investigation of Tin Whisker Growth Using FIB Technology. *Journal of Electronic Materials*, 41(8):2029–2034, 2012. ISSN 0361-5235. doi:10.1007/s11664-012-2065-y.

F. C. Frank. XC. On tin whiskers. *The London, Edinburgh, and Dublin Philosophical Magazine and Journal of Science*, 44(355):854–860, 1953. ISSN 1941-5982. doi:10.1080/14786440808520351.

M. Fujiwara. Deformation anisotropy of β-Sn crystals by microindenter. *Materials Science and Engineering A*, 234-236:991–995, 1997. doi:10.1016/S0921-5093(97)00348-1.

M. Fujiwara and T. Hirokawa. The Strength of Main Obstacles to Dislocation Motion in White Tin Crystals. *Journal of the Japan Institute of Metals*, 51(9):830–838, 1987.

N. Furuta and K. Hamamura. Growth Mechanism of Proper Tin-Whisker. *Japanese Journal of Applied Physics*, 8(12):1404–1410, 1969.

G. Galyon. Whisker Formation Concepts–The End Game. *IEEE Transactions on Components, Packaging and Manufacturing Technology*, 1(7):1098–1109, 2011. doi:10.1109/TCPMT.2010.2103319.

G. T. Galyon. Annotated tin whisker bibliography and anthology. *IEEE Transactions on Electronics Packaging Manufacturing*, 28(1):94–122, 2005. doi:10.1109/TEPM.2005.847440.

G. T. Galyon and L. Palmer. An integrated theory of whisker formation: the physical metallurgy of whisker formation and the role of internal stresses. *IEEE Transactions on Electronics Packaging Manufacturing*, 28(1):17–30, 2005. ISSN 1521-334X. doi:10.1109/TEPM.2005.847443.

V. K. Glazunova and N. T. Kudryavtsev. An investigation of the conditions of spontaneous growth of filiform crystals on electrolytic coatings. *Zhurnal Prikladnoi Khimii*, 36(3):543–550, 1963.

R. Hajali, H. Kim, S. Koh, A. Saxena, and R. Tummala. Nonlinear constitutive models from nanoindentation tests using artificial neural networks. *International Journal of Plasticity*, 24 (3):371–396, 2008. ISSN 0749-6419. doi:10.1016/j.ijplas.2007.02.001.

S. U. Hamim and R. P. Singh. Taguchi-based design of experiments in training POD-RBF surrogate model for inverse material modelling using nanoindentation. *Inverse Problems in Science and Engineering*, 25(3):363–381, 2017. doi:10.1080/17415977.2016.1161036.

A. He and D. G. Ivey. Microstructural study of Sn films electrodeposited on Cu substrates: Sn whiskers and Cu_6Sn_5 precipitates. *Journal of Materials Science*, 50(7):2944–2959, 2015. doi:10.1007/s10853-015-8859-6.

J. Hektor, J-B Marijon, M. Ristinmaa, S. A. Hall, H. Hallberg, S. Iyengar, J-S Micha, O. Robach, F. Grennerat, and O. Castelnau. Evidence of 3D strain gradients associated with tin whisker growth. *Scripta Materialia*, 144:1–4, 2018. ISSN 1359-6462. doi:10.1016/j.scriptamat.2017.09.030.

S. Hémery, A. Nait-Ali, and P. Villechaise. Combination of in-situ SEM tensile test and FFT-based crystal elasticity simulations of Ti-6Al-4V for an improved description of the onset of plastic slip. *Mechanics of Materials*, 109:1–10, 2017. doi:10.1016/j.mechmat.2017.03.013.

V. Herrera-Solaz, J. LLorca, E. Dogan, I. Karaman, and J. Segurado. An inverse optimization strategy to determine single crystal mechanical behavior from polycrystal tests: Application to AZ31 Mg alloy. *International Journal of Plasticity*, 57:1–15, 2014. doi:10.1016/j.ijplas.2014.02.001.

V. Herrera-Solaz, J. Segurado, and J. LLorca. On the robustness of an inverse optimization approach based on the Levenberg–Marquardt method for the mechanical behavior of polycrystals. *European Journal of Mechanics – A/Solids*, 53:220–228, 2015. ISSN 0997-7538. doi:10.1016/j.euromechsol.2015.05.005.

R. Hill. A theory of the yielding and plastic flow of anisotropic metals. *Proceedings of the Royal Society A: Mathematical, Physical and Engineering Sciences*, 193(1033):281–297, 1948. doi:10.1098/rspa.1948.0045.

C-M Huang, D. Nunez, J. Coburn, and M. Pecht. Risk of tin whiskers in the nuclear industry. *Microelectronics Reliability*, 81:22–30, 2018. ISSN 0026-2714. doi:10.1016/j.microrel.2017.12.019.

F. H. Huang and H. B. Huntington. Diffusion of Sb^{124}, Cd^{109}, Sn^{113}, and Zn^{65} in tin. *Physical Review B*, 9(4):1479–1488, 1974. doi:10.1103/PhysRevB.9.1479.

N. Huber and C. Tsakmakis. Determination of constitutive properties from spherical indentation data using neural networks. Part ii: plasticity with nonlinear isotropic and kinematic hardening. *Journal of the Mechanics and Physics of Solids*, 47(7):1589–1607, 1999. doi:10.1016/S0022-5096(98)00110-0.

N. Huber, A. Konstantinidis, and C. Tsakmakis. Determination of Poisson's Ratio by Spherical Indentation Using Neural Networks—Part I: Theory. *Journal of Applied Mechanics*, 68(2): 218–, 2001. ISSN 0021-8936. doi:10.1115/1.1354624.

C. Hunt and M. Wickham. Mitigation of tin whiskers with polymer coatings. pages 78–87, 2010. doi:10.1109/ISAPM.2010.5441379.

J. W. Hutchinson. Bounds and self-consistent estimates for creep of polycrystalline materials. *Proceedings of the Royal Society A*, 348:101–127, 1976. doi:10.1098/rspa.1976.0027.

J. W. Hutchinson. Creep and plasticity of hexagonal polycrystals as related to single crystal slip. *Metallurgical Transactions A*, 8(9):1465–1469, 1977. ISSN 0360-2133. doi:10.1007/BF02642860.

W. Bevis Hutchinson, James Oliver, Margareta Nylén, and Joacim Hagström. Whisker Growth from Tin Coatings. *Materials Science Forum*, 467-470:465–470, oct 2004. doi:10.4028/www.scientific.net/msf.467-470.465. URL https://doi.org/10.4028%2Fwww.scientific.net%2Fmsf.467-470.465.

Balázs Illés and Barbara Horváth. Whiskering behaviour of immersion tin surface coating. *Microelectronics Reliability*, 53(5):755–760, may 2013. doi:10.1016/j.microrel.2013.02.001. URL https://doi.org/10.1016%2Fj.microrel.2013.02.001.

N. Jadhav, E. Buchovecky, E. Chason, and A. Bower. Real-time SEM/FIB studies of whisker growth and surface modification. *JOM*, 62(7):30–37, 2010a. doi:10.1007/s11837-010-0105-8.

N. Jadhav, E. J. Buchovecky, L. Reinbold, S. Kumar, A. F. Bower, and E. Chason. Understanding the Correlation Between Intermetallic Growth, Stress Evolution, and Sn Whisker Nucleation. *IEEE Transactions on Electronics Packaging Manufacturing*, 33(3):183–192, 2010b. doi:10.1109/TEPM.2010.2043847.

N. Jadhav, J. Wasserman, F. Pei, and E. Chason. Stress Relaxation in Sn-Based Films: Effects of Pb Alloying, Grain Size, and Microstructure. *Journal of Electronic Materials*, 41(3):588–595, 2012a. ISSN 0361-5235. doi:10.1007/s11664-011-1829-0.

Nitin Jadhav, Jacob Wasserman, Fei Pei, and Eric Chason. Stress Relaxation in Sn-Based Films: Effects of Pb Alloying, Grain Size, and Microstructure. *Journal of Electronic Materials*, 41 (3):588–595, dec 2011. doi:10.1007/s11664-011-1829-0. URL https://doi.org/10.1007%2Fs11664-011-1829-0.

Nitin Jadhav, Maureen Williams, Fei Pei, Gery Stafford, and Eric Chason. Altering the Mechanical Properties of Sn Films by Alloying with Bi: Mimicking the Effect of Pb to Suppress Whiskers. *Journal of Electronic Materials*, 42(2):312–318, oct 2012b. doi:10.1007/s11664-012-2267-3. URL https://doi.org/10.1007%2Fs11664-012-2267-3.

P. Jagtap and P. Kumar. Manipulating Crystallographic Texture of Sn Coatings by Optimization of Electrodeposition Process Conditions to Suppress Growth of Whiskers. *Journal of Electronic Materials*, 44(4):1206–1219, 2015. ISSN 0361-5235. doi:10.1007/s11664-014-3622-3.

P. Jagtap, A. Chakraborty, P. Eisenlohr, and P. Kumar. Identification of Whisker Grain in Sn Coatings by Analyzing Crystallographic Micro-Texture using Electron Back-Scatter Diffraction. *Acta Materialia*, 134:346–359, 2017. doi:10.1016/j.actamat.2017.05.063.

P. Jagtap, P. Ramesh Narayan, and P. Kumar. Effect of Substrate Composition on Whisker Growth in Sn Coatings. *Journal of Electronic Materials*, 2018. ISSN 0361-5235. doi:10.1007/s11664-018-6275-9.

B. Jiang and A-P Xian. Discontinuous growth of tin whiskers. *Philosophical Magazine Letters*, 86(8):521–527, 2006. ISSN 0950-0839. doi:10.1080/09500830600908996.

J. Kajberg and G. Lindkvist. Characterisation of materials subjected to large strains by inverse modelling based on in-plane displacement fields. *International Journal of Solids and Structures*, 41(13):3439–3459, 2004. ISSN 0020-7683. doi:10.1016/j.ijsolstr.2004.02.021.

J. Kajberg and B. Wikman. Viscoplastic parameter estimation by high strain-rate experiments and inverse modelling – Speckle measurements and high-speed photography. *International Journal of Solids and Structures*, 44(1):145–164, 2007. ISSN 0020-7683. doi:10.1016/j.ijsolstr.2006.04.018.

T. Kakeshita, K. Shimizu, R. Kawanaka, and T. Hasegawa. Grain size effect of electroplated tin coatings on whisker growth. *Journal of Materials Science*, 17(9):2560–2566, 1982. doi:10.1007/BF00543888.

S. R. Kalidindi and S. E. Schoenfeld. On the prediction of yield surfaces by the crystal plasticity models for fcc polycrystals. *Materials Science and Engineering A*, 293(1-2):120–129, 2000. ISSN 0921-5093. doi:10.1016/S0921-5093(00)01048-0.

S. R. Kalidindi, C. A. Bronkhorst, and L. Anand. Crystallographic texture evolution in bulk deformation processing of fcc metals. *Journal of the Mechanics and Physics of Solids*, 40(3): 537–569, 1992. doi:10.1016/0022-5096(92)80003-9.

H. J. Kao, W. C. Wu, S. T. Tsai, and C. Y. Liu. Effect of Cu additives on Sn whisker formation of Sn(Cu) finishes. *Journal of Electronic Materials*, 35(10):1885–1891, 2006. ISSN 0361-5235. doi:10.1007/s11664-006-0172-3.

S. Karim, M. E. Toimil-Molares, F. Maurer, G. Miehe, W. Ensinger, J. Liu, T. W. Cornelius, and R. Neumann. Synthesis of gold nanowires with controlled crystallographic characteristics. *Applied Physics A*, 84(4):403–407, 2006. ISSN 0947-8396. doi:10.1007/s00339-006-3645-6.

S. Kaßbohm, W. H. Müller, and R. Feßler. Improved approximations of Fourier coefficients for computing periodic structures with arbitrary stiffness distribution. *Computational Materials Science*, 37(1-2):90–93, 2006. doi:10.1016/j.commatsci.2005.12.010.

J. Kennedy and R. Eberhart. Particle swarm optimization. In *Proceedings of IEEE International Conference on Neural Networks IV*, pages 1942–1948, 1995. doi:10.1109/ICNN.1995.488968.

Y. Kinoshita, H. Matsushima, and N. Ohno. Predicting active slip systems in β-Sn from ideal shear resistance. *Modelling and Simulation in Materials Science and Engineering*, 20(3): 035003–, 2012. doi:10.1088/0965-0393/20/3/035003.

D. Klötzer, C. Ullner, E. Tyulyukovskiy, and N. Huber. Identification of viscoplastic material parameters from spherical indentation data: Part II. Experimental validation of the method. *Journal of Materials Research*, 21(03):677–684, 2006. ISSN 0884-2914. doi:10.1557/jmr.2006.0077.

S. E. Koonce and S. M. Arnold. Growth of Metal Whiskers. *Journal of Applied Physics*, 24(3): 365–366, 1953. ISSN 0021-8979. doi:10.1063/1.1721283.

L. Kubin, B. Devincre, and T. Hoc. Modeling dislocation storage rates and mean free paths in face-centered cubic crystals. *Acta Materialia*, 56(20):6040–6049, 2008. doi:10.1016/j.actamat.2008.08.012.

K. S. Kumar, L. Reinbold, A. F. Bower, and E. Chason. Plastic deformation processes in Cu/Sn bimetallic films. *Journal of Materials Research*, 23(11):2916–2934, 2008. ISSN 0884-2914. doi:10.1557/JMR.2008.0351.

S. Lal and T. D. Moyer. Role of intrinsic stresses in the phenomena of tin whiskers in electrical connectors. *IEEE Transactions on Electronics Packaging Manufacturing*, 28(1):63–74, 2005. ISSN 1521-334X. doi:10.1109/TEPM.2005.846457.

W. Lange and D. Bergner. Messung der Korngrenzenselbstdiffusion in polykristallinem Zinn. *physica status solidi (b)*, 2(10):1410–1414, 1962. doi:10.1002/pssb.19620021020.

F. Larché and J. W. Cahn. A linear theory of thermochemical equilibrium of solids under stress. *Acta Metallurgica*, 21(8):1051–1063, 1973. ISSN 0001-6160. doi:10.1016/0001-6160(73)90021-7.

R. A. Lebensohn. N-site modeling of a 3D viscoplastic polycrystal using fast Fourier transform. *Acta Materialia*, 49(14):2723–2737, 2001. doi:10.1016/S1359-6454(01)00172-0.

J. B. LeBret and M. G. Norton. Electron microscopy study of tin whisker growth. *International Journal of Materials Research*, 18(3):585–593, 2003. doi:10.1557/JMR.2003.0076.

E. H. Lee. Elastic-plastic deformation at finite strains. *J. Appl. Mech. ASME*, 36(1):1–6, 1969.

T-K Lee, T. R. Bieler, C-U Kim, and H. Ma. *Fundamentals of Lead-Free Solder Interconnect Technology*. Springer US, Boston, MA, 2015. ISBN 978-1-4614-9265-8. doi:10.1007/978-1-4614-9266-5.

Z. B. Lee and N. Z. Lee. Spontaneous growth mechanism of tin whiskers. *Acta Materialia*, 46 (10):3701–3714, 1998. doi:10.1016/S1359-6454(98)00045-7.

H. Li, D. E. Mason, T. R. Bieler, C. J. Boehlert, and M. A. Crimp. Methodology for estimating the critical resolved shear stress ratios of α-phase Ti using EBSD-based trace analysis. *Acta Materialia*, 61(20):7555–7567, 2013. doi:10.1016/j.actamat.2013.08.042.

C-K Lin and T-H Lin. Effects of continuously applied stress on tin whisker growth. *Microelectronics Reliability*, 48(10):1737–1740, 2008. doi:10.1016/j.microrel.2008.04.013.

U. Lindborg. A model for the spontaneous growth of zinc, cadmium and tin whiskers. *Acta Metallurgica*, 24(2):181–186, 1976. doi:10.1016/0001-6160(76)90021-3.

B. Liu, D. Raabe, F. Roters, P. Eisenlohr, and R. A. Lebensohn. Comparison of finite element and fast Fourier transform crystal plasticity solvers for texture prediction. *Modelling and Simulation in Materials Science and Engineering*, 18(8):085005, 2010. doi:10.1088/0965-0393/18/8/085005.

S. H. Liu, C. Chen, P. C. Liu, and T. Chou. Tin whisker growth driven by electrical currents. *Journal of Applied Physics*, 95(12):7742–7747, 2004. ISSN 0021-8979. doi:10.1063/1.1712019.

M-H Lu and K-C Hsieh. Sn-Cu Intermetallic Grain Morphology Related to Sn Layer Thickness. *Journal of Electronic Materials*, 36(11):1448–1454, 2007. ISSN 0361-5235. doi:10.1007/s11664-007-0270-x.

Y. Lu and M. Saka. Fabrication of Al micro-belts by utilizing electromigration. *Materials Letters*, 63(26):2227–2229, 2009. ISSN 0167577X. doi:10.1016/j.matlet.2009.07.031.

A. Ma, F. Roters, and D. Raabe. A dislocation density based constitutive model for crystal plasticity FEM including geometrically necessary dislocations. *Acta Materialia*, 54:2169–2179, 2006. doi:10.1016/j.actamat.2006.01.005.

K. Mahan, Y. Sun, B. Han, S. Han, and M. Osterman. Adhesion and Puncture Strength of Polyurethane Coating Used to Mitigate Tin Whisker Growth. *Journal of Electronic Packaging*, 136(3):031004–, 2014. ISSN 1043-7398. doi:10.1115/1.4026922.

R. Mahnken and E. Stein. Parameter identification for viscoplastic models based on analytical derivatives of a least-squares functional and stability investigations. *International Journal of Plasticity*, 12(4):451–479, 1996. ISSN 0749-6419. doi:10.1016/S0749-6419(95)00016-X.

T. Maiti and P. Eisenlohr. Fourier-based spectral method solution to finite strain crystal plasticity with free surfaces. *Scripta Materialia*, 145:37–40, 2018. doi:10.1016/j.scriptamat.2017.09.047.

T. Maiti, A. Chakraborty, P. Eisenlohr, D. Kang, and T. R. Bieler. A Crystal Plasticity Study on Influence of Dislocation Mean Free Path on Stage II Hardening in Nb Single Crystals. In *Proc. Int. Conf. RF Superconductivity (SRF'17)*, number 18 in International Conference on RF Superconductivity, pages 783–786, Geneva, Switzerland, 2018. JACoW. doi:10.18429/JACoW-SRF2017-THPB025.

M. D. Mathew, H. Yang, S. Movva, and K. L. Murty. Creep deformation characteristics of tin and tin-based electronic solder alloys. *Metallurgical and Materials Transactions A*, 36(1):99–105, 2005. ISSN 1073-5623. doi:10.1007/s11661-005-0142-z.

Sony Mathew, Michael Osterman, Michael Pecht, and Frank Dunlevey. Evaluation of pure tin plated copper alloy substrates for tin whiskers. *Circuit World*, 35(1): 3–8, feb 2009. doi:10.1108/03056120910928662. URL `https://doi.org/10.1108%2F03056120910928662`.

J. R. Mayeur and D. L. McDowell. A three-dimensional crystal plasticity model for duplex Ti–6Al–4V. *International Journal of Plasticity*, 23(9):1457–1485, 2007. doi:10.1016/j.ijplas.2006.11.006.

R. J. McCabe and M. E. Fine. Creep of tin, Sb-solution-strengthened tin, and SbSn-precipitate-strengthened tin. *Metallurgical and Materials Transactions A*, 33(5):1531–1539, 2002. ISSN 1073-5623. doi:10.1007/s11661-002-0075-8.

J. D. Meakin and E. Klokholm. Self-diffusion in tin single crystals. *Transactions of the American Institute of Mining, Metallurgical and Petroleum Engineers*, 218:463–466, 1960.

Á Meggyes. Multiple decomposition in finite deformation theory. *Acta Mechanica*, 146(3-4): 169–182, 2001. doi:10.1007/BF01246731.

L. Meng, P. Breitkopf, and G. Le Quilliec. Identification of material parameters using indentation test—study of the intrinsic dimensionality of P-h curves and residual imprints. *MATEC Web Conf.*, 80:10012, 2016. doi:10.1051/matecconf/20168010012.

D. Mercier and C. Zambaldi. *Slip transfer analysis toolbox (STABiX) CPFE simulation preprocessing GUIs*, 2014. URL `http://stabix.readthedocs.org/en/latest/preCPFE_gui.html`.

F. A. Mohamed, K. L. Murty, and J. W. Morris. Harper-dorn creep in al, pb, and sn. *Metallurgical Transactions*, 4(4):935–940, 1973. ISSN 0360-2133. doi:10.1007/BF02645593.

K-W Moon, C. E. Johnson, M. E. Williams, O. Kongstein, G. R. Stafford, C. A. Handwerker, and W. J. Boettinger. Observed correlation of Sn oxide film to Sn whisker growth in Sn-Cu electrodeposit for Pb-free solders. *Journal of Electronic Materials*, 34(9):L31–L33, 2005. doi:10.1007/s11664-005-0274-3.

K.-W. Moon, S.-K. Kim, M. E. Williams, W. J. Boettinger, and G. R. Stafford. Effect of current density and electrolyte concentration on hillock growth from pure bright Sn electrodeposits. *Journal of Applied Electrochemistry*, 40(9):1671–1681, jul 2010. doi:10.1007/s10800-010-0163-1. URL `https://doi.org/10.1007%2Fs10800-010-0163-1`.

M. D. Morris. Factorial Sampling Plans for Preliminary Computational Experiments. *Technometrics*, 33(2):161–174, 1991. ISSN 0040-1706. doi:10.1080/00401706.1991.10484804.

H. Moulinec and P. Suquet. A fast numerical method for computing the linear and nonlinear properties of composites. *Comptes rendus de l'Académie des sciences. Série II, Mécanique, physique, chimie, astronomie*, 318:1417–1423, 1994.

C. K. S. Moy, M. Bocciarelli, S. P. Ringer, and G. Ranzi. Indentation and imprint mapping for the identification of material properties in multi-layered systems. *Computational Materials Science*, 50(5):1681–1691, 2011a. ISSN 0927-0256. doi:10.1016/j.commatsci.2010.12.029.

C. K. S. Moy, M. Bocciarelli, S. P. Ringer, and G. Ranzi. Identification of the material properties of Al 2024 alloy by means of inverse analysis and indentation tests. *Materials Science and Engineering: A*, 529:119–130, 2011b. ISSN 0921-5093. doi:10.1016/j.msea.2011.09.005.

Y. Nakadaira, S. Jeong, J. Shim, J. Seo, S. Min, T. Cho, S. Kang, and S. Oh. Growth of tin whiskers for lead-free plated leadframe packages in high humid environments and during thermal cycling. *Microelectronics Reliability*, 48(1):83–104, 2008. ISSN 0026-2714. doi:10.1016/j.microrel.2007.01.091.

T. Nakamura and Y. Gu. Identification of elastic–plastic anisotropic parameters using instrumented indentation and inverse analysis. *Mechanics of Materials*, 39(4):340–356, 2007. ISSN 0167-6636. doi:10.1016/j.mechmat.2006.06.004.

T. Nakamura, T. Wang, and S. Sampath. Determination of properties of graded materials by inverse analysis and instrumented indentation. *Acta Materialia*, 48(17):4293–4306, 2000. ISSN 1359-6454. doi:10.1016/S1359-6454(00)00217-2.

J. A. Nelder and R. Mead. A Simplex Method for Function Minimization. *The Computer Journal*, 7(4):308–313, 1965. doi:10.1093/comjnl/7.4.308.

Naoki Okamoto, Yuko Fujii, Hiroaki Kurihara, and Kazuo Kondo. Effects of Microstructure of Deposited Sn Films and Orientation Index of Cu Foils on Sn Whisker Formation Using Substitutionally-Deposited Sn Films. *MATERIALS TRANSACTIONS*, 50(11):2570–2577, 2009. doi:10.2320/matertrans.m2009249. URL `https://doi.org/10.2320%2Fmatertrans.m2009249`.

J. W. Osenbach, R. L. Shook, B. T. Vaccaro, B. D. Potteiger, A. N. Amin, K. N. Hooghan, P. Suratkar, and P. Ruengsinsub. Sn whiskers: material, design, processing, and post-plate reflow effects and development of an overall phenomenological theory. *IEEE Transactions on Electronics Packaging Manufacturing*, 28(1):36–62, 2005. doi:10.1109/TEPM.2005.847438.

J. W. Osenbach, J. M. DeLucca, B. D. Potteiger, A. Amin, and F. A. Baiocchi. Sn-whiskers: truths and myths. *Journal of Materials Science: Materials in Electronics*, 18(1-3):283–305, 2007. doi:10.1007/s10854-006-9030-6.

A. S. Ostrovsky and B. S. Bokstein. Grain boundary diffusion in thin films under stress fields. *Applied Surface Science*, 175-176:312–318, 2001. ISSN 0169-4332. doi:10.1016/S0169-4332(01)00164-7.

D. C. Pagan, P. A. Shade, N. R. Barton, J-S Park, P. Kenesei, D. B. Menasche, and J. V. Bernier. Modeling slip system strength evolution in Ti-7Al informed by in-situ grain stress measurements. *Acta Materialia*, 128:406–417, 2017. ISSN 1359-6454. doi:10.1016/j.actamat.2017.02.042.

D. C. Pagan, J. V. Bernier, D. Dale, J. Y. P. Ko, T. J. Turner, B. Blank, and P. A. Shade. Measuring Ti-7Al slip system strengths at elevated temperature using high-energy X-ray diffraction. *Scripta Materialia*, 142:96–100, 2018. ISSN 1359-6462. doi:10.1016/j.scriptamat.2017.08.029. URL `http://linkinghub.elsevier.com/retrieve/pii/S1359646217304931`.

European Parliament and Council of the European Union. Directive 2002/95/EC of the European Parliament and of the Council of 27 January 2003 on the restriction of the use of certain hazardous substances in electrical and electronic equipment. *Official Journal of the European Union*, L34:19–37, 2003.

M. O. Peach. Mechanism of Growth of Whiskers on Cadmium. *Journal of Applied Physics*, 23 (12):1401–1403, 1952. ISSN 0021-8979. doi:10.1063/1.1702147.

F. Pei, N. Jadhav, E. Buchovecky, A. F. Bower, E. Chason, W. Liu, J. Z. Tischler, G. E. Ice, and R. Xu. *In-situ* synchrotron micro-diffraction study of surface, interface, grain structure, and strain/stress evolution during Sn whisker/hillock formation. *Journal of Applied Physics*, 119 (10):105302–, 2016. doi:10.1063/1.4942920.

F. Pei, E. Buchovecky, A. Bower, and E. Chason. Stress evolution and whisker growth during thermal cycling of Sn films: A comparison of analytical modeling and experiments. *Acta Materialia*, 129:462–473, 2017. ISSN 1359-6454. doi:10.1016/j.actamat.2017.03.005.

Fei Pei, Nitin Jadhav, and Eric Chason. Correlating whisker growth and grain structure on Sn-Cu samples by real-time scanning electron microscopy and backscattering diffraction characterization. *Applied Physics Letters*, 100(22):221902, may 2012. doi:10.1063/1.4721661. URL `https://doi.org/10.1063%2F1.4721661`.

D. Peirce, R. J. Asaro, and A. Needleman. An analysis of nonuniform and localized deformation in ductile single crystals. *Acta Metallurgica*, 30(6):1087–1119, 1982. doi:10.1016/0001-6160(82)90005-0.

L. A. Pinol, J. Melngailis, H. K. Charles, D. M. Lee, R. Deacon, G. Coles, and G. Clatterbaugh. Influence of Tin Deposition Methods on Tin Whisker Formation. *IEEE Transactions on Components, Packaging and Manufacturing Technology*, 1:2028–2032, 2011.

D. A. Porter and K. E. Easterling. *Phase Transformations in Metals and Alloys*. Chapman and Hall, London, UK, 2nd edition, 1992. ISBN 978-0412450303.

G. Rauchs and J. Bardon. Identification of elasto-viscoplastic material parameters by indentation testing and combined finite element modelling and numerical optimization. *Finite Elements in Analysis and Design*, 47(7):653–667, 2011. ISSN 0168874X. doi:10.1016/j.finel.2011.01.008.

L. Reinbold, N. Jadhav, E. Chason, and K. Sharvan Kumar. Relation of Sn whisker formation to intermetallic growth: Results from a novel Sn–Cu ''bimetal ledge specimen''. *Journal of Materials Research*, 24(12):3583–3589, 2009. ISSN 0884-2914. doi:10.1557/jmr.2009.0431.

F. Roters. *Advanced Material Models for the Crystal Plasticity Finite Element Method – Development of a general CPFEM framework*. PhD thesis, RWTH Aachen, Aachen, 2011. URL `http://darwin.bth.rwth-aachen.de/opus3/volltexte/2011/3874/`.

F. Roters, P. Eisenlohr, T. R. Bieler, and D. Raabe. *Crystal Plasticity Finite Element Methods in Materials Science and Engineering*. Wiley-VCH, Weinheim, 2010a. ISBN 978-3527324477. doi:10.1002/9783527631483.

F. Roters, P. Eisenlohr, L. Hantcherli, D. D. Tjahjanto, T. R. Bieler, and D. Raabe. Overview of constitutive laws, kinematics, homogenization, and multiscale methods in crystal plasticity finite element modeling: Theory, experiments, applications. *Acta Materialia*, 58:1152–1211, 2010b. doi:10.1016/j.actamat.2009.10.058.

F. Roters, P. Eisenlohr, C. Kords, D. D. Tjahjanto, M. Diehl, and D. Raabe. DAMASK: The Düsseldorf Advanced Material Simulation Kit for studying crystal plasticity using an FE based or a spectral numerical solver. In O. Cazacu, editor, *Procedia IUTAM: IUTAM Symposium on Linking Scales in Computation: From Microstructure to Macroscale Properties*, volume 3, pages 3–10, Amsterdam, 2012. Elsevier. doi:10.1016/j.piutam.2012.03.001.

F. Roters, M. Diehl, P. Shanthraj, P. Eisenlohr, C. Reuber, S. L. Wong, T. Maiti, A. Ebrahimi, T. Hochrainer, H-O Fabritius, S. Nikolov, M. Friak, N. Fujita, N. Grilli, K. G. F. Janssens, N. Jia, P. J. J. Kok, D. Ma, F. Meier, E. Werner, M. Stricker, D. Weygand, and D. Raabe. DAMASK – The Düsseldorf Advanced Material Simulation Kit for Modelling Multi-Physics Crystal Plasticity, Damage, and Thermal Phenomena from the Single Crystal up to the Component Scale. *Computational Materials Science*, 158:420–478, 2019. doi:10.1016/j.commatsci.2018.04.030.

G. Sachs. *Mitteilungen der deutschen Materialprüfungsanstalten*, chapter Zur Ableitung einer Fließbedingung, pages 94–97. Springer, Berlin, Heidelberg, 1929. doi:10.1007/978-3-642-92045-5_12.

M. Saka, F. Yamaya, and H. Tohmyoh. Rapid and mass growth of stress-induced nanowhiskers on the surfaces of evaporated polycrystalline Cu films. *Scripta Materialia*, 56(12):1031–1034, 2007. ISSN 1359-6462. doi:10.1016/j.scriptamat.2007.02.036.

R. Sánchez-Martín, M. T. Pérez-Prado, J. Segurado, J. Bohlen, I. Gutiérrez-Urrutia, J. Llorca, and J. M. Molina-Aldareguia. Measuring the critical resolved shear stresses in Mg alloys by instrumented nanoindentation. *Acta Materialia*, 71:283–292, 2014. ISSN 1359-6454. doi:10.1016/j.actamat.2014.03.014.

E. Sandnes, M.E. Williams, M.D. Vaudin, and G.R. Stafford. Equi-Axed Grain Formation in Electrodeposited Sn-Bi. *Journal of Electronic Materials*, 37(4):490–497, dec 2007. doi:10.1007/s11664-007-0369-0. URL `https://doi.org/10.1007%2Fs11664-007-0369-0`.

P. Sarobol, A. E. Pedigo, P. Su, J. E. Blendell, and C. A. Handwerker. Defect Morphology and Texture in Sn, Sn–Cu, and Sn–Cu–Pb Electroplated Films. *IEEE Transactions on Electronics Packaging Manufacturing*, 33(3):159–164, 2010. ISSN 1521-334X. doi:10.1109/TEPM.2010.2046172.

P. Sarobol, J. E. Blendell, and C. A. Handwerker. Whisker and hillock growth via coupled localized Coble creep, grain boundary sliding, and shear induced grain boundary migration. *Acta Materialia*, 61(6):1991–2003, 2013. ISSN 1359-6454. doi:10.1016/j.actamat.2012.12.019.

L. Sauter, A. Seekamp, Y. Shibata, Y. Kanameda, and H. Yamashita. Whisker mitigation measures for Sn-plated Cu for different stress tests. *Microelectronics Reliability*, 50(9-11):1631–1635, sep 2010. doi:10.1016/j.microrel.2010.07.083. URL `https://doi.org/10.1016%2Fj.microrel.2010.07.083`.

M. Schneider, F. Ospald, and M. Kabel. Computational homogenization of elasticity on a staggered grid. *International Journal for Numerical Methods in Engineering*, 105(9):693–720, 2015. doi:10.1002/nme.5008.

P. Shanthraj, P. Eisenlohr, M. Diehl, and F. Roters. Numerically robust spectral methods for crystal plasticity simulations of heterogeneous materials. *International Journal of Plasticity*, 66: 31–45, 2015. doi:10.1016/j.ijplas.2014.02.006.

P. Shanthraj, L. Sharma, B. Svendsen, F. Roters, and D. Raabe. A phase field model for damage in elasto-viscoplastic materials. *Computer Methods in Applied Mechanics and Engineering*, 312: 167–185, 2016. doi:10.1016/j.cma.2016.05.006.

P. Shanthraj, M. Diehl, P. Eisenlohr, F. Roters, and D. Raabe. *Handbook of Mechanics of Materials*, chapter Spectral Solvers for Crystal Plasticity and Multi-physics Simulations, pages 1347–1372. Springer, Singapore, 2019. ISBN 978-981-10-6855-3. doi:10.1007/978-981-10-6855-3_80-3.

W. Shim, J. Ham, K-Il Lee, W. Y. Jeung, M. Johnson, and W. Lee. On-Film Formation of Bi Nanowires with Extraordinary Electron Mobility. *Nano Letters*, 9(1):18–22, 2009. ISSN 1530-6984. doi:10.1021/nl8016829.

J. W. Shin and E. Chason. Stress behavior of electroplated Sn films during thermal cycling. *Journal of Materials Research*, 24(04):1522–1528, 2009a. ISSN 0884-2914. doi:10.1557/jmr.2009.0172.

Jae Wook Shin and Eric Chason. Stress behavior of electroplated Sn films during thermal cycling. *Journal of Materials Research*, 24(04):1522–1528, apr 2009b. doi:10.1557/jmr.2009.0172. URL `https://doi.org/10.1557%2Fjmr.2009.0172`.

R. S. Sidhu and N. Chawla. Thermal Fatigue Behavior of Sn-Rich (Pb-Free) Solders. *Metallurgical and Materials Transactions A*, 39(4):799–810, 2008. doi:10.1007/s11661-008-9480-y.

S. Singer and J. Nelder. Nelder-Mead algorithm. *Scholarpedia*, 4(7):2928–, 2009. doi:10.4249/scholarpedia.2928.

J. Smetana. Theory of Tin Whisker Growth: ''The End Game''. *IEEE Transactions on Electronics Packaging Manufacturing*, 30(1):11–22, 2007. doi:10.1109/TEPM.2006.890645.

M. Sobiech, U. Welzel, E. J. Mittemeijer, W. Hügel, and A. Seekamp. Driving force for Sn whisker growth in the system Cu–Sn. *Applied Physics Letters*, 93(1):011906–, 2008. doi:10.1063/1.2953973.

M. Sobiech, C. Krüger, U. Welzel, J.Y. Wang, E.J. Mittemeijer, and W. Hügel. Evolution of microstructure and stress of and associated whisker growth on Sn layers sputter-deposited on Cu substrates. *Journal of Materials Research*, 25(11):2166–2174, nov 2010. doi:10.1557/jmr.2010.0276. URL `https://doi.org/10.1557%2Fjmr.2010.0276`.

M. Sobiech, J. Teufel, U. Welzel, E. J. Mittemeijer, and W. Hügel. Stress Relaxation Mechanisms of Sn and SnPb Coatings Electrodeposited on Cu: Avoidance of Whiskering. *Journal of Electronic Materials*, 40(11):2300–2313, 2011. ISSN 0361-5235. doi:10.1007/s11664-011-1737-3.

J. Spahn, H. Andrä, M. Kabel, and R. Müller. A multiscale approach for modeling progressive damage of composite materials using fast Fourier transforms. *Computer Methods in Applied Mechanics and Engineering*, 268:871–883, 2014. ISSN 0045-7825. doi:10.1016/j.cma.2013.10.017.

J. Stein, C. A. C. Tineo, U. Welzel, W. Huegel, and E. J. Mittemeijer. Microstructural Development and Possible Whiskering Behavior of Thin Sn Films Electrodeposited on Cu(Zn) Substrates. *Journal of Electronic Materials*, 44(3):886–894, 2015a. ISSN 0361-5235. doi:10.1007/s11664-014-3571-x.

J. Stein, U. Welzel, A. Leineweber, W. Huegel, and E. J. Mittemeijer. The crystallographic growth directions of Sn whiskers. *Acta Materialia*, 86:102–109, 2015b. ISSN 1359-6454. doi:10.1016/j.actamat.2014.12.004.

C-H Su, H. Chen, H-Y Lee, and A. T. Wu. Controlled positions and kinetic analysis of spontaneous tin whisker growth. *Applied Physics Letters*, 99(13):131906–, 2011. ISSN 0003-6951. doi:10.1063/1.3643472.

Y. Sun, E. N. Hoffman, P-S Lam, and X. Li. Evaluation of local strain evolution from metallic whisker formation. *Scripta Materialia*, 65(5):388–391, 2011. ISSN 1359-6462. doi:10.1016/j.scriptamat.2011.05.007.

D. Susan, J. Michael, R. P. Grant, B. McKenzie, and W. G. Yelton. Morphology and Growth Kinetics of Straight and Kinked Tin Whiskers. *Metallurgical and Materials Transactions A*, 44(3): 1485–1496, 2013. doi:10.1007/s11661-012-1488-7.

B. Svendsen, P. Shanthraj, and D. Raabe. Finite-deformation phase-field chemomechanics for multiphase, multicomponent solids. *Journal of the Mechanics and Physics of Solids*, 2017. ISSN 0022-5096. doi:10.1016/j.jmps.2017.10.005.

G. I. Taylor. Plastic strain in metals. *Journal of the Institute of Metals*, 62:307–324, 1938.

K. N. Tu. Interdiffusion and reaction in bimetallic Cu-Sn thin films. *Acta Metallurgica*, 21(4): 347–354, 1973. ISSN 0001-6160. doi:10.1016/0001-6160(73)90190-9.

K. N. Tu. Irreversible processes of spontaneous whisker growth in bimetallic Cu-Sn thin-film reactions. *Physical Review B*, 49(3):2030–2034, 1994. doi:10.1103/PhysRevB.49.2030.

K. N. Tu and J. C. M. Li. Spontaneous whisker growth on lead-free solder finishes. *Materials Science and Engineering A*, 409(1-2):131–139, 2005. doi:10.1016/j.msea.2005.06.074.

K. N. Tu, C. Chen, and A. T. Wu. chapter Stress analysis of spontaneous Sn whisker growth, pages 269–281. Springer US, Boston, MA, 2007. ISBN 978-0-387-48431-0. doi:10.1007/978-0-387-48433-4_18.

P. T. Vianco and J. A. Rejent. Dynamic Recrystallization (DRX) as the Mechanism for Sn Whisker Development. Part I: A Model. *Journal of Electronic Materials*, 38(9):1815–1825, 2009. doi:10.1007/s11664-009-0879-z.

P. T. Vianco, M. K. Neilsen, J. A. Rejent, and R. P. Grant. Validation of the Dynamic Recrystallization (DRX) Mechanism for Whisker and Hillock Growth on Sn Thin Films. *Journal of Electronic Materials*, 44(10):4012–4034, 2015. ISSN 0361-5235. doi:10.1007/s11664-015-3779-4.

A. Vicenzo, S. Bonelli, and P. L. Cavallotti. Pulse plating of matt tin: effect on properties. *Transactions of the IMF*, 88(5):248–255, sep 2010. doi:10.1179/002029610x12791981507802. URL `https://doi.org/10.1179%2F002029610x12791981507802`.

F.C. Walsh and C.T.J. Low. A review of developments in the electrodeposition of tin. *Surface and Coatings Technology*, 288:79–94, feb 2016. doi:10.1016/j.surfcoat.2015.12.081. URL `https://doi.org/10.1016%2Fj.surfcoat.2015.12.081`.

J. S. Wang, X. J. Zheng, H. Zheng, S. T. Song, and Z. Zhu. Identification of elastic parameters of transversely isotropic thin films by combining nanoindentation and FEM analysis. *Computational Materials Science*, 49(2):378–385, 2010. ISSN 0927-0256. doi:10.1016/j.commatsci.2010.05.025.

L. Wang, R. I. Barabash, Y. Yang, T. R. Bieler, M. A. Crimp, P. Eisenlohr, W. Liu, and G. E. Ice. Experimental Characterization and Crystal Plasticity Modeling of Heterogeneous Deformation in Polycrystalline α-Ti. *Metallurgical and Materials Transactions A*, 42(3):626–635, 2011. doi:10.1007/s11661-010-0249-8.

L. Wang, Z. Zheng, H. Phukan, P. Kenesei, J-S Park, J. Lind, R. M. Suter, and T. R. Bieler. Direct measurement of critical resolved shear stress of prismatic and basal slip in polycrystalline Ti using high energy X-ray diffraction microscopy. *Acta Materialia*, 132:598–610, 2017. doi:10.1016/j.actamat.2017.05.015.

N. Wang, Y. Cai, and R. Q. Zhang. Growth of nanowires. *Materials Science and Engineering: R: Reports*, 60(1-6):1–51, 2008. ISSN 0927796X. doi:10.1016/j.mser.2008.01.001.

Y. Wang, J. E. Blendell, and C. A. Handwerker. Evolution of tin whiskers and subsiding grains in thermal cycling. *Journal of Materials Science*, 49(3):1099–1113, 2014. ISSN 0022-2461. doi:10.1007/s10853-013-7788-5.

J. Weertman and J. E. Breen. Creep of Tin Single Crystals. *Journal of Applied Physics*, 27(10): 1189–1193, 1956. ISSN 0021-8979. doi:10.1063/1.1722228.

F. Willot. Fourier-based schemes for computing the mechanical response of composites with accurate local fields. *Comptes Rendus Mécanique*, 343(3):232–245, 2015. doi:10.1016/j.crme.2014.12.005.

F. Yang and J. C. M. Li. *Lead-Free Electronic Solders*, chapter Deformation behavior of tin and some tin alloys, pages 191–210. Springer, Boston, MA, 2007. ISBN 978-0-387-48431-0. doi:10.1007/978-0-387-48433-4_12.

F. Yang and Y. Li. Indentation-induced tin whiskers on electroplated tin coatings. *Journal of Applied Physics*, 104(11):113512–, 2008. doi:10.1063/1.3033390.

Y. Yang, L. Wang, T. Bieler, P. Eisenlohr, and M. Crimp. Quantitative Atomic Force Microscopy Characterization and Crystal Plasticity Finite Element Modeling of Heterogeneous Deformation in Commercial Purity Titanium. *Metallurgical and Materials Transactions A*, 42(3):636–644, 2011. doi:10.1007/s11661-010-0475-0.

Yee-Wen Yen, Chao-Kang Li, Meng-Yu Tsou, and Pei-Sheng Shao. Substrate Shape Effect on the Sn Whisker Growth in the Electroplating Matte Sn System. *Japanese Journal of Applied Physics*, 50:01BJ07, jan 2011. doi:10.1143/jjap.50.01bj07. URL `https://doi.org/10.1143%2Fjjap.50.01bj07`.

A. Yonezu, Y. Kuwahara, K. Yoneda, H. Hirakata, and K. Minoshima. Estimation of the anisotropic plastic property using single spherical indentation—An FEM study. *Computational Materials Science*, 47(2):611–619, 2009. doi:10.1016/j.commatsci.2009.10.003.

A. Yonezu, K. Yoneda, H. Hirakata, M. Sakihara, and K. Minoshima. A simple method to evaluate anisotropic plastic properties based on dimensionless function of single spherical indentation – Application to SiC whisker-reinforced aluminum alloy. *Materials Science and Engineering: A*, 527(29-30):7646–7657, 2010. ISSN 0921-5093. doi:10.1016/j.msea.2010.08.014.

C-F Yu, C-M Chan, and K-C Hsieh. The effect of tin grain structure on whisker growth. *Microelectronics Reliability*, 50(8):1146–1151, 2010. doi:10.1016/j.microrel.2010.04.019.

C. Zambaldi and D. Raabe. Plastic anisotropy of γ-TiAl revealed by axisymmetric indentation. *Acta Materialia*, 58(9):3516–3530, 2010. doi:10.1016/j.actamat.2010.02.025.

C. Zambaldi, Y. Yang, T. R. Bieler, and D. Raabe. Orientation informed nanoindentation of α-titanium: Indentation pileup in hexagonal metals deforming by prismatic slip. *Journal of Materials Research*, 27(1):356–367, 2012. doi:10.1557/jmr.2011.334.

C. Zhang, H. Li, P. Eisenlohr, W. J. Liu, C. J. Boehlert, M. A. Crimp, and T. R. Bieler. Effect of realistic 3D microstructure in crystal plasticity finite element analysis of polycrystalline Ti-5Al-2.5Sn. *International Journal of Plasticity*, 69:21–35, 2015a. doi:10.1016/j.ijplas.2015.01.003.

M. Zhang, F. Bridier, P. Villechaise, J. Mendez, and D. L. McDowell. Simulation of slip band evolution in duplex Ti–6Al–4V. *Acta Materialia*, 58(3):1087–1096, 2010. doi:10.1016/j.actamat.2009.10.025.

P. Zhang, Y. Zhang, and Z. Sun. Spontaneous Growth of Metal Whiskers on Surfaces of Solids: A Review. *Journal of Materials Science & Technology*, 31(7):675–698, 2015b. doi:10.1016/j.jmst.2015.04.001.

J-H Zhao, P. Su, M. Ding, S. Chopin, and P. S. Ho. Microstructure-Based Stress Modeling of Tin Whisker Growth. *IEEE Transactions on Electronics Packaging Manufacturing*, 29(4):265–273, 2006. ISSN 1521-334X. doi:10.1109/TEPM.2006.887393.

O. C. Zienkiewicz. *The Finite Element Method in Structural and Continuum Mechanics*. McGraw-Hill, New York, 1967.

O. C. Zienkiewicz, R. L. Taylor, and J. Z. Zhu. *The Finite Element Method: Its Basis and Fundamentals*. Elsevier, 7 edition, 2013. ISBN 9781856176330. doi:10.1016/B978-1-85617-633-0.00019-8.